

Radio Burst and Circular Polarization Studies of the Solar Corona at Low Frequencies

*A thesis submitted to fulfill requirements for the degree of
Doctor of Philosophy*

by

Patrick I. McCauley

*School of Physics
Faculty of Science
University of Sydney
Australia*

October, 2019

Dedicated to Julie. Thanks for everything.

Declaration of originality

To the best of my knowledge, this thesis contains no copy or paraphrase of work published by another person, except where duly acknowledged in the text. This thesis contains no material which has previously been presented for a degree at the University of Sydney or any other university. I certify that the authorship attribution statements on the next page are correct.

Patrick I. McCauley

As supervisor for the candidature upon which this thesis is based, I confirm that the originality and authorship attribution statements above and on the next page are correct.

Iver H. Cairns

Included Papers and Attribution

Chapters [2–4](#) are peer-reviewed journal articles for which I was primarily responsible. They are reproduced as published aside from minor typographical changes for consistency. In addition to general manuscript comments, the main contributions of my coauthors were as follows. Cairns: general supervision and guidance, advice on experimental design and interpretation. Morgan: assistance with data reduction and advice on instrumental effects. Gibson: assistance with observation–model comparisons. Harding: assistance with flux calibration. Lonsdale & Oberoi: facilitation of data collection and advice on data reduction. White: advice on results interpretation. Mondal: independent data validation. Lenc: advice on polarimetry and instrumental effects.

Chapter [2](#) **Type III Solar Radio Burst Source Region Splitting due to a Quasi-separatrix Layer**

Patrick I. McCauley, Iver H. Cairns, John Morgan, Sarah E. Gibson, James C. Harding, Colin Lonsdale, and Divya Oberoi
Published in *The Astrophysical Journal*, [851:151 \(2017\)](#)

Chapter [3](#) **Densities Probed by Coronal Type III Radio Burst Imaging**

Patrick I. McCauley, Iver H. Cairns, and John Morgan
Published in *Solar Physics*, [293:132 \(2018\)](#)

Chapter [4](#) **The Low-Frequency Solar Corona in Circular Polarization**

Patrick I. McCauley, Iver H. Cairns, Stephen M. White, Surajit Mondal, Emil Lenc, John Morgan, and Divya Oberoi
Published in *Solar Physics*, [294:106 \(2019\)](#)

(Blue and red text denote internal and external hyperlinks, respectively.)

Other Works

The following is a reverse-chronological list of other peer-reviewed articles, excluding conference proceedings, that I have authored or coauthored. Items 1–8 were published or submitted during my PhD candidature.

1. Beardsley, A. P., et al. (57 coauthors, including **McCauley, P. I.**), *Science with the Murchison Widefield Array: Phase I Results and Phase II Opportunities*. **Publications of the Astronomical Society of Australia**, *in press*, 2019
2. Cairns, I. H., et al. (15 coauthors, including **McCauley, P.**), *Comprehensive Characterization of Solar Eruptions with Remote and In Situ Observations, and Modeling: The Major Solar Events on 4 November 2015*. **Solar Physics**, *in press*, 2019
3. Mohan, A., **McCauley, P. I.**, Oberoi, D., & Mastrano, A., *A Weak Coronal Heating Event Associated with Periodic Particle Acceleration Episodes*. **The Astrophysical Journal**, **883:45**, 2019
4. Rahman, M., **McCauley, P. I.**, & Cairns, I. H., *On the Relative Brightness of Coronal Holes at Low Frequencies*. **Solar Physics**, **294:7**, 2018
5. Kleint, L., Wheatland, M. S., Mastrano, A., & **McCauley, P. I.**, *Nonlinear Force-Free Modeling of Magnetic Field Changes at the Photosphere and Chromosphere Due to a Flare*. **The Astrophysical Journal**, **865:146**, 2018
6. Jones, G. H., et al. (19 coauthors, including **McCauley, P.**), *The Science of Sungrazers, Sunskirters, and Other Near-Sun Comets*. **Space Science Reviews**, **214:20**, 2018
7. Cairns, I. H., Lobzin, V. V., Donea, A., Tingay, S. J., **McCauley, P. I.**, et al. (46 coauthors), *Low Altitude Solar Magnetic Reconnection, Type III Solar Radio Bursts, and X-ray Emissions*. **Scientific Reports**, **8:1676**, 2018
8. Lenc, E., et al. (28 coauthors, including **McCauley, P. I.**), *The challenges of low-frequency polarimetry: lessons from the Murchison Widefield Array*. **Publications of the Astronomical Society of Australia**, **34:e040**, 2017
9. Janvier, M., Savcheva, A., Pariat, E., Tassev, S., Millholland, S., Bommier, V., **McCauley, P.**, McKillop, S., & Dougan, F., *Evolution of Flare Ribbons, Electric Currents and Quasi-separatrix Layers During an X-class Flare*. **Astronomy and Astrophysics**, **591:A141**, 2016

10. Savcheva, A., Pariat, E., McKillop, S., **McCauley, P.**, Hanson, E., Su, Y., & DeLuca, E. E., *The Relation between CME Topologies and Observed Flare Features II: Dynamical Evolution*. **The Astrophysical Journal**, **817:43**, 2016
11. Savcheva, A., Pariat, E., McKillop, S., **McCauley, P.**, Hanson, E., Su, Y., Werner, E., & DeLuca, E. E., *The Relation between CME Topologies and Observed Flare Features I: Flare Ribbons*. **The Astrophysical Journal**, **810:96**, 2015
12. Su, Y., van Ballegooijen, A. A., **McCauley, P. I.**, Ji, H., Reeves, K. K., & DeLuca, E. E., *Magnetic Structure and Dynamics of the Erupting Solar Polar Crown Prominence on 2012 March 12*. **The Astrophysical Journal**, **807:144**, 2015
13. Reeves, K. K., **McCauley, P. I.**, & Tian, H., *Direct Observations of Magnetic Reconnection Outflow and CME Triggering in a Small Erupting Solar Prominence*. **The Astrophysical Journal**, **807:7**, 2015
14. **McCauley, P. I.**, Su, Y., Schanche, N., Evans, K. E., Su, C., McKillop, S., & Reeves, K. K., *Prominence and Filament Eruptions Observed by the Solar Dynamics Observatory: Statistical Properties, Kinematics, and Online Catalog*. **Solar Physics**, **290:1703**, 2015
15. Tian, H., et al. (27 coauthors, including **McCauley, P.**), *Prevalence of Micro-Jets from the Network Structures of the Solar Transition Region and Chromosphere*. **Science**, **346:6207**, 2014
16. Raymond, J. C., **McCauley, P. I.**, Cranmer, S., & Downs, C., *The Solar Corona as Probed by Comet Lovejoy (C/2011 W3)*. **The Astrophysical Journal**, **788:152**, 2014
17. Masson, S., **McCauley, P.**, Golub, L., Reeves, K. K., & DeLuca, E., *Dynamics of the Transition Corona*. **The Astrophysical Journal**, **787:145**, 2014
18. Savcheva, A. S., McKillop, S. C., **McCauley, P. I.**, Hanson, E. M., & DeLuca, E. E., *New Sigmoid Catalog from Hinode and the Solar Dynamics Observatory: Statistical Properties and Evolutionary Histories*. **Solar Physics**, **289:3297**, 2014
19. **McCauley, P. I.**, Saar, S. H., Raymond, J. C., Ko, Y. -K., & Saint-Hilaire, P., *Extreme-Ultraviolet and X-Ray Observations of Comet Lovejoy (C/2011) in the Lower Corona*. **The Astrophysical Journal**, **768:161**, 2013
20. Cirtain, J. W., et al. (13 coauthors, including **McCauley, P.**), *Energy Release in the Solar Corona from Spatially Resolved Magnetic Braids*. **Nature**, **493:501**, 2013
21. **McCauley, P.**, Mangum, J. G., & Wootten, A., *Formaldehyde Densitometry Of Galactic Star-Forming Regions Using The H₂CO 3(12)-3(13) And 4(13)-4(14) Transitions*. **The Astrophysical Journal**, **742:58**, 2011

Acknowledgements

This thesis contains work done between 2016 and 2019, but I view it as the culmination of my scientific career to date. I have been very fortunate to interact with many wonderful people along the way, all of whom have helped me in large and small ways to achieve this goal. I will take this opportunity to acknowledge all of them, to the best of my memory, back to my earliest research experiences.

First, I am most grateful for the consistent support and encouragement from my family and friends. Particularly from my partner, Julie, my parents, Ken and Carolyn, and my brothers, Nick and Petey. I love you all.

Next, I am extremely grateful to all of my immediate supervisors. I first thank my thesis advisor at the University of Sydney, Iver Cairns. Iver consistently demonstrates great care and respect for all of his students. He was always supportive and kindly afforded me great freedom in my research direction. I next thank Kathy Reeves and the solar group at the Harvard-Smithsonian Center for Astrophysics. Kathy was a wonderful boss, and the whole group could not have been more supportive. They are responsible for my love of solar physics. I am also grateful to Jeff Mangum at the National Radio Astronomy Observatory. Jeff kindly brought me back to NRAO to finish a summer research project that I had failed to complete as an undergraduate. I would not have continued in research without that opportunity. Finally, I thank Harold Butner and William Alexander for supporting me through my first research and outreach experiences at James Madison University, which ultimately led to everything else.

In addition to my supervisors, I have been fortunate to collaborate with and receive assistance from many excellent scientists over the years. In alphabetical order, I am grateful to Alisdair Davey, Ed DeLuca, Kaitlin Evans, Sarah Gibson, Leon Golub, Natasha Hurley-Walker, Kelly Korreck, Kamen Kozarev, Emil Lenc, Colin Lonsdale, Alpha Mastrano, Don Melrose, Atul Mohan, Surajit Mondal, John Morgan, Nick Murphy, Aimee Norton, Divya Oberoi, John Raymond, Steve Saar, Pascal Saint-Hilaire, Jon Sattelberger, Antonia Savcheva,

Mike Stevens, Yingna Su, Bill Thompson, Hui Tian, Mark Weber, Mike Wheatland, Stephen White, and Trae Winter.

I have also made many great friends in my scientific journey, including several people from the previous list. My favorite part of the PhD experience was unquestionably getting to know my wonderful officemates in Sydney: Samira Tasnim, James Harding, Ron Maj, Mozibur Rahman, Fiona Schleyer, Tom Hanly, and Will Trevett. I will miss all of you. In Boston, my fellow support scientists Sean McKillop, Nicole Schanche, and Trish Jibben likewise made my time there infinitely more enjoyable. The same goes for my fellow summer students in Charlottesville: Katy Wyman, Missie Louie, Michael Lam, Jen Shitanishi, Francillia Samuel, and Brian Roper. And from the Astro Lab in Harrisonburg: Dan Simonson, Colin Wilson, Chris Wolfe, and Dillon Trewlany.

Finally, I am very grateful to the Australian government for supporting this work through an Endeavour Postgraduate Scholarship.

Abstract

This thesis presents low-frequency (80–240 MHz) radio observations of the solar corona using the *Murchison Widefield Array* (MWA). It represents the first attempt to process large amounts of solar MWA data with supercomputing facilities. This wavelength regime has been under-explored in recent years, and a number of discoveries are reported. A brief review of the solar corona and associated observations is followed by three research chapters that focus on Type III solar radio bursts and circularly-polarized emission from the quiescent corona. Finally, conclusions are presented with an eye toward future work, including a discussion of preliminary results that compare the observed polarization structure to model predictions and that report novel coronal mass ejection (CME) observations.

The first research chapter details new dynamics in a particular set of Type III bursts. The source region for each burst splits from one dominant component at higher frequencies into two increasingly-separated components at lower frequencies. For channels below ~ 132 MHz, the two components repetitively diverge at high speeds ($0.1\text{--}0.4$ c) along directions tangent to the limb, with each episode lasting just ~ 2 s. Both effects are argued to result from the strong magnetic field connectivity gradient that the burst-driving electron beams move into, which is supported by extreme ultraviolet (EUV) jet observations that outline characteristic magnetic field structures associated with coronal null points. Electrons are accelerated along neighboring field lines that are immediately adjacent in the flare site but diverge with height, causing the beams to reach the requisite height to produce radio emission at slightly different times. This produces an apparent motion that is nearly perpendicular to that of the electron beams themselves. A method for flux calibration is also developed, the structure of the quiescent corona is compared to model predictions, and a coronal hole is reported to transition from being relatively dark at higher frequencies to relatively bright at lower frequencies.

The second chapter uses Type III bursts observed at the limb to probe the coronal density structure. Assuming harmonic plasma emission, they imply

2.4–5.4 \times enhancements over canonical background levels. High densities inferred from Type III source heights can be explained by assuming that the exciting electron beams travel along overdense fibers or by radio propagation effects that may cause a source to appear at a larger height than the true emission site. The arguments for both scenarios are reviewed in light of recent results. A comparison of the extent of the quiescent corona versus model predictions is then used to conclude that propagation effects can largely but not entirely explain the apparent density enhancements for these events.

The third chapter presents the first spectropolarimetric imaging of the quiescent corona at these frequencies, including a survey of circular polarization features detected in over 100 observing runs near solar maximum. Around 700 compact polarized sources are detected with polarization fractions ranging from less than 0.5% to nearly 100%. They are interpreted as a continuum of plasma emission noise storm sources down to intensities and polarization fractions that were not previously observable. A characteristic “bullseye” structure is observed for many low-latitude coronal holes in which a central polarized component is surrounded by a ring of the opposite sense. The central component does not match the sign expected from thermal bremsstrahlung emission, which may be due to propagation effects or an alternative emission mechanism. The large-scale polarimetric structure at the lowest frequencies is shown to be reasonably well-correlated with the line-of-sight (LOS) magnetic field component inferred from a global potential field model, with the boundaries between opposite circular polarization signs being generally aligned with polarity inversion lines in the model. This is not true at the highest frequencies, however, where the LOS magnetic field direction and polarization sign are often not straightforwardly correlated.

The last chapter summarizes conclusions from the previous chapters and outlines future work on a number of open questions. These include steps toward a general understanding of Type III burst source motions, explaining the peculiar low-frequency signatures of coronal holes, using low-frequency spectropolarimetry to constrain global magnetic field models, and exploring the behavior of CMEs in low-frequency observations. Preliminary results are shared that compare observations to model predictions of circularly-polarized bremsstrahlung emission, yielding good agreement in both the qualitative structure and quantitative polarization fractions. Radio CME observations are also presented, revealing an intense arc of emission that is morphologically similar and aligned to the CME front seen in white light, which has not been observed before.

Contents

1	Introduction and Literature Review	1
1.1	The Solar Corona	1
1.2	Observing the Corona	4
1.2.1	White Light Observations	4
1.2.2	Radio Observations	5
1.2.3	Extreme Ultraviolet and Soft X-Ray Observations	7
1.2.4	High-Energy, <i>In situ</i> , and Related Observations	9
1.3	Solar Radio Emission	11
1.3.1	The Magnetoionic Modes	13
1.3.2	Bremsstrahlung (Free-Free) Emission	14
1.3.3	Gyromagnetic Emission	15
1.3.4	Plasma Emission	16
1.3.5	Electron-Cyclotron Maser Emission	18
1.3.6	Propagation Effects	19
1.4	Solar Activity	20
1.4.1	The Solar Cycle	20
1.4.2	The Solar Dynamo	22
1.4.3	Features of the Corona	25
1.4.4	Solar Flares	27
1.4.5	Coronal Mass Ejections	31
1.5	Solar Radio Bursts	33
1.5.1	Type I	34
1.5.2	Type II	35
1.5.3	Type III	35
1.5.4	Type IV	37
1.5.5	Type V	38
1.5.6	Other	38
1.6	Interferometry and Aperture Synthesis	39
1.6.1	Basic Concepts	40
1.6.2	The <i>Murchison Widefield Array</i> (MWA)	41
1.6.3	Data Reduction	43
1.7	Research Aims and Outline	44

2	Type III Solar Radio Burst Source Region Splitting Due to a Quasi-Separatrix Layer	47
2.1	Abstract	47
2.2	Introduction	48
2.3	Observations	50
2.3.1	<i>Murchison Widefield Array</i> (MWA)	53
2.3.2	<i>Solar Dynamics Observatory</i> (SDO)	56
2.4	Analysis & Results	57
2.4.1	Quiescent Structure and Model Comparison	57
2.4.2	Flux Calibration	61
2.4.3	Type III Source Structure and Motion	62
2.4.4	Magnetic Field Configuration	69
2.5	Discussion	71
2.6	Conclusion	78
3	Densities Probed by Coronal Type III Radio Burst Imaging	81
3.1	Abstract	81
3.2	Introduction	81
3.3	Observations	84
3.3.1	<i>Murchison Widefield Array</i> (MWA)	84
3.3.2	Event Selection	85
3.3.3	Context	86
3.4	Analysis and Results	90
3.4.1	Density Profiles	90
3.4.2	Electron Beam Kinematics	95
3.4.3	Propagation Effects	98
3.5	Discussion	103
3.6	Conclusion	105
4	The Low-Frequency Solar Corona in Circular Polarization	107
4.1	Abstract	107
4.2	Introduction	108
4.3	<i>Murchison Widefield Array</i> (MWA)	112
4.4	An Algorithm to Mitigate the Leakage of Stokes I into V	114
4.5	Active Region Noise Storm Sources	120
4.6	Coronal Holes	127
4.7	The Large-Scale Quiescent Structure	134
4.8	Discussion	138

4.9	Conclusion	141
5	Conclusions and Future Work	145
5.1	Results Summary	145
5.2	Type III Burst Source Motions	146
5.3	Coronal Hole Peculiarities	148
5.4	Probing the Large-Scale Magnetic Field	149
5.5	Coronal Mass Ejections	151
	References	155

Chapter 1

Introduction and Literature Review

1.1 The Solar Corona

The *solar corona* is the outer atmosphere of the Sun, which begins thousands of kilometers above the surface and extends to the outer solar system where particles from the Sun meet the interstellar medium. It can be observed by the naked eye only for brief periods during total solar eclipses because it is over a million times fainter than the Sun’s apparent visible surface, and the technology required to reveal the corona’s highly dynamic nature has been developed only fairly recently. Figure 1.1 shows a modern eclipse image alongside what is arguably the corona’s earliest surviving accurate depiction. The first definitive written reference to the corona was by the famed astronomer Johannes Kepler in his 1604 book titled *Astronomiae Pars Optica* (“The Optical Part of Astronomy”), although plausible references exist thousands of years earlier in ancient Babylonian, Greek, and Chinese texts (Golub and Pasachoff, 2010). Kepler believed the corona to be a feature of the Moon, and others would later attribute it to both the Sun and effects related to Earth’s atmosphere. Two technologies of the 1800s, photography and spectroscopy, would ultimately prove the corona to be part of the Sun.

Photographs of the same eclipse from multiple sites demonstrated that the structure of the corona does not vary between terrestrial viewing locations, implying that it cannot be an atmospheric effect (De la Rue, 1864), and images of consecutive eclipses suggested that variation in the corona’s appearance from year to year is tied to the sunspot cycle (Darwin et al., 1889). In the late 1800s, the first spectroscopic measurements of the Sun were made, resulting in the discovery of helium (Lockyer, 1920) and the identification of the characteristic solar Fraunhofer lines in the coronal spectrum (Janssen, 1873). This latter discovery demonstrated the presence of reflected sunlight and further suggested that the corona is part of the Sun. Emission from helium comes from the Sun’s lower atmosphere, but early spectroscopic observations of the corona also revealed puzzling new spectral lines (Young, 1895). Like helium, these were not consistent with any known element, leading astronomers to again posit the ex-



Figure 1.1: A modern image from the 2008 total solar eclipse (*left*) alongside a 1735 eclipse painting by Cosmas Damian Asam (*right*). The modern image is highly processed to accentuate the fine ray and loop structures, still best-observed during eclipses, and the painting is arguably the earliest surviving “accurate” representation of the corona. Image credits: Miloslav Druckmüller, Peter Aniol, Martin Dietzel, and Vojtech Rušin (*left*); Jay Pasachoff (*right*).

istence of a new element, this time called “coronium.” That hypothesis was short-lived, as laboratory experiments in the 1930s would soon demonstrate that the coronium lines actually come from highly-ionized forms of known elements such as iron and calcium (Edlén, 1945). This presented a new mystery in that the temperatures required to produce these high ionization states are in excess of one million Kelvin, much hotter than the Sun’s surface. “The coronal heating problem” remains one of the longest-standing mysteries in astrophysics and space physics (Klimchuk, 2006; De Moortel and Browning, 2015).

Temperature is now generally seen as the primary feature that delineates the Sun’s outer layers (Aschwanden, 2005; Golub and Pasachoff, 2010; Priest, 2014). Light generated in the Sun’s interior escapes through a thin layer called the *photosphere*, commonly referred to as the visible surface, which is composed primarily of neutral gas with a temperature of around 6,000 K. Above the photosphere is the *chromosphere*, which is partially ionized with temperatures upwards of 20,000–50,000 K. Then, over a few hundred kilometers known as the *transition region*, the temperature increases dramatically to beyond 1,000,000 K in the fully-ionized corona. The height of the transition region varies with location but typically occurs between 2,000 and 3,000 km above the photosphere. A schematic of the temperature and density profile from the photosphere into the corona is shown in Figure 1.2.

From its base, the corona expands outward to form the *solar wind*, a variable

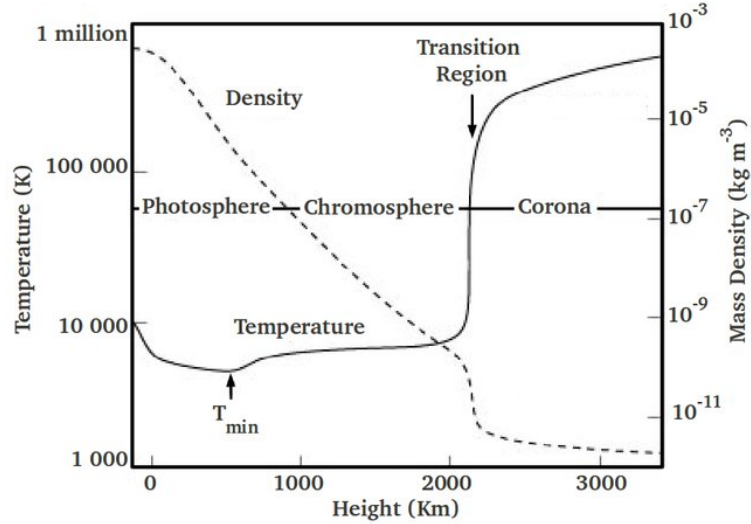


Figure 1.2: The mean variation in temperature and density as a function of height above the photosphere based on the popular VAL model (Vernazza et al., 1973, 1976, 1981). Image credit: Lang (2001).

but persistent flow of plasma that creates a cavity in the interstellar medium known as the *heliosphere*. As the boundary between the corona and the solar wind is not well-defined, a natural definition for the outermost edge of the corona is simply the *heliopause*, where the pressure from the solar wind is balanced by that of interstellar gas (Holzer, 1989; Golub and Pasachoff, 2010). However, most researchers use the term *corona* to refer to structures within less than roughly 5–10 solar radii (R_{\odot}) and the terms *solar wind* or *interplanetary medium* to refer to larger heliocentric distances. The observations presented in this thesis will primarily be confined to $\lesssim 2 R_{\odot}$ from Sun-center.

This chapter reviews some basic concepts and provides context for the research chapters to follow. Section 1.2 discusses the different types of observations used to study the corona, and Section 1.3 reviews the known solar radio emission mechanisms. Section 1.4 outlines the basic forms of solar activity, and Section 1.5 describes the different types of solar radio bursts. Section 1.6 introduces the concepts of interferometry and aperture synthesis, along with describing the radio interferometer used in this thesis. Finally, Section 1.7 describes the main research aims and outlines the subsequent chapters. Note that the references given throughout this chapter are not meant to be exhaustive; early and highly-cited papers, along with review articles and textbooks, are emphasized.

1.2 Observing the Corona

Prior to the 1930s, the corona could be observed only when the photosphere was completely occulted by the Moon during a total solar eclipse. These events occur just once every 18 months on average and are visible only from particular locations on Earth that change for each eclipse, posing obvious barriers to observation. Eclipses continue to be important to coronal research to this day (*e.g.* Phillips et al., 2000; Habbal et al., 2013), but a number of advances over the last century, beginning with the invention of the coronagraph, have made routine observations of the corona possible. This section discusses the main observation types and associated emission mechanisms considered in this thesis, along with a few additional notes on other relevant observations.

1.2.1 White Light Observations

Visible light from the corona is divided into three main components, each of which arise from different mechanisms (Rusin, 2000; Golub and Pasachoff, 2010). The K- (kontinuierlich) corona has the continuous emission spectrum of thermal blackbody radiation from the photosphere that has been Thomson scattered by coronal electrons, which produces a large degree of polarization that can be used to estimate the coronal electron density (van de Hulst, 1950; Hayes et al., 2001). The inner corona seen in Figure 1.1 is dominated by this source. Beyond around 2 solar radii, the F- (Fraunhofer) corona begins to exceed the brightness of the K-corona. Like the K-corona, the F-corona is also produced by scattering of photospheric light, but instead by dust particles in the ecliptic plane. The F-corona is therefore not directly-related to the corona as we understand it today and may instead be considered inner zodiacal light. The E- (emission) corona is comprised of isolated spectral lines emitted by ions in the high-temperature coronal plasma, making it the only component that is produced directly by the corona itself. Although much fainter in integrated light than both the K- and F-coronas, the E-corona can be observed using narrowband filters around the spectral line of interest.

Observing coronal white light outside of an eclipse requires the use of a coronagraph. A coronagraph is a telescope that incorporates an occulting disk to block light coming from the photosphere, creating an artificial eclipse. While this is conceptually straightforward, it is very difficult in practice to block enough photospheric light from reaching the detector because of scattering within the telescope after light strikes the occulting disk. Bernard Lyot was

the first to succeed in sufficiently limiting internal scattering, which revolutionized the study of the corona (Lyot, 1939). Coronagraph observations on Earth are limited by the natural atmospheric scattering of sunlight and can be made only from high-altitude observatories. This limitation can be overcome by placing the telescope in space, which was first done successfully in 1963 using a sounding rocket and later made routine with satellite observations in 1971 (Koutchmy, 1988). One of the most prolific modern coronagraphs is the *Large Angle and Spectrometric Coronagraph* (LASCO; Brueckner et al., 1995) onboard the space-based *Solar and Heliospheric Observatory* (SOHO; Domingo et al., 1995). LASCO data is shown in Section 1.4.5 and will be used in Chapter 3.

1.2.2 Radio Observations

Coronagraph observations are limited in that they cannot observe the corona directly above the photosphere. Fortunately, as a consequence of its high temperature, the corona produces significant emission at radio, extreme ultraviolet (EUV), and X-ray wavelengths. Unlike visible light, this radiation far exceeds that produced by the photosphere, allowing the corona to be observed directly without requiring an eclipse or occulting disk.

Solar radio emission was first reported in the scientific literature by Reber (1944), which corresponded to high-frequency microwave emission from the chromosphere. Intense low-frequency (metric) radio burst emission from the corona was actually detected two years earlier by British radar operators but was not publicly reported until after World War II (Hey, 1946). One of the early achievements of solar radio astronomy was to independently verify the high temperature of the corona, which was identified previously through optical spectroscopy but remained controversial. Beginning with wavelengths below ≈ 1 cm, the quiescent solar radio emission starts to exceed that of the Sun's blackbody spectrum (Pawsey, 1946). Ginzburg (1946) showed that this excess radiation is due to thermal bremsstrahlung emission from the hot coronal plasma. This mechanism, along with the others known to generate solar radio emission, will be reviewed in Section 1.3.

Prior to 1950, most instruments observed at a single frequency (Pick and Vilmer, 2008). Simultaneous observations of radio bursts at several frequencies showed that the onset times varied, suggesting that the bursts were related to disturbances that propagate outward through the corona to excite emission at different frequencies as they move through plasma of different densities (Payne-

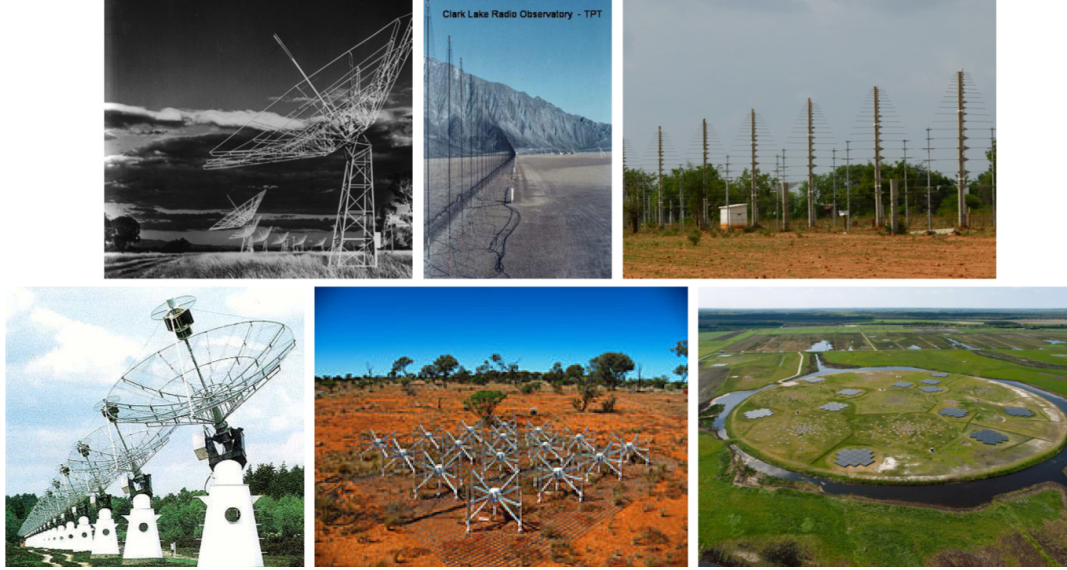


Figure 1.3: Antennas from different low-frequency ($\lesssim 300$ MHz) radio imaging arrays, past and present. From left to right, top to bottom: the *Culgoora Radioheliograph*, *Clark Lake Radioheliograph*, *Guaribidanur Radioheliograph*, *Nançay Radioheliograph*, *Murchison Widefield Array*, and *Low Frequency Array*.

Scott et al., 1947). This motivated the development of solar *radiospectrographs* that could continuously observe the Sun over a range of frequencies. These instruments produce *dynamic spectra* that show the solar emission as a function of both time and frequency. Much of the nomenclature that characterizes the Sun’s behavior at radio wavelengths is based on the appearance of features in dynamic spectra, such as the classification of solar radio bursts by Wild and McCready (1950). Examples of dynamic spectra will be shown with the discussion of radio bursts in Section 1.5.

Radiospectrograph data are limited in that they cannot spatially localize or track features. Generating a radio image of the Sun with adequate time resolution requires an interferometer. *Interferometry* combines the signals received from multiple antennas and will be described in Section 1.6. In the 1950s, a number of simple interferometers with small numbers of elements provided limited tracking of radio bursts, but routine imaging of the corona began with the *Culgoora Radioheliograph* (43–327 MHz; Wild, 1970; Sheridan et al., 1972, 1983). *Radioheliographs* are interferometers that are dedicated to solar observing, although instruments primarily used for other astrophysical sources may also target the Sun. In addition to improved tracking of radio bursts, these instruments allow the quiescent structure to be observed and compared to that

at other wavelengths.

In recent decades, two of the most notable radio imagers dedicated to solar physics have been the *Nançay Radioheliograph* (150–450 MHz; Kerdraon and Delouis, 1997) and the *Nobeyama Radioheliograph* (17–34 GHz; Nakajima et al., 1994). General astrophysical instruments like the *Very Large Array* (VLA; currently 1–50 GHz; Perley et al., 2011) and the *Atacama Large Millimeter Array* (ALMA; 84–950 GHz; Wedemeyer et al., 2016) have also made important solar physics contributions. Since the decommissioning in the 1980s of the *Culgoora Radioheliograph* and later the *Clark Lake Radioheliograph* (20–125 MHz; Kundu et al., 1983), there has been little investment in new low-frequency ($\lesssim 300$ MHz) imaging instrumentation. A notable exception to this is the *Guaribidanur Radioheliograph*, which has been operating since 1997 at 80 MHz (Ramesh et al., 1998, 2005).

In 2012, two new low-frequency interferometers were commissioned, the *Murchison Widefield Array* (MWA; 80–300 MHz; Tingay et al., 2013a) and the *Low Frequency Array* (LOFAR; 10–240 MHz; van Haarlem et al., 2013). While they are not dedicated solar telescopes, these instruments can produce the most sensitive images of the corona to date and represent a significant advance over previous observational capabilities, with improvements in sensitivity, simultaneous frequency coverage, and both spatial and time resolution. This thesis presents results from the MWA, which will be discussed further in Section 1.6.2, and Figure 1.3 shows images of antennas from the low-frequency arrays listed above. Two additional instruments for which solar studies are planned are the *Long Wavelength Array* (LWA; 10–88 MHz; Ellingson et al., 2009) and the *Owens Valley Long Wavelength Array* (OVRO-LWA; 24–82 MHz).

1.2.3 Extreme Ultraviolet and Soft X-Ray Observations

Due to its high temperature, the corona’s radiation energy comes primarily at extreme ultraviolet (EUV) and soft X-ray (SXR) wavelengths (Golub and Pasachoff, 2010). Although the Sun and its corona are composed almost entirely of hydrogen and helium, these elements do not contribute significantly to coronal emission because they are completely ionized at coronal temperatures. Instead, the corona radiates energy predominantly through isolated spectral lines of trace heavy elements such as carbon, oxygen, silicon, and iron. These elements are stripped of their outer shell electrons but still retain some or many of their inner shell electrons. Several effects, primarily collisions with free elec-

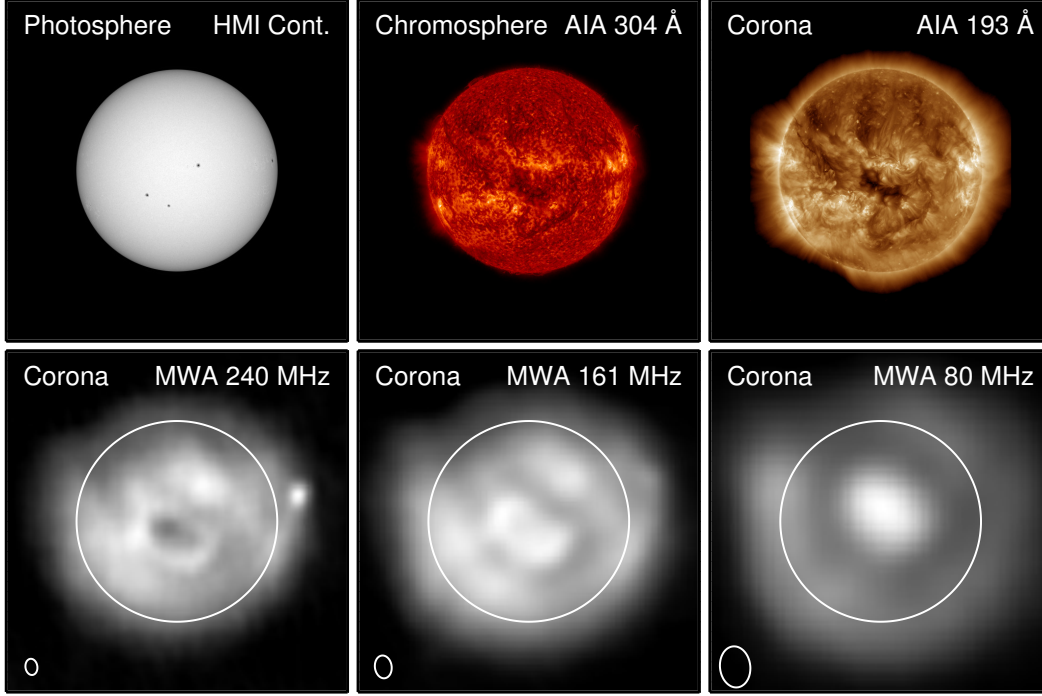


Figure 1.4: *Left-to-right, upper row:* A white light observation of the photosphere, an EUV observation of the chromosphere, and an EUV observation of the corona. *Lower row:* Radio observations of the corona at three frequencies; lower frequencies correspond to larger heights above the photosphere. The upper and lower rows come from the SDO and MWA, respectively.

trons, may then either excite one of the electrons to a higher energy level or remove it from the atom, producing a higher ionization state. When an electron recombines with an ion or a bound electron decays to a lower energy state, a photon is released to balance the energy lost by the atom in that transition. This process predominantly generates EUV and SXR photons because of the ionization states typical of the corona.

Observations at these wavelengths may either be narrowband, targeting just one or more of these spectral line transitions, or broadband, incorporating a range of spectral lines. EUV and X-ray emission is blocked by Earth's atmosphere, meaning that the observations must be conducted from space and thus began after ground-based white-light and radio observations. Attempts to detect X-rays from space began with the U.S. rocketry program after WWII, and techniques for producing high-resolution images developed substantially in the 1960s (Vaiana et al., 1973a). A number of satellite missions culminated in the EUV and X-ray instrumentation flown on the *Skylab* space station (Va-

iana et al., 1973b; Tousey et al., 1973), which is arguably the most productive space-based solar physics mission to date (Golub and Pasachoff, 2010).

Many of the terms used to describe the general features of the solar corona, which will be described in Section 1.4.3, were developed based on *Skylab* observations and those that immediately preceded it. Since *Skylab*, there have been several EUV and SXR telescopes, such as those on the *Yohkoh* (Ogawara et al., 1991), *Hinode* (Kosugi et al., 2007), SOHO (Domingo et al., 1995), STEREO (Kaiser et al., 2008), and PROBA-2 (Berghmans et al., 2006) satellites. The most widely-used instrument of this type today is the *Atmospheric Imaging Assembly* (AIA; Lemen et al., 2012) onboard the *Solar Dynamics Observatory* (SDO; Scherrer et al., 2012), which will feature in each of the research chapters. EUV and radio images of the corona are compared in Figure 1.4, along with corresponding images of the photosphere and chromosphere.

1.2.4 High-Energy, *In situ*, and Related Observations

The observations from the previous subsections are the most relevant to this thesis, but a number of other types are also important to coronal studies. While the temperatures in the corona are not high enough to produce appreciable hard X-ray (HXR) radiation during quiescent periods, intense solar flares can produce significant high energy emission up to and including gamma rays (Ramaty et al., 1975). Observations at these wavelengths have been critical to understanding the physical processes of solar flares and their impacts. The most significant recent mission in this regime was the *Reuven Ramaty High Energy Solar Spectroscopic Imager* (RHESSI; Lin et al., 2002), which was launched in 2002 and decommissioned in 2018.

In addition to remote sensing, coronal studies benefit from *in situ* observations, which refer to those from instruments that are immersed in the interplanetary medium and can directly probe the plasma of the solar wind. Several instruments have been placed near Earth at the L1 Lagrangian point, where satellites may orbit the Sun at a fixed location with respect to Earth. These instruments provide routine measurements of Earth’s “space weather” environment. Examples include SOHO, the *Advanced Composition Explorer* (ACE; Stone et al., 1998), and the *Wind* spacecraft (Ogilvie and Desch, 1997). Similar measurements have been made elsewhere in the heliosphere, notably by the *Helios* (Schwenn et al., 1975) and *Ulysses* (Bame et al., 1992) missions near the Sun and the *Voyager* spacecraft in the outer solar system (Bridge et al., 1977). *In situ* observations have contributed many important results, but one

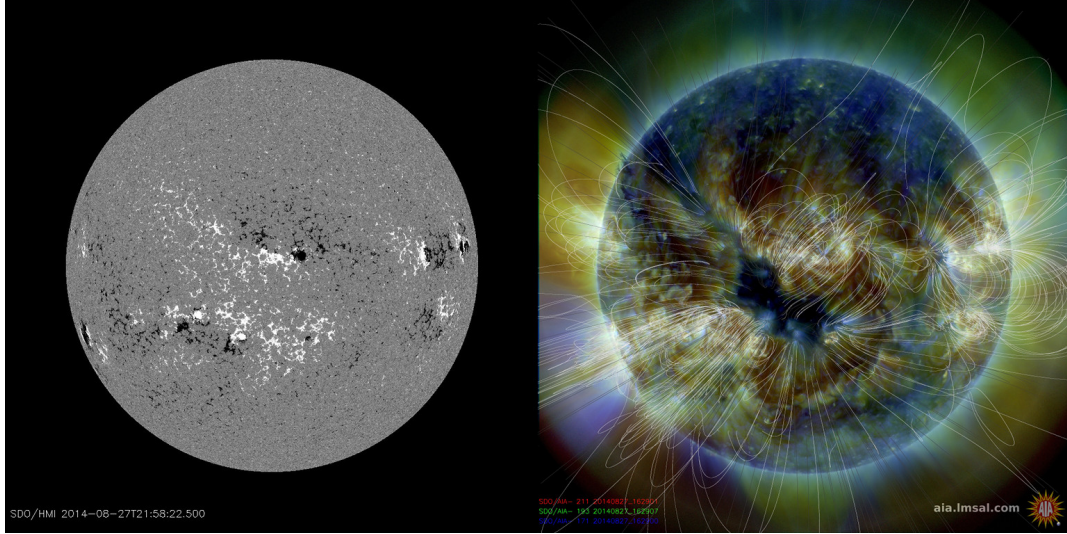


Figure 1.5: Magnetogram observation (*left*) showing the photospheric magnetic field strength next to an EUV observation (*right*) of the corona overlaid with magnetic field lines extrapolated from magnetograms. The EUV image is a red-green-blue composite of three spectral channels, the time period shown is the same as in Figure 1.4, and the observations come from the SDO. Image credit: Lockheed Martin Solar and Astrophysics Laboratory (LMSAL).

of particular interest here was the direct detection of the electrons and plasma oscillations that were theorized to produce Type III solar radio bursts (Frank and Gurnett, 1972; Lin et al., 1973; Gurnett and Anderson, 1976), which will be described in Section 1.5.3.

Finally, while they will not be reviewed here, observations of other parts of the Sun are of course also important to understanding the corona. Of particular importance to this thesis are observations of the photospheric magnetic field. The photospheric field can be measured using the Zeeman effect (Hale, 1908; Babcock, 1953), which is the splitting of spectral lines in the presence of a magnetic field, and such observations are commonly-referred to as *magnetograms*. Today, the most widely-used magnetograms are from the SOHO’s *Michelson Doppler Imager* (MDI; Scherrer et al., 1995) and the SDO’s *Helioseismic and Magnetic Imager* (HMI; Scherrer et al., 2012). Magnetograms are extremely important for coronal studies because they can be used to estimate the coronal magnetic field by extrapolation from the photosphere, and the coronal field is what largely determines both the structure of and activity within the corona. Magnetogram data is presented directly in Chapter 4 and indirectly through models in Chapters 2 and 3.

Extrapolations from the photospheric field are needed because the coronal

magnetic field is very difficult to measure directly. Coronal magnetic field measurements are possible from near-infrared and optical coronagraph observations of the Zeeman and Hanle effects, the latter of which refers to polarization state changes due to the presence of a magnetic field, and a number of advances have been made in recent years on this topic (*e.g.* Tomczyk et al., 2008; Kramar et al., 2016). Polarimetric radio observations may also be used to measure the coronal magnetic field at specific locations (*e.g.* Dulk and McLean, 1978; White and Kundu, 1997), but it has not yet been possible to probe the global coronal field structure with radio observations because of limited instrument sensitivity. Chapter 4 (McCauley et al., 2019) will present the first circular polarization images of the quiescent corona at low frequencies, which will be used to probe the magnetic field in future studies.

1.3 Solar Radio Emission

The Sun produces radio emission largely by converting the energy of moving electrons into radiation via several mechanisms that operate in different contexts with varying levels of complexity. *Incoherent emission* refers to the summation of radiation generated independently by many individual particles, which may be accelerated by Coulomb collisions, as in bremsstrahlung emission, or by gyration in a magnetic field, as in gyromagnetic emission. *Coherent emission* refers to mechanisms that convert electron energy into radiation more efficiently due to electrons emitting in phase or through the development of instabilities that amplify particular wave modes. The coherent mechanisms relevant for solar physics are plasma emission and electron-cyclotron maser emission, both of which require particles to be accelerated by energetic events like solar flares.

Incoherent and coherent mechanisms are often distinguishable by their brightness temperatures $[T_B]$, a common measure of intensity in radio astronomy. A *brightness temperature* is the temperature that a blackbody would need to have to reproduce an observed intensity from a source of a particular size and at a particular frequency. A *blackbody* is a theoretical construct that exists in thermal equilibrium at a single temperature, absorbs all incident radiation perfectly, and emits radiation as a function only of its temperature in accordance with Planck’s Law. For incoherent emission, the brightness temperature is equal to or less than the actual source temperature (*e.g.* the electron temperature), depending primarily on the density and temperature of emitting material along the line of sight. Coherent emission can have brightness temperatures

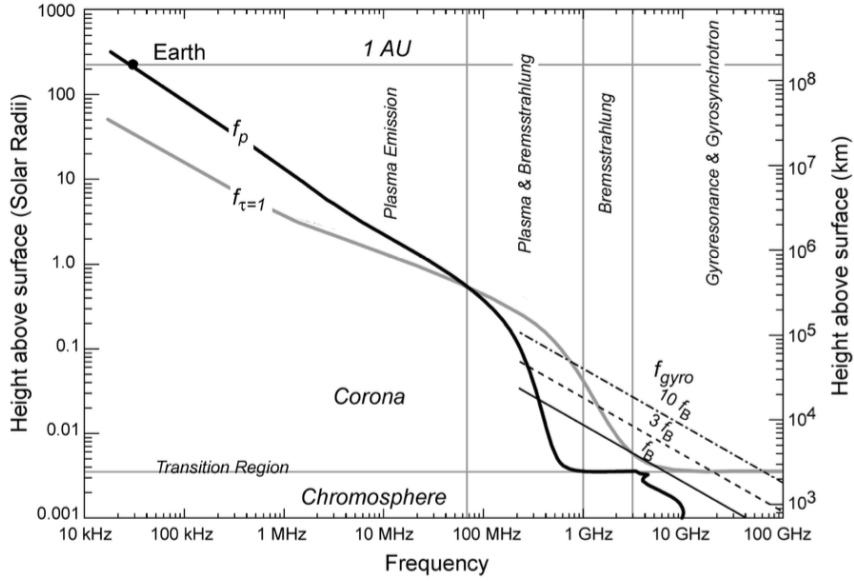


Figure 1.6: The solar atmosphere's characteristic frequencies based on standard models; low heights correspond to active regions. The uppermost curve at any location indicates the dominant emission mechanism based on the relative sizes of f_p , f_B , and the frequency at which bremsstrahlung emission reaches an optical depth of one [$f_{\tau=1}$]. Image credit: Gary and Hurford (2005)

that far exceed the source temperature, implying that the emission mechanism must be nonthermal. However, coherent mechanisms may also produce weak signals that are not distinguishable from incoherent emission using brightness temperature alone.

The emission frequency for each mechanism is determined by the plasma's characteristic frequencies, which depend on parameters such as density and magnetic field strength. Two of the most important quantities are the *electron plasma frequency*,

$$f_p = \sqrt{\frac{e^2 n_e}{\pi m_e}} \approx 0.009 \sqrt{n_e} \text{ MHz}, \quad (1.1)$$

and the *electron gyrofrequency*, also called the *electron-cyclotron frequency*,

$$f_B = \frac{eB}{2\pi m_e c} \approx 2.8B \text{ MHz}, \quad (1.2)$$

where n_e is the electron density in cm^{-3} , B is the magnetic field strength in G, e is the electron charge, m_e is the electron mass, and c is the speed of light. The relative sizes of these two frequencies largely determines the dominant emission

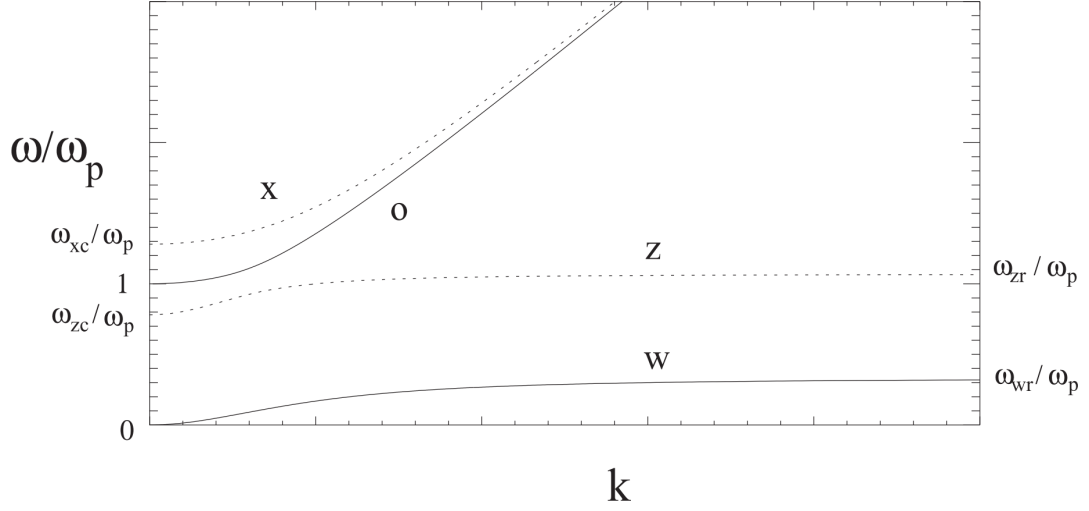


Figure 1.7: Dispersion relations for the magnetoionic modes in a magnetized plasma for which the electron cyclotron frequency $[\Omega_e]$ is smaller than the plasma frequency $[\omega_p]$. The two free-space (electromagnetic radiation) modes are at the top, and ω_{xc} refers to the x -mode cutoff, the frequency above which x -mode radiation begins. This plot uses angular unit notation as opposed to the f_B and f_p in the text for Ω_e and ω_p , respectively. Image credit: Iver Cairns

mechanism in a particular environment. Figure 1.6 shows the characteristic frequencies of the solar atmosphere and their associated emission mechanisms, which will be described in the following subsections.

1.3.1 The Magnetoionic Modes

Before describing the emission mechanisms, it is important to first introduce the magnetoionic theory that is commonly used to describe the propagation of electromagnetic waves in an ionized medium under the presence of an external magnetic field. More detailed reviews of the following discussion can be found in several textbooks (*e.g.* Ginzburg, 1970; Melrose, 1986; Aschwanden, 2005; Koskinen, 2011). The solar corona is most often treated with the cold plasma approach, which assumes that the characteristic velocities of the waves are much faster than the thermal velocity of the plasma particles, allowing thermal effects to be neglected. This approach also generally ignores the motions of ions and assumes that the particles do not interact through collisions.

Under these approximations, the dispersion equation for electromagnetic waves has the four solutions shown in Figure 1.7 for the case where $f_p > f_B$. The two uppermost curves correspond to the two modes that can escape the plasma as radiation (radio waves). These are referred to as the *ordinary* [o] and

extraordinary [x] modes. The ordinary mode is so-named because the plasma response is the same as if there were no magnetic field, while the x -mode has a somewhat different refractive index. Each mode is polarized in opposite senses that depend on the angle with respect to the magnetic field. In most cases, a so-called quasi-circular approximation applies (Melrose, 1986), and the two modes are 100% circularly-polarized with opposite senses. For the x -mode, the electric field vector of the wave rotates in the same direction as the gyromotion of electrons around the magnetic field, whereas an o -mode wave's electric field vector rotates in the opposite direction.

A net circular polarization arises when the two modes are received with unequal intensities, which is characterized by the degree of circular polarization relative to the total intensity. The polarization degree depends on the emission mechanism, plasma parameters, and several effects that may modulate the polarization state during propagation to the observer. These dependencies make the degree of polarization a powerful diagnostic, and Chapter 4 (McCauley et al., 2019) will present the first circular polarization observations of the low-frequency corona that are sensitive enough to detect the weak polarization signals of thermal bremsstrahlung emission and very weak plasma emission sources.

Circularly-polarized radio emission is most prevalent in the corona, but there are circumstances and processes that may produce linear polarizations. However, linearly-polarized radiation propagating through a magnetized plasma experiences Faraday rotation that, during propagation, rotates the polarization plane as a function of frequency and magnetic field strength. The magnetic field strength in the corona is large enough that over a typical observing bandwidth, Faraday rotation will produce many turns of the electric field vector, thereby washing out any linear polarization signal (*e.g.* Bastian, 2010; Gibson et al., 2016). Linear polarizations have not been reported from the radio Sun except for a few cases at GHz frequencies (Alissandrakis and Chiuderi-Drago, 1994; Segre and Zanza, 2001). It is possible, however, to observe linearly-polarized background astrophysical sources that are occulted and Faraday-rotated by the corona, which can be used as a magnetic field diagnostic at large heliocentric distances (Spangler, 2007; Ingleby et al., 2007; Ord et al., 2007).

1.3.2 Bremsstrahlung (Free-Free) Emission

Bremsstrahlung emission, from the German “braking radiation,” refers to electromagnetic waves produced by the acceleration of charged particles, which con-

verts some of the particles' kinetic energy into radiation. The term *bremsstrahlung* was introduced in 1909 in reference to emission generated by electrons in cathode ray tube experiments, and a historical review of the concept is given by Wheaton (2009). Of primary importance are free electrons that are deflected by the Coulomb fields of ions. In a fully-ionized medium like the corona, this is often referred to as *free-free* emission because it does not involve particles transitioning between bound states in an atom. *Thermal bremsstrahlung* refers to radiation produced by a plasma in thermal equilibrium, and this is the dominant source of quiescent emission from the corona at low frequencies (Ginzburg, 1946; Dulk, 1985; Aschwanden, 2005).

The emission frequency is tied to the plasma's electron density through the electron plasma frequency $[f_p]$ from Equation 1.1. Only emission at frequencies at or below f_p can be produced by a plasma with the corresponding density. This limit corresponds to the region below ω_p in Figure 1.7 and may be understood in terms of the refractive index, which is imaginary for frequencies smaller than the plasma frequency, indicating that those waves cannot propagate in the medium (Melrose, 1986; Aschwanden, 2005). The density of the corona generally decreases with height above the photosphere, meaning that lower frequency emission corresponds to larger heights and that the corona appears larger with decreasing frequency. This effect is illustrated by the increasing height of the f_p curve with decreasing frequency in Figure 1.6. Very dense coronal structures may generate bremsstrahlung emission with frequencies into the GHz range, but canonical background coronal density models correspond to frequencies below ≈ 300 MHz (*e.g.* Newkirk, 1961; Saito et al., 1977).

Early radio astronomers quickly recognized that the solar brightness temperature at wavelengths longer than ≈ 1 cm is significantly greater than a blackbody with the Sun's surface temperature of $\approx 5,800$ K (Appleton, 1945; Martyn, 1946; Pawsey, 1946). Ginzburg (1946) showed that this excess could be explained by thermal bremsstrahlung emission from a much hotter corona, the existence of which remained controversial after such high temperatures were first identified using optical spectroscopy. The physics of bremsstrahlung emission in the solar context has since been reviewed by many authors (*e.g.* Dulk, 1985; McLean and Labrum, 1985; Aschwanden, 2005).

1.3.3 Gyromagnetic Emission

Like bremsstrahlung, gyromagnetic emission converts the kinetic energy of charged particles, mainly electrons, into radiation. In this case, the presence of

Ch. 1 Introduction

a magnetic field produces a spiral gyromotion in a particle's trajectory along a particular magnetic field line, resulting in a centripetal acceleration (Dulk, 1985). Different terminology is used for the same basic phenomenon depending on the particle's rotation speed about the magnetic field. *Gyroresonance* emission refers to non-relativistic speeds and is sometimes also called *cyclotron* or *magneto-bremsstrahlung* emission. *Gyrosynchrotron* refers to mildly relativistic speeds, where the particles rotate at a small but significant fraction of the speed of light. *Synchrotron* emission refers to the relativistic case where the speeds approach that of light.

For solar radio emission, we are mainly concerned with gyroresonance and gyrosynchrotron emission, though synchrotron emission may be important in certain contexts (*e.g.* Winske et al., 1983; Bastian, 2007). In each case, emission occurs near the electron gyrofrequency [f_B] from Equation 1.2 or one of its harmonics, which depend primarily on the magnetic field strength, divided by the Lorentz factor [γ]. In the low-frequency observations discussed in this thesis, gyromagnetic emission does not contribute significantly. However, in dense regions of the corona where the magnetic field strength is strong, higher-frequency observations of gyroresonance emission can be used to measure the magnetic field strength (Akhmedov et al., 1982; White and Kundu, 1997; White, 2005). Gyroresonance emission also dominates over bremsstrahlung throughout the chromosphere, where the densities and magnetic field strengths are higher than in the corona such that $f_B > f_p$ (see Figure 1.6). Gyrosynchrotron emission is also the accepted mechanism for certain microwave radio bursts from the chromosphere and is thought to contribute significantly to specific energetic events in the corona, namely Type IV bursts and coronal mass ejections (*e.g.* Melrose, 1980; Alissandrakis, 1986; Nindos et al., 2008).

1.3.4 Plasma Emission

The most common form of coherent radio emission from the Sun is *plasma emission*, which refers to a set of related processes that partially convert the energy of Langmuir waves into radiation (Melrose, 2009). A flowchart of the basic plasma emission stages is shown in Figure 1.8. *Langmuir waves*, also referred to as *electron plasma waves* or simply *plasma oscillations*, are oscillations of a plasma's electron density (Tonks and Langmuir, 1929). They occur when a plasma is perturbed such that an electron population is displaced with respect to the ions, and the Coulomb force then pulls the electrons back, leading them to oscillate back and forth.

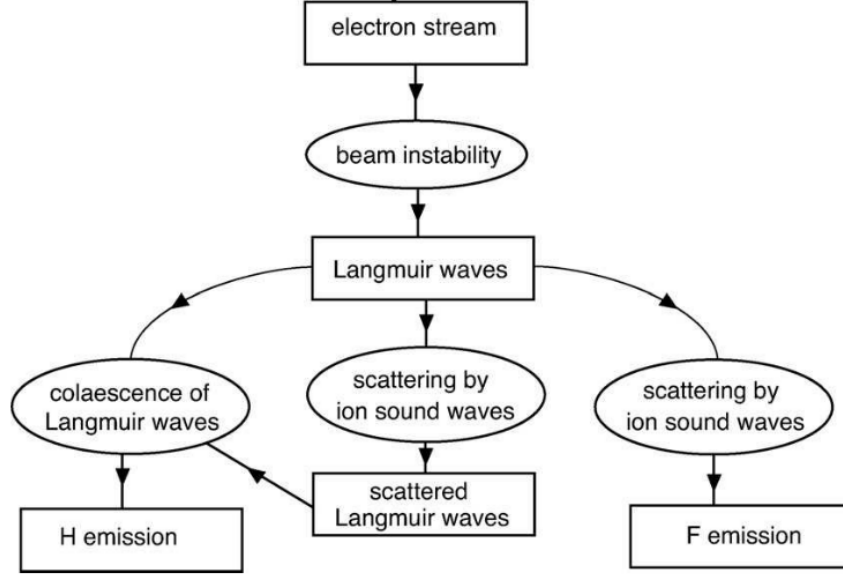


Figure 1.8: A flow chart outlining the stages of plasma emission, which is responsible for most types of solar radio bursts. Image credit: Melrose (2009)

The process that produces Langmuir waves in the solar corona is generally assumed to be an instability driven by a beam of nonthermal electrons that move through the background plasma after being accelerated by magnetic reconnection or a shock wave (Robinson and Cairns, 2000). Langmuir waves are produced by an electron beam through the *two-stream instability*, which is often referred to as the *bump-on-tail instability* in cases where an electron stream is injected into a plasma, creating a “bump” on the high-energy tail of the plasma’s particle velocity distribution. This bump produces a region of wavevector space in which the number of electrons transferring energy to Langmuir waves exceeds the reverse case, leading to exponential Langmuir wave growth. A small fraction of the energy in the Langmuir waves can then be converted into electromagnetic radiation through interactions with other wave modes, namely ion sound waves (Cairns, 1987a,b; Robinson and Cairns, 2000; Melrose, 2009). Depending on the wave interactions outlined by the flowchart in Figure 1.8, radio emission may be produced either at f_p or its harmonic $[2f_p]$.

The theory of plasma emission was first proposed by Ginzburg and Zhelezniakov (1958) to address observations of radio bursts for which the emission frequency drifts to lower values, which was interpreted in terms of disturbances that propagate outward through the corona to excite radio emission at the local

Ch. 1 Introduction

plasma frequency (*e.g.* Payne-Scott et al., 1947). Plasma emission theory has since been developed by many authors (see reviews by Robinson and Cairns, 2000; Melrose, 2009) and is thought to operate in different contexts to produce most types of coronal radio bursts (*e.g.* Dulk, 1985), which will be reviewed in Section 1.5.

1.3.5 Electron-Cyclotron Maser Emission

The word *maser* is an acronym for “microwave amplification by stimulated emission of radiation,” which originally referred to a device that produces intense radiation of a specific frequency. *Stimulated emission* is a process by which a population of atoms or molecules are moved into energy levels above those of thermal equilibrium, which is referred to as a population inversion. The inverted population can then be stimulated to emit photons of a specific wavelength corresponding to a particular energy level transition, producing radiation that has a brightness temperature greater than the source temperature.

After the first laboratory maser was built in 1953, astronomers in the 1960s and 70s identified intense molecular spectral line sources in interstellar space that would also be dubbed *masers* because they are attributed to population inversions that occur naturally (Reid and Moran, 1981). When emission with very high brightness temperatures from the Sun and planetary magnetospheres was identified near f_B and its harmonics, the term *maser* was also adopted. This is somewhat of a misnomer, however, because electron-cyclotron maser emission (ECME) does not involve population inversions of atomic energy levels, but rather involves a plasma instability (Treumann, 2006).

The injection of nonthermal, semi-relativistic (fast) electrons into a plasma produces a population inversion analogous to that of a maser in the sense that a high-energy population was added to an equilibrium distribution. If the plasma density is low and/or the magnetic field strength is high such that $f_B > f_p$, then the excess energy of the nonthermal electrons is not most efficiently converted into Langmuir waves, as in the previous section, and instead direct emission of radiation at f_B via a plasma instability becomes favorable (Treumann, 2006). This is expressed analytically as a negative absorption coefficient (or positive growth rate) for a particular particle distribution, the most famous of which is the loss-cone distribution (*e.g.* Wu and Lee, 1979; Dulk, 1985; Melrose, 2009).

As ECME requires special conditions, namely semi-relativistic nonthermal electrons and $f_B > f_p$, it is less broadly applicable than the other solar radio emission mechanisms. Microwave spike bursts emanating from the chro-

mosphere are the most commonly-accepted example of ECME from the Sun (Dulk, 1985), but the applicability of this mechanism to the corona is less certain. Nevertheless, high-density coronal regions with large magnetic field strengths at relatively low heights can support ECME (Morosan et al., 2016), which is sometimes invoked to explain radio burst features that cannot be easily explained by plasma emission or gyrosynchrotron emission (*e.g.* Winglee and Dulk, 1986; Aschwanden and Benz, 1988; Tang et al., 2013; Wang, 2015; Liu et al., 2018).

1.3.6 Propagation Effects

The observed properties of solar radio emission, particularly at low frequencies, are greatly influenced by propagation effects that occur after the radiation is emitted. These effects depend on the medium that the radiation moved through en route to the observer. The dominant effects occur in the corona and Earth’s ionosphere, though very long wavelengths may encounter similar effects in the interplanetary medium. The corona is highly structured, often with large density contrasts between adjacent regions (*e.g.* Woo 2007; Raymond et al. 2014; Hahn and Savin 2016). Once emitted, a radio wave may be reflected many times by neighboring high-density regions, whether steady-state or turbulent, before the ambient density becomes low enough for the wave to propagate freely. The process of undergoing this successive combination of reflection and propagation is often called *scattering*, and it has many important implications.

Scattering increases the apparent size of a source, which is referred to as *angular broadening* (*e.g.* Steinberg et al., 1985; Bastian, 1994; Ingale et al., 2015). This broadening affects both compact burst sources and the entire Sun, and it has a side effect of decreasing the apparent brightness temperature (*e.g.* Melrose and Dulk, 1988; Alissandrakis and Chiuderi-Drago, 1994; Thejappa and MacDowall, 2008). In addition to angular broadening, scattering dramatically increases the cone-angle over which directed emission may be observed, which can even allow low-frequency detections of events originating from the far side of the Sun (Dulk et al., 1985).

Random scattering may also systematically shift the observed location of a radio burst to larger heights because the structures responsible for scattering are not randomly arranged, instead consisting of high-density fibers that are aligned with the magnetic field and are generally radial (Robinson, 1983; Poquerusse et al., 1988). This is analogous to *ducting*, which refers to the guiding of radio waves through a coherent low-density structure through successive

reflections against the high-density “walls” of the duct (Duncan, 1979). We will discuss these effects further in the context of Type III bursts in Chapter 3 (McCauley et al., 2018). Finally, scattering tends to depolarize emission and is thought to be responsible for the fact that many radio bursts have much lower circular polarization fractions than are expected by standard theories (*e.g.* Wentzel et al., 1986; Melrose, 2006; Kaneda et al., 2017).

In addition to scattering, simple refraction is also important. The density of the corona generally decreases radially, which means that radio waves will tend to refract toward the radial direction (Stewart, 1976; Mann et al., 2018). The o - and x -modes described in the previous section also have slightly different refractive indices. This difference means that refraction may separate the two modes, influencing the sense and/or degree of polarization. For ground-based observations, refraction becomes important again when the radiation passes through Earth’s ionosphere, which may significantly shift the apparent source location depending on how the instrument was calibrated.

Propagation effects related to the magnetic field may also modulate the polarization state through *mode coupling*, which refers to how the polarization of the o - and x -modes are changed by different plasma conditions. Regions for which the magnetic field orientation is nearly perpendicular to the ray propagation direction are referred to as *quasi-transverse* (QT) regions (Zheleznyakov, 1970; Ryabov, 2004). Passing through a QT region may cause the circular polarization sign to flip if the emission frequency is below a certain threshold (Cohen, 1960; Zheleznyakov and Zlotnik, 1964; Melrose and Robinson, 1994). This concept is vital to the interpretation of polarization reversals in microwave observations (*e.g.* Ryabov et al., 1999; Sharykin et al., 2018) and may also be relevant in certain low-frequency radio burst contexts (*e.g.* Suzuki and Sheridan, 1980; White et al., 1992; Kaneda et al., 2015; Kong et al., 2016).

1.4 Solar Activity

1.4.1 The Solar Cycle

The earliest known form of solar activity is sunspots, which are dark regions on the photosphere. Sunspots are dark because they are cooler than the surrounding material due to the presence of strong magnetic fields that inhibit the convective flow of energy from the interior. Very large sunspots can be seen with the naked eye, and their presence was routinely documented by early Chinese astronomers, with the first written record appearing in the *Book of*

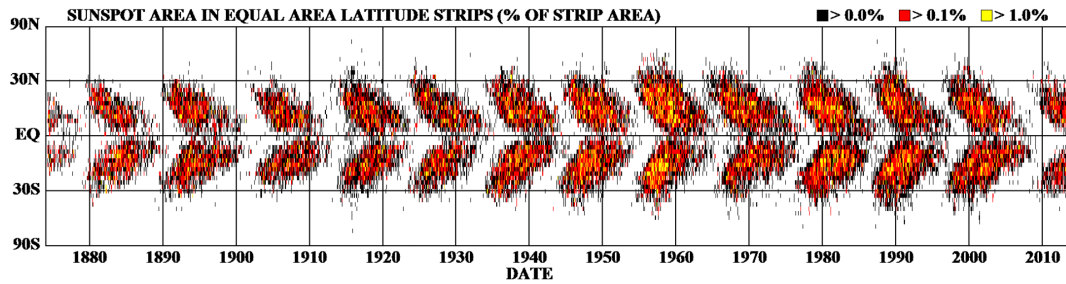


Figure 1.9: “Butterfly diagram” showing the total sunspot area as a function of time and latitude from 1875 to the present day. Each set of “wings” corresponds to one solar cycle. Image credit: [NASA Marshall Spaceflight Center](#).

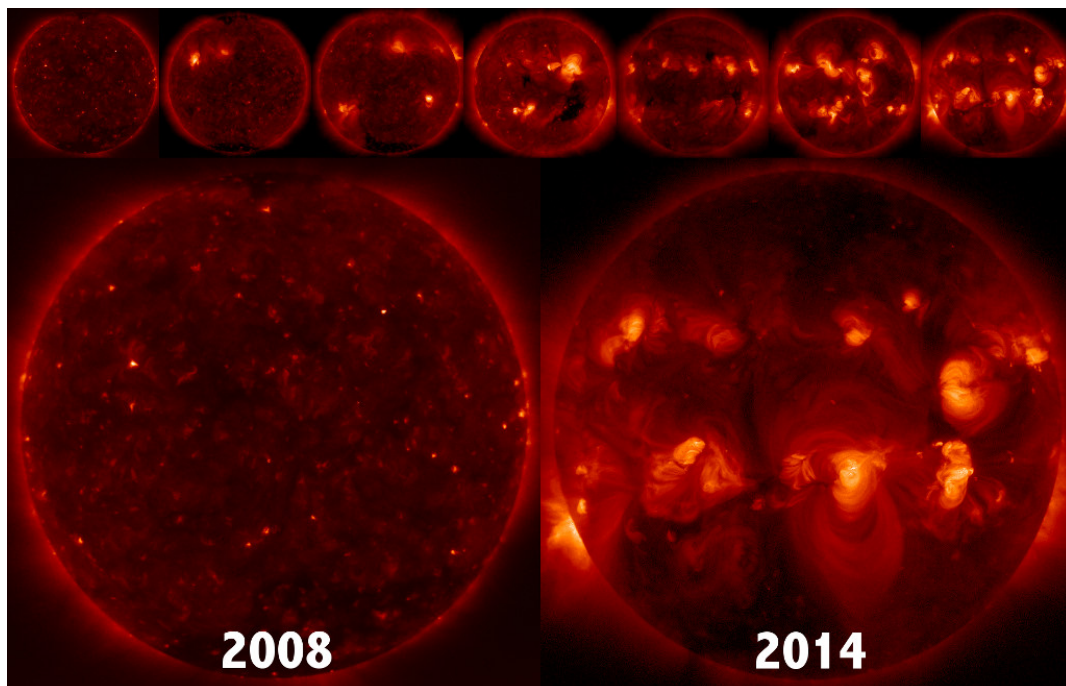


Figure 1.10: The corona in soft X-rays across the solar cycle. There is one image in the upper row for each year from last sunspot minimum (2008) to the last maximum (2014). Data are from the *Hinode X-Ray Telescope* (XRT). Image credit: Patrick McCauley, [Smithsonian Astrophysical Observatory](#) (SAO)

Changes in the late 9th century BC (Xu, 1990). In the mid 1800s, it was discovered that the number of sunspots varies on an approximately 11-year cycle (Schwabe, 1844) and that their latitudes drift from high to low over the course of the cycle (Carrington, 1858; Maunder, 1903). This is famously represented by the “butterfly diagram,” which shows the number and distribution of sunspots over time (Maunder, 1904). An example covering the period from 1875 to the present is shown in Figure 1.9.

In 1908, sunspots were discovered to be regions with strong magnetic fields through the first astrophysical observations of the Zeeman effect (Hale, 1908). This implied that the sunspot cycle was really a cycle in the Sun’s magnetic field (Hale et al., 1919), and it was later discovered that the Sun’s magnetic poles reverse with each cycle (Babcock, 1959). Because the structure of and activity within the corona is largely determined by the magnetic field, solar cycle variations in the corona are dramatic. Figure 1.10 shows soft X-ray images of the corona between 2008 and 2014, which were the years of the most recent sunspot minimum and maximum, respectively. The observations presented in this thesis were taken in 2014 and 2015, near the maximum phase of the solar cycle. There are many more important and interesting details on solar cycle variations and their implications that can be found in several textbooks (*e.g.* Foukal, 2004; Aschwanden, 2005; Golub and Pasachoff, 2010; Priest, 2014) and review articles (Hathaway, 2015). The next section will introduce the process that is thought to drive the cycle and ultimately give rise to all of the Sun’s activity.

1.4.2 The Solar Dynamo

The solar cycle and solar activity in general are ultimately byproducts of the dynamo process that generates the Sun’s magnetic field, which is both the scaffolding for structures in the corona and the energy reservoir that powers eruptions. A dynamo is a process that generates a magnetic field through induction by the rotation of a convecting, turbulent, and electrically-conductive fluid. Different versions of this process can exist in a variety of different contexts at vastly different spatial scales, from the dynamos that generate Earth’s magnetic field to the large-scale magnetic fields of galaxies. To introduce the solar dynamo, it is helpful to first outline the Sun’s interior structure.

There are three basic layers to the solar interior: the *core*, *radiative zone*, and *convection zone*. The core is the innermost region where mass is converted into energy by nuclear fusion of hydrogen into helium. Energy from the core is

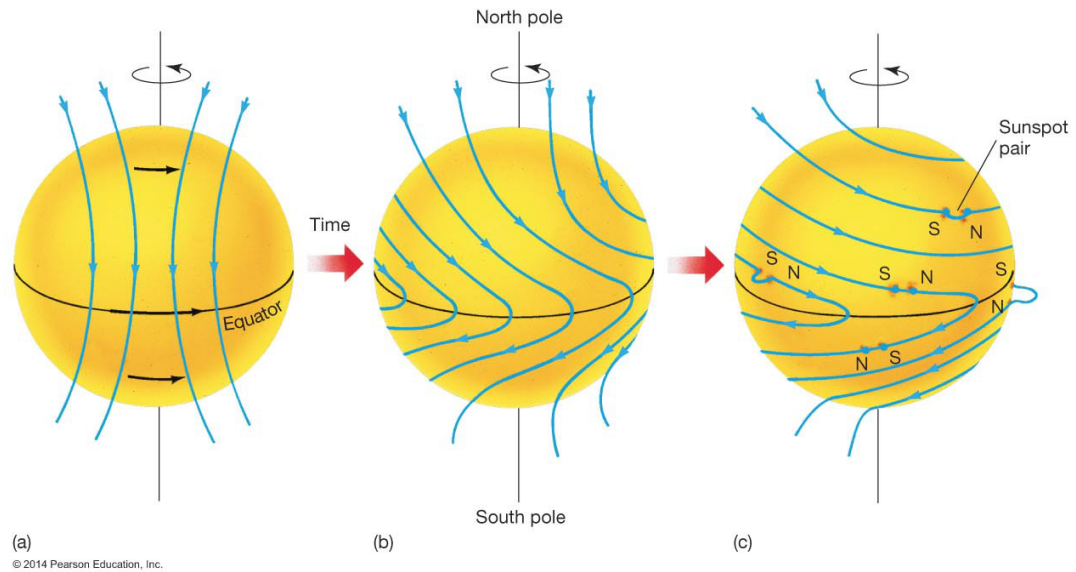


Figure 1.11: Differential rotation's effect on the Sun's magnetic field. Poloidal field on the left, representing the start of the solar cycle, is warped into toroidal field as low latitudes rotate faster than high latitudes. This is the *omega effect*, which has a less-easily-illustrated corollary in the *alpha effect* that regenerates poloidal field to renew the cycle. Image credit: Pearson Education, Inc.

first transported toward the exterior by radiative transfer in the radiative zone, where photons are absorbed and reemitted many times before reaching the base of the convection zone, after which energy is transported outward primarily by a cycle of hot plasma bubbles that rise to the surface, cool, and sink back down. The modern picture of the Sun's interior came initially from models based on the transport of fusion energy from the core, the existence of which was proposed in 1920 (Eddington, 1920) and confirmed experimentally through the detection of solar neutrinos (Davis Jr, 1964; Bahcall and Davis, 1976). Additional advances came after the discovery of global oscillations visible at the surface (Leighton et al., 1962), which led to the development of *helioseismology* (see reviews by Turck-Chieze et al., 1993; Basu, 2016).

Perhaps the most critical insight of helioseismology has been the discovery of a thin layer at the base of the convection zone called the *tachocline*, where the Sun's large-scale magnetic field is now thought to be primarily generated (Dziembowski et al., 1989; Spiegel and Zahn, 1992; Tomczyk et al., 1995). Beneath the tachocline, the Sun rotates nearly as a rigid body, and above the tachocline, different latitudes exhibit significantly different rotation rates. This is referred to as *differential rotation*. At the surface, material at the equator has a rotation rate of around 25 days compared to around 35 days near the poles,

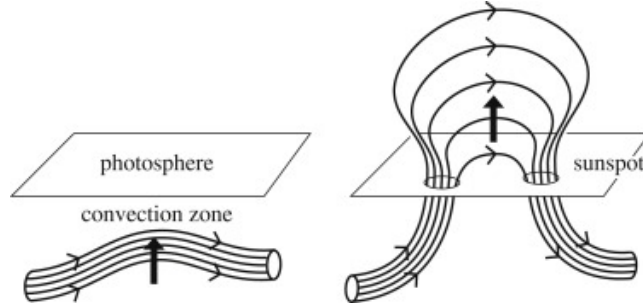


Figure 1.12: Magnetic buoyancy and flux emergence illustration. Concentrations of strong toroidal field rise to the surface, forming a bipolar sunspot with a magnetic field extending into the corona. Image credit: Priest (2019)

and this pattern continues smoothly in the interior down to the base of the convection zone. The onset of differential rotation in the tachocline introduces a strong shear that is thought to be a key ingredient in the cyclic nature of the solar dynamo.

At the beginning of the solar cycle, the Sun’s magnetic field is largely *poloidal*, where the field is perpendicular to the rotational flow direction and resembles that of a bar magnet. As the cycle progresses, differential rotation converts poloidal field into *toroidal* field, where the field is instead aligned with the rotational flow. This is referred to as the *omega effect*, and it occurs because the plasma pressure inside the Sun is larger than the magnetic pressure, so the magnetic field may be dragged along by the differential plasma motion. The omega effect, illustrated by Figure 1.11, is countered by the *alpha effect*, which regenerates the poloidal field from the toroidal field to renew the cycle. This basic picture is commonly-accepted, but many challenges remain in developing a dynamo model that can reproduce all of the observed solar cycle features. A recent review of solar dynamo models is given by Charbonneau (2010).

Once the toroidal field generated in the tachocline becomes strong enough in a particular region, the magnetized plasma becomes buoyant and rises to the surface (Babcock, 1961; Parker, 1975; Fan et al., 1993). *Magnetic buoyancy* thereby transports toroidal flux from the interior to the surface, where it emerges to form a bipolar sunspot with a magnetic field extending into the corona. This process, illustrated by Figure 1.12, is referred to as *flux emergence* (Golub et al., 1981; Archontis, 2008; Schmieder et al., 2014). The coronal magnetic field then develops as new flux continues to emerge and interact with preexisting field structures, along with other processes such as photospheric flows that may alter the coronal magnetic field topology. This constant evolu-

tion of the magnetic field gives rise to both the observed structure of the corona and energetic events such as solar flares and coronal mass ejections, which allow the abrupt release of energy stored in the magnetic field.

1.4.3 Features of the Corona

The ever-evolving features of the corona are themselves indicators of solar activity. This section briefly outlines the basic features that are relevant for this thesis, though a number of important features like prominences are excluded because they are not important for the radio observations that will be presented. Complete reviews of the corona’s features can be found in several textbooks (*e.g.* Aschwanden, 2005; Golub and Pasachoff, 2010; Priest, 2014). The low corona is frequently divided into three main region types: *active regions*, *coronal holes*, and the *quiet Sun*. This nomenclature developed largely around the interpretation of early soft X-ray observations.

Active regions are, as their name implies, sites of enhanced activity, where energetic events like flares and coronal mass ejections are most likely to originate. They have strong magnetic field concentrations and are easily distinguished as bright features in EUV and soft X-ray observations (Golub and Pasachoff, 2010). In radio observations, active regions are also bright at higher frequencies ($\gtrsim 300$ MHz) where gyroresonance emission from the strong magnetic fields either contributes significantly or dominates (White and Kundu, 1997; Lee, 2007; Shibasaki et al., 2011). With decreasing frequency, corresponding to increasing heights, they become less distinguishable from the background but are often sites of persistent nonthermal emission referred to as noise storms (Le Squeren, 1963; Gergely and Erickson, 1975; Elgarøy, 1977; Alissandrakis et al., 1985).

Active regions are the atmospheric counterparts of photospheric sunspots, although it is possible to have an active region without a visible sunspot if the magnetic flux is relatively weak. As described in the previous section and illustrated by Figure 1.12, active regions are produced by the generation of toroidal field in the interior that then rises to the surface in a process called flux emergence. New regions typically emerge with a bipolar field configuration (Harvey and Zwaan, 1993), including a pair of sunspots with opposite polarities. However, more complicated configurations are also possible either intrinsically or through additional flux emergence and interactions with preexisting structures (McIntosh, 1990; Jaeggli and Norton, 2016), and more magnetically complex regions tend to be more active (McAteer et al., 2005). Regions of opposite

Ch. 1 Introduction

polarity at the surface are often visibly linked by closed coronal loops, which are distinct magnetic field structures that radiate when populated by sufficient plasma (Reale, 2014). Once emerged, the magnetic flux dissipates until the region is no longer distinguishable as an active region, which typically takes a few weeks, though very large active regions may persist for 1-2 months (van Driel-Gesztelyi, 1998; Hathaway and Choudhary, 2008).

Coronal holes are regions where the magnetic field is open to interplanetary space, allowing material to flow freely away from the Sun to form the fast solar wind (Cranmer, 2009). They were first discovered in X-ray images from sounding rocket experiments in 1970 and characterized in greater detail shortly thereafter by *Skylab* data (Timothy et al., 1975), which definitively associated coronal holes with high speed solar wind streams (Krieger et al., 1973; Zirker, 1977). The term *hole* was chosen because they appear dark in EUV and X-ray images due to the plasma not being confined by closed fields, resulting in much lower densities and therefore emissivities. Coronal holes also appear dark in higher-frequency radio observations of the corona, but for reasons that are not yet clear, they often become increasingly bright structures with decreasing frequency below around 120 MHz (Lantos, 1999; McCauley et al., 2017; Rahman et al., 2019). Coronal holes form when a large swath of the Sun becomes dominated by a single magnetic polarity, leading to a unipolar open-field region. Near solar maximum, this configuration can arise at lower latitudes from the right combination of decayed active regions, and the resulting coronal hole may last for weeks to months (Wang et al., 2010; Petrie and Haislmaier, 2013). Around solar minimum and for much of the solar cycle, coronal holes are also continuously present at both poles (Waldmeier, 1981; Harvey and Recely, 2002).

The *quiet Sun* is a somewhat ill-defined term that is generally used to refer to regions that are absent of features such as active regions, coronal holes, and others not discussed here such as X-ray bright points and filaments, although it may also include quiescent features like coronal holes. At the surface, quiet Sun regions have weaker, granular magnetic fields that are not dominated by a single polarity as in coronal holes (Lin and Rimmele, 1999; Bellot Rubio and Orozco Suárez, 2019). In X-ray images, quiet Sun regions are often populated with large-scale diffuse structures that are the lower portions of large loops connected to the remnants of decayed active regions (Golub and Pasachoff, 2010). At radio wavelengths, quiet Sun regions are typically taken to be those that are absent of obvious nonthermal emission (Smerd, 1950; Kundu et al., 1977). Although they are quiet in comparison to active regions, there is considerable magnetic energy in the quiet Sun (Trujillo Bueno et al., 2004) and small-scale energetic

events are ubiquitous (Habbal, 1992; Harrison, 1997).

Finally, coronal *streamers* are the most prominent features seen in white light images of the corona. They are long-lived, high-density structures that extend radially outward to several solar radii from the surface (Koutchmy and Livshits, 1992). Like all coronal structures, streamers are related to the magnetic field configuration and generally represent regions of large-scale closed fields adjacent to open-field regions. Helmet streamers refer to the often particularly large and symmetric streamers that connect regions of opposite polarity in active regions. The closed-field structure of streamers generally constrains the outflow of material rather than freely permitting it, as in the open fields of coronal holes, although they also generate intermittent but persistent outflows due to dynamical interactions with neighboring field structures (Wang et al., 2000). Streamers are associated with moderately enhanced quiescent radio emission (Thejappa and Kundu, 1994; Ramesh, 2000), but they are not easily distinguished from the quiet Sun in radio images of the corona. There are, however, many reports of spatial associations between streamers and radio bursts (Trottet et al., 1982; Kundu and Stone, 1984; Gopalswamy et al., 1987; Mugundhan et al., 2018), which will also be found in Chapter 3 (McCauley et al., 2018).

1.4.4 Solar Flares

Solar flares are sudden brightenings of the solar atmosphere caused by an explosive release of energy stored in the local magnetic field. The first flare observations were reported from white light observations of a sunspot region in 1859 (Carrington, 1859; Hodgson, 1859). Radiation levels are enhanced across the electromagnetic spectrum, but only the largest flares produce a significant white light signature at the photosphere (Neidig, 1989). The primary response comes from the corona at X-ray wavelengths, and flares are now generally classified by their peak X-ray flux observed by the *Geostationary Operational Environmental Satellites* (GOES), although an earlier classification scheme also exists based on optical $H\alpha$ observations (Golub and Pasachoff, 2010). In ascending order, the GOES flare classes are A, B, C, M, and X. Each class is an order of magnitude more intense than the previous, with A-class flares beginning at 10^{-8} W m^{-2} and X-class flares beginning at 10^{-4} W m^{-2} .

Flares generally exhibit three distinct phases: the pre-flare, impulsive rise, and gradual decay phases (Aschwanden, 2005; Golub and Pasachoff, 2010; Priest, 2014). These are illustrated by Figure 1.13. Many, but not all, flares

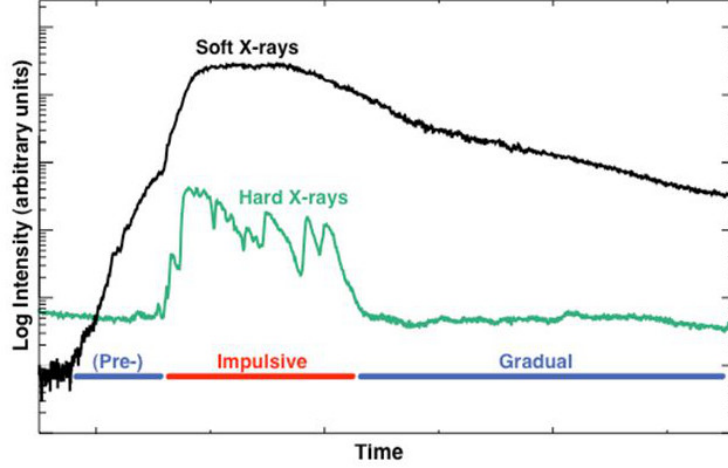


Figure 1.13: The three basic phases of a solar flare: the pre-flare, impulsive rise, and gradual decay phases. The impulsive phase also commonly includes nonthermal radio burst emission. Image credit: Amir Caspi

are preceded by minor activity at EUV and X-ray wavelengths from the flare site during the pre-flare phase, after which the soft X-ray flux abruptly spikes during the impulsive phase. The impulsive phase represents an abrupt release of stored magnetic energy into plasma heating, particle acceleration, and bulk outflow. The soft X-ray peak is largely due to thermal emission from the heated plasma. Particle acceleration during the impulsive phase leads to intense and rapidly-fluctuating bursts of radio, hard X-ray, and sometimes gamma radiation. The impulsive phase lasts only a few minutes, after which the bursty emissions subside and the soft X-ray radiation gradually decreases during the decay phase as the plasma cools back to the pre-flare temperatures.

The physical processes that drive solar flares are actively debated and are not very well understood. There is general consensus, however, that the magnetic field configuration in the corona develops into an unstable configuration that leads to *magnetic reconnection*, which produces an explosive release of energy. In the corona, the ratio of the plasma pressure to the magnetic pressure (the plasma beta) is very small. This means that the motion of coronal plasma is tightly constrained by the magnetic field [\mathbf{B}], primarily being only along particular magnetic field structures except for certain plasma drifts perpendicular to \mathbf{B} (i.e., the $\mathbf{E} \times \mathbf{B}$, $\nabla \mathbf{B}$, and curvature drifts). The opposite is true in the photosphere, where the density is much larger and the magnetic field can be dragged by plasma motions. As the magnetic field of the corona is rooted in the photosphere, the footpoints of coronal loops may be shifted

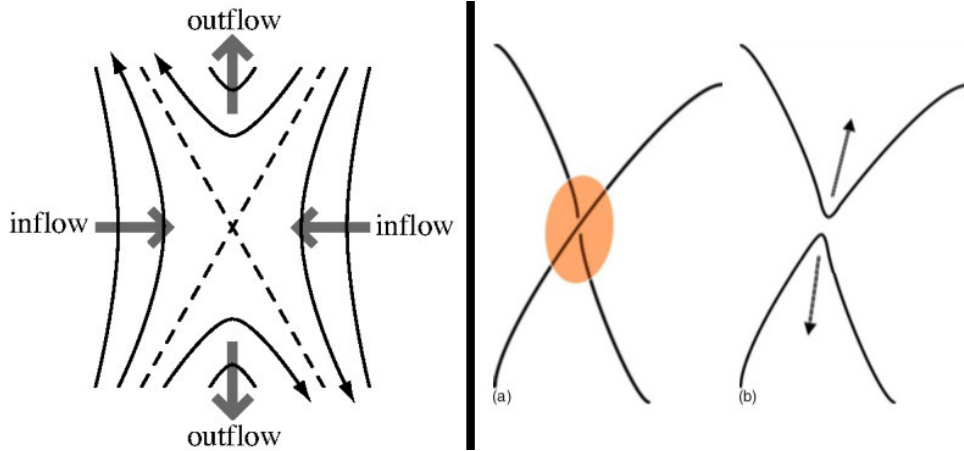


Figure 1.14: Simple magnetic reconnection cartoons. The left panel illustrates how inflows force magnetic field lines of opposite polarity toward an x -point, where they *reconnect* to form new field lines that relax to produce outflows. The right panel illustrates how the field connectivity changes at the x -point. Image credits: Brown et al., 2002 (*left*); Yamada et al., 2010 (*right*)

around by photospheric flows. Along with continued flux emergence and interactions between neighboring field structures, photospheric flows can lead to the development of sheared and/or twisted magnetic field structures in the corona (Hagyard et al., 1984; Wang, 1993; van Ballegoijen, 1999). These are referred to as *non-potential* field configurations, whereas a *potential* field corresponds to the lowest-energy configuration in which magnetic field lines straightforwardly connect opposite polarities. Energy is gradually stored in the magnetic field as it becomes increasingly non-potential, and that energy can then be catastrophically released through magnetic reconnection.

Magnetic reconnection is process that converts stored magnetic energy into kinetic and thermal energy through the reconfiguration of the magnetic field topology (Biskamp, 2000; Priest and Forbes, 2000; Yamada et al., 2010). In the simplest form, two opposite-polarity field lines are forced together by oppositely-directed inflows. The field lines collide at a central diffusion region, where they “reconnect” to form two new field lines that are accelerated out of the diffusion region by the magnetic tension force, resulting in outflows that are perpendicular to the initial inflow. Cartoons of this process are shown in Figure 1.14. In addition to bulk outflows, collimated beams of particles are accelerated out of the diffusion region due primarily to the presence of very strong electric fields (Reames, 1999; Petrosian, 1999; Schlickeiser, 2003). The theory of magnetic reconnection still faces a number of challenges to account for all of the observed

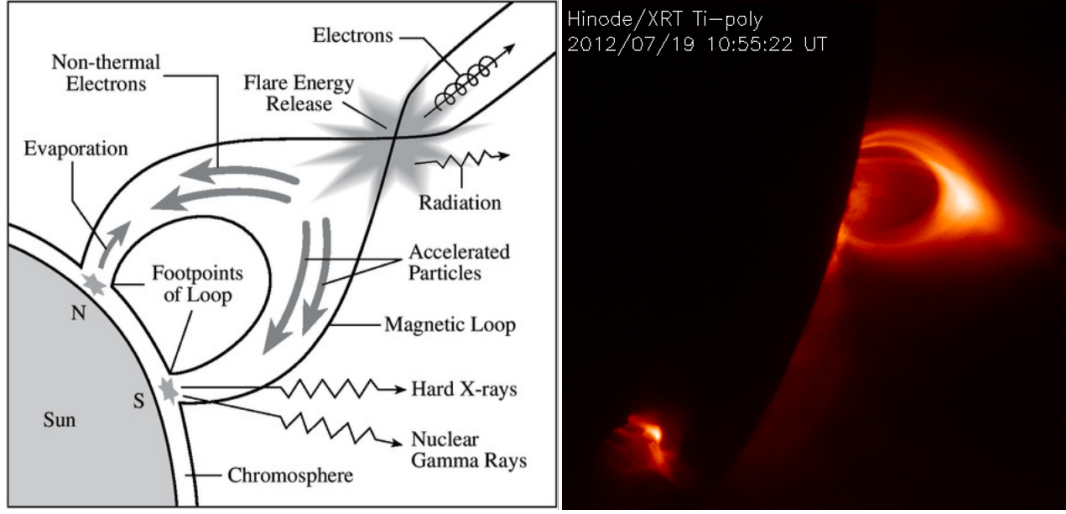


Figure 1.15: Simplified schematic of the “standard” (CSHKP) flare model (*left*) next to a *Hinode* XRT image exhibiting the classic cusp loop structure in soft X-rays (*right*). Image credits: Lang, 2006 (*left*); Patrick McCauley, SAO (*right*)

properties of solar flares. For instance, the predicted reconnection rates are too slow and the observed widths of current sheets are too large, requiring the introduction of effects such as turbulence and/or various plasma instabilities (*e.g.* Shibata and Tanuma, 2001; Lazarian et al., 2015; Cairns et al., 2018). Nevertheless, reconnection is widely-believed to be the driver of nearly all impulsive activity on the Sun.

Figure 1.15 shows a simplified schematic of the CSHKP flare model (Carmichael, 1964; Sturrock, 1966; Hirayama, 1974; Kopp and Pneuman, 1976), which places reconnection in the flare context and can explain many commonly-observed features. Reconnection occurs relatively high in the corona above the cusp-shaped loop, accelerating particles both toward and away from the Sun. Particles accelerated toward the Sun impact the chromosphere, which radiates hard X-rays and sometimes gamma rays. The chromospheric material is rapidly heated and expands into the corona, a process called *chromospheric evaporation*, which populates the cusp-shaped loop with hot plasma that produces intense EUV, soft X-ray, and microwave radiation. An observation of such a cusp loop is also shown in Figure 1.15. Particles, mainly electrons, accelerated away from the Sun stimulate waves in the background plasma as they stream through it, resulting in radio bursts that can cover a broad range of frequencies depending on the height at which the electron beams start. Finally, plasma that is suspended above the reconnection point can be accelerated away from the Sun to

produce coronal mass ejections, which will be discussed in the next section.

The CSHKP model has proven to be so successful that it is often referred to simply as the “standard model,” though other flare models exist and other reconnection scenarios are important in different contexts, such as breakout reconnection (Antiochos et al., 1999), interchange reconnection (Edmondson, 2012), or reconnection driven by emerging flux (Shibata et al., 1992). More complete descriptions of solar reconnection models can be found in solar physics textbooks (Aschwanden, 2005; Golub and Pasachoff, 2010; Priest, 2014).

1.4.5 Coronal Mass Ejections

Coronal mass ejections (CMEs) are large expulsions of plasma and magnetic fields that were first discovered in the 1970s using white light coronagraph observations (Tousey, 1973; Gosling et al., 1974). CMEs are the most impactful form of space weather and can have a number of potentially severe consequences, from threatening the health of astronauts to causing widespread power blackouts (Committee On The Societal and Economic Impacts Of Severe Space Weather Events, 2008). Prior to the discovery of CMEs, a connection between geomagnetic storms and solar flares had long been recognized (*e.g.* Sabine, 1852; Hale, 1931; McLean, 1959), implying that flares must sometimes be associated with the expulsion of solar material that later interacts with Earth’s magnetosphere.

CMEs are related to solar flares in that they are both driven by the restructuring of the coronal magnetic field, likely as a result of magnetic reconnection. Whereas a flare represents the conversion of magnetic energy largely into thermal energy, a CME moves energy stored in the magnetic field into the kinetic energy of a macroscopic outflow. While most large flares are accompanied by a CME and their production is incorporated into the “standard” flare model discussed in the previous subsection, is important to note that CMEs may occur without a corresponding flare and vice versa (Kahler, 1992; Yashiro and Gopalswamy, 2009). A CME may also begin before the associated flare, which is contrary to the standard model (Harrison, 1991). There is therefore no perfectly clear causal relationship between the two phenomenon, which may instead be understood as different manifestations of the same or similar processes that lead to abrupt changes in the coronal magnetic field (Hudson et al., 1995; Golub and Pasachoff, 2010).

CMEs often exhibit a three-part structure in coronagraph observations that consists of a bright plasma pileup at the leading edge followed by a dark cavity

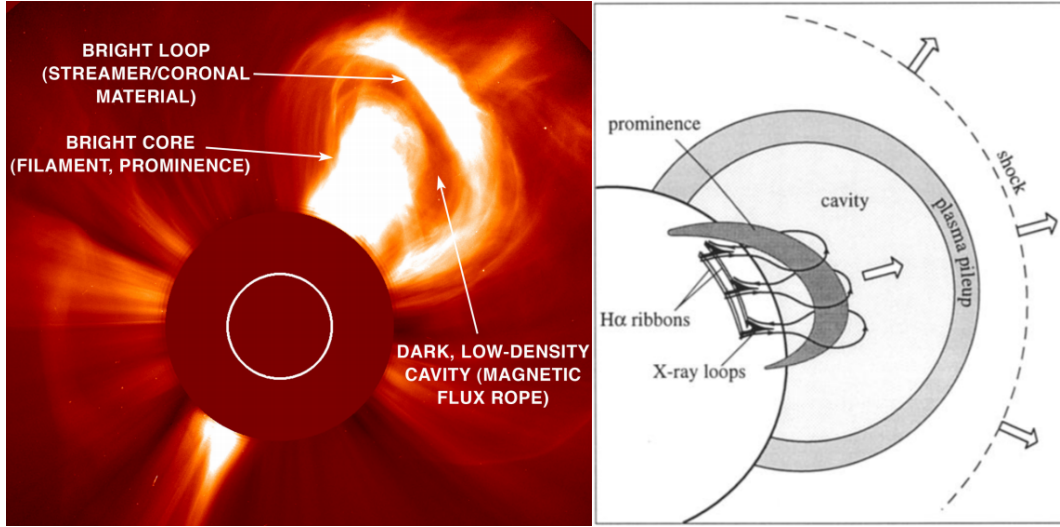


Figure 1.16: LASCO coronagraph image (*left*) and schematic (*right*) of a CME exhibiting the classic three-part structure of a bright plasma pileup followed by a dark cavity and bright core. The schematic also shows the leading shock wave along with X-ray and H α features back at the Sun. The white circle in the LASCO image represents the photosphere at the center of the coronagraph's occulting disk. Image credits: Müller et al., 2013 (*left*); Forbes, 2000 (*right*)

and dense core (Hundhausen, 1999; Schwenn et al., 2006). The Sun produces around 1 CME per day on average, though the CME rate exhibits a strong solar cycle dependence, with less than one per day near solar minimum and as high as 5 per day near solar maximum (Yashiro et al., 2004). They range in speed from less than 100 km s^{-1} to greater than 1500 km s^{-1} (Yurchyshyn et al., 2005), averaging around 300 km s^{-1} near solar minimum and 600 km s^{-1} near solar maximum (Gopalswamy et al., 2009). As these speeds generally exceed the sound speed and often exceed the Alfvén speed, shock waves may develop just ahead of the CME in the low corona and/or interplanetary medium. These shocks accelerate electrons, which may produce Type II radio bursts through the plasma emission process (*e.g.* Wild and McCready, 1950; Nelson and Melrose, 1985; Gopalswamy, 2006; Cairns, 2011), along with heavier particles referred to as *solar energetic particles* (SEPs) that may be observed directly with *in situ* observations (Reames, 2013). Plasma emission was discussed in Section 1.3.4. Type II bursts are described in Section 1.5.2 along with Type IV bursts, which are also associated with CMEs.

CME cores may be directly imaged in high-frequency microwave observations (Gopalswamy et al., 2003; Alissandrakis et al., 2013), but the primary low-frequency signatures of CMEs are the radio bursts associated with the

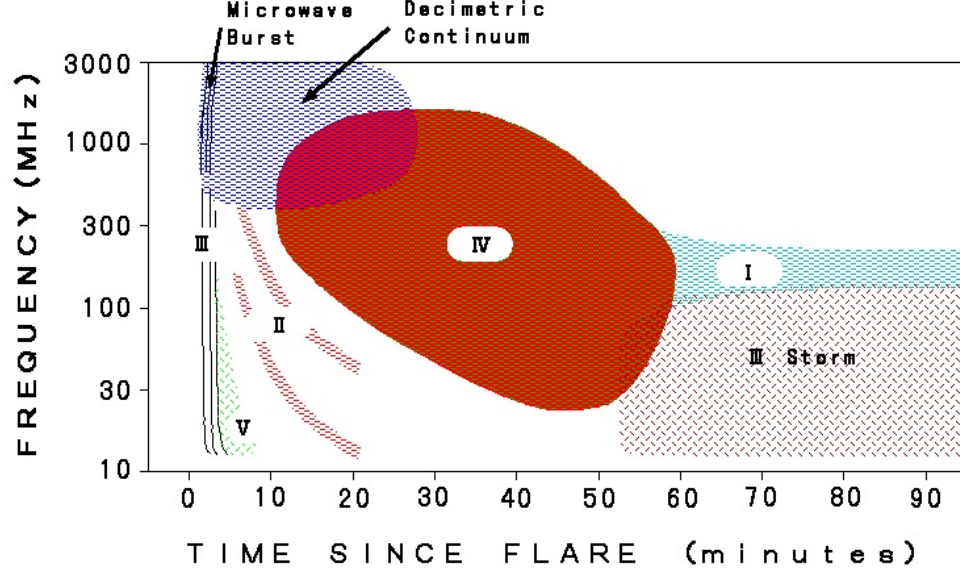


Figure 1.17: Dynamic spectrum schematic of radio burst types for an idealized event. Note that all types are seldom neatly observed for a single event. Real dynamic spectra are shown in Figure 1.18. Image credit: nict.go.jp

shock-accelerated electrons (Nindos et al., 2008). Gyrosynchrotron emission from the expanding magnetic fields of a CME may also be observed in radio observations, though this has so far been rare (Bastian et al., 2001; Maia et al., 2007). Chapter 5 includes a preliminary account of novel radio CME observations that were reduced in the course of this thesis but have yet to be analyzed in detail.

1.5 Solar Radio Bursts

Solar radio bursts are brief periods during which the Sun’s radio emission is elevated above the thermal background level. Bursts may exceed the background level only slightly or by many orders of magnitude depending on the amount of energy released, along with a variety of other effects related to the structure of the source region, the viewing geometry, and the medium through which the radiation propagates en route to the observer. There are several types of radio bursts, most of which are produced by plasma emission operating in different contexts, although some types are attributed to (gyro)synchrotron and/or electron-cyclotron maser emission. These emission processes were reviewed in Section 1.3.

Ch. 1 Introduction

The classification of radio bursts is largely based on how they appear in dynamic spectra produced by radiospectrographs, which record the Sun’s intensity as a function of both time and frequency. Wild and McCready (1950) defined the first three types using the earliest radiospectrograph observations of metric bursts, primarily based on variations in their apparent drifts in the emission frequency over time, and Types IV and V were added later. Since they were initially defined, numerous subtypes have been added and many of the associated physical processes have been identified. What follows are brief descriptions of the five main classes of solar radio bursts, along with references to a few additional types. An idealized schematic of how radio bursts appear in dynamic spectra is shown in Figure 1.17.

1.5.1 Type I

Type I bursts are spikes of enhanced radio emission that last around one second and occur over a relatively narrow frequency range ($\Delta f/f \approx 0.025$), with little-to-no discernible drift in the frequency. They generally occur in groups, referred to as *noise storms*, that are superimposed on enhanced continuum emission of the same frequency range (see reviews by Elgarøy, 1977; Klein, 1998). While each individual spike does not drift in frequency, a chain of Type I bursts may slowly drift from higher to lower frequencies over a few minutes. An example of a Type I burst noise storm is shown in the upper panel of Figure 1.18.

Noise storms are associated with active regions, they may last anywhere from hours to weeks, and they are most commonly observed at relatively low frequencies ($\approx 50 - 500$ MHz). Although the association with active regions has been known for decades (*e.g.* Le Squeren, 1963; Gergely and Erickson, 1975; Alissandrakis et al., 1985), it is still not entirely clear what conditions within active regions lead to noise storms. Not all active regions that exhibit activity at other wavelengths generate noise storms, and unlike other radio burst types, non-radio signatures are often scant (Willson, 2005; Iwai et al., 2012; Li et al., 2017).

Type I bursts are generally attributed to fundamental plasma emission, largely due to their often high circular polarizations, but there is not yet a consensus on what accelerates the electrons. Minor reconnection events (Benz and Wentzel, 1981) or shocks associated with different types of upward-propagating waves (Spicer et al., 1982) are the two leading ideas. Recent work has favored reconnection in different contexts, either between open and closed fields at the boundaries of active regions (Del Zanna et al., 2011; Mandrini et al., 2015) or

driven by moving magnetic features at the photosphere (Bentley et al., 2000; Li et al., 2017). We will present polarization measurements of noise storm continua in Chapter 4 (McCauley et al., 2019), including much weaker sources than have been previously reported.

1.5.2 Type II

Type II bursts drift slowly ($\approx 1 \text{ MHz s}^{-1}$) from high to low frequencies, typically lasting a few minutes. They often exhibit two distinct bands of emission that are interpreted as being fundamental–harmonic pairs of plasma emission from a single source region (Roberts, 1959; Sturrock, 1961). Examples of Type II bursts exhibiting such a structure are shown in the lower panel of Figure 1.18. Type II bursts are associated with coronal mass ejections and are believed to be caused by electrons accelerated by a shock wave at the leading edge of the CME (*e.g.* Cane and Stone, 1984; Gopalswamy et al., 2001; Cairns, 2011). The emission frequency drifts down to lower frequencies because it depends on the local density, which generally decreases as a function of radial distance from the Sun. By assuming a density model, the frequency drift rate may be converted to a physical speed that then refers to the speed of the disturbance moving outward through the corona. For Type II bursts, this procedure typically yields speeds of around 1000 km s^{-1} , which adequately matches that of CME shocks.

Although Type II bursts are also attributed to plasma emission, they do not exhibit the high circular polarizations seen in Type I bursts, instead exhibiting little-to-no polarized intensities (*e.g.* Komesaroff, 1958; Akabane and Cohen, 1961). The reason for the low polarization is not entirely understood, but dispersion effects related to the inhomogeneous magnetic field near a magnetohydrodynamic shock wave is a leading hypothesis (McLean and Labrum, 1985). Type II bursts also sometimes exhibit short-lived fine structures called herringbone bursts that emanate from the main burst and extend to lower frequencies, suggesting that beams of shock-accelerated electrons were able to escape far beyond the shock region (Cairns and Robinson, 1987). A review of the theory and space weather implications of Type II bursts is given by Cairns et al. (2003).

1.5.3 Type III

Type III bursts are similar to Type IIs in that they also drift from high to low frequencies and are attributed to plasma emission. However, Type IIIs drift at a much faster rate ($\approx 100 \text{ MHz s}^{-1}$) and must therefore be excited by dis-

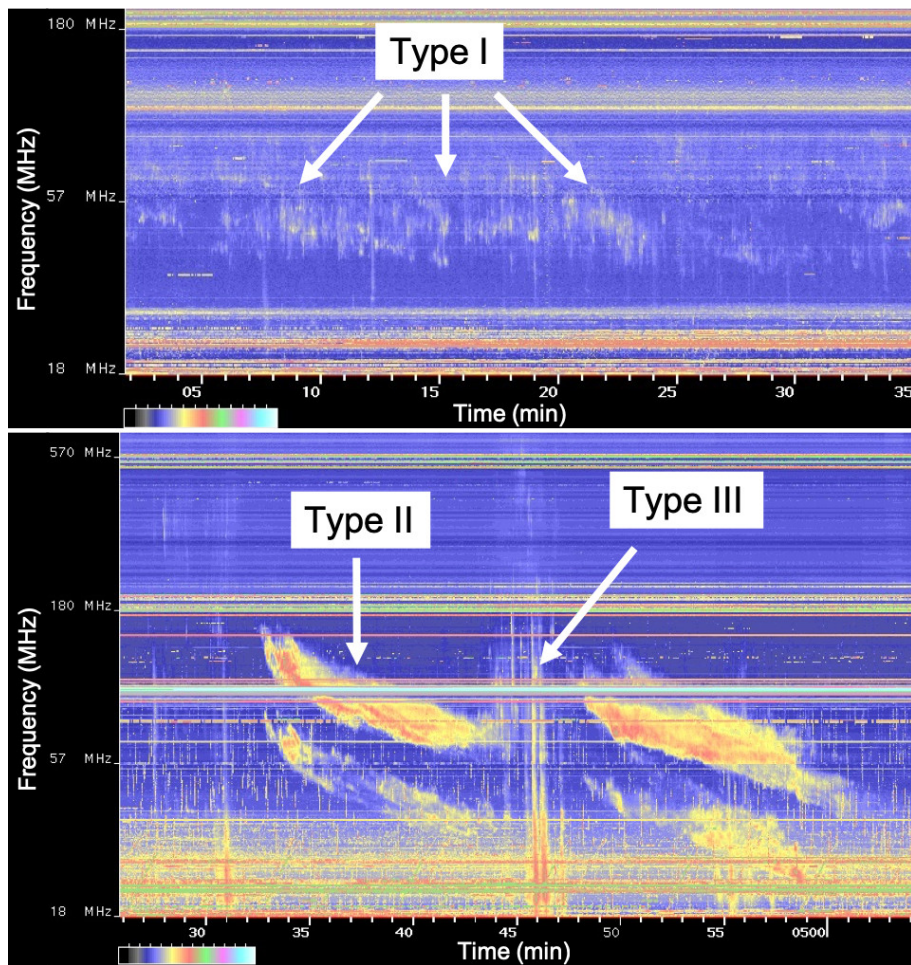


Figure 1.18: Learmonth solar radiospectrograph dynamic spectra showing Type I bursts (*top*), along with Types II and III bursts (*bottom*). Adapted from spectra published by the Bureau of Meteorology's [Space Weather Service](#).

turbances moving outward through the corona more quickly than the shocks responsible for Type II bursts. Examples of Type III bursts are shown in the lower panel of Figure 1.18. Type IIIs are attributed to semi-relativistic electron beams accelerated by magnetic reconnection, the process that underpins solar flares. Correspondingly, Type III bursts are strongly associated with X-ray flares. Nearly all large flares have associated non-thermal radio emission, typically Type III bursts (Benz et al., 2005, 2007). However, not all small-to-moderate X-ray flares have associated Type III bursts and vice versa due to the different conditions required to produce the high- and low-energy emission (*e.g.* Alissandrakis et al., 2015; Reid and Vilmer, 2017; Cairns et al., 2018).

Type III bursts may occur in isolation, small groups, or chains lasting many minutes that are referred to as Type III storms. They exhibit moderate circular polarization fractions, typically less than 50%. Like Type IIs, the observed polarization fractions of Type III bursts are much lower than theoretical predictions (*e.g.* Wentzel, 1984). Scattering by density inhomogeneities and other propagation effects are likely responsible for this discrepancy, though this has yet to be fully resolved (*e.g.* Wentzel et al., 1986; Melrose, 2006; Kaneda et al., 2017). A review of recent Type III burst literature is provided by Reid and Ratcliffe (2014), and a review focused on the theoretical aspects is given by Robinson and Cairns (2000). Type III bursts will be discussed in more detail in Chapters 2 and 3 (McCauley et al., 2017, 2018), which focus on their relationship with the coronal magnetic field and density structures, respectively.

1.5.4 Type IV

Type IV bursts are broad-band continuum emissions that come in a few distinct varieties that are associated with different phenomena and different emission mechanisms. *Moving* Type IV bursts were the first to be defined and require an interferometer to be detected (i.e. imaging observations), as they are characterized by an outward-moving continuum source (Boischot, 1958; McLean and Labrum, 1985). The emission mechanism is unclear and is generally attributed to gyrosynchrotron emission, plasma emission, or some combination thereof associated with fast electrons trapped within the magnetic fields of an erupting CME (Dulk, 1985; Morosan et al., 2019). As they are also related to CMEs, Type IV bursts are often preceded by a Type II burst driven by the shock at the leading edge of the eruption.

Stationary Type IV bursts are more common and are broad-band continuum emissions that are either associated with solar flares or Type I bursts

Ch. 1 Introduction

(McLean and Labrum, 1985; Dulk, 1985). Flare-associated Type IVs are referred to as *flare continuum* bursts, typically beginning at or shortly after the impulsive phase of the flare. These bursts are thought to be caused by plasma emission generated by electrons trapped in large, closed magnetic loops (Dulk, 1985). The flare continuum may be followed by a second phase referred to as a *storm continuum* burst that commonly occurs with larger flares (Pick-Gutmann, 1961). The storm continuum lasts for hours to days, progressively becoming an ordinary Type I noise storm if the duration is long enough (Pick and Vilmer, 2008). Both phases are thought to be caused by plasma emission, although the contexts must be somewhat different because the storm continuum tends to exhibit a much larger degree of circular polarization (Dulk, 1985).

1.5.5 Type V

Type V bursts are continuum emissions that last for one to a few minutes, immediately following a group of Type III bursts and generally occurring at frequencies below ≈ 120 MHz (Suzuki and Dulk, 1985; Dulk, 1985; Reid and Ratcliffe, 2014). This radiation is much less common than Type III bursts and is generally thought to be caused by harmonic plasma emission associated with the same electron streams responsible for the associated Type III bursts (Zheleznyakov and Zaitsev, 1968; Robinson, 1978; Dulk, 1985), perhaps moving along different field structures to explain the sometimes large positional offsets from the associated Type III bursts (Weiss and Stewart, 1965; Robinson, 1977). Type V emission may last longer because it is generated by a slower electron population that is less collimated than the Type III bursts, which contributes to the broader-band emission and also leads to a reversal in the sense of the circular polarization from that of the Type IIIs due to the different angular distribution of Langmuir waves (Dulk et al., 1980; Dulk, 1985). Alternatively, some authors have suggested that Type V bursts may be an example of electron cyclotron maser emission (Winglee and Dulk, 1986; Tang et al., 2013).

1.5.6 Other

In addition to Types I–V, there are a number of additional classes of radio bursts. These include variants of the standard types, fine structure within a particular type, and wholly distinct phenomena. Examples of variants include Types J and U bursts, which are Type III bursts for which the frequency drift reverses, indicating that the associated electron beams reverse direction and travel back toward the Sun along closed magnetic field lines (Reid and Ratcliffe,

2014). Examples of fine structure bursts include the zebra patterns (Slottje, 1972) and fibre bursts (Rausche et al., 2008) that may be observed in association with Type IV bursts, along with the herringbone bursts that sometimes accompany Type II bursts (Cairns and Robinson, 1987). Additional distinct classes include Type S bursts (Ellis, 1969; Morosan et al., 2015), which last just milliseconds, along with a variety of microwave bursts such as microwave Type IV bursts, impulsive bursts, postbursts, and spike bursts (Kundu and Vlahos, 1982).

1.6 Interferometry and Aperture Synthesis

Interferometry is the superposition of waves, usually electromagnetic, to generate interference patterns that can be used to extract information about the source that generated the waves and/or the medium through which the waves propagated. Since the development of the first interferometers in the late 1800s (Michelson and Morley, 1887), variations of this concept have been implemented in many fields of science. Two types of interferometry are relevant to the study of the solar corona, Fabry-Pérot interferometry (Fabry and Perot, 1899) and aperture synthesis, sometimes called synthesis imaging. Fabry-Pérot interferometers, which will not be discussed further, are commonly-used to develop narrowband filters that precisely isolate particular spectral lines for imaging telescopes or tuneable spectrographs (*e.g.* Brueckner et al., 1995; Puschmann et al., 2012; Prabhakar et al., 2019).

In the astrophysical context, *interferometry* usually refers to *aperture synthesis*, which is a type of interferometry that combines signals from multiple telescopes. An array of telescopes can be used to synthesize the aperture of a much larger telescope, permitting an angular resolution up to that of a telescope with a diameter equal to the largest separation between interferometer elements. This is particularly important for radio astronomy because the long wavelengths mean that impractically large telescopes would be needed to achieve high angular resolutions without interferometry. Interferometers are also much easier to construct at radio wavelengths because the signals can be combined electronically, whereas infrared and optical interferometers require precise optics that have been developed only fairly recently and may still support only a small number of elements.

This section will introduce a few basic concepts and terms, including a description of the main instrument used in this thesis and some notes on data reduction. More details on interferometry and the associated mathematics can

be found in several textbooks (*e.g.* Taylor et al., 1999; Thompson et al., 2017).

1.6.1 Basic Concepts

Synthesis imaging is the reconstruction of an image from measurements of the Fourier transforms of its brightness distribution (Thompson et al., 2017). The fundamental measurements of interferometers are called *visibilities*, which are cross correlations (interference patterns) of the signals received from each pair of antennas in the array. The relative position between any pair of antennas is referred to as a *baseline*, and each baseline represents a single point in the u - v plane, where u is the east-west separation and v is the north-south separation. The length of a baseline determines its sensitivity to different spatial scales on the sky, with longer baselines being sensitive to smaller spatial scales and shorter baselines being sensitive to larger scales. Arrays with longer baselines therefore have finer spatial resolutions, while more compact arrays are more sensitive to large-scale diffuse structures.

The combination of all the baselines in an array is referred to its u - v coverage. This represents the sampling of a target’s brightness distribution, with the visibilities $[V(u, v)]$ being the two-dimensional Fourier transform of the brightness on the sky $[T(x, y)]$. Because the u - v coverage can never be complete given the finite number of array elements, the reconstruction of a source’s brightness distribution (image) is an approximation that improves with the density of u - v coverage (i.e. the array density).

The initial inversion of $V(u, v)$ is usually done by interpolating the data onto a regular grid and applying the fast Fourier transform algorithm, which results in a so-called *dirty image*. The image is “dirty” in the sense that it is the brightness distribution convolved with an instrumental response function referred to as the *synthesized beam* or *point spread function* (PSF), which is analogous to the PSF of an optical telescope. The size and orientation of the synthesized beam will be shown in one corner of every MWA image in this thesis, and it is effectively the image’s resolution element; features smaller than the synthesized beam cannot be spatially resolved.

The PSF cannot be straightforwardly deconvolved out because it contains null points due to the incomplete sampling of the u - v plane. Instead, a number of deconvolution algorithms have been developed. The most widely-used and the one implemented here is CLEAN (Högbom, 1974; Schwarz, 1978; Clark, 1980; Schwab, 1984), the basic steps of which are as follows: find the location of peak intensity, subtract a multiple of the PSF centered at the peak, and

repeat until the next peak location is below some threshold, often specified by the user. The resultant image is then convolved with a **CLEAN** beam, which is generally a two-dimensional Gaussian fit to the central component of the PSF, and the residuals of the dirty image are added back in.

The deconvolved **CLEAN** image now represents the brightness distribution as viewed by that particular array, which has a particular response to the sky that determines the instrument’s field of view and is referred to as its *primary beam*. The primary beam is effectively how the interferometer “sees” the sky, and its pattern varies significantly with antenna type and array configuration. A model of the primary beam can then be divided out to obtain the “true” instrument-independent brightness distribution. The beam model may be derived either from an analytic description of the combined antenna response or empirical measurements of known sources. Imperfections in the beam model have important consequences for polarimetry that will be discussed in Chapter 4 (McCauley et al., 2019), which includes the development of an algorithm to mitigate beam-related errors.

The description above is a very simplified overview of aperture synthesis and its fundamental terminology. An important caveat is that the consideration of $V(u, v)$ as the Fourier transform of $T(x, y)$ is valid only for fairly small angles on the sky. Widefield instruments such as the MWA require specialized algorithms to invert $V(u, v)$, such as w -stacking, which is implemented in the **WSCLEAN** software used to reduce the data presented in this thesis (Offringa et al., 2014).

1.6.2 The *Murchison Widefield Array* (MWA)

The MWA is a low-frequency (80–300 MHz) interferometer located in the Murchison Shire of Western Australia, which is an exceptional site for radio astronomy because of limited radio frequency interference (RFI) from the small human population. A technology demonstrator and precursor telescope for the *Square Kilometre Array* (SKA; Dewdney et al., 2009), which is planned to be the world’s largest telescope, the MWA has four main science themes (Bowman et al., 2013).

These are 1) attempting to detect redshifted 21-cm emission from the early Universe’s Epoch of Reionization (EoR), 2) conducting galactic and extragalactic surveys, 3) searching for and localizing various radio transients (i.e. time-domain astrophysics), and 4) solar, heliospheric, and ionospheric (SHI) studies. The latter category includes direct observations of the Sun, which is the subject of this thesis. The MWA can also probe the solar wind through

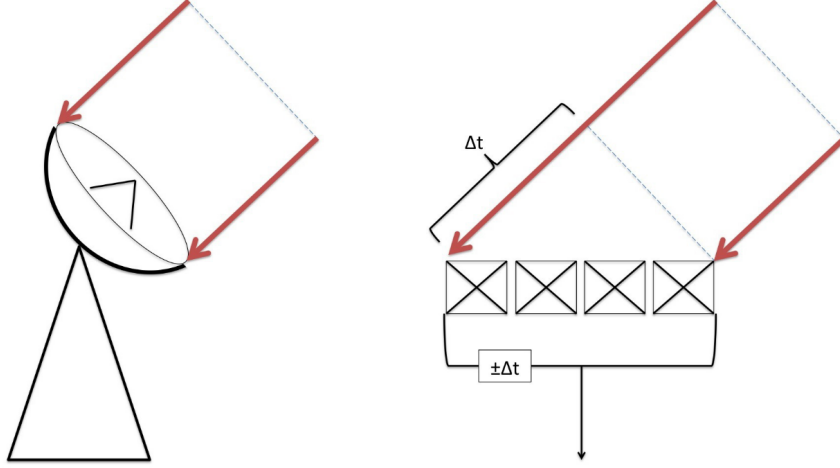


Figure 1.19: Illustration of the electronic “steering” of an aperture array (*right*) versus the mechanical steering of a parabolic dish (*left*). The time lag $[\Delta t]$ between radiation arriving at different antennas is specific to a specific location on the sky, and shifting the signals by $\pm \Delta t$ before they are correlated focuses the telescope on that location. Image credit: (Carroll, 2016)

observations of interplanetary scintillation, which refers to brightness fluctuations (twinkling) exhibited by astronomical sources as their radiation passes through the solar wind plasma (Morgan et al., 2018). These observations are also sensitive to the passage of CMEs (Kaplan et al., 2015), and a major goal of the SHI collaboration is to make Faraday rotation measurements of linearly-polarized background sources occulted by a CME, which can be used to deduce the strength and orientation of the CME’s magnetic field.

The MWA is comprised of many individual dual-polarization dipole antennas arranged in 4×4 grids called “tiles,” one of which is pictured in the lower-middle panel of Figure 1.3. A prototype array with 32 tiles operated between 2009 and 2011 (Lonsdale et al., 2009), followed by the commencement of Phase I operations with 128 tiles in 2013 (Tingay et al., 2013a). The data presented in this thesis are from Phase I. Phase II operations began in 2018 with 256 tiles, half of which can be used simultaneously in different configurations (Wayth et al., 2018). Each MWA tile is an individual *aperture array*, which is a collection of antennas that receive signals from the entire sky but are “steered” electronically to target specific regions. This is in contrast to parabolic dish antennas, which resemble satellite dishes and are mechanically pointed to reflect radiation from a specific region toward a receiver placed in front of the dish.

Figure 1.19 illustrates how an aperture array is pointed. Radiation is re-

ceived by different elements in the array at slightly different times, with a specific time delay corresponding to a specific location on the sky. The array can be focused to a particular location by adding the characteristic time delay for that location to the signals received by each antenna. In addition to providing a wide and flexible field of view (FOV), steering the telescope in this way requires no moving parts, which greatly reduces hardware costs. However, electronic steering and wide FOVs require complicated and computationally-expensive signal processing and data reduction methods. Parabolic dishes have dominated radio astronomy since the late 1960s partly for this reason, but aperture arrays are currently experiencing a revival due to advances in signal processing, digital electronics, and high-performance computing that have made possible large arrays like the MWA and LOFAR (Garrett, 2012).

The MWA’s novel hardware, signal processing backend, and observational capabilities are described by Tingay et al. (2013a). It has an instantaneous bandwidth of 30.72 MHz that can be distributed in different configurations between 80 and 300 MHz. For solar observations, data are typically recorded with a 0.5 s time resolution and 40 kHz spectral resolution. More details on the solar observing configuration and data reduction methods used in this thesis, along with solar science results from other studies, are given in Chapters 2–4.

1.6.3 Data Reduction

As mentioned in the previous section, reducing aperture array data is computationally expensive, and high-performance computers are required to turn the MWA’s enormous volume of raw visibilities into science-ready images. The observations that are presented here were processed using the Pawsey Supercomputing Centre. Incidentally, this facility is named for Joseph Pawsey, who made several important early contributions to solar radio astronomy, such as the identification of thermal emission from a million-degree corona and the localization of radio bursts to sunspot groups using sea interferometry (Pawsey et al., 1946; Pawsey, 1946; Pawsey and Smerd, 1953).

The data reduction methods used in this thesis were adapted from those used by the MWA’s astronomical surveys, which required some modifications to suit solar observations. Chapter 2 (McCauley et al., 2017) will describe this procedure, which is further developed for polarimetry in Chapter 4 (McCauley et al., 2019). The development and implementation of a semi-automated data processing pipeline, along with associated visualization and analysis software, occupied a significant fraction of my candidature, and this subsection briefly

Ch. 1 Introduction

describes some aspects that are not documented elsewhere.

Because of the computational requirements, observation periods with activity identified by other instruments were initially targeted for data reduction. A metadata catalog¹ of solar observations was developed that associates each contiguous MWA observing window with radio bursts, flares, CMEs, and other events that are published in various event catalogs such as the NOAA event reports², Heliophysics Event Knowledgebase (HEK; Hurlburt et al., 2012), and CACTus CME catalog (Robbrecht et al., 2009).

120 five-minute observation periods were reduced from 82 different days in 2014 and 2015. Around half of these were chosen to include isolated Type III bursts and were imaged at the full 0.5-sec time resolution, while the other half targeted different observing days with the same “picket fence” observing mode and were generally sampled at a 4-sec cadence. Including all of the frequency channels and polarization states, an archive of over 4.5 million images was compiled, corresponding to around 50,000 individual time steps. This was a significant computational expenditure, requiring around 1.5 million core hours on the Pawsey system. A further 750,000 core hours were awarded through the National Computational Merit Allocation Scheme (NCMAS) in 2019. This allocation is currently being used to target CMEs using the same pipeline, including further processing of serendipitous detections made with the initial archive, and some preliminary CME results are shown in Chapter 5.

1.7 Research Aims and Outline

This thesis represents the first attempt to reduce and analyze large amounts of solar MWA data. As described in the previous section, the development of a data processing pipeline led to an archive of millions of images. Broadly speaking, my thesis aims to exploit this dataset, and the enclosed projects developed somewhat organically from what presented itself in the observations. Much more science can be supported by the data already reduced, along with the much larger volume of unprocessed data, and the archive developed for this thesis has already facilitated published and ongoing research beyond what is presented here.

Observation periods that included isolated Type III bursts were initially targeted because they are common and of general interest to researchers at the

¹<http://www.physics.usyd.edu.au/~pmcc8541/mwa/catalog/>

²<https://www.swpc.noaa.gov/products/solar-and-geophysical-event-reports>

University of Sydney, who have developed state-of-the-art theoretical simulations over many years (*e.g.* Cairns, 2000; Li et al., 2006, 2008). New Type III burst behavior was discovered soon after compiling several observations. The characterization and interpretation of this behavior is the subject of Chapter 2 (McCauley et al., 2017), which among other things, demonstrates the usefulness of these observations for probing magnetic field connectivities in the corona. In the course of developing a rough flux calibration method for Chapter 2, previously-known but rarely-observed coronal hole behavior was also detected. Additional serendipitous coronal hole observations were then identified in the archive and analyzed by Rahman et al. (2019), whose results are summarized in Chapter 4.

Having collected a sample of Type III burst imaging observations, a small number of events at the limb with uncomplicated dynamics were employed to probe the coronal density structure. Chapter 3 (McCauley et al., 2018) is an updated repetition of classic experiments conducted using some of the earliest two-dimensional burst measurements. A novel addition is to relate Type III source heights to the increased extent of the quiescent corona over that of modern model predictions.

Examination of the image archive also revealed the initial MWA detections of circularly-polarized sources on the Sun. However, it was also immediately obvious that the polarimetric images frequently suffered from contamination that would need to be mitigated before the images could be used. While the calibration artefacts responsible for this effect were known from other MWA studies, the existing mitigation techniques could not be directly applied to solar observations. Different methods were explored and one ultimately proved successful, leading to the first low-frequency spectropolarimetric imaging sensitive enough to detect the weak polarization signals from thermal bremsstrahlung emission. Chapter 4 (McCauley et al., 2019) introduces the mitigation strategy and surveys the range of circular polarization features found in over 100 observing runs.

Conclusions from each chapter are summarized in Chapter 5, as well as discussions of open questions and future work ideas that can be addressed with the existing dataset produced for this thesis. These include natural extensions of the work on Type III bursts, coronal holes, and polarimetry, along with a preview of a CME discovery that has yet to be reported in the literature.

Chapter 2

Type III Solar Radio Burst Source Region Splitting Due to a Quasi-Separatrix Layer

Published as McCauley et al. (2017), *Astrophys. J.*, 851:151

2.1 Abstract

We present low-frequency (80–240 MHz) radio imaging of Type III solar radio bursts observed by the *Murchison Widefield Array* (MWA) on 2015/09/21. The source region for each burst splits from one dominant component at higher frequencies into two increasingly-separated components at lower frequencies. For channels below ~ 132 MHz, the two components repetitively diverge at high speeds (0.1–0.4 c) along directions tangent to the limb, with each episode lasting just ~ 2 s. We argue that both effects result from the strong magnetic field connectivity gradient that the burst-driving electron beams move into. Persistence mapping of extreme ultraviolet (EUV) jets observed by the *Solar Dynamics Observatory* reveals quasi-separatrix layers (QSLs) associated with coronal null points, including separatrix dome, spine, and curtain structures. Electrons are accelerated at the flare site toward an open QSL, where the beams follow diverging field lines to produce the source splitting, with larger separations at larger heights (lower frequencies). The splitting motion within individual frequency bands is interpreted as a projected time-of-flight effect, whereby electrons traveling along the outer field lines take slightly longer to excite emission at adjacent positions. Given this interpretation, we estimate an average beam speed of 0.2 c. We also qualitatively describe the quiescent corona, noting in particular that a disk-center coronal hole transitions from being dark at higher frequencies to bright at lower frequencies, turning over around 120 MHz. These observations are compared to synthetic images based on the Magnetohydrodynamic Algorithm outside a Sphere (MAS) model, which we use to flux-calibrate the burst data.

2.2 Introduction

Type III solar radio bursts are among the principal signatures of magnetic reconnection, the process thought to underlie solar flares. Their high brightness temperatures demand a coherent, nonthermal emission mechanism that is generally attributed to plasma emission stimulated by semi-relativistic electron beams. Electrons accelerated at the reconnection site generate Langmuir waves (plasma oscillations) in the ambient plasma through the bump-on-tail beam instability. Those Langmuir waves then shed a small fraction of their energy in radio emission near the fundamental plasma frequency (f_p) or its second harmonic. This theory was proposed by Ginzburg and Zhelezniakov (1958) and has since been developed by many authors (see reviews by Robinson and Cairns 2000; Melrose 2009).

Radio bursts are classified by their frequency drift rates, and Type IIIs are so named because they drift faster than Types I and II (Wild and McCready, 1950). A recent review of Type III literature is provided by Reid and Ratcliffe (2014). Starting frequencies are typically in the 100s of MHz, and because the emission frequency is proportional to the square of the ambient electron density ($f_p \propto \sqrt{n_e}$), standard Type III radiation drifts to lower frequencies as the accelerated electrons stream outward. *Coronal* Type III bursts refer to those that drift down to tens of MHz or higher. Beams that escape along open field lines may continue to stimulate Langmuir waves in the solar wind plasma, producing *interplanetary* Type III bursts that may reach 20 kHz and below around 1 AU and beyond. We will focus on coronal bursts for which some fraction of the electrons do escape to produce an interplanetary Type III.

X-ray flares and Type III bursts have been linked by many studies. Various correlation rates have been found, with a general trend toward increased association with better instrumentation. Powerful flares (\geq C5 on the GOES scale) almost always generate coherent radio emission, generally meaning a Type III burst or groups thereof (Benz et al., 2005, 2007). Weaker flares may or may not have associated Type IIIs depending on the magnetic field configuration (Reid and Vilmer, 2017), and Type IIIs may be observed with no GOES-class event if, for instance, the local X-ray production does not sufficiently enhance the global background (Alissandrakis et al., 2015). Flares that produce X-ray or extreme ultraviolet (EUV) jets are frequently associated with Type III emission (Aurass et al., 1994; Kundu et al., 1995; Raulin et al., 1996; Trotter, 2003; Chen et al., 2013b; Innes et al., 2016; Mulay et al., 2016; Hong et al., 2017; Cairns et al., 2018). Such jets are collimated thermal plasma ejections that

immediately follow, are aligned with, and are possibly heated by the particle acceleration responsible for radio bursts (Saint-Hilaire et al., 2009; Chen et al., 2013a). We will exploit the alignment between EUV jets and Type III electron beams to develop an understanding of radio source region behavior that, to our knowledge, has not been previously reported.

This is the first Type III imaging study to use the full 128-tile *Murchison Widefield Array* (MWA; Lonsdale et al. 2009; Tingay et al. 2013a), which follows from Type III imaging presented by Cairns et al. (2018) using the 32-tile prototype array. The MWA’s primary science themes are outlined by Bowman et al. (2013), and potential solar science is further highlighted by Tingay et al. (2013b). The first solar images using the prototype array and later the full array are detailed by Oberoi et al. (2011) and Oberoi et al. (2014), respectively. Suresh et al. (2017) present a statistical study of single-baseline dynamic spectra, which exhibit the lowest-intensity solar radio bursts ever reported. We present the first time series imaging.

Along with the *Low Frequency Array* (LOFAR; van Haarlem et al. 2013; Morosan et al. 2014), the MWA represents a new generation of low frequency interferometers capable of solar imaging. Previous imaging observations at the low end of our frequency range were made by the decommissioned *Culgoora* (Sheridan et al., 1972, 1983) and *Clark Lake* (Kundu et al., 1983) radioheliographs, along with the still-operational *Gauribidanur Radioheliograph* (Ramesh et al., 1998, 2005). The high end of the MWA’s frequency range overlaps with the *Nançay Radioheliograph* (NRH; Kerdraon and Delouis 1997), which has facilitated a number of Type III studies referenced here.

This paper is structured as follows. Section 2.3 describes our observations and data reduction procedures. Our analyses and results are detailed in Section 2.4. Section 2.4.1 considers the quiescent corona outside burst periods, which we compare to synthetic images used to flux calibrate the burst data in Section 2.4.2. Section 2.4.3 characterizes the Type III source region structure and motion, and the local magnetic field configuration is inferred using EUV observations in Section 2.4.4. In Section 2.5, our results are combined to produce an interpretation of the radio source region behavior. Section 2.6 provides concluding remarks.

Ch. 2 Type III Burst Source Splitting

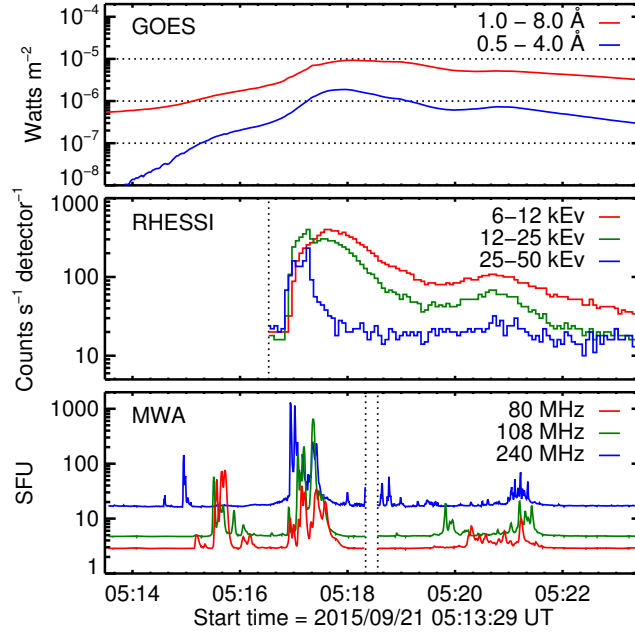


Figure 2.1: *Top*: GOES soft X-ray light curves, showing the C8.8 flare that peaked at 05:18 UT. Dotted lines from bottom to top indicate the B, C, and M-class thresholds. *Middle*: RHESSI count rates from 6–50 keV. The dotted line indicates the end of RHESSI’s night (Earth-eclipse) period. *Bottom*: MWA light curves at 80, 108, and 240 MHz. Dotted lines indicate the transition between continuous observing periods.

2.3 Observations

We focus on a brief series of Type III bursts associated with a C8.8 flare that peaked at 05:18 UT on 2015/09/21. The flare occurred in Active Region 12420¹ on the east limb. This investigation began by associating MWA observing periods that utilize the mode described in Section 2.3.1 with isolated Type III bursts logged in the National Oceanic and Atmospheric Administration (NOAA) solar event reports². A small sample of bursts detected from 80 to 240 MHz were selected, and we chose this event for a case study because of the unusual source structure and motion. A survey of other Type III bursts is ongoing.

Figure 2.1 shows the soft X-ray (SXR) light curves from the *Geostationary Operational Environmental Satellite* (GOES³) for our MWA observation

¹AR 12420 summary: <https://www.solarmonitor.org/index.php?date=20150921®ion=12420>

²NOAA event reports: <http://www.swpc.noaa.gov/products/solar-and-geophysical-event-reports>

³GOES X-ray flux: <http://www.swpc.noaa.gov/products/goes-x-ray-flux>

period, along with those from the *Reuven Ramaty High-Energy Solar Spectroscopic Imager* (RHESSI; Lin et al. 2002). The corresponding MWA light curves, as derived in Section 2.3.1 and Section 2.4.1, show that the radio bursts occur primarily around the hard X-ray (HXR, 25–50 keV) peak and just before the SXR peak, with some minor radio bursts scattered throughout the SXR rise and decay phases. HXR and Type III emissions are known to be approximately coincident in time (Arzner and Benz, 2005) and are generally attributed to oppositely-directed particle acceleration, with HXR production resulting from heating by the sunward component. The same process may underlie both, however small differences in the timing, along with large differences in the requisite electron populations, suggest there may be multiple related acceleration processes (e.g. Brown and Melrose 1977; Krucker et al. 2007; White et al. 2011; Cairns et al. 2018). In contrast, SXR emission is associated with thermal plasma below the reconnection site, generally peaking somewhat later with a more gradual profile as in Figure 2.1.

Our initial radio burst detections relied on observations from the *Learmonth* and *Culgoora* solar radio spectrographs. Part of the global *Radio Solar Telescope Network*⁴ (RSTN; Guidice et al. 1981), the *Learmonth* spectrograph covers 25 to 180 MHz in two 401-channel bands that run from 25–75 and 75–180 MHz. Additional technical details are provided by Kennewell and Steward (2003). The *Culgoora* spectrograph⁵ (Prestage et al., 1994) has broader frequency coverage (18–1800 MHz) over four 501-channel bands. Only the 180–570 MHz band is relevant here, and we show just a portion of it because the *Learmonth* spectrograph is more sensitive where they overlap. Both instruments perform frequency sweeps every 3 s. Dynamic spectra are plotted in Figure 2.2, each being log-scaled and background-subtracted by 5-min boxcar averages.

Figure 2.2 also includes dynamic spectra from the *Radio and Plasma Wave Investigation* (WAVES; Bougeret et al. 1995) on the *Wind* spacecraft. These data demonstrate an interplanetary component to the coronal Type III bursts, which requires there be connectivity to open field lines along which electrons escaped the corona. This will be important to our interpretation of the magnetic field configuration in Section 2.5.

⁴RSTN data: <ftp://ftp.ngdc.noaa.gov/STP/space-weather/solar-data/solar-features/solar-radio/rstn-spectral>

⁵Culgoora data: ftp://ftp-out.sws.bom.gov.au/wdc/wdc_spec/data/culgoora/

Ch. 2 Type III Burst Source Splitting

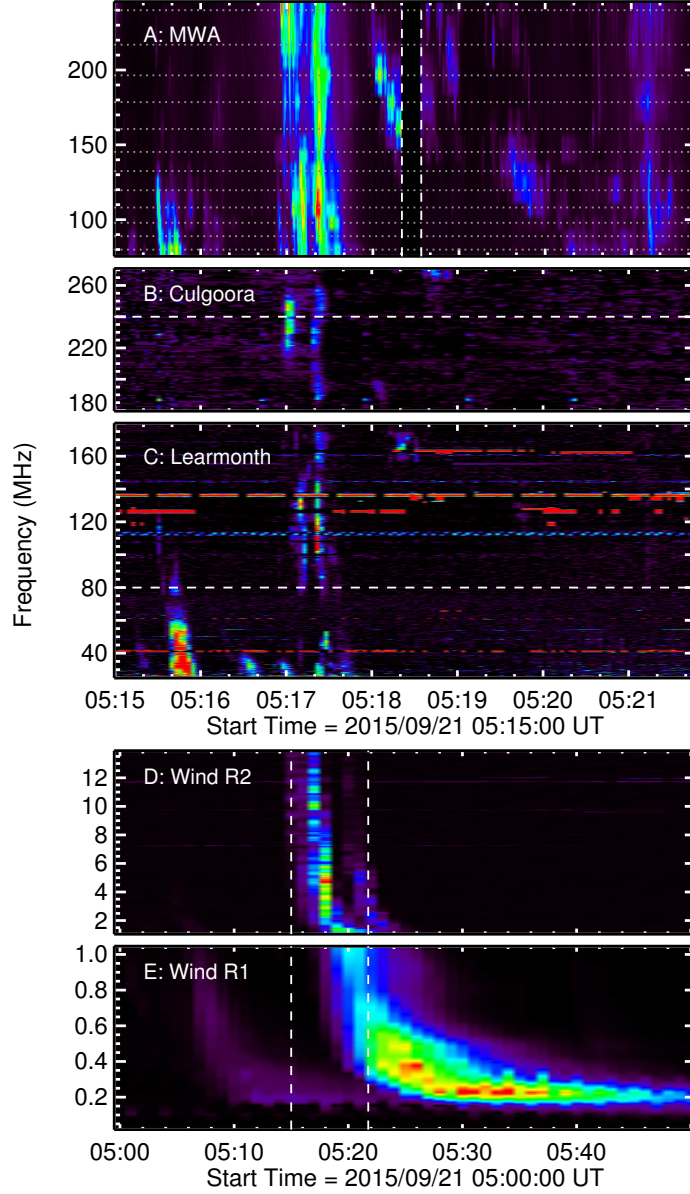


Figure 2.2: A: MWA dynamic spectrum (DS) produced from total image intensities and interpolated to a spectral resolution equal to the minimum separation between observing bandwidths (see Section 2.3.1.) Dashed vertical lines indicate the transition between continuous observing periods, and dotted horizontal lines mark the 12, 2.56 MHz-wide frequency channels. B–C: Culgoora and Learmonth DS. Dashed lines indicate the MWA frequency coverage bounds (80–240 MHz). D–E: *Wind*/WAVES RAD2 and RAD1 DS. Note that the time axis is expanded to show the low-frequency tail. The dashed lines indicate the period covered by panels A–C. All DS are log-scaled and then background-subtracted. A corresponding movie is available in the [online material](#).

2.3.1 *Murchison Widefield Array* (MWA)

The MWA is a low-frequency radio interferometer in Western Australia that consists of 128 aperture arrays (“tiles”), each comprised of 16 dual-polarization dipole antennas (Tingay et al., 2013a). It has an instantaneous bandwidth of 30.72 MHz that can be spread flexibly from 80 to 300 MHz. Our data employ a “picket fence” observing mode, whereby twelve 2.56 MHz bands are distributed between 80 and 240 MHz with gaps of 9–23 MHz between them. This configuration is chosen to maximize spectral coverage while avoiding radio frequency interference (RFI). Data are recorded with a time resolution of 0.5 s and a spectral resolution of 40 kHz, which we average across the 2.56 MHz bandwidths to produce images centered at 80, 89, 98, 108, 120, 132, 145, 161, 179, 196, 217, and 240 MHz. Figures 2.3 and 2.4 show images at six frequencies during quiescent and burst phases, respectively, and a movie showing all twelve bands over the full time series is available in the [online material](#)⁶.

Visibilities were produced using the standard MWA correlator (Ord et al., 2015) and `cotter` (Offringa et al., 2015). For our calibrator observations, this included 8-s time averaging and RFI flagging using the `aoflagger` algorithm (Offringa et al., 2012). RFI flagging was disabled for the solar observations, as it tends to flag out burst data. Calibration solutions for the complex antenna gains were obtained with standard techniques (Hurley-Walker et al., 2014) using observations of a bright and well-modelled calibrator source (Centaurus A) made ~ 2 hours after the solar observations. To improve the calibration solutions, the calibrator was imaged and ten loops of self-calibration were performed in the manner described by Hurley-Walker et al. (2017).

This last step is typically performed on science target images, but we apply it instead to the calibrator for two reasons. First, we find that day-time observations generally produce inferior calibration solutions compared to analogous night-time data. We attribute this to contamination of the calibrator field by sidelobe emission from the Sun, but ionospheric and temperature effects may also be important. Second, the `clean` algorithm essential to the self-calibration process works best when the field is dominated by compact, point-like sources, which is not the case for the Sun. The same steps performed on our solar images tended to degrade the overall quality of the calibration solutions and bias the flux distribution of the final images. However, we find that it is best to self-calibrate on the field source to obtain quality polarimetry because trans-

⁶Movies available at <https://iopscience.iop.org/article/10.3847/1538-4357/aa9cee>

Ch. 2 Type III Burst Source Splitting

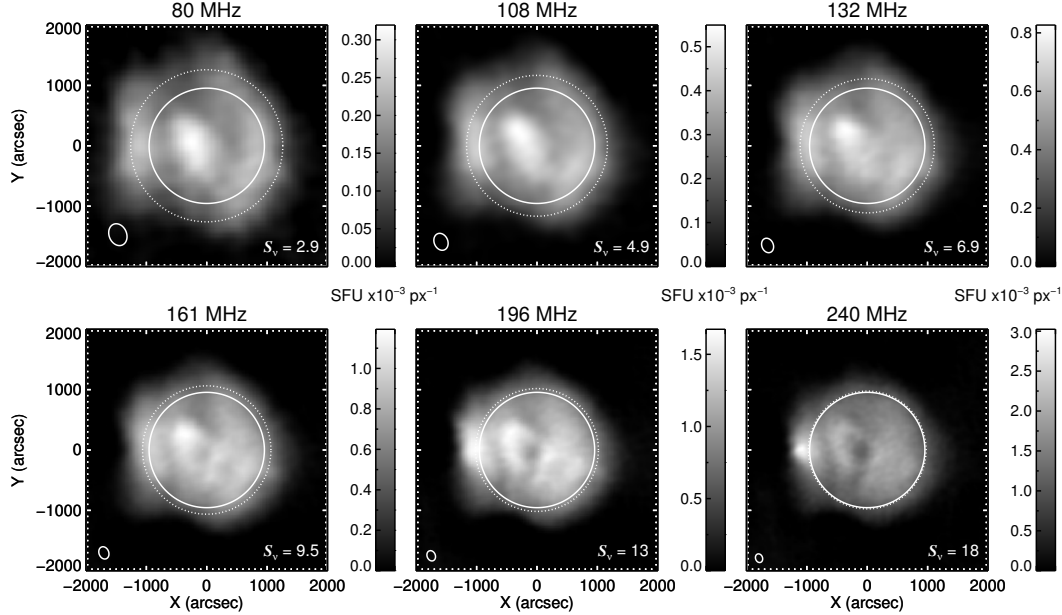


Figure 2.3: MWA Stokes I images for 6 of the 12 frequency bands during a quiescent period at 2015/09/21 05:13:33.20 UT. The solid inner circles denote the optical disk, and the dotted outer circles denote the Newkirk-model (Newkirk, 1961) limb for a given frequency. Ellipses in the bottom-left corners represent the synthesized beams. Values in the bottom-right corners are full-Sun integrated flux densities (S_{ν}) in SFU, and the color bars represent the flux density enclosed by each $20''$ pixel in $\text{SFU} \times 10^{-3}$ (see Section 2.4.2 for details). A movie showing the full time series for all 12 bands is available in the [online material](#).

ferring calibration solutions from a lower-elevation pointing typically produces overwhelming Stokes I leakage into the other Stokes portraits. For this reason, we do not include polarimetry here. Progress has been made on producing reliable polarimetric images of the Sun with the MWA, as well as improving the dynamic range, but that is beyond the scope of this paper.

Once calibrated, imaging for each 0.5 s integration is accomplished using WSClean (Offringa et al., 2014) with the default settings except where noted below. Frequencies are averaged over each 2.56 MHz bandwidth, excluding certain fine channels impacted by instrumental artefacts. To emphasize spatial resolution, we use the Briggs -2 weighting scheme (Briggs, 1995). Cleaning is performed with ~ 10 pixels across the synthesized beam, yielding $16\text{--}36'' \text{ px}^{-1}$ from 240–80 MHz. We use a stopping threshold of 0.01, which is roughly the average RMS noise level in arbitrary units obtained for quiescent images cleaned with no threshold. Major clean cycles are used with a gain of 0.85 (`-mgain 0.85`), and peak finding uses the quadrature sum of the instrumental polarizations (`-joinpolarizations`). Finally, Stokes I images are produced using

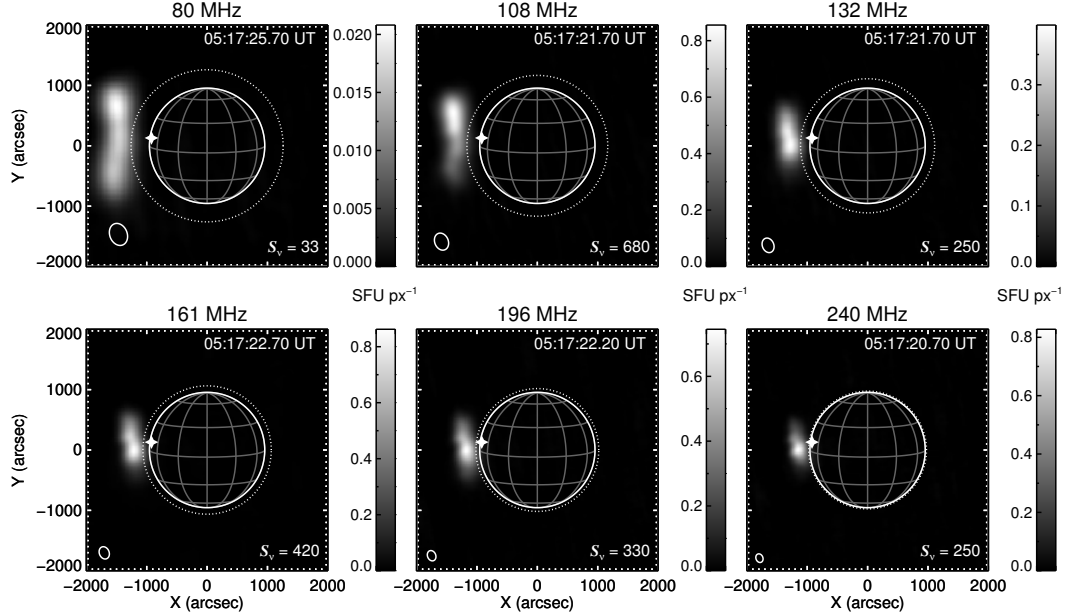


Figure 2.4: Same as Figure 2.3 but for the frequency-specific peak intensity times associated with the event from 05:17:20 to 05:17:25 UT, which may comprise multiple overlapping bursts (see Section 2.4.3 & Section 2.5). Color bar units are in SFU px⁻¹, and stars mark the X-ray flare site.

the primary beam model described by Sutinjo et al. (2015).

To compare MWA data with other solar imaging observations, we introduce the `mwa_prep` routine, now available in the SolarSoftWare libraries for IDL (SSW⁷, Freeland and Handy 1998). WSClean and the alternative MWA imaging tools produce FITS images using the SIN-projected celestial coordinates standard in radio astronomy. Solar imaging data typically use “helioprojective-cartesian” coordinates, which is a TAN projection aligned to the solar rotation axis with its origin at Sun-center (Thompson, 2006). To convert between the two coordinate systems, `mwa_prep` rotates the image about Sun-center by the solar P angle, interpolates onto a slightly different grid to account for the difference between the SIN and TAN projections, and scales the images to a uniform spatial scale (20'' px⁻¹). By default, the final images are cropped to 6×6 R_⊙, yielding 289×289 pixels. FITS headers are updated accordingly, after which the various SSW mapping tools can be used to easily overplot data from different instruments.

We will consider quiescent radio structures in Section 2.4.1 against corresponding model images that are used for flux calibration in Section 2.4.2. Burst

⁷SSW: <https://www.lmsal.com/solarsoft/>

Ch. 2 Type III Burst Source Splitting

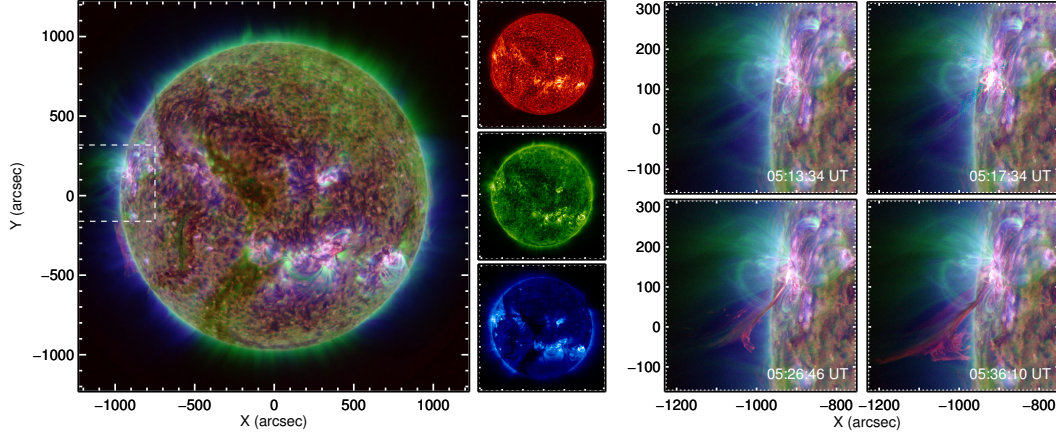


Figure 2.5: An overview of the event seen by SDO/AIA using RGB composites of the 304, 171, and 211 Å channels. The top panels on the right half show nearly the same times as Figures 2.3 (left) and 2.4 (right), with the rightmost panel corresponding to just before the SXR peak. The bottom-right panels show snapshots of the EUV jets that follow the radio bursts.

structure and dynamics are discussed in Section 2.4.3.

2.3.2 *Solar Dynamics Observatory* (SDO)

The *Solar Dynamics Observatory* (SDO, Pesnell et al. 2012) is a satellite with three instrument suites, of which we use the *Atmospheric Imaging Assembly* (AIA; Lemen et al. 2012). We also indirectly use photospheric magnetic field observations from the *Helioseismic and Magnetic Imager* (HMI; Scherrer et al. 2012), which inform the synthetic images in Section 2.4.1. The AIA is a full-Sun imager consisting of four telescopes that observe in seven narrowband EUV channels with a $0.6'' \text{ px}^{-1}$ spatial resolution and 12 s cadence, along with three UV bands with a lower cadence.

Calibrated (“level 1”) data are obtained from the Virtual Solar Observatory (VSO⁸, Hill et al. 2009). The SSW routine `aia_deconvolve_richardsonlucy` is used to deconvolve the images with filter-specific point spread functions, and `aia_prep` is used to co-align and uniformly scale data from the different telescopes. Figure 2.5 presents an overview of our event using RGB composites of the 304, 171, and 211 Å channels. These bands probe the chromosphere, upper transition region / low corona, and corona, respectively, with characteristic temperatures of .05 (He II), 0.63 (Fe IX), and 2 MK (Fe XIV).

The AIA observations show a fairly compact flare that produces several

⁸VSO: <http://sdac.virtualsolar.org/>

distinct EUV jets beginning just before the soft X-ray peak at 05:18 UT. This includes higher-temperature material visible in up to the hottest band (94 Å, 6.3 MK), along with cooler ejecta at chromospheric temperatures that appears in emission at 304 Å and in absorption at other wavelengths. These outflows reveal a complex magnetic field configuration south of the flare site, which we will explore in Section 2.4.4 and in Section 2.5 with respect to the radio emission.

2.4 Analysis & Results

2.4.1 Quiescent Structure and Model Comparison

We examine model images of the coronal intensity at MWA frequencies to qualitatively compare the expected and observed structures outside of burst periods. In the next subsection, we also use the predicted quiescent flux densities to obtain a rough flux calibration of our burst data. Synthetic Stokes I images are obtained using FORWARD⁹, an SSW package that can generate a variety of coronal observables using different magnetic field and/or thermodynamic models. At radio wavelengths, FORWARD computes the expected contributions from thermal bremsstrahlung (free-free) and gyroresonance emission based on the modeled temperature, density, and magnetic field structure. Details on those calculations, along with the package’s other capabilities, are given by Gibson et al. (2016).

Our implementation uses the Magnetohydrodynamic Algorithm outside a Sphere (MAS¹⁰; Lionello et al. 2009) medium resolution (hmi_mast_mas_std_0201) model. The MAS model combines an MHD extrapolation of the coronal magnetic field (e.g. Mikić et al. 1999) based on photospheric magnetogram observations from the HMI with a heating model adapted from Schrijver et al. (2004). Comparisons between MAS-predicted images and data have been made a number of times for EUV and soft X-ray observations, with generally good agreement for large-scale structures (e.g. Riley et al. 2011; Reeves and Golub 2011; Downs et al. 2012). We make the first radio comparisons.

The top row of Figure 2.6 shows synthetic images at four MWA frequencies. Beam-convolved versions are shown in the middle row, but note that this does not account for errors introduced by the interferometric imaging process, such

⁹FORWARD: <https://www2.hao.ucar.edu/modeling/FORWARD-home>

¹⁰MAS: http://www.predsci.com/hmi/data_access.php

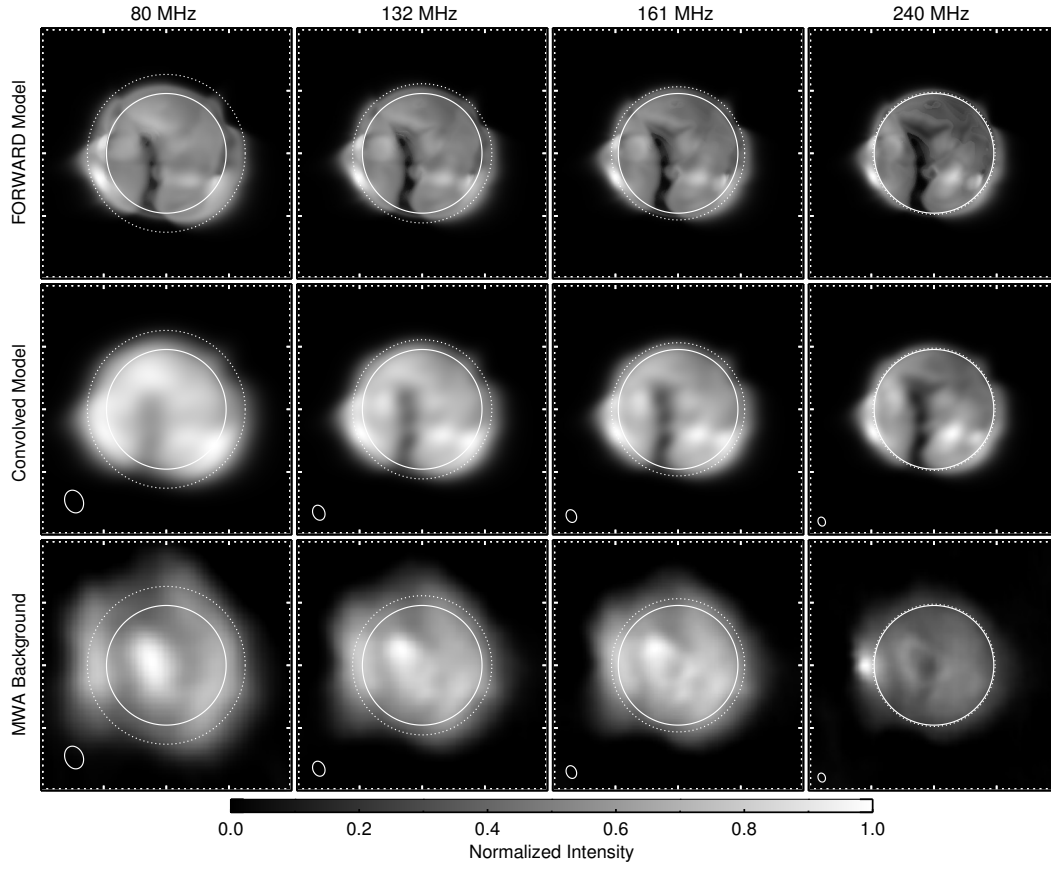


Figure 2.6: *Top*: Expected free-free and gyroresonance emission at four frequencies predicted by FORWARD based on the MAS thermodynamic MHD model. *Middle*: Model images convolved with the corresponding MWA beams. *Bottom*: Median MWA emission outside burst periods over the first 4-min observation period, which is assumed to be the quiescent background for flux calibration. Plot axes and annotations are as in Figure 2.3. An animation with all 12 channels is available in the [online material](#).

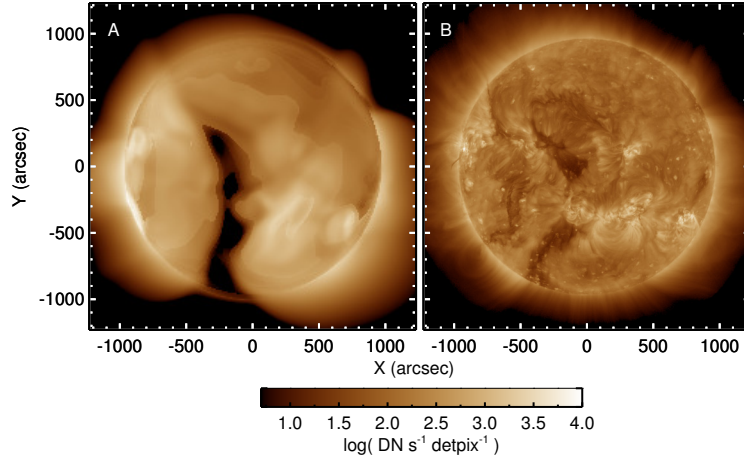


Figure 2.7: 193 Å synthetic image (A) and SDO observation (B). The synthetic image applies the telescope response function so that both images are plotted on exactly the same scale in instrumental units (DN) per sec per detector pixel (detpix).

as effects related to deconvolving a mixture of compact and diffuse emission or to nonlinearities in the **clean** algorithm. MWA data are shown in the bottom row and reflect median pixel values over the first five-minute observation (05:13:33 to 05:18:20), excluding burst periods defined as when the total image intensities exceed 105% of the first 0.5 s integration for each channel. An animation with all 12 channels is available in the [online material](#). For context, we also show a comparison of a 193 Å SDO observation and prediction using the same model in Figure 2.7.

The agreement between the observed and modelled radio images is best at our highest frequencies ($\gtrsim 179$ MHz), where the correspondence is similar to that of the EUV case. For both, the model reproduces structures associated with coronal holes near the central meridian and the large active region complexes in the southwest. The large-scale structure associated with the southern polar coronal hole is also well-modelled for the radio case. A similar structure is predicted for the EUV but is disrupted by the observed polar plumes in the manner described by Riley et al. (2011). The modelled images also underpredict emission from EUV coronal holes, which may be due to contributions from low-temperature ($< 500,000$ K) material ignored by the emissivity calculations. Other contributing factors might be inaccuracies in the heating model, evolution of the magnetic boundary from that used for the simulation, or 193 Å emission from non-dominant ions formed at low temperatures.

A number of discrepancies between the model and MWA observations are

Ch. 2 Type III Burst Source Splitting

also apparent, particularly with decreasing frequency. With the exception of the bright region on the east limb at 240 MHz, which we will revisit in Section 2.5, we suspect these differences underscore the importance of propagation effects to the appearance of the corona at low frequencies. In particular, refraction (ducting) of radio waves as they encounter low-density regions, as well as scattering by density inhomogeneities, can profoundly alter the observed source structure (see reviews by Lantos 1999; Shibasaki et al. 2011). Both effects can increase a source’s spatial extent, decrease its brightness, and alter its apparent location (e.g. Aubier et al. 1971; Alissandrakis and Chiuderi-Drago 1994; Bastian 1994; Thejappa and MacDowall 2008; Ingale et al. 2015). We likely see the effects of scattering and/or refraction in the increased radial extent of the observed emission at all frequencies compared to the beam-convolved model images, though an enhanced density profile may also contribute. Likewise, these propagation effects may be responsible for dispersing the signatures of the southwestern active regions, which are prominent in the synthetic images but only barely discernible in our observations.

Most conspicuously, the disk-center coronal hole gradually transitions from a dark feature at high frequencies to a bright one at low frequencies in the observations but not in the synthetic data. This could be due to the diminished spatial resolution at low frequencies, meaning the coronal hole signature is swamped by emission from the bright region to the northeast. However, that effect should serve only to reduce the coronal hole contrast, as it does for the beam-convolved synthetic images. Indeed, another set of observations of a different disk-center coronal hole also show this dark-to-bright transition from high to low frequencies with even less ambiguity. In both cases, the transition is gradual and turns over around 120 MHz. Above the ~ 120 MHz transition we observe, coronal holes are consistently reported as intensity depressions (e.g. Mercier and Chambe 2012), which is expected given their low densities. At longer wavelengths, coronal holes have sometimes been seen in emission (Dulk and Sheridan, 1974; Lantos et al., 1987), as in our lower frequency channels. Again, scattering (Riddle, 1974; Hoang and Steinberg, 1977) and/or refraction (Alissandrakis and Chiuderi-Drago, 1994) may be able to explain low-frequency enhancements in low-density regions, but a satisfactory explanation has not been achieved, in part because of limited data. The MWA appears to be uniquely poised to address this topic given that the transition of certain coronal holes between being dark or bright features occurs within the instrument’s frequency range, but an analysis of this is beyond the scope of this paper.

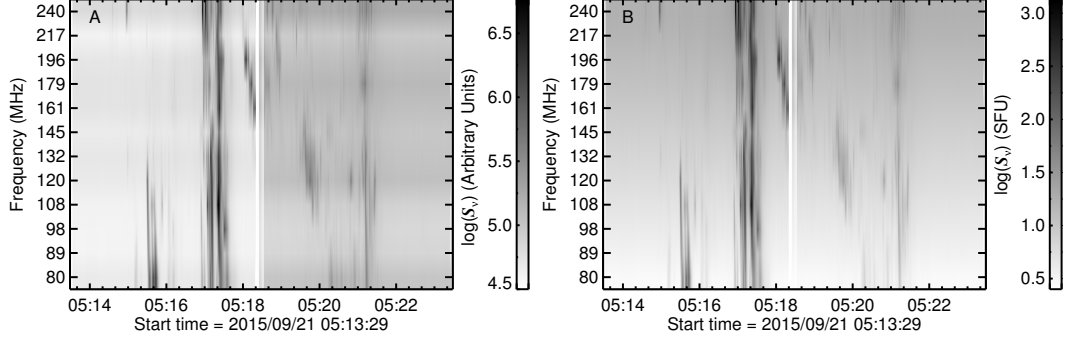


Figure 2.8: Uncalibrated (A) and flux-calibrated (B) dynamic spectra generated from total image intensities. The Y axes intervals are not uniform; values refer to the 12 2.56-MHz-wide observing bandwidths separated by gaps of 9–23 MHz (see Section 2.3.1). An interpolated dynamic spectrum with a uniform Y axis is shown in Fig 2.2.

2.4.2 Flux Calibration

Absolute flux calibration is challenging for radio data because of instrumental uncertainties and effects related to interferometric data processing. Astrophysical studies typically use catalogs of known sources to set the flux scale, and many MWA projects now use results from the GaLactic and Extragalactic All-sky MWA Survey (GLEAM; Hurley-Walker et al. 2017). We cannot take this approach because calibrator sources are not distinguishable in close proximity to the Sun given the dynamic range of our data. Even calibrators at sufficiently large angular separations from the Sun to be imaged are likely to be contaminated by solar emission due to the MWA’s wide field of view (see Section 2.3.1).

To express our burst intensities in physical units, we take brightness temperature images from FORWARD and convert them to full-Sun integrated flux densities (S_ν), which we then assume to be equal to the total flux density in the quiescent background images from Figure 2.6. From this comparison, we obtain a simple multiplicative scaling factor to convert between the uncalibrated image intensities and solar flux units (SFU; $1 \text{ SFU} = 10^4 \text{ Jy} = 10^{-22} \text{ W m}^{-2} \text{ Hz}^{-1}$). This procedure is performed separately for both observing periods, and Figure 2.8 illustrates the result by plotting an uncalibrated dynamic spectrum next to the calibrated version.

In the calibrated spectrum, we see that the quiescent intensities are coherently ordered in the pattern expected for thermal emission, with flux density increasing with frequency. Importantly, the adjacent MWA observing periods are also set onto very similar flux scales. We find an overall peak flux density

Ch. 2 Type III Burst Source Splitting

of 1300 SFU at 240 MHz. Relative to the background, however, the burst series is most intense around 108 MHz, peaking at 680 SFU around $140\times$ the background level (see the log-scaled and then background-subtracted dynamic spectrum in Figure 2.2). This makes our event of moderate intensity compared to those in the literature (e.g. Saint-Hilaire et al. 2013).

This technique provides a simple way to obtain reasonable flux densities for radio bursts in order to place them generally in context. Given the differences between the observations and synthetic images, this method should not be applied if very accurate flux densities are important to the results, which is not the case here. It would also not be appropriate for analyzing quiet-Sun features, nor for cases where non-thermal emission from a particular active region dominates the Sun for the entire observation period. However in this case, we see primarily thermal emission that we suspect is modulated by propagation effects not considered by FORWARD. These effects are not expected to dramatically affect the total intensity but may decrease it somewhat, which would cause our flux densities to be overestimated.

A more sophisticated solar flux calibration method has recently been developed by Oberoi et al. (2017), who use a sky brightness model to subtract the flux densities of astronomical sources, leaving just that produced by the Sun. This method is applied to data from a single short baseline, yielding a total flux density that can be used to calibrate images with a scaling factor analogous to ours. This approach would be appropriate for quiet-Sun studies and preferable for burst studies that make significant use of the fluxes. We note that our method yielded quiescent fluxes within a factor of 2 of those found by Oberoi et al. (2017) for a different day, after accounting for the different polarizations used. Future work will explicitly compare the two approaches.

2.4.3 Type III Source Structure and Motion

The Type III bursts begin around 05:15:30 UT during the early rise phase of the X-ray flare and continue at intervals through the decay phase. The two main bursts distinguishable in the *Learmonth* and *Culgoora* spectrographs are approximately coincident with the hard X-ray peak around 05:17 UT (Figure 2.1). The more sensitive and temporally-resolved MWA observations reveal these events to have a complicated dynamic spectrum structure that we interpret as the overlapping signatures of multiple electron injections in a brief period (Figure 2.2).

Throughout all of the bursts, a consistent pattern emerges in both the

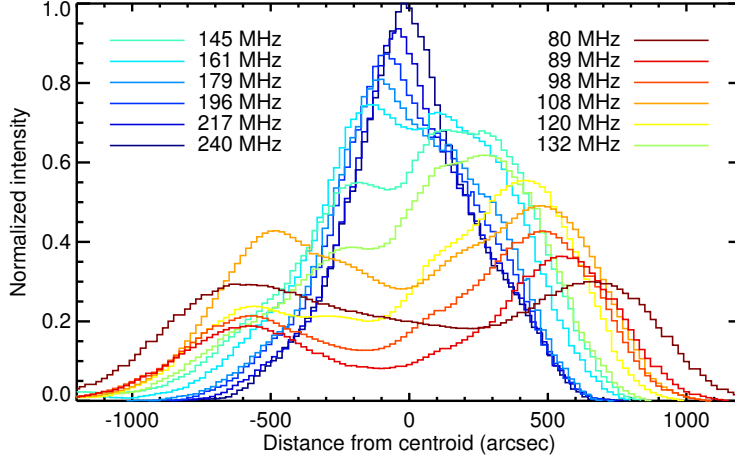


Figure 2.9: Image slit intensities for each of the 12 MWA channels along the elongation axes of the individual burst source regions, illustrating the splitting of the source region from high to low frequencies. These data correspond to a period when the source regions are maximally extended at 05:17:26.6 UT. Each curve is normalized and multiplied by a scaling factor from 0.3–1.0 for clarity.

spatial structure of the source regions as a function of frequency and in their motions at particular frequencies. At higher frequencies, the Type III source region is dominated by one spatial component with a much fainter component immediately to the north. Moving to lower frequencies and correspondingly larger heights, the two components separate along a direction tangent to the limb, reaching a peak-to-peak separation of $1200''$ ($1.25 R_{\odot}$) at 80 MHz. This structure is clear from the burst images in Figure 2.4 and is illustrated in further detail by Figure 2.9.

Figure 2.9 plots intensities extracted from image slits along the directions for which the emission is maximally extended. Slit orientations are determined by fitting ellipses to the overall source region in each channel after thresholding the images above 20% of their peak intensities. Distances refer to that from the ellipse centers along their major axes, with values increasing from south to north. For clarity, the intensities are normalized and then multiplied by arbitrary scaling factors between 0.3 and 1.0 from low to high frequencies. At least two Gaussian components are required to fit the curves at all frequencies, though the northern component is manifested only as a non-Gaussian shoulder on the dominant component at high frequencies. At some frequencies (e.g. 108 MHz), there are also additional weaker peaks between the two main components. Interpretation of the varying burst morphology as a function of frequency is given in Section 2.5.

Ch. 2 Type III Burst Source Splitting

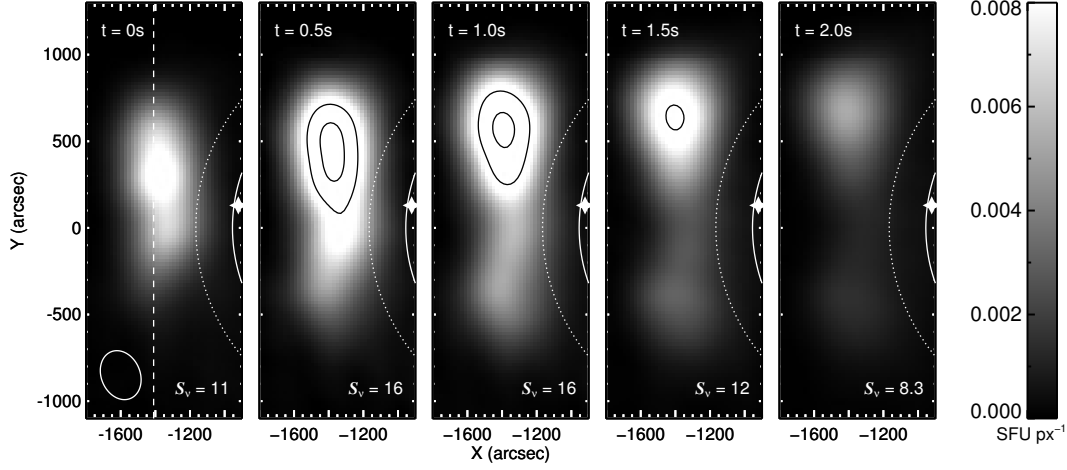


Figure 2.10: Source splitting motion at 108 MHz, beginning at 05:16:53.70 UT. The dashed line in the left panel denotes the slit used in Figure 2.11. The two solid black contours in the source region are at 0.010 and 0.015 SFU px^{-1} . Additional annotations are as in Figure 2.4.

The Type III source region components also spatially diverge as a function of time within single-channel observations below ~ 132 MHz. At higher frequencies, for which there are one or two closely-spaced components, the source regions instead become increasingly elongated with time. The direction of this motion is essentially the same as that of the frequency-dependent splitting, and the timescales for it are quite short, on the order of ~ 2 s. This motion is repeated many times throughout the event, with each burst and corresponding “split” interpreted as a distinct particle acceleration episode. An example image set is shown in Figure 2.10 for 108 MHz, the frequency that exhibits the highest intensities relative to the background.

To quantify this behavior, we employ distance-time maps to track movement along a particular slice through the images. The emission along the slit shown in the left panel of Figure 2.10 is extracted from each observation and stacked against those from adjacent images, such that each vertical column of Figures 2.11a and 2.11b represents the slit intensity at a given time. Slopes in the “slit image” correspond to plane-of-sky velocity components in the slit direction. Figure 2.11a shows the result of this analysis for the bursts during the first MWA observation period, lasting nearly 3 minutes after 05:15 UT. Intensities have been divided by the time-dependent noise level, defined as the standard deviation of values within a 5-pixel-wide border around the edge of each image (equivalent in area to a 75×75 px, or 25×25 arcmin, box). Because the noise level is roughly proportional to the total intensity, which varies

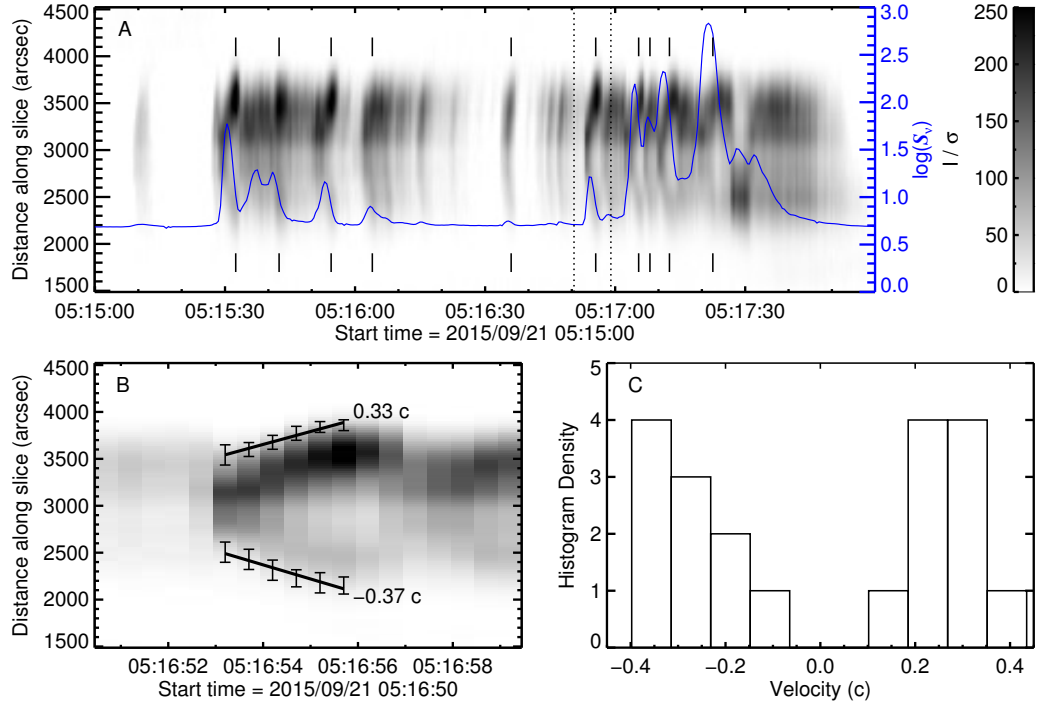


Figure 2.11: An overview of the source splitting kinematics at 108 MHz. Panel A shows a distance-time plot using the slit shown in Figure 2.10 along with a light curve of the total flux density in blue. Dotted vertical lines demarcate the zoomed-in section in Panel B, which corresponds to the images shown in Figure 2.10. Vertical ticks mark the 10 speed measurement periods whose results are collected in Panel C. Error bars in Panel B reflect the range of leading-edge estimates, obtained by thresholding the two components by 15–25% of their maximum $I \cdot \sigma^{-1}$ values.

by 2–3 orders of magnitude, this operation flattens the dynamic range of the distance-time map and provides for the uniform thresholding scheme described next.

Throughout the series, the bursts peak in intensity at around the midpoint in the splitting motion, which is illustrated by the blue light curve in Figure 2.11a. When the motion ends, the source regions gradually fade into the background with constant morphologies, or they are supplanted by those of a subsequent burst. This decay phase manifests as the flat region in the distance-time profile in Figure 2.11b. Note that the time period for Figure 2.9 is chosen so that each of the frequencies are in the declining phase, which is possible in that case because a subsequent burst does not follow for several seconds.

The leading edges of the two source regions (north and south) are defined and tracked independently by thresholding the slit image above a percentage of the peak signal-to-noise ratio (SNR) for each component. Measurements are

Ch. 2 Type III Burst Source Splitting

made for each burst using 11 integer thresholds between 15 and 25% of the peak SNR. This corresponds to values of 40–67 σ for the northern component and 19–32 σ for the southern. Error bars in Figure 2.11b represent the resulting range of leading edge locations, and corresponding speed uncertainties are on the order of 15%. An SNR percentage is used instead of a single set of values for both sources because it expands the range of reasonable thresholds, better representing the measurement uncertainties compared to a more restrictive range that would be appropriate for both sources.

We also explored quantifying the same motion by instead tracking the centroid positions of the two source components. This approach was ultimately discarded because of difficulties in reliably separating the two main components across the full time series, particularly when the region is most compact at the beginning of each burst. Our results may be hindered somewhat by scattering of the type described in Section 2.4.1, which will be most pronounced near the source region perimeter. However, this would only affect the measured speeds if the scattering properties change significantly over the distance covered, and there appears to be little deviation of the leading edge slope from that of the overall source pattern in Figure 2.11b.

Vertical ticks in Figure 2.11a mark the 10 bursts for which speed measurements were made at 108 MHz, and a histogram of the results is plotted in Figure 2.11c. The time periods were chosen for particularly distinct source separation for which both components could be tracked. It is clear from Figure 2.11a that the splitting motion occurs over a few additional periods for which measurements were precluded by confusion with adjacent events, faintness, or duration. We find speeds ranging between 0.11 and 0.40 c, averaging 0.26 c for the northern component and 0.28 c for the southern. The southern component is consistently faster for the 6 measurements before 05:16:55 UT and consistently slower after, but these differences are not statistically significant. These values cannot be straightforwardly interpreted as the exciter or electron beam speed (i.e. the average speed of accelerated electrons) because that would require electrons traveling along flux tubes parallel to the limb in a manner inconsistent with the inferred magnetic field configuration (Section 2.4.4). In Section 2.5, we will argue that this motion is a projected time-of-flight effect such that the splitting speeds here exceed the beam speed by a factor of $\lesssim 1.2$.

The beam speed may be estimated more directly by examining the burst location at different frequencies as a function of time. We do this in Figure 2.12, which shows a distance-time plot similar to Figure 2.11. Instead of the emission along a particular slit, each column of Figure 2.12 corresponds to the total

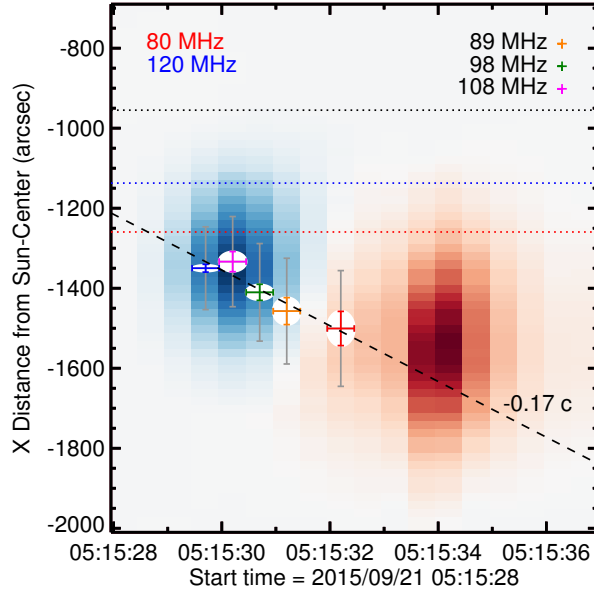


Figure 2.12: Distance-time plot for burst emission from 05:15:28 to 05:15:37 UT. Red (80 MHz) and blue (120 MHz) images represent background-subtracted intensities averaged in the solar-Y direction, such that the slope reflects overall source motion in the solar-X direction. Crosshairs denote the burst onset times and centroid positions for each given frequency, where the onset is defined as exceeding $5\times$ the background. Error bars correspond to the 0.5s time resolution (horizontal), the 3σ variation in position over the burst period (vertical), and the minor synthesized beam axes (vertical, grey). Dotted horizontal lines represent the optical limb (black) and the Newkirk-model limbs at 80 (red) and 120 (blue) MHz.

image intensity binned down to a single row. Pixels with the same horizontal X coordinate are averaged, and these Y-averaged curves are stacked vertically against each other to show movement in the X direction. This is done so that the bidirectional vertical motion, which is primarily exhibited in single-channel observations (Figures 2.10 & 2.11), can be ignored to track the outward progression of the overall source region across frequency channels. Since our source regions are distributed on either side of the equator, this roughly corresponds to radial motion in the plane of the sky.

To quantify this motion, we track the center position at the onset of the burst for each channel, which we define as $5\times$ the background intensity. We use the onset as opposed the times of peak intensity to avoid potential confusion between fundamental and second harmonic emission. Previous studies have shown from both observational (Dulk et al., 1984) and theoretical (Robinson and Cairns, 1994) perspectives that emission at the fundamental plasma fre-

Ch. 2 Type III Burst Source Splitting

quency arrives before associated harmonic emission, which may follow around the overall peak time after a frequency-dependent offset. Tracking the position at the onset of the burst thus ensures that we follow a coherent progression. Note, however, that there is no standard in the literature. Estimates of Type III beam speeds using the frequency drift rate technique, which will be discussed in Section 2.5, have used both onset and peak times (see review by Reid and Ratcliffe 2014).

Center positions are determined by fitting a Gaussian to the relevant time column. We track center positions here because the same difficulties described for Figure 2.11 do not exist in this case and also because it mitigates the potential influence of frequency-dependent scattering. Scattering may still impact our result if the source locations are modulated significantly as a function of frequency, but we cannot readily test that possibility. We choose to examine the earliest burst period, occurring from 05:15:29–05:15:35 UT at frequencies below ~ 132 MHz, because that event can be easily followed from high to low frequencies, whereas the more intense bursts later appear to comprise several overlapping events. Fitting a line to the resulting spatiotemporal positions in Figure 2.12, we find a speed of 0.17 c. This result reflects the average outward motion of the entire source, which can be taken as a lower limit to the exciter speed.

In comparison, the 108 MHz splitting speed for the same period averages to 0.28 c for both components, which as we will discuss in Section 2.5, exceeds the beam speed by a small factor based on the field geometry. Thus we have a range of 0.17–0.28 c for the burst from 05:15:29–05:15:35 UT. Note that although the speeds from Figures 2.11 and 2.12 are measured in orthogonal directions, we cannot combine them in a quadrature sum as though they were components of one velocity vector. As we will explain next, this is because we interpret the source behavior in terms of several adjacent electron beams, each with a slightly different trajectory than the next, as opposed to one coherent system. Also note that in all cases, we are estimating two-dimensional (plane-of-sky) velocity components of three-dimensional motion, which has a somewhat greater magnitude depending on the projection geometry. Given this event’s position on the limb and the direction of the EUV jets considered in the next section, we assume that the line-of-sight component is much smaller than its plane-of-sky counterpart.

2.4.4 Magnetic Field Configuration

Electron beams responsible for Type III bursts propagate along magnetic field lines from the reconnection site, and therefore understanding the magnetic field configuration is critical to understanding the radio source region behavior and vice versa. Active region 12420, where the flare occurs, had just rotated into visibility on the east limb at the time of this event. EUV jets that immediately follow the radio bursts after the flare peak reveal a complex magnetic field configuration that connects AR 12420 to a small, diffuse dipole to the south near the equator. The southern region was just behind the limb during the flare, and based on its evolution in HMI magnetograms over the following days, appears to have been a decaying active region near the end of its evolution.

Unfortunately, this system is a poor candidate for local magnetic field modeling because of its partial visibility and position on the limb, where magnetogram observations are hampered by projection effects. The east limb position prevents us from using data from a few days prior, which is a possibility for west-limb events, and the decay of the southern dipole, along with the emergence of a neighboring region, dissuades us from attempting any dedicated modeling using data from subsequent days. Fortunately, the EUV jets trace out the field structure to an extent that we believe is sufficient to understand our observations. Previous studies have also demonstrated that Type III electron beams are aligned with corresponding EUV and X-ray jets (e.g. Chen et al. 2013a), meaning that field lines traced out by the jets are preferentially those traversed by the accelerated electrons.

We employ maximum-value persistence mapping to compile the separate EUV jet paths into one image. This style of persistence map refers simply to plotting the largest value a given pixel achieves over some period (Thompson and Young, 2016). Our maps cover from 05:18 to 05:39 UT, which corresponds to when the EUV jets begin around the peak flare time until they reach their full spatial extent visible to AIA around 20 minutes later. To further enhance the contrast, we subtract the persistence maps by a median-value background over the same period (i.e. $I_{\max} - I_{\text{med}}$). Figures 2.13a and 2.13b show maximum-value and background-subtracted persistence maps for both the 304 and 171 Å channels, which are most sensitive to the jet material. Figure 2.13c shows a version of the 304 Å map that has been Fourier filtered to suppress noise using a Hann window and then sharpened using an unsharp mask to accentuate the structure.

The EUV jets trace out a topology, not apparent just prior to the flare,

Ch. 2 Type III Burst Source Splitting

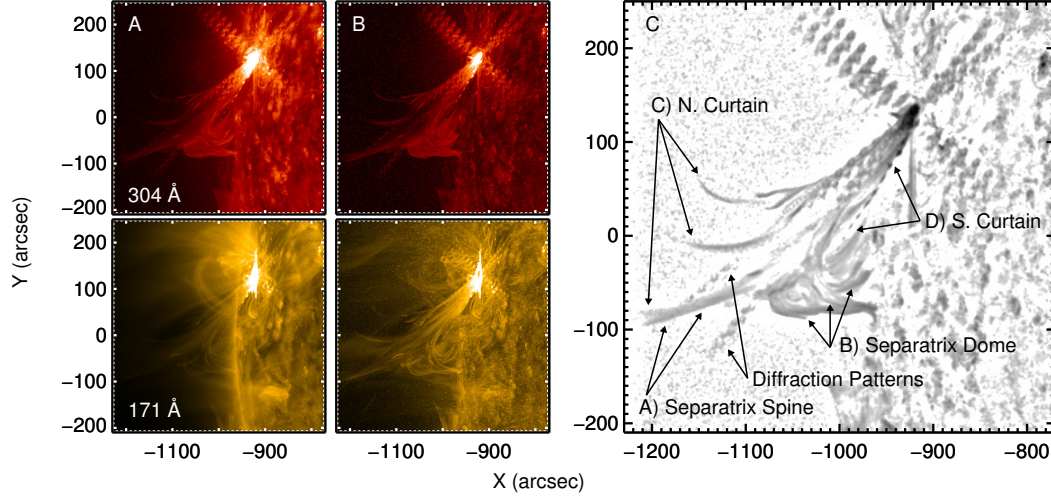


Figure 2.13: A) Maximum value persistence maps for AIA 304 (top) and 171 Å (bottom). B) Column A subtracted by median backgrounds. C) Annotated 304-Å, background-subtracted persistence map, further processed to accentuate features. See Section 2.4.4 for processing details and Figure 2.15 for a corresponding cartoon model. A corresponding movie is available in the [online material](#).

where the field connectivity changes rapidly. Such regions are generally known as *quasi-separatrix layers* (QSLs; Priest and Démoulin 1995; Démoulin et al. 1996), which are 3D generalizations of 2D separatrices that separate magnetic field connectivity domains. The key distinction is that the field linkage across a QSL is not discontinuous as in a true separatrix but instead changes drastically over a relatively small spatial scale, which can be quantified by the *squashing factor* Q (Titov, 2007). QSLs are important generally because they are preferred sites for the development of current sheets and ultimately magnetic reconnection (Aulanier et al., 2005). They are an essential part of 3D generalizations of the standard flare model (Janvier et al., 2013), and modeling their evolution can reproduce a number of observed flare features (e.g. Savcheva et al. 2015, 2016; Janvier et al. 2016). Here, we are less concerned with the dynamics of the flare site itself and focus instead on the neighboring region revealed by the EUV jets, which exhibits a topology associated with coronal null points.

We first note that our observed structure is similar in several ways to that modeled by Masson et al. (2012) and observed by Masson et al. (2014). The essential components are firstly the closed fan surface, or *separatrix dome*, and its single *spine* field line that is rooted in the photosphere and crosses the dome through the null point (Lau and Finn, 1990; Pontin et al., 2013). Open and

closed flux domains are bounded above and below a separatrix dome, which can form when a dipole emerges into a preexisting open field region (e.g. Török et al. 2009). Above the dome and diverging around the null point is a vertical fan surface, or *separatrix curtain*, comprised of field lines extending higher into the corona, with those closest to the separatrix spine likely being open to interplanetary space. Potential field source surface (PFSS¹¹; Schrijver and De Rosa 2003) extrapolations (not shown) do predict open field in this region but do not reproduce other topological features, which is to be expected given the modeling challenges described above. Some openness to interplanetary space must also have been present to facilitate the corresponding interplanetary burst observed by *Wind* and shown in Figure 2.2.

The separatrix dome, spine, and part of the curtain are clearly delineated by the EUV jets and are labeled in Figure 2.13c. Note that some of the features, namely the closed field line associated with the southern portion of the separatrix curtain, are somewhat difficult to follow in Figure 2.13c but can be clearly distinguished in the corresponding movie available in the [online material](#). In the following section, we will discuss how both types of source splitting described in Section 2.4.3 are facilitated by this topology.

2.5 Discussion

When we overplot contours of the Type III burst emission on the persistence map of the EUV jets (Figure 2.14), we see that the 240 MHz emission is concentrated just above the separatrix dome. As we described in Section 2.4.3, the burst emission splits with decreasing frequency (increasing height) into two increasingly-separated components. Figure 2.14 shows that the two components are distributed on either side of the separatrix spine. This implies a two-sided separatrix curtain with open field lines on either side of the spine, of which only the northern set are readily apparent in the EUV images. Given the position of the southern radio source and the closed field line that appears to form part of the southern curtain (D) in Figure 2.13, the southern half of the separatrix curtain seems to be oriented largely along the line of sight, which may explain why it is difficult to discern from the EUV jet structure. This two-sided separatrix curtain differs from the one-sided structure of Masson et al. (2012, 2014), but a number of other studies consider somewhat similar topologies (Maclean et al., 2009; van Driel-Gesztelyi et al., 2012; Titov et al., 2012;

¹¹PFSS Software Package: <http://www.lmsal.com/~derosa/pfsspack/>

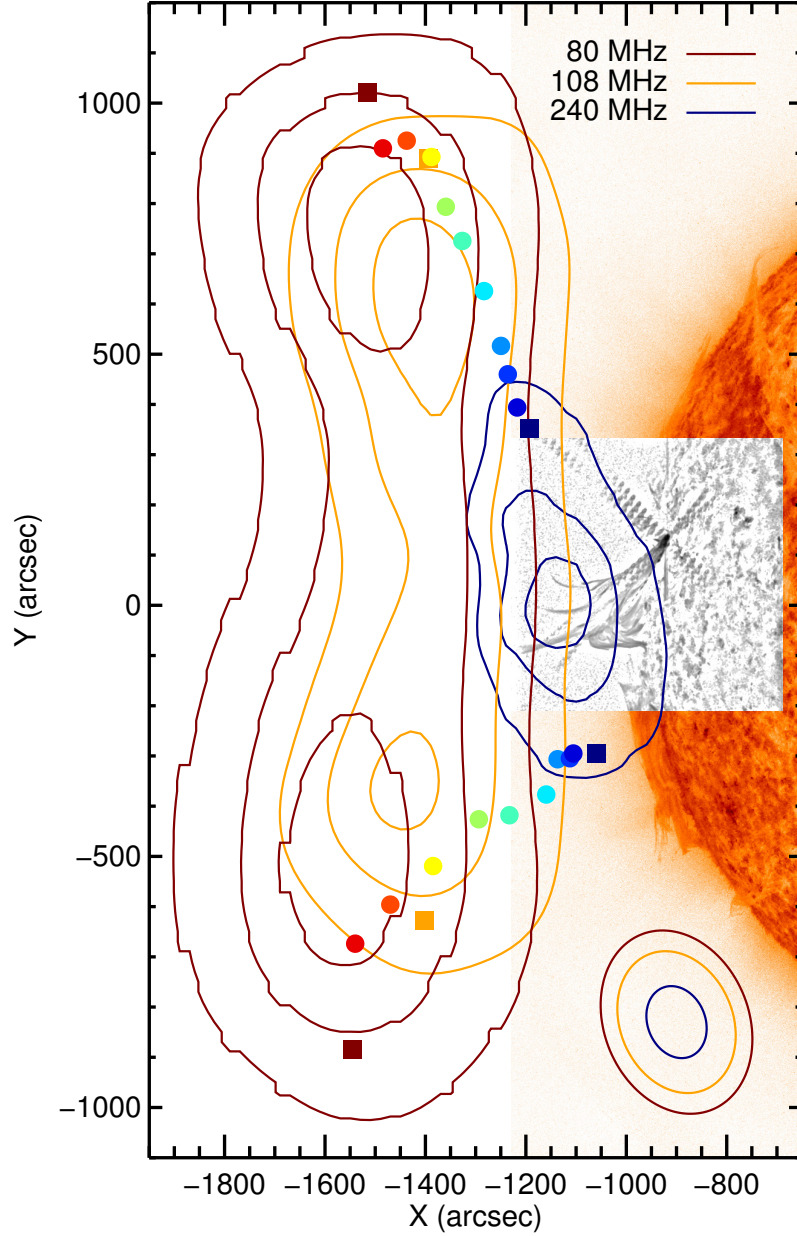


Figure 2.14: MWA Type III burst contours overlaid on a 304 Å SDO image. The greyscale inset is the persistence map from Figure 2.13c. Pairs of colored dots represent the angular extent of the MWA source region in all 12 channels, with the squares from left to right corresponding to the reddish brown (80 MHz), orange (108 MHz), and dark blue (240 MHz) contours, respectively. Contour levels are at 20, 50, and 80% of the peak intensity. The MWA data are from a period when the source regions are maximally extended around 05:17:26.6 UT, and the SDO image combines data from the EUV jet period that follows (see Section 2.4.4).

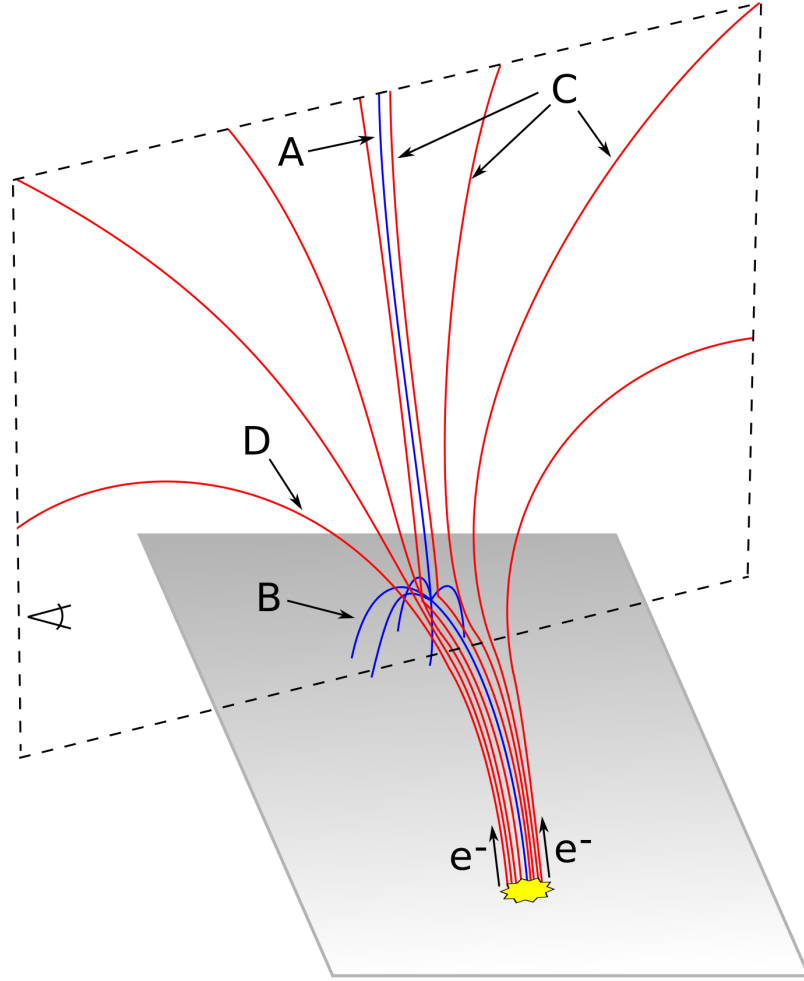


Figure 2.15: Cartoon interpretation of the magnetic field configuration inferred from the EUV jet morphology and radio source regions (Figure 2.14). The yellow region denotes the flare site, which is connected to a neighboring region with open and closed QSLs. Red field lines form a separatrix curtain, with the field closest to the center being open to interplanetary space. The blue field lines represent the closed separatrix dome, with a single spine field line that crosses the dome through a magnetic null point. Electrons travel along the diverging field lines of the separatrix curtain to produce the radio source structure and motion. Capital letters correspond to features apparent in the EUV observations (Figure 2.13).

Ch. 2 Type III Burst Source Splitting

Craig and Pontin, 2014; Pontin and Wyper, 2015).

In Figure 2.15, we sketch a 3D field configuration based on the aforementioned modeling studies that fits the EUV structure and extrapolates from there to satisfy the connectivity required by the radio source distribution. This cartoon can parsimoniously explain both the spatial splitting of the source from high to low frequencies and the source motion observed for individual frequency channels. Type III bursts emit at the local plasma frequency or its second harmonic ($f \approx f_p$ or $2f_p$), which is proportional to the square of the ambient electron density. Thus, emission at a particular frequency can be associated with a particular height corresponding to the requisite background density. In our interpretation, electrons travel simultaneously along each of the red field lines in Figure 2.15. The electron beams diverge on either side of the separatrix curtain, such that the beams are nearest to each other at lower heights (higher frequencies) and furthest apart at larger heights (lower frequencies). This produces the spatial source splitting and the dramatic increase of the overall angular extent toward lower frequencies, which is illustrated by the pairs of colored dots in Figure 2.14. The dots correspond to vertices of ellipses fit the overall source regions thresholded above 20% of their peak intensities in the same manner and for the same time period used in Section 2.4.3 for Figure 2.9.

The source motions illustrated by Figures 2.10 and 2.11 can then be accounted for as a projected time-of-flight effect. Electrons moving along the increasingly curved outer field lines take slightly longer to reach the same height, producing emission at adjacent positions along the separatrix curtain at slightly later times for a given frequency. This assumes that adjacent field lines have roughly the same radial density gradient, which implies decreasing density gradients along the field lines themselves as path lengths to specific heights (densities) increase with distance from the separatrix spine. Thus, the splitting speeds measured in Section 2.4.3 are not the exciter or electron beam speeds. They are instead somewhat faster, depending on the difference in travel time to a given height along adjacent flux tubes. Adopting the geometry in Figure 2.16, the expression for this is:

$$v_s = \frac{y_2 - y_1}{d_2 - d_1} v_b , \quad (2.1)$$

where v_s is the apparent source splitting speed, v_b is the electron beam speed, $y_{1,2}$ are solar Y coordinates, and $d_{1,2}$ are the distances traveled along the field lines to reach $y_{1,2}$.

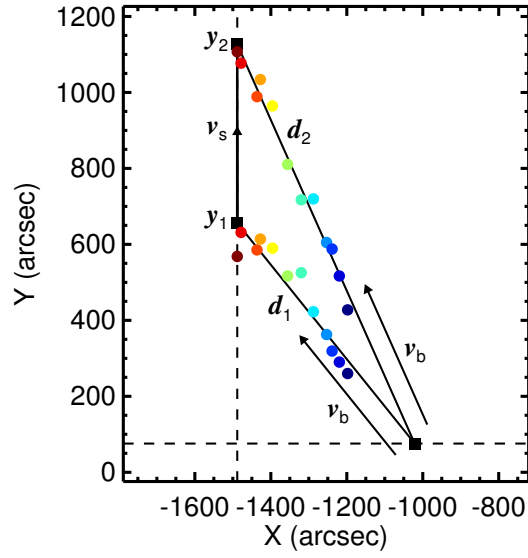


Figure 2.16: Model schematic for the source splitting motion (Equation 2.1). Pairs of colored dots represent the average minimum and maximum vertical extents during each splitting episode; colors indicate frequency as in Figures 2.9 & 2.14. The flux tubes along which the Type III beams travel are approximated by the solid fit lines, which intersect near the observed null point (Figure 2.13). Electrons take slightly longer to reach y_2 compared to y_1 , which produces the apparent vertical motion with velocity v_s . In reality, there would be a number of adjacent curved flux tubes between and below the two lines with nearby, but not identical, origins.

Ch. 2 Type III Burst Source Splitting

To estimate these parameters, we determine the average minimum and maximum vertical extents of the source regions for each frequency by fitting ellipses to every burst image, as was done for a single time step to illustrate the source region extents in Figures 2.9 and 2.14. The X coordinates of the northern vertices are averaged, and the Y coordinates one standard deviation above and below the mean are averaged separately to obtain the pairs of colored dots in Figure 2.16. We take this approach rather than tracking the northern component's centroid because, along with the associated difficulties described in Section 2.4.3, it allows us to capture consistent information from the higher-frequency channels where there is only one component and also because it is similar to the leading edge method used to estimate v_s in Figure 2.11.

If we approximate the field lines as linear fits to these points, which intersect close to the observed null point (Figure 2.13), then the speed of the source motion is $1.16\times$ the beam speed. Taking each of the lower-frequency points individually, we find factors ranging from 1.14 at 120 MHz to 1.19 at 80 MHz. Slightly larger factors are found for lower frequencies because of the larger separations between y_1 and y_2 compared to the fit projection, which may be due to the field lines curving out with height.

As with the v_s estimates in Section 2.4.3, scattering may impact these results if the effect changes significantly between the colored dots in Figure 2.16. Lower frequencies also tend to be more strongly scattered, which may enlarge the source regions as a function of decreasing frequency beyond the effect of the magnetic field divergence. Accounting for scattering would therefore preferentially decrease the Y-axis positions of the lower-frequency points in Figure 2.16, which would flatten the slopes of both lines and slightly decrease the ratio v_s/v_b . Including this effect would require an understanding of the local density structure and is beyond our scope. Also note that the model defined by Equation 2.1 and Figure 2.16 is specific to this magnetic field configuration and projection geometry. While the same basic effect may be observed for other events, different expressions may be needed to relate the observed motion to the beam speed.

Using the 1.16 factor, the average speed (v_s) from Figure 2.11 corresponds to an average plane-of-sky beam speed (v_b) of 0.2 c. This value is consistent with and provides independent confirmation of beam speeds estimated from frequency drift rates, which is possible if one assumes a density model. Modest fractions of light speed are typical in the corona (e.g. Alvarez and Haddock 1973; Aschwanden et al. 1995; Meléndez et al. 1999; Kishore et al. 2017), but some studies have found values in excess of 0.5 c (Poquerusse, 1994; Carley

et al., 2016) and even superluminal velocities given the right projection geometry (Klassen et al., 2003). We also note that similar observations could be used to independently probe the coronal density structure and beam speed because our imaging capability allows us to estimate v_b without assuming a density model using time- and frequency-varying source positions in the manner illustrated by Figure 2.12. This particular event is not ideal for that analysis because of the complicated source structure, but a followup study is planned for a small ensemble of events that exhibit simple source structures without the type of motion described here. A similar study was also recently performed at lower frequencies (larger heights) by Morosan et al. (2014) using Type III imaging from LOFAR. They found speeds ranging from 0.3–0.6 c and observed emission at significantly larger heights than would be expected from standard density models.

A few other connections to the literature should be mentioned with respect to the observed radio structure and inferred field configuration. First, we see from Figure 2.6 and in the movie associated with Figures 2.3 and 2.4 that the source region of the bursts at 240 MHz is consistently enhanced and exhibits low-level burst activity outside of the intense burst periods. Figure 2.14 demonstrates that this emission is concentrated just above the separatrix dome and associated null point. These structures are interface regions between closed and open magnetic flux, where interchange reconnection may be ongoing (e.g. Masson et al. 2012, 2014). Such regions have previously been associated with radio enhancements and noise storms (Wen et al., 2007; Del Zanna et al., 2011; Régnier, 2013).

A few *Nançay Radioheliograph* (NRH) observations exhibit characteristics reminiscent of those described here. For instance, Paesold et al. (2001) conclude that the spatial separation of temporally adjacent Type III events predominantly resulted from different field line trajectories followed by the electron beams. Reid et al. (2014) show a number of elliptically extended Type III source regions that are represented as enveloping the diverging paths of electrons accelerated from the same site. Our observations that overlap in frequency with the NRH range (≥ 150 MHz) are similarly extended to a larger degree before separating into two primary components at lower frequencies. Carley et al. (2016) describe a “radio arc” in their lowest-frequency images that is strikingly similar to our observations (e.g. Figure 2.14) but is suggested instead to trace the boundary of an erupting coronal mass ejection.

We also note that the complicated structure exhibited by the MWA dynamic spectrum (Figures 2.2 & 2.8) may indicate the presence of other burst types.

Ch. 2 Type III Burst Source Splitting

Classic Type III emission drifts from high to low frequencies as electron beams propagate outward into interplanetary space. If confined to closed field lines, the same beams may produce type U or J bursts for which the frequency drift rate switches signs as electrons crest the closed loops and propagate back toward the Sun (Maxwell and Swarup, 1958; Aurass and Klein, 1997; Reid and Kontar, 2017). We see hints of this in our dynamic spectrum at ~ 196 MHz around 05:17:40 UT (Figure 2.2), but it is difficult to interpret because of the MWA’s sparse frequency coverage. Given that our interpretation of the magnetic field configuration (Figure 2.15) includes closed field lines on either side of the separatrix curtain, such features in the dynamic spectrum would not be surprising. Our splitting motion could also be due partially to beams traveling largely tangent to the limb along such closed field lines, while adjacent beams make it to larger heights along field lines closer to the separatrix spine, but evidence for downward propagation is lacking in the images.

Finally, the bursts in this series do not all exhibit the statistical tendency for increasing Type III flux densities with decreasing frequency (e.g. Weber 1978; Dulk et al. 2001; Saint-Hilaire et al. 2013), which is clear for the main event shown in Figure 2.4 and others visible in the flux-calibrated dynamic spectrum (Figure 2.8b). Individual Type III bursts often deviate from this pattern, exhibiting enhancements at particular frequencies or breaks in the emission over a particular frequency range. This behavior may be attributed to, among other things, density turbulence along the beam path (Li et al., 2012; Loi et al., 2014) and/or variations in the ambient electron and ion temperatures (Li et al., 2011a,b). Additionally, electrons streaming along closed field lines, as considered in the previous paragraph, may contribute to enhancements at particular frequencies.

2.6 Conclusion

We have presented the first time series imaging study of MWA solar data. Our observations reveal complex Type III burst source regions that exhibit previously unreported dynamics. We identify two types of source region splitting, one being a frequency-dependent structure and the other being source motion within individual frequency channels. For the former, the source regions splits from one dominant component at our highest frequency (240 MHz) into two increasingly separated sources with decreasing frequency down to 80 MHz. This corresponds to a straightforward splitting of the source region as a function of height, with larger separations at larger heights.

With high time resolution imaging, we observe a splitting motion within the source regions at individual frequencies, particularly in the lower channels ($\lesssim 132$ MHz), that is tangent to the limb in essentially the same direction as the source splitting from high to low frequencies. This motion is short-lived (~ 2 s), fast ($0.1\text{--}0.4$ c), and repetitive, occurring multiple times over a period of 7 min before, during, and after the X-ray flare peak. We interpret the repetitive nature as multiple electron beam injections that produce distinct radio bursts with overlapping signatures in the dynamic spectrum, which is consistent with there being several distinct EUV jet episodes that immediately follow the radio bursts.

The EUV jets, which are assumed to have very similar trajectories to the Type III electron beams, trace out a region where the magnetic field connectivity rapidly diverges over a small spatial scale. These types of configurations are broadly referred to as QSLs, and we argue that this field structure facilitates the radio source region splitting. Several common topological features associated with coronal null points are identifiable in persistence maps of the EUV outflows, including a separatrix dome, spine, and curtain. Electrons are accelerated simultaneously along adjacent field lines that connect the flare site to an open QSL, where their paths diverge to produce the source region splitting. At 240 MHz, the burst emission is concentrated just above the separatrix dome, a region that is consistently enhanced outside of burst periods. Moving to larger heights (lower frequencies), the source regions split on either side of the separatrix spine. The diverging field thereby enlarges the source regions at lower frequencies, an effect that may compound with angular broadening by refraction and scattering in this and other events. The northern radio component is consistent with field lines apparent from the EUV observations, but the southern component implies a two-sided separatrix curtain that is not obvious from the EUV observations. Thus, the radio imaging provides additional constraints on the magnetic field connectivity.

The magnetic field configuration also offers a straightforward explanation for the radio source motion via a projected time-of-flight effect, whereby electrons moving along slightly longer outer field lines take slightly longer to excite emission at adjacent positions of roughly the same radial height. Given this interpretation, the speed of the source region is a factor of $\lesssim 1.2\times$ greater than the electron beam speed. We estimate an average beam speed of 0.2 c, which is an independent confirmation of speeds estimated from frequency drift rates. We note that the same characteristics are observed in another Type III burst from the same region three hours earlier. This implies that the field topology is

Ch. 2 Type III Burst Source Splitting

stable at least on that timescale and strengthens our conclusion that the radio dynamics are caused by interaction with a preexisting magnetic field structure, as opposed to peculiarities of the flare process itself.

Lastly, we motivate future studies of MWA solar observations. A survey of Type III bursts is underway. From preliminary results, we note that the dual-component splitting behavior described here is uncommon. However, analogous source region motion in one direction is common and could be explained in the same manner if coupled with a consistent picture of the particular field configurations. Similar events that occur near disk center or on the opposite (west) limb could be combined with magnetic field modeling to develop a more detailed topological understanding. The coronal density structure can also be probed by examining events with less complicated source structures. Finally, we showed a coronal hole that gradually transitions from dark to bright from high to low frequencies, turning over around 120 MHz. This adds a transition point to the small body of literature reporting coronal holes in emission at low frequencies, an effect that is not well-explained and could be addressed with additional MWA observations.

Acknowledgements: PIM thanks Natasha Hurley-Walker for instruction on MWA data processing, Mike Wheatland and Yuhong Fan for discussions related to the magnetic field configuration, Emil Lenc for discussions related to polarization, and the Australian Government for supporting this work through an Endeavour Postgraduate Scholarship. We thank the anonymous referee for their constructive comments. JM, CL, and DO acknowledge support from the Air Force Office of Space Research (AFOSR) via grant FA9550-14-1-0192, and SEG acknowledges support from AFOSR grant FA9550-15-1-0030. This scientific work makes use of the Murchison Radio-astronomy Observatory (MRO), operated by the Commonwealth Scientific and Industrial Research Organisation (CSIRO). We acknowledge the Wajarri Yamatji people as the traditional owners of the Observatory site. Support for the operation of the MWA is provided by the Australian Government’s National Collaborative Research Infrastructure Strategy (NCRIS), under a contract to Curtin University administered by Astronomy Australia Limited. We acknowledge the Pawsey Supercomputing Centre, which is supported by the Western Australian and Australian Governments. The SDO is a National Aeronautics and Space Administration (NASA) satellite, and we acknowledge the AIA and HMI science teams for providing open access to data and software. NCAR is supported by the National Science Foundation (NSF). This research has made use of NASA’s Astrophysics Data System (ADS).

Chapter 3

Densities Probed by Coronal Type III Radio Burst Imaging

Published as McCauley et al. (2018), *Solar Phys.*, 293:132

3.1 Abstract

We present coronal density profiles derived from low-frequency (80–240 MHz) imaging of three Type III solar radio bursts observed at the limb by the *Murchison Widefield Array* (MWA). Each event is associated with a white-light streamer at larger heights and is plausibly associated with thin extreme-ultraviolet rays at lower heights. Assuming harmonic plasma emission, we find average electron densities of $1.8 \times 10^8 \text{ cm}^{-3}$ down to $0.20 \times 10^8 \text{ cm}^{-3}$ at heights of 1.3 to 1.9 R_{\odot} . These values represent approximately $2.4\text{--}5.4\times$ enhancements over canonical background levels and are comparable to the highest streamer densities obtained from data at other wavelengths. Assuming fundamental emission instead would increase the densities by a factor of four. High densities inferred from Type III source heights can be explained by assuming that the exciting electron beams travel along overdense fibers or by radio propagation effects that may cause a source to appear at a larger height than the true emission site. We review the arguments for both scenarios in light of recent results. We compare the extent of the quiescent corona to model predictions to estimate the impact of propagation effects, which we conclude can only partially explain the apparent density enhancements. Finally, we use the time- and frequency-varying source positions to estimate electron beam speeds of between 0.24 and 0.60 c .

3.2 Introduction

Type III solar radio bursts are caused by semi-relativistic electrons streaming through and perturbing the ambient coronal or interplanetary plasma. A recent review is given by Reid and Ratcliffe (2014). The dominant theory,

Ch. 3 Coronal Densities from Type III Burst Imaging

proposed by Ginzburg and Zhelezniakov (1958), invokes a two-step process beginning with the stimulation of Langmuir waves (plasma oscillations) in the background plasma by an electron beam. A small fraction of the Langmuir wave energy is then converted into electromagnetic radiation at either the local electron plasma frequency $[f_p]$ or its harmonic $[2f_p]$ (see reviews by Robinson and Cairns, 2000; Melrose, 2009). The emission frequency depends mainly on the ambient electron density $[n_e]$ because $f_p \propto \sqrt{n_e}$. This relationship produces the defining feature of Type III bursts, a rapid drift from high to low frequencies as the exciter beam travels away from the Sun through decreasing densities (Wild and McCready, 1950).

The rate at which the emission frequency drifts $[df/dt]$ is therefore related to the electron beam speed, which can be obtained in the radial direction by assuming a density model $n_e(r)$. Many authors have employed this technique for various events with various models, generally finding modest fractions of light speed (0.1–0.4 c; *e.g.* Alvarez and Haddock, 1973; Aschwanden et al., 1995; Mann et al., 1999; Meléndez et al., 1999; Krupar et al., 2015; Kishore et al., 2017). Alternatively, the coronal and/or interplanetary density gradient can be inferred by instead assuming a beam speed (*e.g.* Fainberg and Stone, 1971; Leblanc et al., 1998) or by simply assuming that the beam speed is constant (Cairns et al., 2009). While these methods can yield robust estimates for the density gradient, they cannot be converted into an explicit density structure $[n_e(r)]$ without normalizing the gradient to a specific value at a specific heliocentric distance. This normalization has typically been done using estimates from white-light polarized brightness data close to the Sun, *in-situ* data in the interplanetary medium, or the observed height of Type III burst sources at various frequencies.

Densities inferred from Type III source heights, particularly at lower frequencies, have frequently conflicted with those obtained from other methods. The earliest spatial measurements found larger source heights than would be expected from fundamental plasma emission, implying density enhancements of an order of magnitude or more (Wild et al., 1959). This finding was confirmed by subsequent investigations (*e.g.* Morimoto, 1964; Malitson and Erickson, 1966), and along with other arguments, led many authors to two conclusions: First, that harmonic $[2f_p]$ emission likely dominates (*e.g.* Fainberg and Stone, 1971; Mercier and Rosenberg, 1974; Stewart, 1976). This brings the corresponding densities down by a factor of four, then implying only a moderate enhancement over densities inferred from white-light data. (Counterarguments for the prevalence of fundamental emission will be referenced in Section 3.4.1.)

Second, that the electron beams preferentially traverse overdense flux tubes (*e.g.* Bougeret et al., 1984), a conclusion bolstered by spatial correlations between several Type III bursts and white-light streamers (*e.g.* Trotter et al., 1982; Kundu and Stone, 1984; Gopalswamy et al., 1987; Mugundhan et al., 2018).

The overdense hypothesis has been challenged by evidence that the large source heights can instead be explained by propagation effects. If Type III emission is produced in thin, high-density structures, then it can escape relatively unperturbed through its comparatively rarefied surroundings. However, if the emission is produced in an environment near the associated plasma level (*i.e.* with an average n_e corresponding to the radio waves' equivalent f_p), then refraction and scattering by density inhomogeneities may substantially shift an observed source from its true origin (*e.g.* Leblanc, 1973; Riddle, 1974; Bougeret and Steinberg, 1977). Duncan (1979) introduced the term *ducting* in this context, which refers to emission being guided to larger heights within a low-density structure through successive reflections against the high-density “walls” of the duct. This concept was generalized for a more realistic corona by Robinson (1983), who showed that random scattering of radio waves by thin, overdense fibers has the same net effect of elevating an observed source radially above its emission site. Additional details on this topic, along with coronal refraction, will be given in Section 3.4.3.

Many authors came to favor propagation effects instead of the overdense structure interpretation for a few reasons. Despite the aforementioned case studies, Type IIIs did not appear to be statistically associated with regions of high average density in the corona (Leblanc et al., 1974; Leblanc and de La Noe, 1977) or in the solar wind (Steinberg et al., 1984). Interplanetary (kHz-range) Type III source regions are also so large as to demand angular broadening by propagation effects (*e.g.* Steinberg et al., 1985; Lecacheux et al., 1989). Invoking propagation effects can also be used to explain apparent spatial differences between fundamental and harmonic sources (*e.g.* Stewart, 1972; Kontar et al., 2017), along with large offsets between radio sources on the disk and their likely electron acceleration sites (*e.g.* Bisoi et al., 2018). These arguments are reviewed by Dulk (2000), and further discussion with additional recent references will be presented in Sections 3.4.3 and 3.5.

Both the interpretation of electron beams moving along overdense structures and of radio propagation effects elevating burst sources rely on the presence of thin, high-density fibers. Either the electron beams are traveling within these structures or the Type III emission is being scattered by them. In this arti-

cle, we will suggest that propagation effects are important but cannot entirely explain the density enhancements for our events. Section 3.3 describes our observations: Section 3.3.1 outlines our data reduction, Section 3.3.2 details our event-selection criteria, and Section 3.3.3 describes the multi-wavelength context for the selected Type III bursts. Section 3.4 describes our analysis and results: Section 3.4.1 infers densities from Type III source heights, Section 3.4.2 estimates electron beam speeds from imaging data, and Section 3.4.3 examines propagation effects by comparing the extent of the quiescent corona to model predictions. In Section 3.5, we discuss the implications of our results, along with other recent developments, on the debate between the overdense and propagation effects hypotheses. Finally, our conclusions are summarized in Section 3.6.

3.3 Observations

3.3.1 *Murchison Widefield Array* (MWA)

The MWA is a low-frequency radio interferometer in Western Australia with an instantaneous bandwidth of 30.72 MHz that can be flexibly distributed from 80 to 300 MHz (Tingay et al., 2013a). Our data were recorded with a 0.5 second time cadence and a 40 kHz spectral resolution, which we average over 12 separate 2.56 MHz bandwidths centered at 80, 89, 98, 108, 120, 132, 145, 161, 179, 196, 217, and 240 MHz. We use the same data processing scheme as McCauley et al. (2017), and what follows is a brief summary thereof.

Visibilities were generated with the standard MWA correlator (Ord et al., 2015) and the `cotter` software (Offringa et al., 2012, 2015). Observations of bright and well-modelled calibrator sources were used to obtain solutions for the complex antenna gains (Hurley-Walker et al., 2014), which were improved by imaging the calibrator and iteratively self-calibrating from there (Hurley-Walker et al., 2017). WSClean (Offringa et al., 2014) was used to perform the imaging with a Briggs -2 weighting (Briggs, 1995) to maximize spatial resolution and minimize point spread function (PSF) sidelobes. The primary beam model of Sutinjo et al. (2015) was used to produce Stokes I images from the instrumental polarizations, and the SolarSoftWare (SSW¹, Freeland and Handy, 1998) routine `mwa_prep` (McCauley et al., 2017) was used to translate the images onto solar coordinates. Flux calibration was achieved by comparison with thermal bremsstrahlung and gyroresonance emission predictions from FOR-

¹SSW: www.lmsal.com/solarsoft/

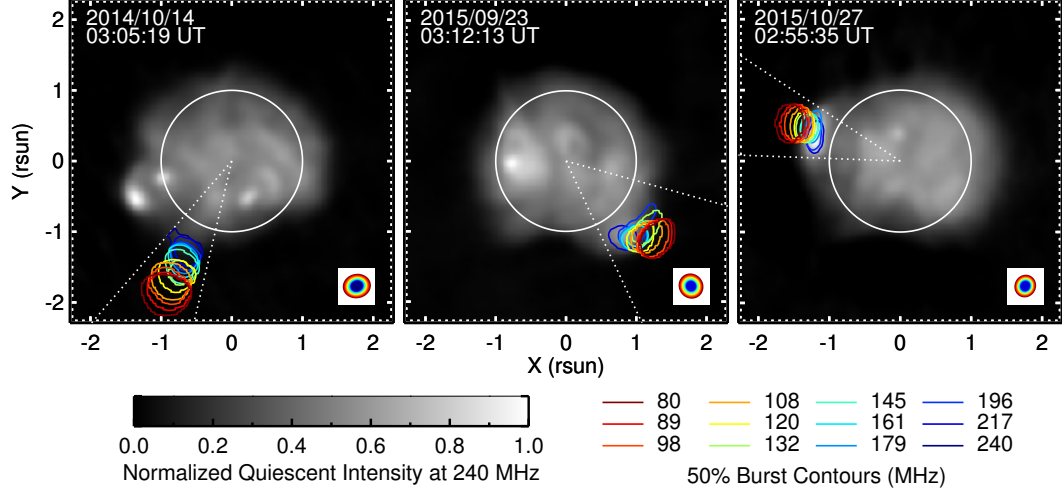


Figure 3.1: MWA Type III burst contours at 50% of the peak intensity for each channel overlaid on 240 MHz images of the quiescent corona. The solid circle represents the optical disk, and dotted lines bound the region included in the dynamic spectra (Figures 3.2 and 3.3). Colored ellipses in the lower-right corners show the synthesized beam sizes for each channel.

WARD² (Gibson et al., 2016) based on the Magnetohydrodynamic Algorithm outside a Sphere model (MAS³; Lionello et al., 2009).

3.3.2 Event Selection

These data are part of an imaging survey of many Type III bursts observed by the MWA during 45 separate observing periods in 2014 and 2015. McCauley et al. (2017) performed a case study of an event that exhibits unusual source motion, and future work will present statistical analyses. Burst periods during MWA observing runs were identified using the daily National Oceanic and Atmospheric Administration (NOAA) solar event reports⁴ based on observations from the *Learmonth* (Guidice et al., 1981; Kennewell and Steward, 2003) and *Culgoora* (Prestage et al., 1994) solar radio spectrographs, which overlap with the MWA’s frequency range at the low and high ends, respectively.

Three events were selected from the full sample based on the following criteria. First, the burst sites needed to be located at the radio limb with roughly radial progressions across frequency channels. Limb events minimize projec-

²FORWARD: www2.hao.ucar.edu/modeling/FORWARD-home

³MAS: www.predsci.com/hmi/data_access.php

⁴NOAA event reports: www.swpc.noaa.gov/products/solar-and-geophysical-event-reports

Ch. 3 Coronal Densities from Type III Burst Imaging

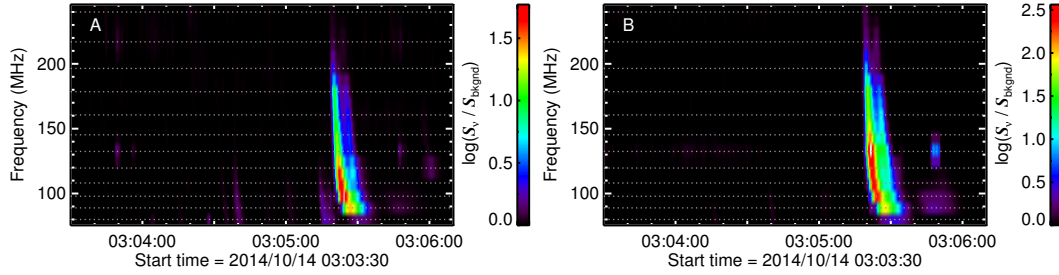


Figure 3.2: Dynamic spectra constructed from image intensities for the Type III burst near 03:05:20 UT on 14 October 2014. Panel A includes the full FOV, while panel B includes only the segment bounded by the dotted lines in Figure 3.1. Dotted horizontal lines show the locations of the 12 channels, each having a spectral width of 2.56 MHz. Intensities have been divided by the background level and plotted on a logarithmic scale.

tion effects, allowing us to reasonably approximate the projected distance from Sun-center as the actual radial height. Second, to eliminate potential confusion between multiple events and to maximize spectral coverage, the bursts needed to be sufficiently isolated in time and frequency, with a coherent drift from high to low frequencies across the full MWA bandwidth. Third, the source regions needed to be relatively uncomplicated ellipses with little-to-no intrinsic motion of the sort described by McCauley et al. (2017). This again minimizes projection effects and ensures that we follow a single beam trajectory for each event.

Figure 3.1 shows the burst contours for each channel overlaid on quiescent background images at 240 MHz. Each of the three events occurred on a different day, and we refer to them by the UTC date on which they occurred (SOL identifiers: SOL2014-10-14T03:05:19, SOL2015-09-23T03:12:12, and SOL2015-10-27T02:55:34). Figure 3.2 shows dynamic spectra for the 14 October 2014 event, with the left panel covering the full Sun and the right panel including only the region demarcated by the dotted lines in Figure 3.1. The partial-Sun spectrum excludes a neighboring region that is active over the same period, allowing the Type III frequency structure to be more easily followed. This approach is similar to that of Mohan and Oberoi (2017), who discuss the utility of spatially resolved dynamic spectra. Figure 3.3 shows the masked spectra for all three events.

3.3.3 Context

In this section, we briefly describe the context for each of the radio bursts with respect to observations at other wavelengths and associated phenomena.

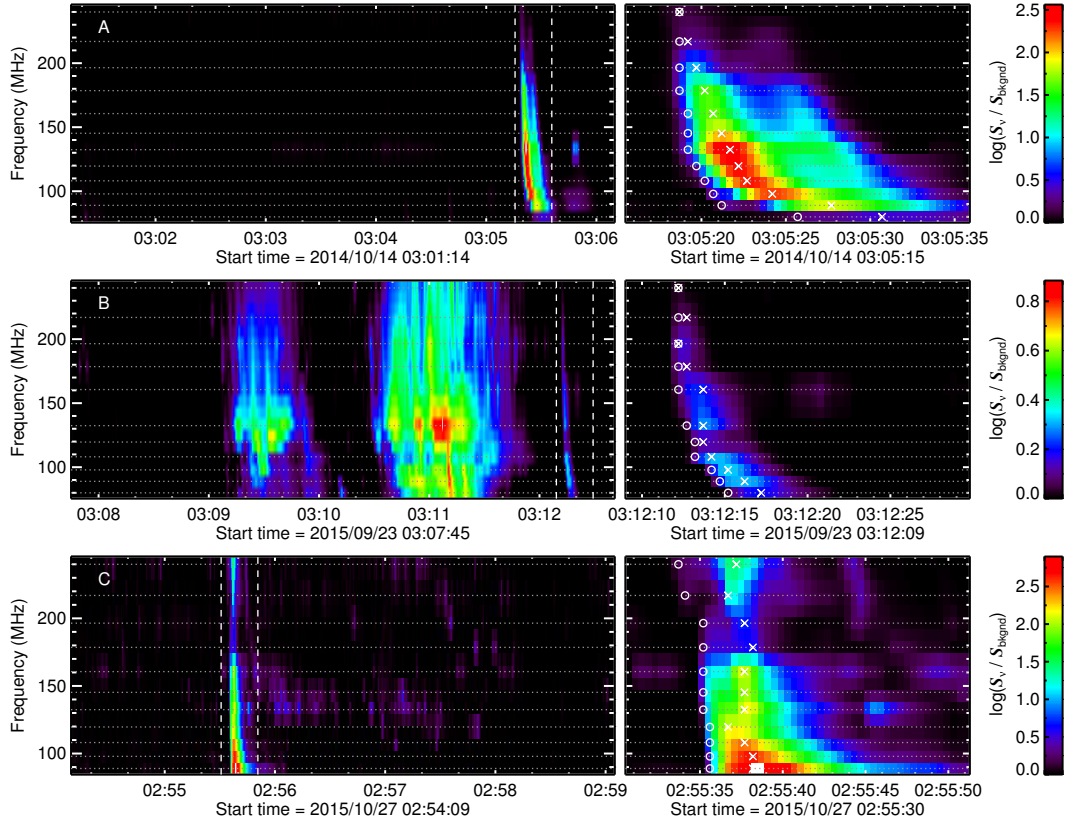


Figure 3.3: Dynamic spectra constructed from partial image intensities, including only the FOV segment bounded by the dotted lines in Figure 3.1. The left column shows the full five-minute observation intervals, while the right column shows 20-second periods surrounding the selected Type III bursts. Circles and crosses denote the onset and peak burst times for each channel.

Ch. 3 Coronal Densities from Type III Burst Imaging

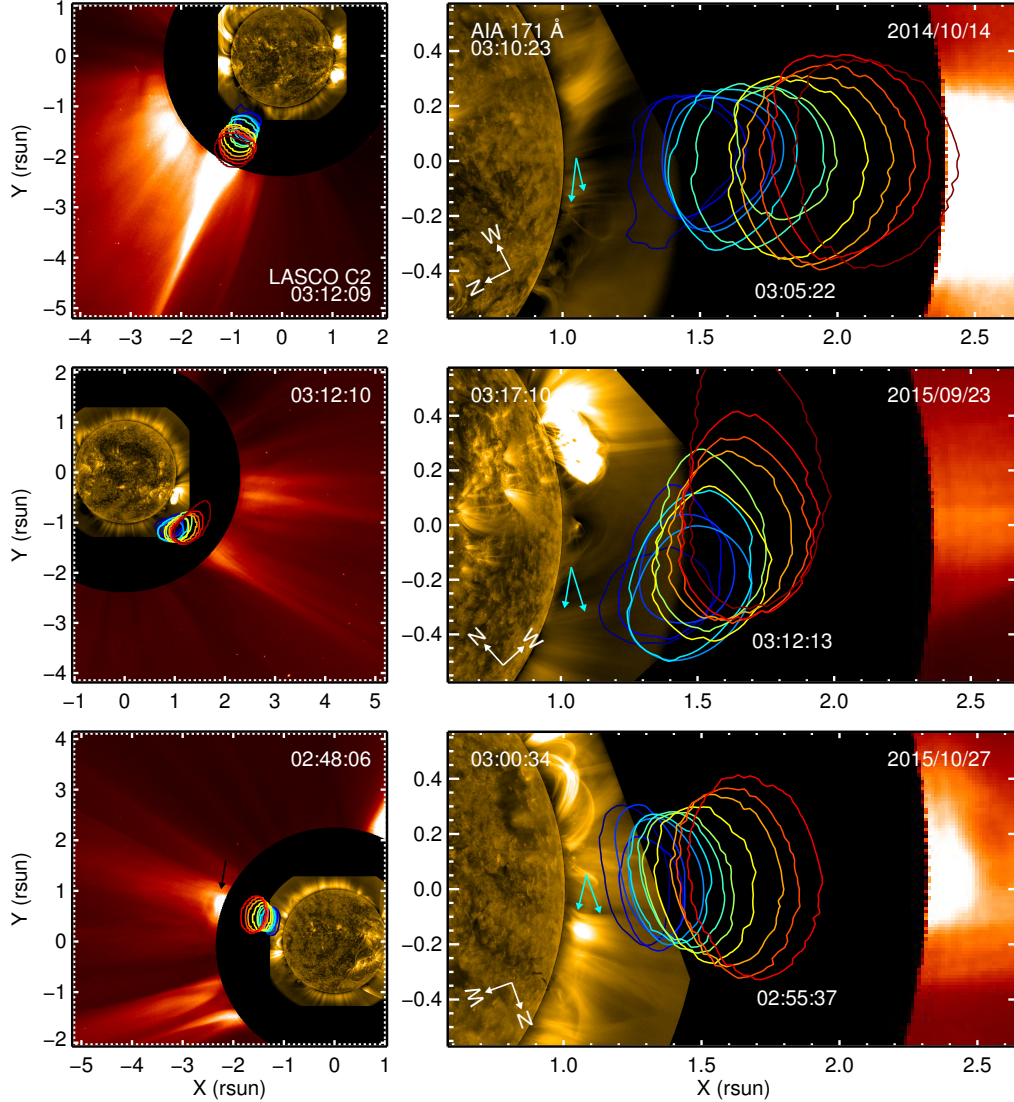


Figure 3.4: Overlays of the 50% MWA burst contours onto AIA 171 Å and LASCO-C2 images. Contour colors are for spectral channels from 80–240 MHz, as in Figure 3.1, where dark red represents the lowest frequency and dark blue represents the highest. UTC observation times are shown for LASCO in the left panel, for AIA in the upper-left of the right panel, and for MWA in the middle of the right panel. The MWA times reflect the average peak time across frequency channels (see Figure 3.3). The AIA images are ten-minute (50-image) averages processed with a radial filter to accentuate off-limb features; times reflect the middle of these ten-minute windows, which begin at the burst onsets and cover the subsequent periods over which associated EUV signatures would be expected. Images are rotated in the right column such that the burst progression is roughly horizontal, which helps illustrate the extent to which each event progresses radially. Cyan arrows point to the EUV structures that exhibit activity during or just after the radio bursts. The black arrow in the lower-left panel points to a CME that originated behind the limb and passed the C2 occulting disk around 20 minutes prior to the Type III burst.

Figure 3.4 overlays the burst contours from Figure 3.1 onto contemporaneous extreme-ultraviolet (EUV) and white-light data. The white-light images were produced by the *Large Angle and Spectrometric Coronagraph C2* (LASCO-C2: Brueckner et al., 1995) onboard the *Solar and Heliospheric Observatory* (SOHO: Domingo et al., 1995). C2 has an observing cadence of 20 min, and Figure 3.4 includes the nearest images in time to our radio bursts.

The EUV data come from the *Atmospheric Imaging Assembly* (AIA: Lemen et al., 2012) onboard the *Solar Dynamics Observatory* (SDO: Pesnell et al., 2012). We use the 171 Å AIA channel, which is dominated by Fe IX emission produced by plasma at around 0.63 MK, because it most clearly delineates the fine magnetic structures along which Type III beams are expected to travel. To further accentuate off-limb features, we apply a radial filter using the SSW routine `aia_rfilter` (Masson et al., 2014). Note that the apparent brightness of a given pixel in a radial filter image corresponds to its true intensity relative only to pixels of the same radial height (*i.e.* equally bright structures at different heights do not have the same physical intensity). AIA has an observing cadence of 12 seconds, and Figure 3.4 uses ten-minute (50-image) averages that cover the periods during and immediately after the radio bursts. This temporal window is used because a potential EUV signature associated with a Type III burst will propagate at a much lower speed than the burst-driving electron beam and will likely be most apparent in the minutes following the burst (*e.g.* McCauley et al., 2017; Cairns et al., 2018).

In all cases, the radio bursts appear to be aligned with dense structures visible to AIA at lower heights and to LASCO-C2 at larger heights. The latter case is obvious, with each set of burst contours situated just below bright white-light streamers. Cyan arrows in the right panels of Figure 3.4 identify the associated EUV structures, each of which exhibits a mild brightening and/or outflow during or immediately after the corresponding radio burst. This activity may be indicative of weak EUV jets, which are frequently associated with Type III bursts (*e.g.* Chen et al., 2013a; Innes et al., 2016; McCauley et al., 2017; Cairns et al., 2018), but robust outflows are not observed here. The alignment between the EUV and radio burst structure is particularly striking for the 23 September 2015 event in that both appear to follow roughly the same non-radial arc. A correspondence between EUV rays and Type III bursts was previously reported by Pick et al. (2009).

Type III bursts are commonly, but not always, associated with X-ray flares (*e.g.* Benz et al., 2005, 2007; Cairns et al., 2018) and occasionally with coronal mass ejections (CMEs; *e.g.* Cane et al., 2002; Cliver and Ling, 2009). Our

Ch. 3 Coronal Densities from Type III Burst Imaging

14 October 2014 event is not associated with either, but the other two are. On 23 September 2015, a weak B-class flare occurred just to the north of our radio sources from Active Region 12415. The flare peaked around 3:11 UT, which corresponds to a period of relatively intense coherent radio emission that precedes the weaker burst of interest here (see Figure 3.3). Given the radio source positions and associated EUV structure, we do not believe the flare site to be the source of accelerated electrons for our event, although the flare may have been responsible for stimulating further reconnection to the south.

On 27 October 2015, a CME was ongoing at the time of the radio burst, and its leading edge, indicated by the black arrow in the lower left panel of Figure 3.4, can be seen just above the C2 occulting disk. Inspection of images from the Extreme Ultraviolet Imager (EUVI; Howard et al., 2008) onboard the *Solar Terrestrial Relations Observatory A* (STEREO-A) spacecraft shows that the CME originated from a large active region close to the east limb but occulted by the disk from AIA’s perspective. The CME was launched well before our Type III burst, but the region that produced it was very active over this period and is likely connected to the activity visible to AIA immediately after the radio burst along the structure indicated by the cyan arrows in the lower-right panel of Figure 3.4. So while we do not think the CME was directly involved in triggering the radio burst, it may have impacted the medium through which the Type III electron beam would later propagate, which is relevant to a hypothesis proposed by Morosan et al. (2014) that will be discussed in Section 3.5.

3.4 Analysis and Results

3.4.1 Density Profiles

Standard plasma emission theory expects Type III radiation at either the ambient electron plasma frequency $[f_p]$ or its harmonic $[2f_p]$. The emission frequency $[f]$ is related to electron density $[n_e]$ in the following way [cgs units]:

$$f = Nf_p = N\sqrt{\frac{e^2 n_e}{\pi m_e}} \Rightarrow n_e = \pi m_e \left(\frac{f}{eN}\right)^2, \quad (3.1)$$

where e is the electron charge, m_e is the electron mass, and N is either 1 (fundamental) or 2 (harmonic). For frequencies in Hz and densities in cm^{-3} , $n_e \approx 1.24 \times 10^{-8} f^2$ for fundamental and $3.10 \times 10^{-9} f^2$ for harmonic emission.

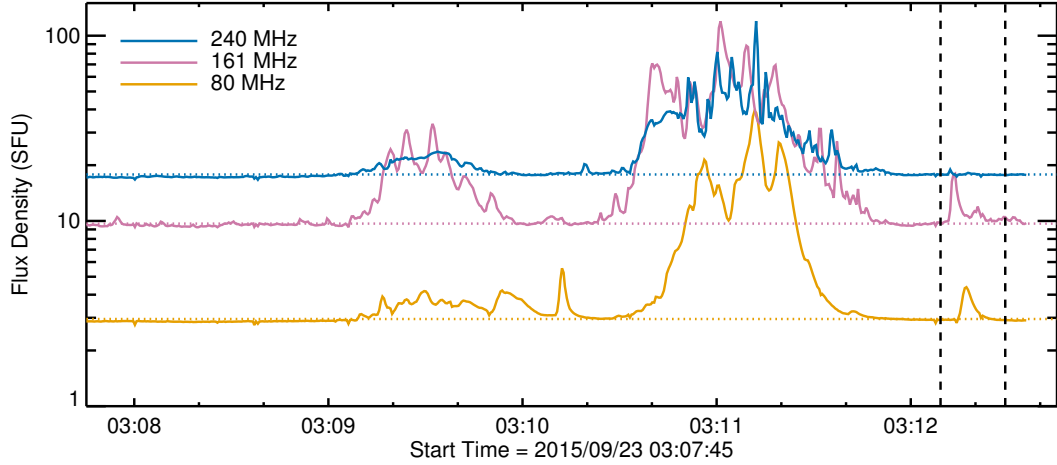


Figure 3.5: Light curves for the 23 September 2015 observation, shown to illustrate the background level determination. Backgrounds (dotted lines) are obtained by taking the median intensity, excluding points two standard deviations above that, and iterating until no more points are excluded. The dashed lines mark the burst period from the right column of Figure 3.3.

Density can thus be easily extracted given the emission mode and location. Unfortunately, neither property is entirely straightforward. Harmonic emission is often favored in the corona because being produced above the ambient f_p makes it less likely to be absorbed (Bastian et al., 1998) and because Type IIIs tend to be more weakly circularly polarized than expected for fundamental emission (Dulk et al., 1980). Harmonic emission also implies lower densities by a factor of four, which are easier to reconcile with the large heights often observed (see Section 3.2). However, fundamental-harmonic pairs can be observed near our frequency range (*e.g.* Kontar et al., 2017), fundamental emission is expected to contribute significantly to interplanetary Type III burst spectra (*e.g.* Robinson and Cairns, 1998), and fundamental emission is thought to be the more efficient process from a theoretical perspective (*e.g.* Li and Cairns, 2013, 2014). As described in Section 3.2, a source’s apparent height may also be augmented by propagation effects, which we will consider in Section 3.4.3.

We measure source heights at the onset of burst emission, which we define as when the total intensity reaches $1.3\times$ the background level. Background levels are determined for each frequency by taking the median intensity, excluding points 2 standard deviations above that, and iterating until no more points are excluded. Figure 3.5 shows the result of this baseline procedure for three frequencies from the 23 September 2015 event, which is shown because it exhibits the most complicated dynamic spectrum. Onset times are represented

Ch. 3 Coronal Densities from Type III Burst Imaging

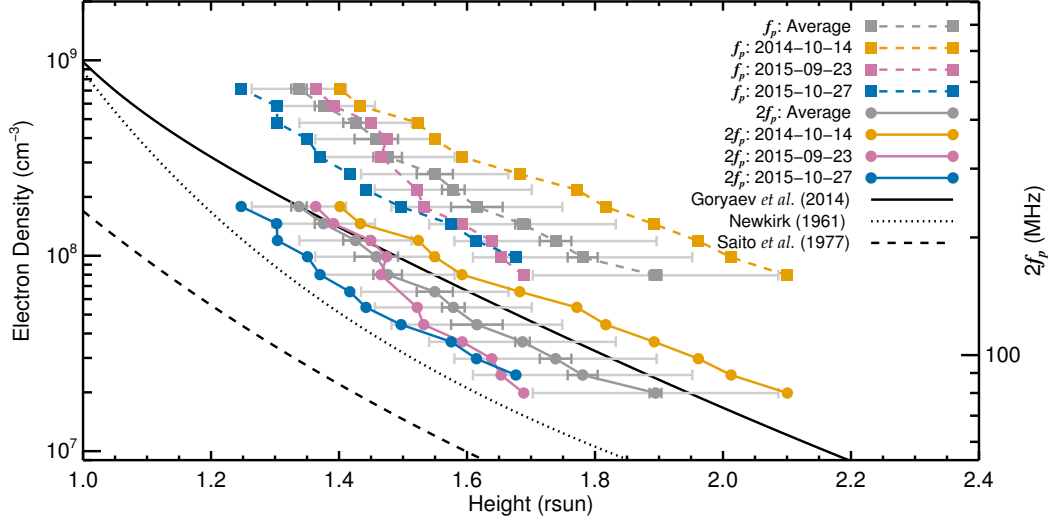


Figure 3.6: Densities inferred from the Type III source positions assuming fundamental [f_p ; dashed] or harmonic [$2f_p$; solid] emission. Background coronal models based on white-light data near solar minimum (Saito et al., 1977) and maximum (Newkirk, 1961) are shown for comparison, along with a recent streamer model based on EUV data (Goryaev et al., 2014). Only the average uncertainties are shown for clarity; the dark-gray bars represent the one- σ centroid variability over the full burst, and the light-gray bars represent the major axes of the synthesized beams.

by circles in Figure 3.3, and centroids are obtained at these times from two-dimensional (2D) Gaussian fits. As mentioned in Section 3.3.2, these events were chosen because they appear at the radio limb and thus the 2D plane-of-sky positions can reasonably approximate the physical altitude. Geometrically, these heights are lower limits to the true radial height, but propagation effects that increase apparent height are likely to be more important than the projection angle (see Section 3.4.3).

Figure 3.6 plots height *versus* density for both the fundamental and harmonic assumptions. Two sets of height uncertainties are shown for the average density profiles. The smaller, dark-gray error bars reflect the one- σ position variability over the full burst durations, and the larger, light-gray bars reflect the full width at half maximum (FWHM) of the synthesized beam major axes. Note that if the source is dominated by a single compact component, which would be a reasonable assumption here, then the FWHM resolution uncertainty can be reduced by a factor inversely proportional to the signal-to-noise ratio (SNR) (Lonsdale et al., 2018; Reid et al., 1988). Given our high SNRs, which average 217σ at the burst onsets, this “spot mapping” approach typically results in sub-arcsecond position uncertainties on the apparent source location.

However, spatial shifts may be introduced by changes in the ionosphere between the solar and calibration observation times, and more importantly, an apparent source may differ significantly from its actual emission site due to propagation effects (*i.e.* refraction and scattering). For these reasons, we opt to show the more conservative uncertainties outlined above.

For comparison, Figure 3.6 includes radial density models from Saito et al. (1977), Newkirk (1961), and Goryaev et al. (2014). The Saito et al. profile refers to the equatorial background near solar minimum based on white light polarized brightness data, while the Newkirk curve is based on similar data near solar maximum and implies the largest densities among “standard” background models. The Goryaev et al. model instead refers to a dense streamer and is based on a novel technique using widefield EUV imaging. This profile is somewhat elevated above streamer densities inferred from contemporary white-light (*e.g.* Gibson et al., 1999) and spectroscopic (*e.g.* Parenti et al., 2000; Spadaro et al., 2007) measurements at similar heights, although some earlier white-light studies found comparably large streamer densities (*e.g.* Saito and Owaki, 1967). For additional coronal density profiles, see also Allen (1947); Koutchmy (1994); Guhathakurta et al. (1996); Mann et al. (1999); Mercier and Chambe (2015); Wang et al. (2017) and references therein.

From Figure 3.6, we see that the Type III densities assuming fundamental emission are an average of $3-4\times$ higher than the EUV streamer model. These values may be unreasonably large, meaning either that the fundamental emission hypothesis is not viable here or that fundamental emission originating from a lower altitude was observed at a larger height due to propagation effects (see Section 3.4.3). Assuming harmonic emission, the 14 October 2014 burst implies electron densities of $1.8\times 10^8\text{ cm}^{-3}$ (240 MHz) at 1.40 R_{\odot} down to $0.20\times 10^8\text{ cm}^{-3}$ (80 MHz) at 2.10 R_{\odot} . This represents a moderate ($\approx 1.4\times$) enhancement over the Goryaev et al. streamer model or a significant ($\approx 4.1\times$) enhancement over the Newkirk background. The other two events fall between the EUV streamer and solar-maximum-background models, with the 27 October 2015 source heights implying densities of $1.8\times 10^8\text{ cm}^{-3}$ (240 MHz) at 1.25 R_{\odot} down to $0.20\times 10^8\text{ cm}^{-3}$ (80 MHz) at 1.68 R_{\odot} . Note that the 23 September 2015 burst implies an unusually steep density gradient that is not consistent with standard radial density models, perhaps because that event deviates significantly from the radial direction (see Figure 3.4).

Figure 3.7 shows how our results compare to densities inferred from recent Type III imaging at higher and lower frequencies, all assuming harmonic emission. The high-frequency (1.0–1.5 GHz) results come from Chen et al.

Ch. 3 Coronal Densities from Type III Burst Imaging

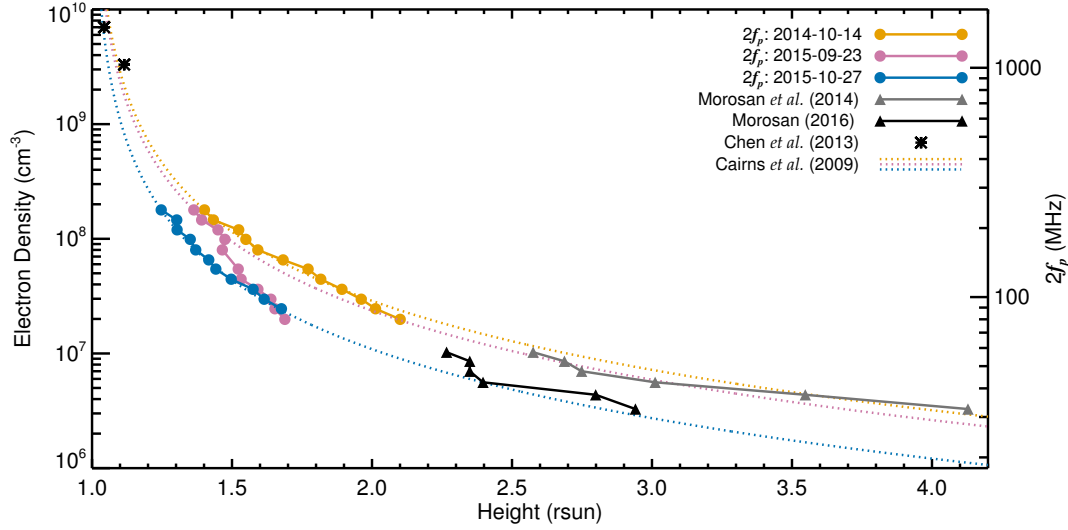


Figure 3.7: Densities assuming harmonic emission compared to recent Type III results at higher (Chen et al., 2013a) and lower (Morosan et al., 2014, 2016) frequencies. The Morosan et al. (2014) points (gray triangles) correspond to the same data as the Morosan et al. (2016) values (black triangles), but the latter have been adjusted to account for ionospheric refraction. The dotted lines apply the $n_e(r) = C(r - 1)^{-2}$ profile detailed by Cairns et al. (2009), where the constant C has been normalized to the density implied by our 240 MHz source positions.

(2013a), who used the *Very Large Array* (VLA) to find densities around an order of magnitude above the background. The low-frequency (30–60 MHz) points were obtained using the *Low Frequency Array* (LOFAR) by Morosan et al. (2014), who also found large enhancements. We plot data from their “Burst 2” (see Figures 3 and 4) because it began beyond our average radio limb height at 80 MHz. Their other two events exhibit 60 MHz emission near the optical limb, which may indicate that the 2D plane-of-sky positions significantly underestimate the true altitudes (*i.e.* those electron beams may have been inclined toward the observer). The Morosan et al. (2014) data are also reproduced in Chapter 4 of Morosan et al. (2016), who notes that ionospheric refraction likely contributed significantly to the observed source heights (D.E. Morosan, private communication, 2018), and adjusted values are also shown in Figure 3.7. As previously noted, ionospheric refraction may affect our positions as well if conditions changed significantly in the roughly 2 hours between the calibrator and solar observation times. This effect would likewise shift the solar disk, and given that this is not noticeable (see Figure 3.1), we conclude that any positional shifts imparted by a changing ionosphere are within our conservative uncertainty estimates.

Figure 3.7 also includes density curves of the form $n_e(r) = C(r-1)^{-2}$, where r is in solar radii and C is normalized to match the densities implied by our 240 MHz source heights. This model was introduced by Cairns et al. (2009) based on Type III frequency drift rates over 40–180 MHz and was subsequently validated over a larger frequency range by Lobzin et al. (2010). The Cairns et al. model is somewhat steeper than others over the MWA’s height range ($\approx 1.25\text{--}2.10 R_\odot$) but becomes more gently sloping at larger heights, effectively bridging the corona to solar-wind transition. From Figure 3.7, we see that this model is a good fit to the 14 October 2014 and 27 October 2015 data. The 23 September 2015 event is not well-fit by this or any other standard model, which may be attributed to its aforementioned non-radial structure. Extending these gradients to larger heights matches the LOFAR data fairly well and likewise with the VLA data at lower heights, which come from higher frequencies than have been examined with this model previously.

3.4.2 Electron Beam Kinematics

Type III beams speeds are known primarily from frequency drift rates $[df/dt]$ observed in dynamic spectra. Assuming either fundamental or harmonic emission, a given burst frequency can be straightforwardly converted into a radial height given a density model $n_e(r)$, and df/dt then becomes dr/dt . The literature includes a wide range of values using this technique, reflecting the variability among models as well as any intrinsic variability in electron speed. Modest fractions of light speed are typically inferred from drift rates of coronal bursts ($\approx 0.1\text{--}0.4 c$; Alvarez and Haddock, 1973; Aschwanden et al., 1995; Meléndez et al., 1999; Kishore et al., 2017), though speeds larger than $0.5 c$ have been reported by some studies (Poquerusse, 1994; Klassen et al., 2003; Carley et al., 2016). Our imaging observations allow us to measure the exciter speed without assuming $n_e(r)$ by following the apparent height progression of Type III sources at different frequencies.

As in the previous section, we obtain radial heights from centroid positions at the onset of burst emission for each frequency. These data are plotted in Figure 3.8 along with linear least-squares fits to the speed using the time and spatial resolutions as uncertainties. The 14 October 2014 event exhibits an anomalously late onset time at 80 MHz (see the circles in Figure 3.3a and the orange asterisk in Figure 3.8). This is likely due to the diminished intensity at that frequency, which precludes an appropriate comparison to the onset times at higher frequencies where the burst is much more intense. Figure 3.8 shows

Ch. 3 Coronal Densities from Type III Burst Imaging

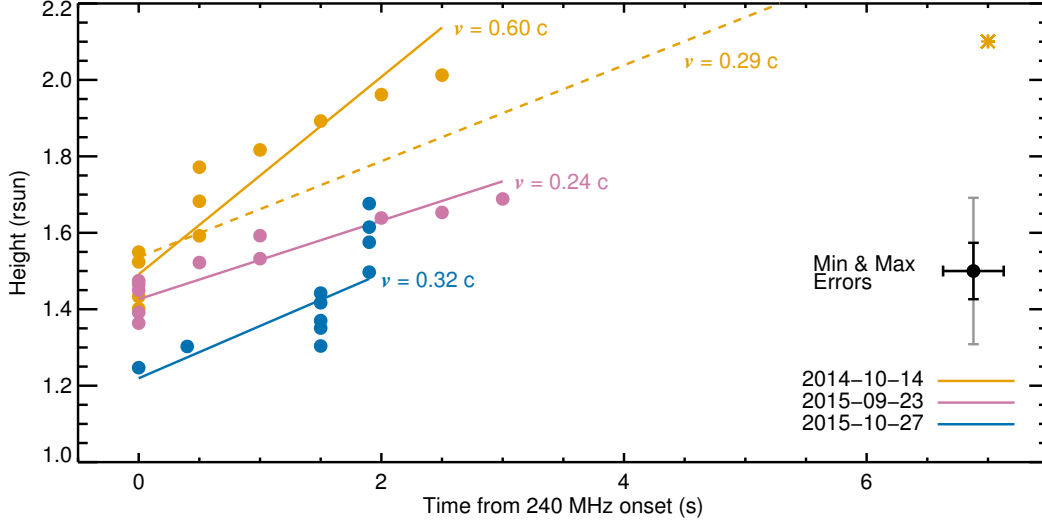


Figure 3.8: Exciter speed estimates from the time- and frequency-varying source positions. The dashed orange line includes the high time outlier (orange asterisk). The uncertainties shown in the lower right are the same for a given frequency and reflect the time and spatial resolutions. The black bar represents the smallest synthesized beam size at 240 MHz (corresponding to the lower-left points), and the gray bar represents the largest beam size at 80 MHz (corresponding to the upper-right points).

fits both including (0.29 c) and excluding (0.60 c) the 80 MHz point for the 14 October 2014 event, and the latter value is used in the discussion to follow because of the better overall fit. Note that while the onset of 80 MHz emission is at a later time than expected given the prior frequency progression, the source location is consistent with the other channels and thus its inclusion does not impact the inferred density profile from Figures 3.6 and 3.7.

We find an average speed across events of 0.39 c, which is consistent with results from other imaging observations. The same strategy was recently employed at lower frequencies by Morosan et al. (2014), who found an average of 0.45 c. McCauley et al. (2017) indirectly inferred a beam speed of 0.2 c from MWA imaging. Chen et al. (2013a) also tracked centroid positions at higher frequencies, although in projection across the disk, finding 0.3 c. Mann et al. (2018) recently examined the apparent speeds of three temporally adjacent Type III bursts imaged by LOFAR. They find that the sources do not propagate with uniform speed, with each burst exhibiting an acceleration in apparent height, and they conclude that the exciting electron beams must have broad velocity distributions. From Figure 3.8, we observe an apparent acceleration only for one event (27 October 2015), with the other two events exhibiting the opposite trend to some extent. However, our data are consistent with Mann

Table 3.1: Imaging Beam Speeds vs. df/dt Model Predictions

Event	Imaging	Beam Speed [c]			
		Assuming $f_p - 2f_p$ emission			Cairns <i>et al.</i> ^b
		Goryaev <i>et al.</i>	Newkirk	Saito <i>et al.</i> ^a	
14 Oct 2014 ^c	0.60 ± 0.13	$0.38 - 0.45$	$0.22 - 0.31$	*** - 0.30	0.58
23 Sep 2015	0.24 ± 0.10	$0.34 - 0.40$	$0.20 - 0.28$	*** - 0.27	0.50
27 Oct 2015	0.32 ± 0.12	$0.44 - 0.55$	$0.26 - 0.36$	*** - 0.48	0.40

^a f_p case not viable because model does not include densities above $f_p \approx 116$ MHz.

^bModel normalized to match the densities implied by our 240 MHz heights.

^cExcludes the 80 MHz outlier (orange asterisk in Figure 3.8).

et al. (2018) in that a uniform speed is not a particularly good fit for any of our events, but the MWA’s 0.5-second temporal resolution limits our ability to characterize the source speeds in great detail.

Taken together, we see that speeds measured from imaging observations tend to produce values at the higher end of what is typical for df/dt inferences. We compare the two approaches for the same events in Table 3.1 using the same models shown in Figure 3.6. We also include speeds derived using the Cairns et al. (2009) model, normalized to the densities implied by our 240 MHz source heights. These values are separated from the others in Table 3.1 because the normalization precludes direct comparisons to the other models. The df/dt -inferred speeds are consistently smaller than the imaging results for the 14 October 2014 event, which was also true for the bursts studied by Morosan et al. (2014), but there is no major difference between the two approaches for our other events given the range of values. Note that this comparison is arguably a less direct version of the height *versus* density comparison from the previous section in that the extent to which the imaging and model-dependent df/dt speeds agree unsurprisingly mirrors the extent to which the density profiles themselves agree. The 14 October 2014 speeds are closest to those derived using $n_e(r)$ from Goryaev et al., and the 27 October 2015 result is closest to the Newkirk-derived speed, both assuming harmonic emission, because those density profiles are most closely matched in Figure 3.6. Likewise, the speeds from those events agree well with df/dt speeds obtained using the normalized Cairns et al. curves because a $C(r - 1)^{-2}$ gradient fits those data nicely. The 23 September 2015 speed is between the two values derived using the Newkirk model assuming either fundamental and harmonic emission, but this may be coincidence given that the modeled and observed density profiles are widely discrepant. That event’s non-radial profile may also prevent meaningful agreement with any simple $n_e(r)$ model (see Figure 3.4).

3.4.3 Propagation Effects

As described in Section 3.2, a number of authors have argued that radio propagation effects, namely refraction and scattering, can explain the large source heights frequently exhibited by Type III bursts. Bougeret and Steinberg (1977) introduced the idea of scattering by overdense fibers in the context of radio burst morphologies, and Stewart (1974) suggested that Type III emission may be produced in underdense flux tubes as a way of explaining observed harmonic–fundamental ratios. These two concepts were combined by Duncan (1979), who introduced the term *ducting* to refer to radiation that is produced in an underdense environment and subsequently guided to a larger height by reflections against a surrounding “wall” of much higher-density material, which eventually becomes transparent with sufficient altitude. While plausible, this concept generalizes poorly in that electron beams are not expected to be found preferentially within coherent sets of low-density structures that would be conducive to ducting.

Robinson (1983) addressed this by showing that random reflections against overdense fibers can have the same effect of elevating an observed burst site above its true origin, but without requiring any peculiarities of the emission site (*i.e.* low density). Because the high-density fibers known to permeate the corona are not randomly arranged and are generally radial, random scattering against them does not randomly modulate the aggregate ray path, but it instead tends to guide the emission outward to larger heights in a manner that is analogous to the classic ducting scenario. For this reason, other authors (*e.g.* Poquerusse et al., 1988) have chosen to retain *ducting* to refer to the similar but more general impact of scattering, without implying that the emission is guided within a particular density structure as originally proposed by Duncan (1979). Here, we will simply refer to *scattering* to avoid potential confusion between the two concepts.

After being scattered for the last time upon reaching a height with sufficiently low densities, a radio wave will then be refracted through the corona before reaching an observer, further shifting the source location. As the coronal density gradient generally decreases radially, radio waves will tend to refract toward to the radial direction such that a source originating at the limb will appear at a somewhat lower height than its origin, which could be either the actual emission site (*e.g.* Stewart, 1976) or, more likely, the point of last scatter (*e.g.* Mann et al., 2018). Accounting for the refractive shift, which becomes larger with decreasing frequency, therefore requires that the emission be gen-

erated at or scattered to an even larger height than is implied by the observed source location. Recent results on this topic from Mann et al. (2018) will be discussed in the next section.

Propagation effects are also thought to be important to the observed structure of the quiescent corona, where the dominant emission mechanism is thermal bremsstrahlung (free-free) radiation at MWA frequencies. Outside of coronal holes, this emission is expected to be in or close to the optically thick regime (*e.g.* Kundu and Vlahos, 1982; Gibson et al., 2016), which means that the observed brightness temperature should be the same as the coronal temperature. However, well-calibrated 2D measurements have generally found lower brightness temperatures than expected from temperatures derived at other wavelengths (see review by Lantos, 1999). Additionally, the size of the corona appears to be larger than expected at low frequencies (*e.g.* Aubier et al., 1971; Thejappa and Kundu, 1992; Sastry, 1994; Subramanian, 2004; Ramesh et al., 2006). The prevailing explanation for these effects is also scattering by density inhomogeneities (*e.g.* Melrose and Dulk, 1988; Alissandrakis and Chiuderi-Drago, 1994; Thejappa and MacDowall, 2008), although the refractive effect described in the previous paragraph is also important (Thejappa and MacDowall, 2008).

Thus, the scattering process that may act to elevate Type III sources also affects quiescent emission, increasing the apparent size of the corona. We will take advantage of this by using the difference in extent between observed and modeled quiescent emission as a proxy for the net effect of propagation effects on our Type III source heights. This approach is limited in that, although both are related to scattering, the extent to which the magnitudes of these two phenomena are related is unclear. In particular, previous studies on the broadening of the radio Sun by scattering have considered random density inhomogeneities as opposed to the more realistic case of high density fibers capable of producing the ducting-like effect for Type III sources.

Figure 3.9 shows the observed background emission *versus* synthetic images based on a global MHD model. The MWA images are obtained by averaging every frame with a total intensity less than two σ above the background level, which is determined via the procedure shown in Figure 3.5. Synthetic images are obtained using FORWARD (Gibson et al., 2016), a software suite that calculates the expected bremsstrahlung and gyroresonance emission given a model atmosphere. We use the Magnetohydrodynamic Algorithm outside a Sphere (MAS; Lionello et al., 2009) medium resolution (`hmi_mast_mas_std_0201`) model, which extrapolates the coronal magnetic field from photospheric mag-

Ch. 3 Coronal Densities from Type III Burst Imaging

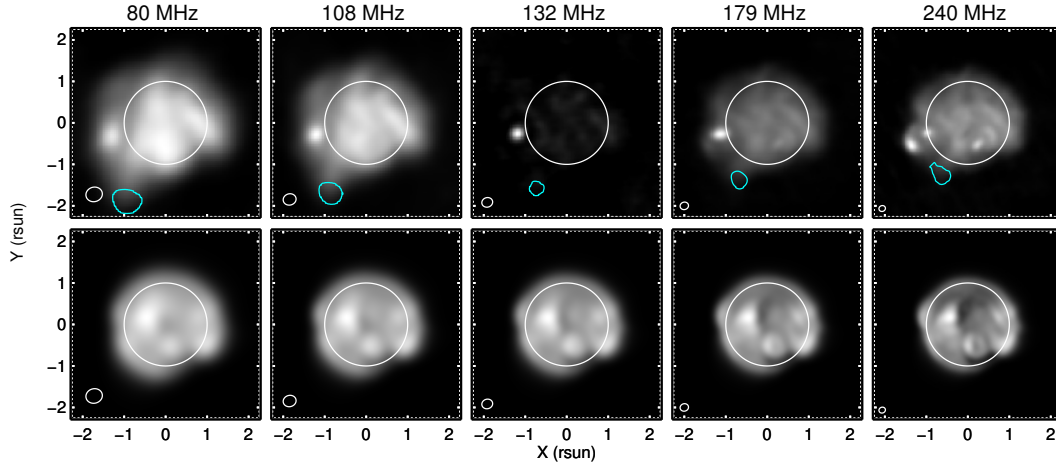


Figure 3.9: MWA background images for the 14 October 2014 event (top) and corresponding MAS-FORWARD synthetic images convolved with the MWA beam (bottom). Beam ellipses are shown in the lower-left corners, and the cyan curves are the 50% burst contours from Figures 3.1 & 3.4. This day is shown because thermal emission is only barely distinguishable at 132 MHz, precluding the Figure 3.10 analysis at that frequency, which was not the case for any other event-channel combination.

netograms (*e.g.* Mikić et al., 1999) and applies a heating model adapted from Schrijver et al. (2004) to compute density and temperature.

McCauley et al. (2017) established the use of these model images for flux calibration and included a qualitative comparison to MWA observations. As in the aforementioned literature, the radial extent of the corona is somewhat larger in the observations than in the beam-convolved model images. To quantify this difference, we divide both image sets into concentric rings about Sun-center. The average intensity within each ring is plotted against its radial distance in the left panel of Figure 3.10, where the intensities have been normalized by the median value below one solar radius. We then measure the offset Δh between the observed and modeled profiles at the heights obtained from the Type III positions. Δh is sensitive to how the intensity curves are normalized, and we quantify this uncertainty by repeating the procedure for ten different normalization factors that reflect the median intensities within radial bins of width $0.1 R_{\odot}$ from 0 to $1 R_{\odot}$. The right panel of Figure 3.10 plots the Δh results for each event, which have one- σ uncertainties of less than $\pm 0.025 R_{\odot}$. The offset appears to depend roughly linearly on frequency, with larger offsets at lower frequencies. Fitting a line through all of the points, we find that:

$$\Delta h \approx -1.5 \times 10^{-3} f + 0.41; 80 \leq f \leq 240 \text{ MHz} \quad (3.2)$$

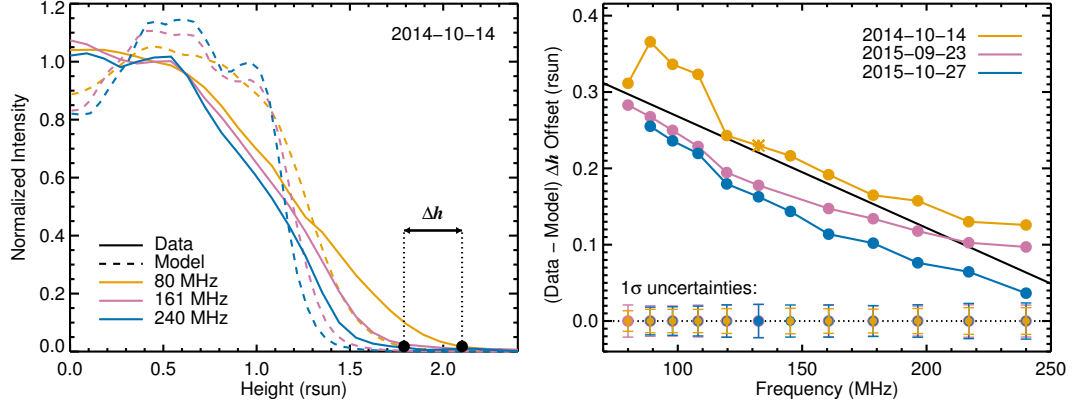


Figure 3.10: *Left*: Average intensity *versus* radial distance obtained from the Figure 3.9 images and normalized by the median value below $1 R_{\odot}$. Δh refers to the height offset between the observed and modeled intensity profiles at the apparent Type III burst height at 80 MHz. *Right*: Δh for each frequency and event. An orange asterisk marks the one instance where data was available but a measurement could not be made because the thermal background emission was not well-detected (see Figure 3.9), so an average of the adjacent points is used. The uncertainties reflect the sensitivity of Δh to the normalization choice in the left panel (see Section 3.4.3).

where Δh is in solar radii and f is in MHz. This yields $0.30 R_{\odot}$ at 80 MHz and $0.06 R_{\odot}$ at 240 MHz. We do not expect this expression to be relevant much outside of the prescribed frequency range, but extrapolating slightly, we obtain $0.32 R_{\odot}$ at 60 MHz. This value is a bit more than half of the $< 0.56 R_{\odot}$ limit found by Poquerusse et al. (1988).

Poquerusse et al., and others who have quantified the scattering effect (*e.g.* Robinson, 1983), obtained their results by computing ray trajectories through a model corona. That approach allows a fuller understanding of the propagation physics, but the result is dependent on the assumed concentration and distribution of high-density fibers, which are not well constrained. Our critical assumption is that emission produced at significantly lower heights would be absorbed, as would be the case in our optically thick model corona. However, low coronal brightness temperatures could also be explained by lower opacities (*e.g.* Mercier and Chambe, 2009) or a low filling factor, which would allow burst emission to escape from lower heights and lead us to underestimate the potential impact of propagation effects.

Figure 3.11 shows how the Figure 3.6 density results change after subtracting the height offsets from Figure 3.10. The 14 October 2014 harmonic $[2f_p]$ profile remains reasonable with the offsets, lying just below the Goryaev et al. (2014) model instead of just above it, while the fundamental emission densities

Ch. 3 Coronal Densities from Type III Burst Imaging

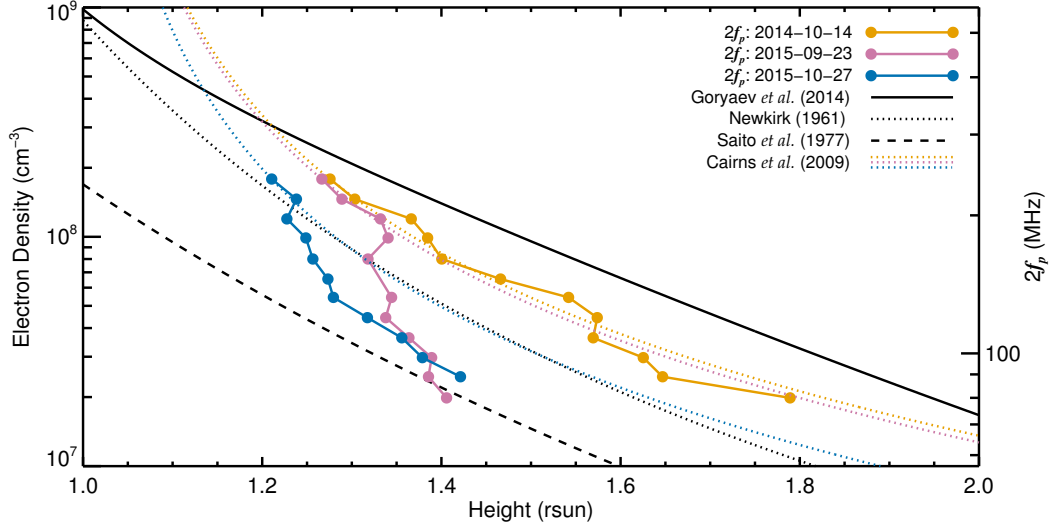


Figure 3.11: Imaging density profiles after applying the Δh offsets from Figure 3.10 and assuming harmonic emission. The solid (Goryaev et al., 2014), dotted (Newkirk, 1961), and dashed (Saito et al., 1977) black curves are density models corresponding to a dense streamer, the solar-maximum background, and the solar-minimum background, respectively (see Section 3.4.1). The dotted color lines apply the $n_e(r) = C(r-1)^{-2}$ profile detailed by Cairns et al. (2009), where the constant C has been normalized to the density implied by the corresponding 240 MHz source position.

for that event would still be quite large. Given that the Goryaev et al. model is among the highest-density streamer models in the literature, we conclude that harmonic emission from a beam traveling along an overdense structure is consistent with 14 October 2014 data. Our assessment for this event is that propagation effects may contribute to some but not all the apparent density enhancement.

The other two events exhibit unusually steep density profiles once the offsets are subtracted. That was true also for the original 23 September 2015 results, which we attributed to its non-radial trajectory in Section 3.4.1. However, the original 27 October 2015 densities were well-matched to the Cairns et al. (2009) $C(r-1)^{-2}$ gradient but become too steep to match any standard density gradient with the inferred offsets. This may simply reflect the intrinsic density gradient of the particular structure. Alternatively, it is possible that we have over- or underestimated the impact of propagation effects at the low or high end of our frequency range, respectively. However, the frequency dependence of scattering and refraction means that any treatment will steepen the density gradient. Aside from their slopes, the offsets bring the densities implied by both bursts to generally within the normal background range assuming harmonic

emission or to a moderately enhanced level assuming fundamental emission.

3.5 Discussion

The previous section suggests that propagation effects can partially explain the apparent density enhancements implied by our Type III source heights. Assuming harmonic emission, our estimates for the potential magnitude of propagation effects bring the densities to within normal background levels for two events, while one event remains enhanced at a level consistent with a dense streamer. In Section 3.4.1, we showed that our original density profiles are consistent with those found from recent Type III burst studies at lower and higher frequencies, which together are well-fit by the Cairns et al. (2009) $C(r - 1)^{-2}$ gradient. Both the low- and high-frequency studies conclude that their large densities imply electron beams traveling along overdense structures, but neither consider the impact of propagation effects.

Morosan et al. (2014) propose a variation of the overdense hypothesis based on their 30–60 MHz LOFAR observations. They suggest that the passage of a CME just prior to an electron beam’s arrival may compress streamer plasma enough to facilitate Type III emission at unusually large heights. This was consistent with their events being associated with a CME and could be relevant to our 23 September 2015 event, which was also preceded by a CME (see Section 3.3.3). While this interpretation is plausible, we do not think such special conditions need to be invoked given that the densities inferred from the Morosan et al. results are consistent with ours (Figure 3.7) and are broadly consistent with the large Type III source heights found using the previous generations of low-frequency instruments (*e.g.* Wild et al., 1959; Morimoto, 1964; Malitson and Erickson, 1966; Stewart, 1976; Kundu and Stone, 1984). Propagation effects seem particularly likely to have contributed (at least partially) to their inferred density enhancement, as the effects become stronger with decreasing frequency.

Recently, Mann et al. (2018) also examined the heights of Type III sources observed at the limb by LOFAR. After accounting for the refractive effect described in Section 3.4.3, and relying on scattering to direct emission toward the observer at large heights prior to being refracted, their results imply a density enhancement of around $3.3\times$ over the Newkirk (1961) density model, assuming fundamental emission. Incorporating our offsets from Section 3.4.3 gives us an average enhancement of $4.6\times$ over the same model across our three events, also assuming fundamental emission. Our results are therefore consistent with

Ch. 3 Coronal Densities from Type III Burst Imaging

those of Mann et al. (2018), though our attempts to quantify the impact of propagation effects are quite different.

Chen et al. (2013a) also found large densities using VLA data at higher frequencies (1.0–1.5 GHz). Scattering is also thought to be important at high frequencies given the apparent lack of small-scale structure (Bastian, 1994), but the extent to which scattering may also elevate radio sources in that regime has not been addressed to our knowledge. Chen et al. observed an on-disk event, from which they obtain source heights by comparing their projected positions to stereoscopic observations of an associated EUV jet, which is assumed to have the same inclination as the Type III electron beam. This method would also be impacted by any source shifting caused by scattering. Although these shifts would be much smaller than at low frequencies, the background gradient is much steeper, so a reasonably small shift may still strongly influence the inferred density relative to the background.

If we accept the densities obtained at higher frequencies, albeit from just one example, then their consistency with low-frequency observations in general is striking. As we describe in Section 3.2, the community largely came to favor propagation effects over the overdense hypothesis in the 1980s, and the topic has not had much consideration since. If new observations at low heights (high frequencies) also suggest beams moving preferentially along dense structures, then it elicits the question of whether or not that interpretation is again viable at larger heights (lower frequencies). In that case, this would need to be reconciled with the fact that electron beams have not been found to be preferentially associated with particularly high-density regions in *in-situ* solar wind measurements (Steinberg et al., 1984), along with the evidence for other impacts of scattering such as angular broadening (*e.g.* Steinberg et al., 1985; Bastian, 1994; Ingale et al., 2015).

Selection effects may be relevant, as radiation produced well above the ambient plasma frequency is less likely to be absorbed before reaching the observer. Thus, coronal Type III bursts may imply high densities because beams traveling along dense structures are more likely to be observed. Type III bursts also have a range of starting frequencies, which has been interpreted in terms of a range in acceleration (*i.e.* reconnection) heights that are often larger than those inferred from X-ray observations (Reid et al., 2014). Alternatively, a beam may be accelerated at a smaller height than is implied by the resultant Type III starting frequency due to unfavorable radiation-escape conditions (absorption) below the apparent starting height. Simulations also suggest that electron beams may travel a significant distance before producing observable

emission (Li and Cairns, 2013, 2014) and that they may be radio loud at some frequencies but not at others due to variations in the ambient density (Li et al., 2012; Loi et al., 2014) and/or temperature (Li et al., 2011a,b).

The magnetic structures along which electron beams travel also evolve with distance from the Sun. A popular open flux tube model is an expanding funnel that is thin at the base of the corona and increasingly less so into the solar wind (*e.g.* Byhring et al., 2008; He et al., 2008; Pucci et al., 2010). Such structures may allow a dense flux tube to become less dense relative to the background as it expands with height. Moreover, a beam following a particular magnetic field line from the corona into the high- β solar wind may not necessarily encounter a coherent density structure throughout the heliosphere. Turbulent mixing, corotation interaction regions, CMEs, and other effects influence solar wind density such that it is not obvious that an electron beam traversing an overdense structure near the Sun should also be moving in an overdense structure at large heliocentric distances.

We also note that one of the main conclusions from many of the Type III studies referenced here is unchanged in either the overdense or propagation effects scenarios. Both cases require a very fibrous corona that can supply dense structures along which beams may travel and/or dense structures capable of scattering radio emission to larger heights. This is consistent with the fine structure known from eclipse observations (*e.g.* Woo, 2007) that has more recently been evidenced by EUV observations. For instance, analyses of a sun-grazing comet (Raymond et al., 2014) and of EUV spectra (Hahn and Savin, 2016) independently suggest large density contrasts ($\gtrsim 3-10$) between neighboring flux tubes in regions where the structures themselves are undetected. As our understanding of such fine structure improves, better constraints can be placed on them for the purpose of modeling the impact of propagation effects on radio sources.

3.6 Conclusion

We presented imaging of three isolated Type III bursts observed at the limb on different days using the MWA. Each event is associated with a white-light streamer and plausibly associated with EUV rays that exhibit activity around the time of the radio bursts. Assuming harmonic plasma emission, density profiles derived from the source heights imply enhancements of approximately $2.4-5.4\times$ over background levels. This corresponds to electron densities of $1.8\times 10^8\text{ cm}^{-3}$ (240 MHz) down to $0.20\times 10^8\text{ cm}^{-3}$ (80 MHz) at average heights

Ch. 3 Coronal Densities from Type III Burst Imaging

of 1.3 to 1.9 R_{\odot} . These values are consistent with the highest streamer densities inferred from other wavelengths and with the large radio source heights found using older instruments. The densities are also consistent with recent Type III results at higher and lower frequencies, which combined are well-fit by a $C(r - 1)^{-2}$ gradient. By comparing the extent of the radio limb to model predictions, we estimated that radio propagation effects, principally the ducting-like effect of random scattering by high-density fibers, may be responsible for 0.06–0.30 R_{\odot} of our apparent source heights. This shift brings the results from two of our three events to within a standard range of background densities. We therefore conclude that propagation effects can partially explain the apparent density enhancements but that beams moving along overdense structures cannot be ruled out. We also used the imaging data to estimate electron beam speeds of 0.24–0.60 c .

Acknowledgements: Support for this work was provided by the Australian Government through an Endeavour Postgraduate Scholarship. We thank Stephen White and Don Melrose for helpful discussions and the anonymous referee for their constructive comments. This scientific work makes use of the Murchison Radio-astronomy Observatory (MRO), operated by the Commonwealth Scientific and Industrial Research Organisation (CSIRO). We acknowledge the Wajarri Yamatji people as the traditional owners of the Observatory site. Support for the operation of the MWA is provided by the Australian Government’s National Collaborative Research Infrastructure Strategy (NCRIS), under a contract to Curtin University administered by Astronomy Australia Limited. We acknowledge the Pawsey Supercomputing Centre, which is supported by the Western Australian and Australian Governments. SDO is a National Aeronautics and Space Administration (NASA) spacecraft, and we acknowledge the AIA science team for providing open access to data and software. The SOHO/LASCO data used here are produced by a consortium of the Naval Research Laboratory (USA), Max-Planck-Institut für Aeronomie (Germany), Laboratoire d’Astronomie (France), and the University of Birmingham (UK). SOHO is a project of international cooperation between ESA and NASA. This research has also made use of NASA’s Astrophysics Data System (ADS), along with JHelioviewer (Müller et al., 2017) and the Virtual Solar Observatory (VSO: Hill et al., 2009).

Chapter 4

The Low-Frequency Solar Corona in Circular Polarization

Published as McCauley et al. (2019), *Solar Phys.*, 294:106

4.1 Abstract

We present spectropolarimetric imaging observations of the solar corona at low frequencies (80–240 MHz) using the *Murchison Widefield Array* (MWA). These images are the first of their kind, and we introduce an algorithm to mitigate an instrumental artefact by which the total intensity signal contaminates the polarimetric images due to calibration errors. We then survey the range of circular polarization (Stokes V) features detected in over 100 observing runs near solar maximum during quiescent periods. First, we detect around 700 compact polarized sources across our dataset with polarization fractions ranging from less than 0.5% to nearly 100%. These sources exhibit a positive correlation between polarization fraction and total intensity, and we interpret them as a continuum of plasma emission noise storm (Type I burst) continua sources associated with active regions. Second, we report a characteristic “bullseye” structure observed for many low-latitude coronal holes in which a central polarized component is surrounded by a ring of the opposite sense. The central component does not match the sign expected from thermal bremsstrahlung emission, and we speculate that propagation effects or an alternative emission mechanism may be responsible. Third, we show that the large-scale polarimetric structure at our lowest frequencies is reasonably well-correlated with the line-of-sight (LOS) magnetic field component inferred from a global potential field source surface (PFSS) model. The boundaries between opposite circular polarization signs are generally aligned with polarity inversion lines in the model at a height roughly corresponding to that of the radio limb. This is not true at our highest frequencies, however, where the LOS magnetic field direction and polarization sign are often not straightforwardly correlated.

4.2 Introduction

Radio emission in a magnetized plasma is produced in one or both of two modes, the ordinary $[o]$ and extraordinary $[x]$, which are each 100% circularly polarized with opposite senses in the quasi-circular approximation generally used for the solar corona (Zheleznyakov, 1977; Melrose, 1980). The x -mode refers to when the electric field vector of the electromagnetic wave rotates in the same direction as the gyromotion of electrons around the magnetic field where the emission was generated. A net circular polarization arises when the two modes are received unequally, which is characterized by the degree $[r_c]$ of circular polarization [Stokes V] relative to the total intensity [Stokes I]. In detail,

$$r_c = \frac{T_{b,x} - T_{b,o}}{T_{b,x} + T_{b,o}}, \quad (4.1)$$

where $T_{b,x}$ and $T_{b,o}$ refer to the brightness temperatures of the o and x modes, respectively (Dulk, 1985). The quantity r_c , also labeled dcp or V/I , depends on the emission mechanism and plasma parameters, along with a number of effects such as mode coupling and refraction that may modulate the polarization state or separate the two modes during propagation. Low-frequency (meter-wave) emission from the solar corona is dominated by two mechanisms, thermal bremsstrahlung and plasma emission (*e.g.* Dulk, 1985; White, 1999; Aschwanden, 2005). Other mechanisms are also important in specific contexts, such as (gyro)synchrotron emission in coronal mass ejections, but these will not be discussed in detail here.

Bremsstrahlung emission is produced by the conversion of kinetic energy into radiant energy that occurs when a charged particle accelerates, and thermal bremsstrahlung refers to a plasma in thermal equilibrium for which free electrons are deflected by the Coulomb fields of ions and atomic nuclei. This is often referred to as free-free radiation for a fully-ionized plasma like the corona because the particles are not in bound states throughout the entire process. Emission at a particular frequency is generated only by plasma with electron densities $[n_e]$ equal to or below that corresponding to the local fundamental electron plasma frequency $[f_p \approx 9 \times 10^{-3} \sqrt{n_e} \text{ MHz, for } n_e \text{ in cm}^{-3}]$. Lower-frequency emission therefore corresponds to lower-density material at generally larger heights above the surface, meaning that the corona appears larger with decreasing frequency. Canonical coronal background density models (*e.g.* Newkirk, 1961; Saito et al., 1977) correspond to frequencies of below

≈ 300 MHz, but dense coronal structures may produce free-free emission well into the GHz range.

Thermal bremsstrahlung slightly favors the x -mode to a degree that depends primarily on the line-of-sight (LOS) magnetic field strength. The opacity, κ , can be written as

$$\kappa = 0.2 \frac{n_e^2}{T_e^{1.5} (f \pm f_B |\cos \theta|)^2} \text{ cm}^{-1}, \quad (4.2)$$

where T_e is the electron temperature, f is the emission frequency, f_B is the electron gyrofrequency [$f_B = 2.8 \times 10^6 B_{\text{gauss}}$ Hz], and θ is the angle between the line of sight and the magnetic field direction (Dulk, 1985; Gelfreikh, 2004; Gibson et al., 2016). The plus sign refers to the o -mode, the minus sign refers to the x -mode, and the difference between the two modes produces the net circular polarization. Equation 4.2 is a quasi-linear (QL) approximation that is valid for most angles θ . Values of θ close to 90° , for which the propagation direction is nearly perpendicular to the magnetic field orientation, are referred to as quasi-transverse (QT) propagation and produce linear polarizations (Zheleznyakov, 1970; Ryabov, 2004). Circularly-polarized emission that passes through a QT region may also experience polarization state changes, which will be discussed in Section 4.8. Equation 4.2 also assumes that $f \gg f_B$. This condition means that the difference between the two modes, and therefore the polarization fraction, will always be fairly small, generally a few percent or less at the low frequencies considered in this article (Sastry, 2009). For a homogenous, optically-thin plasma, $r_c \approx 2 \cos \theta (f_B/f)$, while for the optically-thick case, a temperature gradient is required for the two modes to be produced unequally (Dulk, 1985; Gibson et al., 2016).

Thermal bremsstrahlung radiation generates a continuous background that slowly varies as the corona evolves. This may be slightly or dramatically augmented by transient emission associated with nonthermal electrons that are accelerated through a variety of mechanisms underpinned either by magnetic reconnection or shock waves. These electron streams produce oscillations in the background plasma known as Langmuir waves, which then deposit energy into radio emission through scattering by ion sound waves or by other nonlinear Langmuir wave processes (Ginzburg and Zhelezniakov, 1958; Robinson and Cairns, 2000; Melrose, 2009). These are typically coherent mechanisms, often grouped together under the term “plasma emission,” for which the intensity is related nonlinearly to the energy of the nonthermal electrons. Plasma emission is responsible for most types of solar radio bursts (Dulk, 1985), which may

Ch. 4 Spectropolarimetric Imaging of the Corona

exceed the thermal background by several orders of magnitude, but it is also likely the source of very weak nonthermal emissions that enhance the background only slightly (Suresh et al., 2017; Sharma et al., 2018). Like thermal bremsstrahlung, plasma emission is tied to the ambient density through the electron plasma frequency. However, in this case, the emission frequency is highly localized to just above the plasma frequency or its harmonic.

The polarization of plasma emission depends firstly on the harmonic number. For fundamental [f_p] emission, the circular polarization fraction should be 100% in the sense of the o -mode because, for frequencies expressed in Hz, f_p is above the cutoff for x -mode production, meaning that x -mode radiation begins only at frequencies slightly lower than the plasma frequency (Melrose, 2009). Polarization fractions approaching 100% are indeed sometimes observed for Type I bursts (*e.g.* Kai, 1962; Tsuchiya, 1963; Dulk et al., 1984; Aschwanden, 1986; Mugundhan et al., 2018). However, this is almost never true for other radio burst types that are also attributed to fundamental plasma emission (*e.g.* Wentzel, 1984; Reid and Ratcliffe, 2014; Kaneda et al., 2015). The reason for this remains an open question, but a common explanation is that scattering of the radio emission by other wave modes or by sharp density gradients tends to have a depolarizing effect (*e.g.* Wentzel et al., 1986; Melrose, 1989, 2006; Kaneda et al., 2017). The polarization fraction of harmonic [$2f_p$] emission is more complicated because it depends on the angular distribution of the Langmuir waves. Polarization in the sense of the o -mode is still generally expected, assuming that the Langmuir waves are confined to relatively small angles with respect to the magnetic field, which is generally assumed to be true because of the associated magnetic field strengths (Melrose et al., 1978). However, it is possible for the x -mode to dominate in specific, and likely less common, contexts (Willes and Melrose, 1997). Thus, for the same LOS magnetic field direction, the two dominant low-frequency emission mechanisms generally produce opposite circular polarization signatures.

Radio polarimetry has long been a powerful tool for diagnosing solar magnetic fields, particularly using high-frequency observations of gyroresonance emission (Akhmedov et al., 1982; White and Kundu, 1997) and, more recently, bremsstrahlung emission (Grebinskij et al., 2000). Low-frequency polarimetry has generally been restricted to radio bursts because their high intensities and large polarization fractions are easiest to detect. An early review on the polarization of metric bursts and their utility as magnetic field probes is given by Dulk and McLean (1978). Very few instruments have been capable of making two-dimensional polarimetric measurements of the low-frequency Sun, and

until now, none have been sensitive enough to detect the weak polarization signatures during quiescent periods. In recent decades, this type of analysis could be done with two instruments, the Nançay Radioheliograph (NRH; Kerdraon and Delouis, 1997), which operates between 150 and 450 MHz, and the Gauribidanur Radioheliograph (GRH; Ramesh et al., 1998), which usually operates at 80 MHz.

A few studies have utilized the polarimetric imaging capabilities of the NRH to examine spatial variation in radio bursts. For example, Mercier (1990) showed that Type III bursts have different spatial characteristics in circular polarization compared to the total intensity, and Bouratzis et al. (2016) investigated similar differences in spike bursts as a function of time. Several others have examined source positions and structures in total intensity NRH observations, while using the polarization information to help discriminate between emission mechanisms (*e.g.* Gopalswamy et al., 1994; Tun and Vourlidas, 2013; Kong et al., 2016; Liu et al., 2018). The radioheliograph at Gauribidanur does not have a polarimetric capability itself, but several one-dimensional polarimeters have been installed alongside it (Ramesh et al., 2008; Sasikumar Raja et al., 2013; Kishore et al., 2015).

GRH imaging and simultaneous polarimeter observations have been used for studies of Type I noise storms (Ramesh et al., 2011, 2013; Mugundhan et al., 2018), Type II bursts (Hariharan et al., 2014, 2015; Kumari et al., 2017), Type III bursts (Ramesh et al., 2010a; Sasikumar Raja and Ramesh, 2013; Kishore et al., 2017), Type IV bursts (Hariharan et al., 2016), and gyrosynchrotron emission from CMEs (Sasikumar Raja et al., 2014). Most of these results include estimates of the associated magnetic field strength assuming a particular emission mechanism. Additionally, Ramesh et al. (2010b) report polarized emission from streamers that is attributed to thermal bremsstrahlung, though the polarization fraction ($\approx 15\%$) is unusually large for bremsstrahlung emission. Moreover, the polarized source cannot be localized beyond assuming that it comes from the dominant total intensity source, and as we will show, polarized emission from the low-frequency corona is often not straightforwardly correlated with total intensity, particularly during quiescent periods.

This article presents the first spectropolarimetric imaging observations of the Sun from the *Murchison Widefield Array* (MWA; Tingay et al., 2013a). These are the first circular polarization images of the low-frequency corona that are sensitive enough to detect the polarimetric signatures associated with thermal bremsstrahlung emission and very weak plasma emission outside of major burst periods. We will survey the range of features detected in over 100 ob-

serving runs near solar maximum and motivate future studies with these novel data. Section 4.3 describes the MWA instrument, and Section 4.4 introduces an algorithm used to mitigate an important calibration artefact. Section 4.5 discusses active region noise storm sources, Section 4.6 characterizes the polarimetric signature of coronal holes, and Section 4.7 details the large-scale quiescent structure. We discuss the implications of our results and motivate future studies in Section 4.8. Our conclusions are summarized in Section 4.9.

4.3 *Murchison Widefield Array* (MWA)

The MWA is a low-frequency radio interferometer located in Western Australia (Lonsdale et al., 2009; Tingay et al., 2013a), and heliophysics is among the instrument’s principal science themes alongside astrophysical topics (Bowman et al., 2013). Direct solar observations have characterized the weakest non-thermal emissions reported to-date (Suresh et al., 2017; Sharma et al., 2018), provided definitive evidence for the standard theory of Type III bursts (Cairns et al., 2018), detailed new radio burst dynamics (McCauley et al., 2017; Mohan et al., 2019a), used radio bursts to probe the coronal density structure (McCauley et al., 2018), characterized the low-frequency signature of coronal holes (Rahman et al., 2019), and provided evidence for coronal heating via weak particle acceleration episodes (Mohan et al., 2019b). Solar imaging with the MWA has also motivated advances in data processing techniques related to flux calibration (Oberoi et al., 2017), spatially resolved dynamic spectra (Mohan and Oberoi, 2017), and high dynamic range imaging (Mondal et al., 2019). Additionally, widefield interplanetary scintillation observations may be used for studies of the solar wind and of coronal mass ejections (CMEs) propagating through the heliosphere (Kaplan et al., 2015; Morgan et al., 2018).

The MWA is comprised of 4096 dipole antennas arranged in 128 aperture arrays called “tiles”. This refers to the Phase I array used here, which began observing in 2013. An expanded Phase II array began full operations in 2018 with twice as many tiles, of which 128 can be used simultaneously in different configurations (Wayth et al., 2018). The MWA has an instantaneous bandwidth of 30.72 MHz that can be distributed between 80 and 300 MHz in various configurations. Our data utilize a “picket fence” mode with 12 contiguous 2.56 MHz bandwidths centered at 80, 89, 98, 108, 120, 132, 145, 161, 179, 196, 217, and 240 MHz. The data were recorded with a 0.5 sec time resolution and a 40 kHz spectral resolution, but the observations presented here are averaged over each 2.56 MHz bandwidth before imaging and then time-averaged to different

degrees after imaging. The spatial resolution is defined by the synthesized beam sizes, which have major axes of around 6.4 arcmin ($0.40 R_{\odot}$) at 80 MHz and 2.5 arcmin ($0.16 R_{\odot}$) at 240 MHz. The beam sizes and orientations, shown in the lower-left corners of each image, vary somewhat between observations due to pointing differences and occasional antenna failures.

We use the same data processing scheme as McCauley et al. (2017) and McCauley et al. (2018), and what follows is a brief summary thereof. Visibilities were generated with the standard MWA correlator (Ord et al., 2015) and the `cotter` software (Offringa et al., 2012, 2015). Observations of bright and well-modelled calibrator sources were used to obtain solutions for the complex antenna gains (Hurley-Walker et al., 2014), which were improved by imaging the calibrator and iteratively self-calibrating from there (Hurley-Walker et al., 2017). All of our observations were calibrated using either Centaurus A or Hercules A. WSClean (Offringa et al., 2014) was used to perform the imaging with a Briggs -2 weighting (Briggs, 1995) to emphasize spatial resolution and minimize point spread function (PSF) sidelobes. The primary beam model of Sutinjo et al. (2015) was used to produce Stokes I and V images from the instrumental polarizations, and the SolarSoftWare (SSW; Freeland and Handy, 1998) routine `mwa_prep` (McCauley et al., 2017) was used to translate the images onto solar coordinates. The data presented here are not flux calibrated on an absolute scale. Intensities are expressed either relative to the Stokes I background level or in units of signal-to-noise.

The next section will describe further steps required to calibrate the polarization images. We use the International Astronomical Union (IAU) and Institute of Electrical and Electronics Engineers (IEEE) convention on circular polarization, which defines positive as being right-handed (clockwise) from the source’s perspective (IEEE, 1969; IAU, 1973), where right-handed refers to the rotation of the electric field vector of the electromagnetic wave about the orthogonal direction of motion. This convention is convenient here because it means that a net polarization in the sense of the x -mode will match the sign of the line-of-sight magnetic field component $[B_{\text{LOS}}]$, where positive is outward.

Each observation period lasted around 5 minutes, and a total of 111 such periods in 2014 and 2015 were reduced. 52 of these were imaged at the full 0.5-sec time resolution and 59 were sampled at a 4-sec cadence. Our objective is to survey the longer-lived features that are present in the corona on timescales of at least minutes, outside of transient radio burst periods. All of the images presented in this article are median averages of the individual 0.5-sec integrations with total intensities that are within two standard deviations

of the background level during each 5-min observing window. Depending on the sources present, these averaged background images may still contain significant nonthermal emission. Identifying which images to include in the average is done automatically using the baseline procedure illustrated by Figure 5 of McCauley et al. (2018). This involves finding the total intensity in each image, excluding times for which the intensity is greater than two standard deviations above the median, and iterating until no more images are excluded. Each pixel in the output image then contains the median of the corresponding pixels in those low-intensity images. The consideration of time dependent behavior on scales of less than 5 minutes will be a topic of future work.

4.4 An Algorithm to Mitigate the Leakage of Stokes I into V

To obtain useful polarimetric images, it is necessary to account for possible “leakage” of the Stokes I signal into the other Stokes parameters. The MWA uses dual-polarization dipole antennas arranged in 4×4 grids, or “tiles”, where the signals for each tile component are combined in an analog beamformer that produces two outputs representing orthogonal X and Y linear polarizations (Tingay et al., 2013a). The beamformer outputs are correlated into products that fully describe the polarization state in “instrumental” polarizations (XX , YY , XY , and YX) that may be converted into the standard Stokes parameters (I , Q , U , and V) using a model of the MWA beam pattern. However, there are significant differences between the analytic beam pattern and that measured empirically by imaging known sources (Sutinjo et al., 2015). These differences between the actual instrumental response and the complex primary beam model lead to “leakage” errors in the Stokes images where some fraction of I contaminates the other parameters.

A more detailed description of this problem and of MWA polarimetry in general is given by Lenc et al. (2017). Sources of discrepancy between the beam model and the true response include imperfections in the model itself along with instrumental effects, such as individual dipole failures during a particular observing run, that may cause the true response to vary from an otherwise perfect beam model. Importantly, the polarimetric response is also affected by a source’s position within the beam and zenith angle, which means that the response changes somewhat between the observation used to calibrate the array and the solar observation. Changes in the ionosphere over the $\lesssim 5$ hours

between the calibrator and solar observations may also degrade the calibration solution. Our data were reduced using the Sutinjo et al. (2015) beam model, which dramatically reduced leakage from Stokes I into Stokes Q but somewhat increased the leakage from I into V compared to previous beam models.

The leakage fraction also varies with a source’s position on the sky and its position within the field-of-view for a given calibration solution (Sutinjo et al., 2015; Lenc et al., 2017, 2018). Sources observed at lower elevations and/or near the edge of the field tend to exhibit higher leakage fractions. It is possible to reduce the leakage by means of iterative self-calibration on the source of interest, but this may affect the polarimetric calibration in ways that are difficult to understand, and self-calibration can also be difficult to effectively apply to diffuse sources like the Sun. Instead, the leakage effect can be mitigated with an empirical correction if there are sources within the field for which the polarization fractions are known. For the very large fields typical of many astrophysical MWA observations, a two-dimensional fit to the leakage fraction may be obtained from the known sources scattered throughout the field. The leakage fraction may vary by as much as 8% across a 25 deg² patch (Lenc et al., 2017), but we do not expect significant variations across the spatial extent of the radio Sun ($\lesssim 1.2^\circ$ at 80 MHz) or over the duration of a typical observation (≈ 5 min).

For the solar observations presented here, it is not possible to simultaneously observe background sources alongside the Sun due to limited dynamic range. Recent advances in calibration techniques may enable this capability (Mondal et al., 2019), but those methods cannot yet be used for polarimetry and are not used here. In other words, the astronomical sources that may be present are too faint to be observed in close proximity to the Sun and cannot be used to characterize the Stokes I into V leakage. We also do not know what the polarization fraction of any particular region on the Sun should be at any given time, as the polarization fraction may vary considerably depending on the dominant emission mechanism and local plasma parameters. However, outside of radio bursts, solar emission at low frequencies is dominated by the thermal bremsstrahlung (free-free) process. The importance of this is that under normal quiet-Sun conditions at MWA wavelengths, we can expect to see bremsstrahlung radiation in most locations that is only slightly polarized, and we can use this statistical information to estimate the leakage fraction with an algorithm that minimizes the number of pixels with polarization fractions greater than some threshold (*i.e.* $|V/I| > r_{\text{c,thresh}}$).

To determine this threshold, we generated synthetic Stokes V/I images for

Ch. 4 Spectropolarimetric Imaging of the Corona

each of our observing periods and frequencies using the forward modeling code FORWARD (Gibson et al., 2016) in SolarSoft IDL. FORWARD calculates the Stokes I and V intensities expected from thermal bremsstrahlung emission using Equation 4.2, with the temperature, density, and magnetic field parameters taken in this case from the month-averaged Magnetohydrodynamic Algorithm outside a Sphere (MAS; Lionello et al., 2009) global coronal model. On average 50% of pixels in these images with Stokes I brightness temperatures greater than 100,000 K have fractional polarizations of less than 0.3%. We choose a slightly larger threshold of 0.5% because we wanted to implement our procedure uniformly, and the noise level in some of our observations makes a lower threshold impractical. This value is also consistent with the predictions of Sasstry (2009), and the effect of varying the threshold is folded into V/I uncertainty estimates presented in Section 4.6.

Our algorithm therefore assumes that most of the pixels in our images of the quiescent corona should exhibit polarization fractions of less than 0.5% and determines the leakage fraction that minimizes the number of pixels with V/I values greater than 0.005. The algorithm can be expressed formally as:

$$f(L) = \sum_{k=1}^n \left[\left| \frac{V_k - L \cdot I_k}{I_k} \right| > r_{c,\text{thresh}} \right] \quad (4.3)$$

$$L_{\min} = \arg \min_{L \in (-1,1)} f(L), \quad (4.4)$$

where $f(L)$ is the number of pixels with polarization fractions greater than $r_{c,\text{thresh}}$ as a function of L , the constant fraction of Stokes I that is assumed to have leaked into Stokes V . The aim is to find the value L_{\min} that minimizes $f(L)$, where k is a given pixel in an image and n is the number of pixels to be considered. We consider only pixels for which a Stokes I signal is detected above 5σ . The square brackets in Equation 4.3 refer to the Iverson bracket notation, meaning that their contents evaluate to 1 if the condition is satisfied and 0 otherwise. In this case, that simply means that a pixel is counted if its polarization fraction is greater than 0.005 (0.5%). Equation 4.4 is evaluated using an adaptive grid search with increments in L of 0.1, 0.01, and 0.001. Note that this strategy is not the same as minimizing the total polarized intensity, which is not advisable because the two senses may not be equally represented and specific regions may have large polarized intensities that would bias the result if one were to simply find L that minimizes the total polarization fraction in the image.

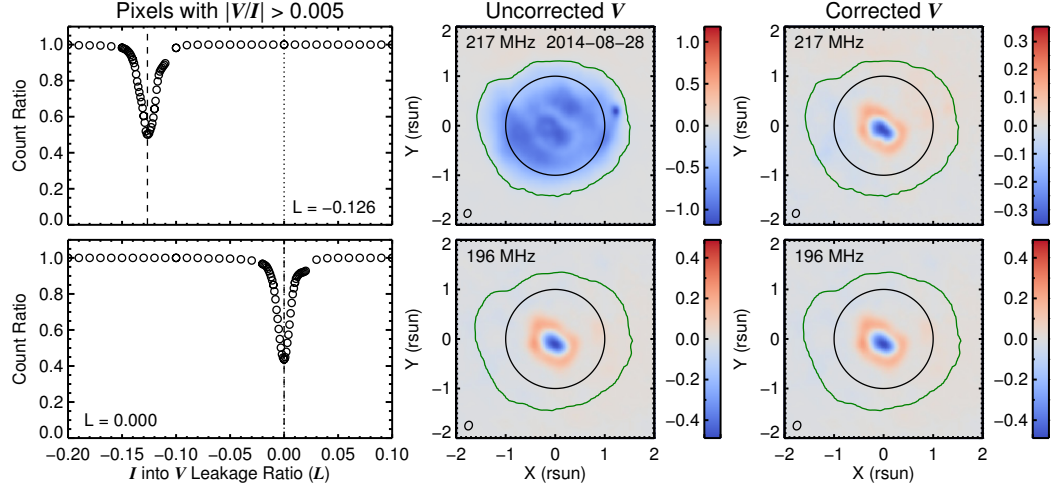


Figure 4.1: An illustration of the leakage subtraction algorithm. The left panels show the implementation of Equation 4.4 to find the L that minimizes the number of pixels with $|V/I| > 0.005$. At 217 MHz (top), we estimate that -12.5% of the Stokes I signal leaked into Stokes V , and at 196 MHz, the same procedure estimates there to be no leakage. The middle panels show the uncorrected Stokes V images, and the right panels show the corrected images (*i.e.* $V - L \cdot I$). The corrected image at 217 MHz is shown as a function of L in an animated version of this figure available in the [online material](#).

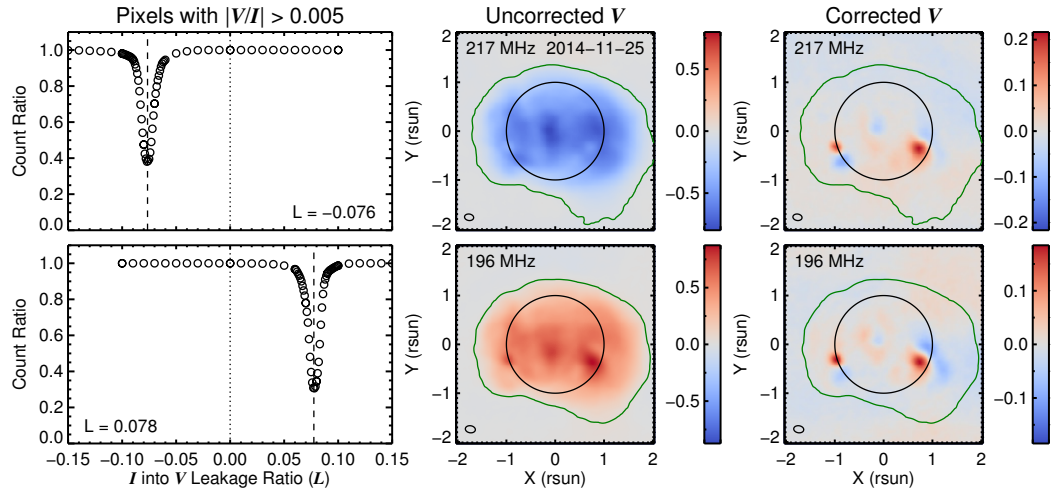


Figure 4.2: Same as Figure 4.1 but for a different observation with different structures and a different leakage behavior.

Ch. 4 Spectropolarimetric Imaging of the Corona

Figures 4.1 and 4.2 show the result of applying this algorithm to images from two frequency channels on two different days. In Figure 4.1, we see that the uncorrected Stokes V image at 217 MHz would imply that the entire corona is highly circularly polarized with a single sense, while the uncorrected 196 MHz image suggests a very different structure with a mixture of opposite signs. We know that entire corona at 217 MHz should not be polarized with a single sense to the extent implied by the uncorrected 217 MHz image. Our algorithm suggests that $L = -0.125$ in this case, and applying that correction recovers the same structure that is apparent in the 196 MHz image. Importantly, the same procedure can also be applied to observations for which there is little or no leakage, as is illustrated by the 196 MHz example in Figure 4.1. Figure 4.2 shows another example for which the two frequency channels shown are impacted by significant leakage of opposite signs, but once corrected, they exhibit very similar structures.

The examples in Figures 4.1 and 4.2 are cases for which the leakage is fairly severe. Figure 4.3 summarizes the leakage behavior across our dataset. 83% of the images exhibit leakage fractions less than or equal to 10%. $L \leq 0.05$ and 0.01 for 66% and 25% of the images, respectively. Figure 4.3d shows that the standard deviation of L is lowest at 179 MHz, which is consistent with the astrophysical MWA literature that indicates the leakage tends to be worst near the ends of the bandwidth. This summary includes 106 different sets of spectroscopic imaging observations for a total of 1144 images to which the algorithm could be applied. In Section 4.3, we stated that 111 observing periods were analyzed, which would imply 1332 images given our 12 frequency channels. Some images are rejected for polarimetry because they do not contain enough pixels detected above 5σ in Stokes I , generally because a nonthermal active region source is so intense as to elevate the noise floor above the level of the thermal disk. In other words, there is insufficient dynamic range to simultaneously detect both the thermal and nonthermal components present at those times.

These observations must be excluded because the algorithm relies on the statistical expectation that most pixels are dominated by thermal bremsstrahlung emission, and in these cases, there are not enough “thermal” pixels with sufficient signal-to-noise ratios for the algorithm to function. Images were rejected for polarimetry if they contained fewer pixels above 5σ in Stokes I than that enclosed by a circle of radius equal to the height of the plasma frequency layer at a given frequency given a $3\times$ Newkirk (1961) density model, which roughly approximates the height of the radio limb in our observations. Around 14% of

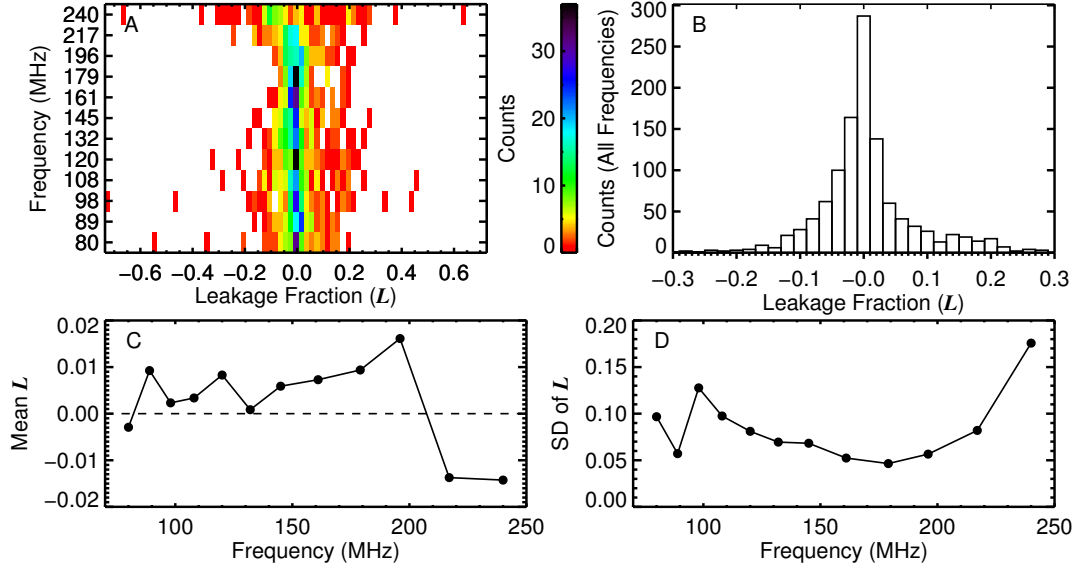


Figure 4.3: Summary of results from applying the Equation 4.4 algorithm to 1144 different observations. **(A)**: Two-dimensional histogram showing the leakage fraction [L] as a function of frequency with a bin size of 0.02 in L . **(B)**: Histogram of L across all frequencies. **(C)**: The average L for each frequency channel. **(D)**: The standard deviation of L for each frequency channel. Around 26% of observations have $|L| < 0.01$, and around 84% have $|L| < 0.1$. Panels A and D show that the leakage is most severe and variable at the extremes of the bandwidth.

our data failed this test and are excluded from further analysis. It is important to note that this introduces a bias in the next section on active region sources because the most intense sources tend to be the most highly polarized, but the leakage artefact cannot be constrained using our method for the brightest among them. The intense and highly-polarized population is therefore very likely to be underrepresented.

Leakage may also occur from Stokes U into V (Lenc et al., 2017), but this is not a concern here because linear polarizations from the corona are negligible at our frequencies and observing bandwidths (*e.g.* Gibson et al., 2016). Of potential concern, however, is possible leakage from V into I . This could add to or subtract from the Stokes I levels, decreasing the reliability of measured polarization fractions. Unlike leakage from Stokes I into the other parameters, the reverse case has not been investigated for the MWA because the polarization fractions of astrophysical sources are generally so low as to make this effect very difficult to characterize and unlikely to significantly impact the results. However, solar radio bursts may have large circular polarization fractions, meaning that Stokes V into I leakage could be a significant contaminant in some cases.

Ch. 4 Spectropolarimetric Imaging of the Corona

We currently have no way to assess or mitigate this contamination, but we anticipate that the effect should occur at a similar or lower level than leakage from Stokes I into V , as the mechanism would be similar but with generally lower magnitudes.

Of concern are sources with high polarization fractions and large leakage fractions. This is relevant mainly for the next section, which focuses on non-thermal active region sources. Assuming that V into I leakage may occur at up to the same level estimated for I into V , this introduces an uncertainty in V/I of less than 1% for 79% of the sources and an uncertainty of less than 5% for 95% of the sample described by Figure 4.5. The remainder have uncertainties of 10% on average, and up to 19% for one event, due to this effect. We have chosen to represent this latter population with a different symbol in Figure 4.5 to indicate that their polarization fractions should be treated with additional skepticism. For Figure 4.11 in Section 4.6, we estimate uncertainties on V/I of $\lesssim 3\%$ by combining several effects for two cases where different observations on the same day with different values of L could be compared. These observations correspond to thermal or very weak nonthermal emission for which the polarization fractions are lower than 5%. Potential V into I leakage is therefore not a significant concern in that case and constitutes an average of 14% of the total error bars in Figure 4.11.

4.5 Active Region Noise Storm Sources

The most common features in these images are compact polarized sources, the most intense of which are identified here as noise storm continua associated with Type I bursts. This is apparent from the variability in their associated dynamic spectra along with their high polarization fractions. However, as we will see, there are also very weak and weakly-polarized sources for which the source type and emission mechanism is less obvious.

Noise storms are periods of extended burstiness that are associated with active regions and may persist for several days as an active region transits the disk. They are characterized by many distinct, narrowband Type I bursts, often with enhanced continuum emission around the same frequency range (Elgarøy, 1977; Klein, 1998). As our data reflect the background levels during each observation period, our detections correspond to the continuum enhancement, along with any burst periods that could not be filtered out by our baseline procedure because they occurred on timescales less than the 0.5-sec time resolution. Despite decades of study, there are a number of unanswered questions about the

nature of Type I bursts. Not all active regions that are productive at other wavelengths produce noise storms, and the non-radio signatures are often scant (Willson, 2005; Iwai et al., 2012; Li et al., 2017), unlike Type II and III bursts, which have obvious associations with CMEs and flares (Cairns et al., 2003; Reid and Ratcliffe, 2014). There is general agreement that both the burst and continuum components of noise storms are produced by plasma emission, largely due to their often high circular polarizations (Aschwanden, 1986; Mugundhan et al., 2018), but what accelerates the electrons is still debated. Small-scale reconnection events (Benz and Wentzel, 1981) or weak shocks associated with upward-propagating waves (Spicer et al., 1982) are the two leading ideas, and recent work has favored persistent interchange reconnection between open and closed fields at the boundaries of active regions (Del Zanna et al., 2011; Mandrini et al., 2015) or reconnection driven by moving magnetic features (Bentley et al., 2000; Li et al., 2017).

To automatically detect these features in the Stokes V images, we developed a simple algorithm that begins with suppressing any diffuse polarized emission that may be present by applying a Butterworth bandpass filter to the fast Fourier transform (FFT) of each image. The filter aims to flatten the frequency response over a particular passband, in this case the FFT frequencies corresponding to larger spatial scales, without producing sharp discontinuities between the filtered and unfiltered frequencies (Butterworth, 1930). The filtered FFT is transformed back, and the resulting image is thresholded into two binary masks, one for each polarization sense, that include pixels with values above the larger of 10σ or 20% of the maximum value. Ellipses are fit to all of the contiguous regions in the masks, and several criteria are imposed to obtain the final detections. These criteria include ensuring that 1) the signal-to-noise ratio of pixels pulled from the filtered image are above 10σ in the original image and are of the same polarization sense, 2) the areas of the fitted ellipses are within $0.75 - 1.5\times$ that of the corresponding synthesized beam for a given frequency, 3) the fitted ellipses have aspect ratios no more than $1.1\times$ that of the synthesized beams, and 4) the masked regions are sufficiently elliptical, which we defined as filling at least 95% of the fitted ellipse.

These criteria all serve to eliminate false positives that arise from the band-pass filtering, which may amplify noise, introduce artefacts near very bright sources, and/or not entirely suppress the large-scale diffuse emission. Adjusting the tolerance parameters of this algorithm can satisfactorily extract sources from any given image, but finding a set of defaults that could serve the entire dataset was somewhat difficult. We opted to aggressively tune the parame-

Ch. 4 Spectropolarimetric Imaging of the Corona

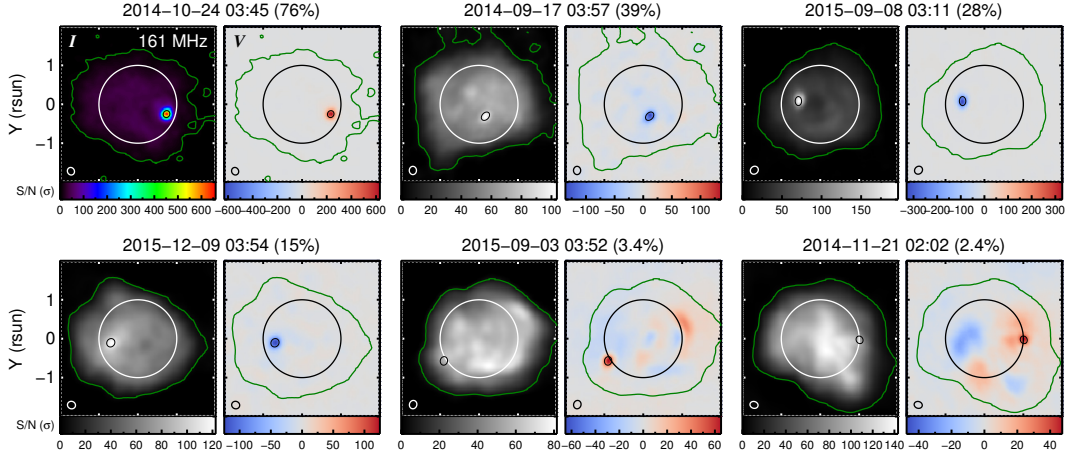


Figure 4.4: Six randomly chosen examples of compact polarized sources detected at 161 MHz, sorted by polarization fraction. The titles correspond to UTC times followed by the peak polarization fraction in parentheses. The color scales are linear, and the first example is plotted with a different color scheme to better reflect the dynamic range of that observation. Color bar intensities are expressed in units of signal-to-noise [σ], and the green contour reflects the $5\text{-}\sigma$ level in Stokes I . Black ellipses around the sources show the region identified by the source finder algorithm. The large solid circles represent the optical disk, and the ellipses in the lower-left corners represent the synthesized beam sizes.

ters to eliminate false positives at the cost of excluding false negatives. This procedure is run independently for all of the frequency channels in a given observation. The detections are then grouped across frequencies by checking for overlap among the fitted ellipses. Only sources that are detected in at least three frequency channels are kept and incorporated into the following plots. We find 693 sources with this method from 112 separate regions, and at least one source is found on 64 out of 82 days (78%). Solar Cycle 24 peaked in April 2014, and our data correspond to between August 2014 and December 2015, meaning that we are examining the early part of the declining phase in the solar cycle. As these features are associated with active regions, we would likely have found a higher fraction of days with at least one noise storm if our observations were shifted one year earlier and a lower fraction if the observations were taken in subsequent years.

Figure 4.4 shows six randomly-selected examples of these sources at the center of our bandwidth, 161 MHz. They exhibit polarization fractions ranging from 2.4 to 76% and well represent the range of sources found. Most sources in the full sample are unipolar and are fairly isolated in the polarization images, and those with very low polarization fractions are sometimes embedded in diffuse emission of the same sign. A small number of bipolar sources were also

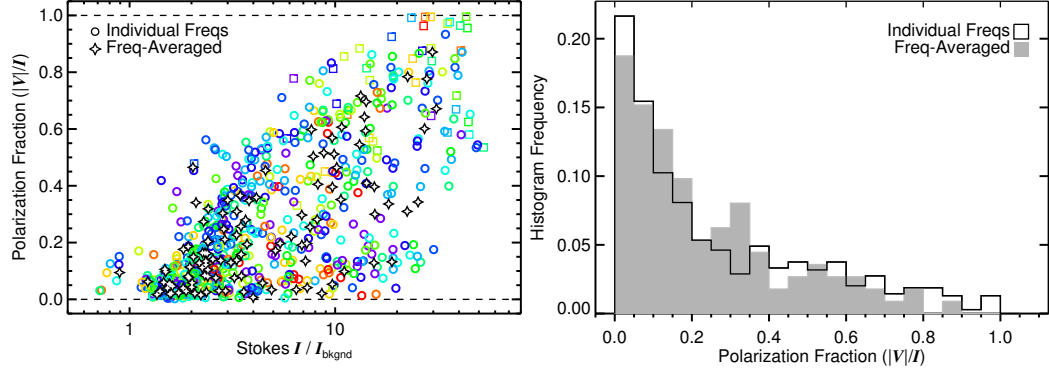


Figure 4.5: *Left*: Scatterplot of polarization fraction $[|V|/I]$ versus Stokes I intensity for 693 compact polarized sources. Values are measured at the location of peak Stokes V intensity, and the Stokes I intensities are normalized by the median intensity of pixels detected above $5\text{-}\sigma$ $[I_{\text{bgnd}}]$. Colored circles represent measurements from individual frequency channels; purple refers to the highest frequency (240 MHz) and red refers to the lowest (80 MHz). All sources are detected in at least three channels, representing 112 separate regions, and the stars represent averages across frequency for a given region. Squares indicate the 5% of sources for which the V/I uncertainty is large ($\approx 10\%$) due to possible calibration errors that could not be accounted for (see Section 4.4). *Right*: Histogram of $|V|/I$, where the white region corresponds to the colored circles and the shaded region corresponds to the stars from the left panel.

found. This is somewhat inconsistent with White et al. (1992), who found that bipolar sources were nearly as common as unipolar sources in 327 MHz Very Large Array (VLA) observations. Bipolar sources are presumably less common in our observations because we are looking at lower frequencies for which the emission is generated at a larger height and the spatial resolution is lower. Preliminary analysis has revealed interesting potential anti-correlations in the intensities of the two components of one bipolar source, and this sort of time variability may be explored in future work.

Figure 4.5 shows a scatterplot of polarization fraction $[|V|/I]$ versus the total intensity divided by the background level $[I/I_{\text{bgnd}}]$ in the left panel, along with a simple histogram of $|V|/I$ in the right panel. These are plotted both for each frequency channel independently and for averages of the same source detected in multiple channels. The background is defined as the median intensity in pixels detected above 5σ , and the noise level $[\sigma]$ is defined as the standard deviation within a 1-pixel border (1156 pixels) that run along the edge of the 289×289 -pixel ($\pm 3 R_{\odot}$) field-of-view. We find a very broad range of source intensities, ranging from slightly below the background level to 50 times greater, with polarization fractions ranging from a few tenths of a percent to nearly 100%. The average source has a Stokes I intensity of $7.6\times$ the

Ch. 4 Spectropolarimetric Imaging of the Corona

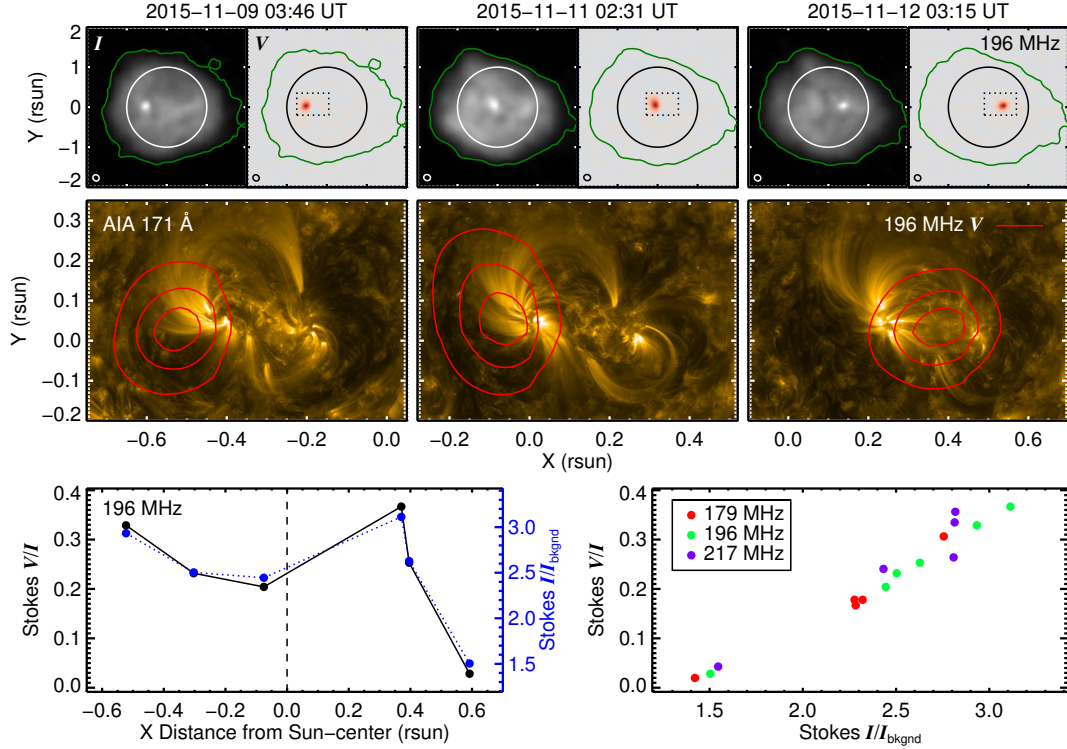


Figure 4.6: *Top*: The same compact source observed on consecutive days at 196 MHz. *Middle*: Overlays of the 196 MHz circular polarization signal onto 171 Å images from AIA. The field-of-view is marked by the dotted region in the top row, and the contours are at 20, 50, and 80% of peak intensity. *Bottom*: The left panel plots polarization fraction $[V/I]$ and Stokes I/I_{bgnd} as a function of horizontal distance from Sun-center at 196 MHz for the same source over five days from 9 to 13 November 2015. The right panel plots the same two parameters against each other for three different frequency channels.

background level and a polarization fraction of 27%. The most striking aspect of Figure 4.5 is the relationship between total intensity over the background and polarization fraction, which are positively correlated with a Pearson correlation coefficient $[r]$ of 0.64.

Figure 4.6 displays results from one of the few sources in our sample for which we have observations on several consecutive days and for which a compact radio source appears in association with the same active region on each day. The source is polarized between 3% and 37% in the same sense in six observations between 9 and 13 November 2015. Our goal here is to investigate a potential relationship between distance from Sun-center and polarization fraction, as previous studies have found noise storms to exhibit higher polarization fractions near disk center. We do not find such a relationship in Figure 4.6, and instead this exercise further reinforces the positive correlation between to-

tal intensity and polarization fraction, which apparently becomes stronger if one considers several observations of the same source. Recall from Section 4.3 that the observations presented in this paper all represent the baseline intensity over 5-min observing periods, constructed from the averages of images with the lowest total intensities. These sources do fluctuate in intensity, so it may be possible to control for the intensity relative to the background and then recheck if the polarization fraction has a longitudinal dependence in a future study, ideally with more observations of individual sources detected on consecutive days.

Figure 4.6 also overlays circular polarization contours onto 171 Å images from the *Atmospheric Imaging Assembly* (AIA; Lemen et al., 2012) onboard the *Solar Dynamics Observatory* (SDO; Pesnell et al., 2012). The radio source is associated with a large active region (AR 12448) and is located over fan-loop structures that represent the bases of loops extending to larger heights. This make sense, as the accelerated electrons that are presumably responsible for this radiation must be able to escape to sufficiently large heights, corresponding to densities that are sufficiently low for low-frequency emission. It is also interesting to note that when the source is east of disk-center, the radio source is associated with the trailing sunspot. Noise storms have long been associated with active regions (*e.g.* Le Squeren, 1963; Gergely and Erickson, 1975; Alissandrakis et al., 1985), and previous observations have found noise storm sources to be more often associated with the leading spot (White et al., 1992). A natural followup would be to investigate that aspect systematically for the sources detected here. The site of radio emission within the active region also shifts somewhat in time, with the apparent Carrington longitude jumping by 12 degrees between 11 and 12 November 2015. This is likely due to evolution in the active region shifting the region where the energetic electrons either originate or are able to reach in height.

The main question posed by these results, particularly the scatterplot in Figure 4.5, is whether or not these sources all represent the same basic phenomenon. Our average polarization fraction (27%) is lower than previous measurements of noise storm continua. Most studies report similar polarization levels for the Type I burst and continuum components of noise storms, which generally exceed 80% (Elgarøy, 1977), but sources with lower polarization fractions have also been reported. Dulk et al. (1984) observed noise storm continua with polarization fractions of $\approx 40\%$, around 15–20% lower than the associated bursts. As discussed in Section 4.4, the most intense and likely highly-polarized sources in our dataset could not be included because the leakage mitigation al-

Ch. 4 Spectropolarimetric Imaging of the Corona

gorithm could not be applied. This diminishes the overall average, but more importantly, our sample includes a large number of weak and weakly-polarized sources that could not have been characterized by previous instruments. For example, the 3 September 2015 source ($V/I = 3.4\%$) shown in Figure 4.4 is prominent in the polarization map but is visually indistinguishable from the quiet Sun in total intensity. Given that there does not appear to be any separation into distinct populations in Figure 4.5, we suggest that the data represent a continuum of plasma emission noise storm continua sources with intensities and polarization fractions down to levels that were not previously detectable.

For sources with relatively low total intensities (*e.g.* $I/I_{\text{bgnd}} \lesssim 5$; 61% of the population), where the nonthermal component is not entirely dominant, very low polarization fractions can be explained by there being a mixture of thermal and nonthermal emission within the same resolution element. Recall from Section 4.2 that the thermal bremsstrahlung and nonthermal plasma emission mechanisms generally produce opposite polarization signs for the same magnetic field orientation, but the plasma emission component is much more highly polarized. Therefore, a pixel may be dominated in total intensity by bremsstrahlung emission while the polarized intensity is dominated by plasma emission. The polarization fraction then rises with intensity relative to the background because the relative contribution from plasma emission increases.

Filling factors and beam dilution are also likely to be important, as the thermal component is likely to fill the resolution element while the nonthermal component may come from a sub-resolution structure. This would mean that the more highly-polarized nonthermal signal is diluted, which would further bring down the polarization fraction. Nonthermal emission sources may not necessarily be intrinsically smaller than the beam size, however. For instance, Mohan et al. (2019a) found the scattering-deconvolved sizes of type III burst sources to be significantly larger than the PSF. As the total intensity becomes much larger than the background and the nonthermal component becomes entirely dominant, physical effects related to the emission mechanism and radio wave propagation become increasingly important to the interpretation of relatively low polarization fractions in plasma emission sources. As described in Section 4.2, scattering by density inhomogeneities may reduce the polarization fraction, as can other propagation effects such as mode coupling. These ideas are discussed further in Section 4.8 in the context of our other results.

4.6 Coronal Holes

Perhaps the most surprising finding to immediately emerge from these data is a characteristic “bullseye” structure that is frequently exhibited by low-latitude coronal holes and, more generally, that coronal holes are the Sun’s most prominent features in circular polarization at low frequencies in the absence of intense noise storm emission. Coronal holes are regions where the magnetic field is open, allowing material to freely flow into interplanetary space to form the fast solar wind (Cranmer, 2009). Because the plasma is not confined by closed fields, the densities inside coronal holes are considerably lower than in the surrounding corona, and they are correspondingly fainter in the soft X-ray and extreme ultraviolet (EUV) observations that are typically used to characterize them. This is also true at our highest frequencies, which can be seen for two different coronal holes in the Stokes I images shown in the upper row of Figure 4.7.

As frequency decreases across our bandwidth, many coronal holes transition from being relatively dark to relatively bright with respect to their surroundings. This effect had been known from a few previous observations (Dulk and Sheridan, 1974; Lantos et al., 1987; Lantos, 1999; McCauley et al., 2017) and was recently characterized in more detail using MWA observations (Rahman et al., 2019). The mechanism that produces this increase in brightness is unclear, but different authors have suggested that refraction near the coronal hole boundary may systematically redirect emission generated outside of the coronal hole to the interior from an observer’s perspective (Lantos et al., 1987; Alissandrakis and Chiuderi-Drago, 1994; Rahman et al., 2019). As discussed by Rahman et al. (2019), this leads to a ring of enhanced emission around the coronal hole edge, which is apparent in our higher-frequency images but cannot be distinguished at the lower frequencies, likely due to the lower spatial resolution. A corollary of this effect is a ring of diminished intensity in the regions from which the refracted emission originated, which we see prominently in the low-frequency images at the bottom of Figure 4.7.

The second and third columns of Figure 4.7 show the corresponding Stokes V and V/I images, respectively. Both coronal holes in Figure 4.7 exhibit a central polarized component of one sense surrounded by a ring of the opposite sense. The outer ring grows in area as the frequency decreases, while the central component shrinks until it may or may not be completely gone by 80 MHz. This bullseye structure is peculiar in that coronal holes have unipolar line-of-sight (LOS) magnetic field configurations that we expected to result in unipolar

Ch. 4 Spectropolarimetric Imaging of the Corona

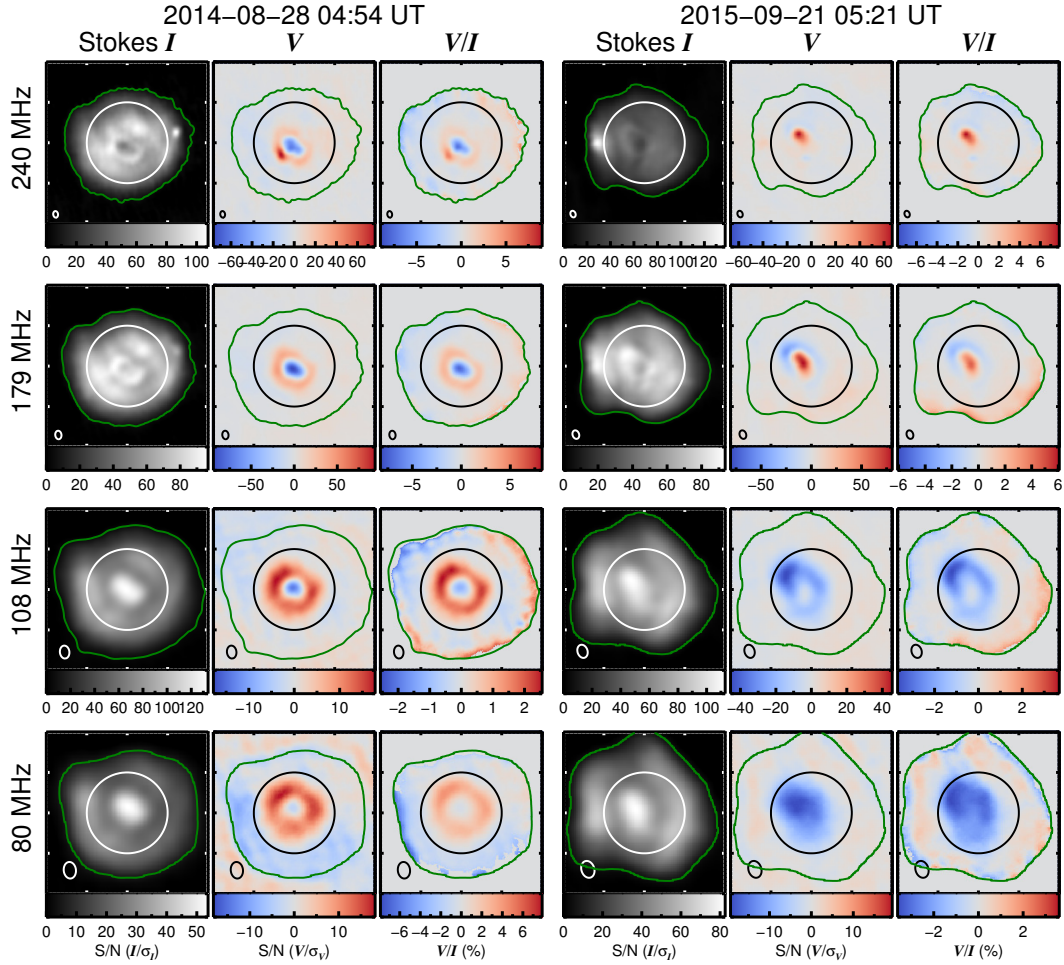


Figure 4.7: Stokes I , V , and V/I at four frequencies across our bandwidth for two different coronal holes with opposite polarization signatures. Color bar units are in signal-to-noise [S/N] for I and V and percent for polarization fraction $[V/I]$. The green contours represent the 5σ level in Stokes I , the solid circles represent the optical disk, and the ellipses in the lower-left corners represent the synthesized beam sizes.

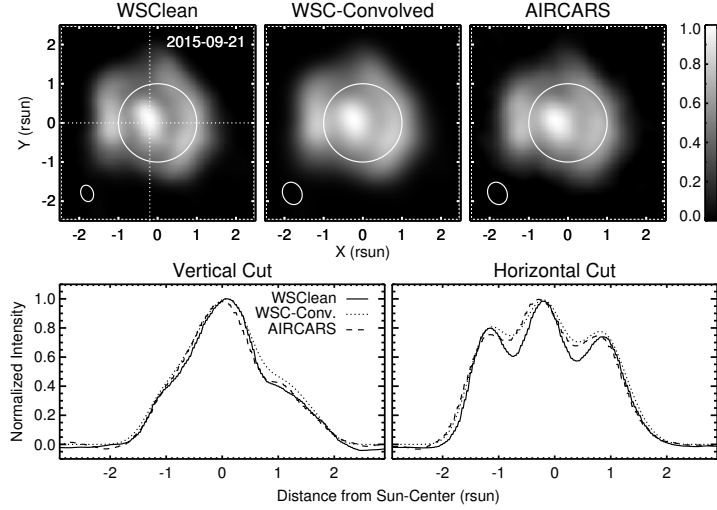


Figure 4.8: A comparison of the same dataset independently reduced with different calibration techniques and different implementations of the CLEAN algorithm. The Stokes I image at 80 MHz is shown for the 21 September 2015 coronal hole from Figure 4.7. Our reduction on the left, the AIRCARS reduction on the right, and the WSClean image convolved with the AIRCARS beam is in the middle. Dotted lines in the left panel indicate the cuts shown in lower two panels. The convolved WSClean and AIRCARS images appear nearly identical, and the cuts demonstrate that this is also true quantitatively.

Stokes V maps across our entire observing band. We therefore first consider if the feature might be an instrumental or calibration artefact. While we cannot validate this signature with a completely independent observation and data reduction procedure, we have strong evidence to believe that this structure is real for the reasons outlined below.

First, we can validate the structure seen in Stokes I with an independent reduction. Figure 4.8 compares our 80 MHz image of the 21 September 2015 coronal hole, which was produced using WSClean, to an image produced using the AIRCARS pipeline (Mondal et al., 2019). AIRCARS uses an entirely different calibration scheme through iterative self-calibration on the Sun itself without the need to observe a separate calibrator source. This approach is advantageous in that the calibration is tuned to the specific observation of interest, which may greatly improve the dynamic range, but it cannot yet be used for polarimetry. Our method determines the calibration solutions solely from a known calibrator source, generally observed before or after an observing campaign of several hours. Figure 4.8 shows that we obtain nearly identical results from the two pipelines. Both methods do use the CLEAN algorithm for deconvolution, as is the standard, although implemented through different software packages.

Ch. 4 Spectropolarimetric Imaging of the Corona

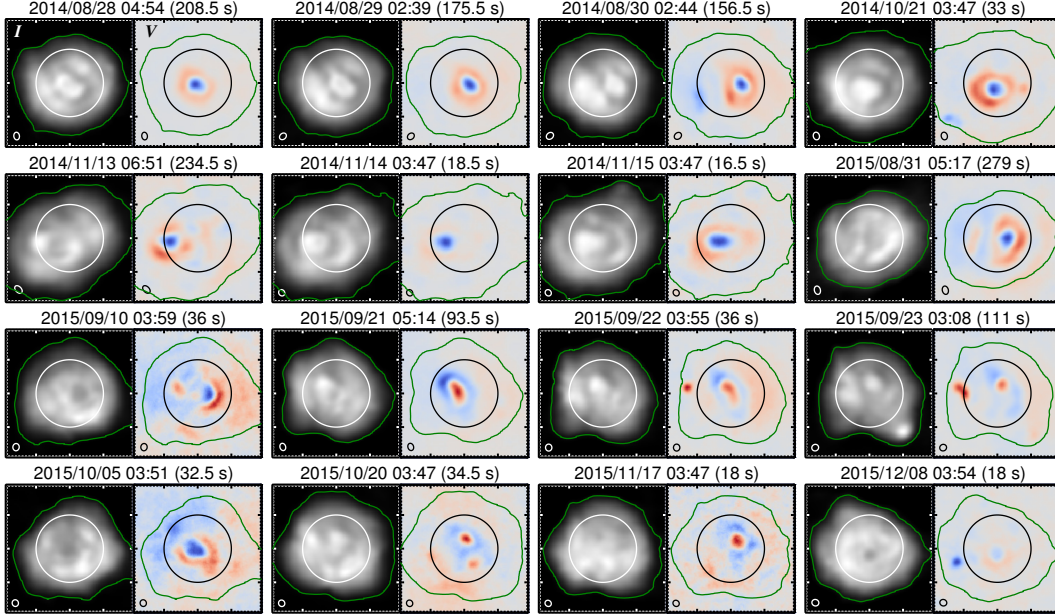


Figure 4.9: Mosaic of coronal hole observations at 161 MHz, with Stokes I on the left and Stokes V on the right. The green contours show the $5\text{-}\sigma$ levels for Stokes I , the solid circles denote the optical limb, and ellipses in the lower-left corners reflect the synthesized beam sizes. The titles correspond to UTC times followed by the effective integration times in parentheses. Linear color scales are as in Figure 4.7, with red, blue, and gray corresponding to positive, negative, and zero Stokes V intensity, respectively. Images for all 12 frequency channels can be seen in an animated version of this figure available in the [online material](#). Note that some dates do not have observations at all frequency channels because of calibration failures, and two observation periods exhibit bright nonthermal sources at higher frequencies that prevent the coronal hole structure from being visible due to limited dynamic range.

However, we can be confident that we are not seeing an artefact of the CLEAN algorithm because the features of interest are also present in the undeconvolved “dirty images”.

We are also confident that the Stokes I into V leakage subtraction method has not introduced this feature. As described in Section 4.4, the leakage fraction (L) is assumed to be constant across the relatively small spatial scale of the Sun based on results from widefield astronomical studies (Lenc et al., 2017). Because L is constant, varying it changes the fractional polarization level without changing the qualitative structure. Figure 4.1 illustrates how the subtraction algorithm works for one of the same coronal hole observations shown in Figure 4.7, and the animated version of Figure 4.1 (available [online](#)) shows how the “corrected” images look as a function of L . The animation shows that the polarization reversal bullseye pattern remains for all values of L until reaching

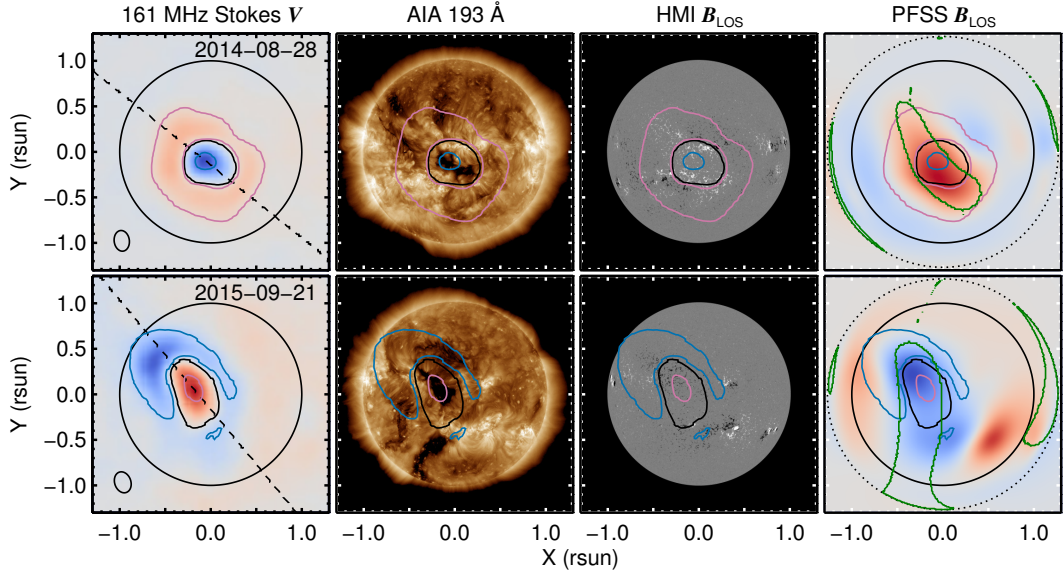


Figure 4.10: The first column shows Stokes V at 161 MHz for the two coronal holes from Figure 4.7. The solid black circle represents the optical disk, the black contour is where $V = 0$ in that region, the blue contour is at 75% of the central components’ maxima, and the pink contour is at 25% of the ring components’ maxima. The dashed lines denote the slits used in Figure 4.11. The second and third columns plot AIA 193 Å and HMI line-of-sight $[B_{\text{LOS}}]$ magnetograms with the V contours from the first column. The last column shows the B_{LOS} component of the PFSS model at a height roughly corresponding to that of the radio limb ($1.27 R_{\odot}$). Red, blue, and gray colors represent positive, negative, and zero B_{LOS} , respectively, and green contours represent open field regions in the model at that height.

the extremes, where 80–100% of pixels across the Sun are too highly polarized of the same sense to be believable. Further, varying L by just 1–2% on either side of the value obtained from the correction algorithm quickly pushes into this extreme case. And even at the extremes, the qualitative ring pattern remains as a sharp change in polarization fraction instead of a reversal.

Next, this polarization ring structure is not rare and seems to be characteristic of low-latitude coronal holes across our dataset. We have 28 separate observations of 13 different coronal holes in 2014 and 2015 that exhibit this effect. A mosaic of examples is shown in Figure 4.9 at 161 MHz, the center of our observing band, and the other channels can be seen in the corresponding animation. Several coronal holes in the mosaic are shown on consecutive days, and they move with the solar rotation as expected. This structure is not observed in association with other solar features, despite noise storms often having similar appearances in total intensity at the lowest frequencies. Therefore, from both a data reduction perspective and with respect to its association with

Ch. 4 Spectropolarimetric Imaging of the Corona

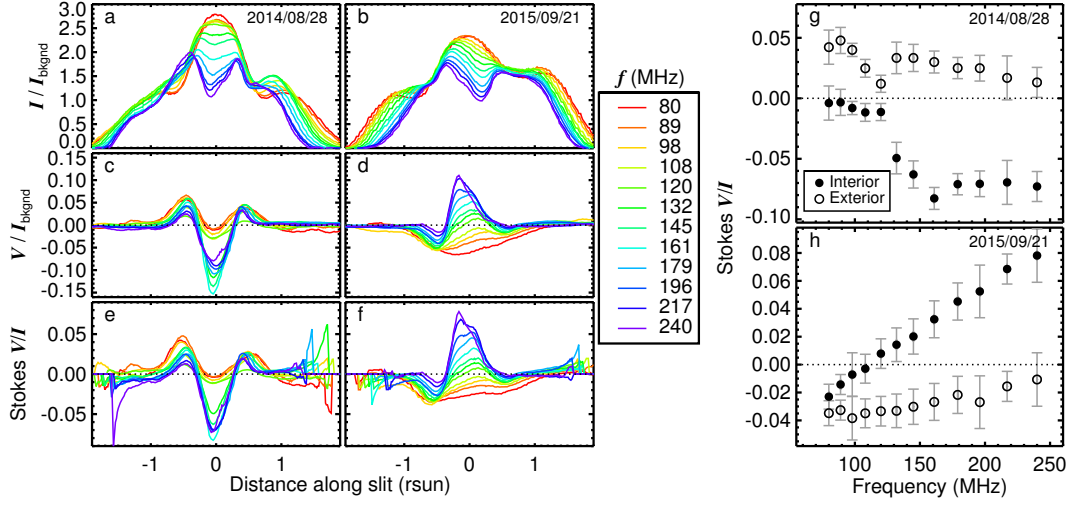


Figure 4.11: **(a–b)**: Stokes I intensity for each frequency channel along the slits shown in Figure 4.10 through two coronal holes on 28 August 2014 (left) and 21 September 2015 (right). **(c–d)**: Stokes V intensities along the same slits. Panels a–d are shown in normalized units, where the normalization factor corresponds to the median Stokes I intensity of pixels detected above 5σ (*i.e.* the background level). **(e–f)**: The corresponding Stokes V/I fractional polarization levels. **(g–h)**: Peak Stokes V/I for the coronal holes’ interior (filled circles) and exterior ring (open circles) components as a function of frequency.

solar features, the bullseye feature does not appear to be consistent with an instrumental effect. Moreover, while this feature is a surprise to us, we do find various points of consistency between the observations and our expectations that will be discussed later.

Figure 4.10 overlays contours of the 161 MHz polarimetric signal from the two coronal holes shown in Figure 4.7 onto 193 Å images from the AIA and LOS magnetograms from the *Helioseismic and Magnetic Imager* (HMI; Scherrer et al., 2012) onboard the SDO. These two coronal holes were chosen for this exercise because they have opposite polarization signatures, which is consistent with them having opposite magnetic field configurations at the photosphere, and because we have two observations of each on the same day, which we will use to estimate the uncertainty in V/I . The last column of Figure 4.10 overlays the polarization contours onto the LOS component [B_{LOS}] of a potential field source surface (PFSS; Schrijver and De Rosa, 2003) model at a height roughly corresponding to that of the radio limb. The models were obtained from the PFSS module in SolarSoft IDL and manipulated using the **FORWARD** codes. A height of $1.27 R_{\odot}$ is used, which corresponds to the height of the plasma frequency layer at 161 MHz in a $3\times$ Newkirk (1961) density model.

Crucially, the central polarized components do not match the orientation of

B_{LOS} , as would be expected from the thermal bremsstrahlung process that is assumed to be the dominant, if not sole, emission mechanism in coronal holes. This effect is further characterized in Figure 4.11, which plots cuts through the same two coronal holes in Stokes I , V , and V/I . The I and V cuts are normalized by the background intensity in Stokes I , which we define as the median pixel intensity for pixels detected above 5σ . The gradual transition with decreasing frequency of both coronal holes from being dark to bright relative to the background is nicely illustrated by the Stokes I curves for both examples, as is the oppositely-oriented ring structure in Stokes V . Note that the large spikes in V/I near the ends of the slits are in locations where both the total intensity and polarized signals approach the noise level, making the fractional polarizations unreliable.

While the overall pattern is similar for both coronal holes, the behavior of the central component is somewhat different in each case. The rightmost panels (g and h) of Figure 4.11 show the peak V/I for the central and ring components. The central component is most highly polarized ($\approx 5\text{--}8\%$) at our highest frequency (240 MHz) and gradually decreases in polarization fraction with decreasing frequency. For the 28 August 2014 example, the central component falls to nearly 0% polarization at 80 MHz but remains of the same sign at all frequencies, whereas the 21 September 2015 examples crosses 0% around 108 MHz and gradually approaches the same polarization level as the ring component. The latter scenario is somewhat more common in our experience. That is, by 80 MHz, the entire source is typically polarized in the same sense expected by bremsstrahlung emission and at a similar level, often with a small dip in polarization fraction at the center where the source is oppositely-polarized at higher frequencies.

The uncertainties in panels g and h of Figure 4.11 are the combination of measurement noise and three effects related to the leakage subtraction algorithm described in Section 4.4. The first is the range of values found by varying the minimization parameter $r_{\text{c,thresh}}$ in Equation 4.3 between 0.3 and 0.8%, along with varying the pixels included in the operation between those detected above 5σ and those detected above 15σ . The second is the difference in polarization fraction at the same locations in two observations separated by 2–3 hours, and the third is the potential for unaccounted for leakage of Stokes V into I at up to the same level as that measured for I into V . These combined uncertainties in V/I average $\pm 1.2\%$ and are as large as $\pm 2.9\%$. In both cases, the sign of the leakage fraction flips for each frequency channel between the two observations as the Sun moves to different locations in the primary beam

with respect to the phase center. (The MWA does not continuously track an object and instead has a set of discrete pointings that may be changed after every ≈ 5 -min observing period.)

Despite the sign change in the leakage artefact between observations separated by 2–3 hours, after implementing the subtraction algorithm, the polarization fraction remains consistent to within 1% for a given location and frequency channel. However, a sharp discontinuity remains between the 120 and 132 MHz channels in the 28 August 2014 observation. The leakage is more severe in this observation as compared to the 21 September 2015 data, and the sign of the leakage also changes between those two channels. The discontinuity in the polarization fraction trend shown in Figure 4.11g is therefore likely to be a calibration artefact that cannot be removed by uniformly implementing our correction algorithm. This suggests an additional source of uncertainty in the polarization fraction that is not accounted for by the methods described in the previous paragraph. However, note that leakage affects the polarization level uniformly across the image and cannot warp the qualitative structure observed because the leakage does not vary on the small angular scale of the Sun, given what we know from widefield astrophysical observations.

The puzzle with respect to this feature is again the fact that the polarization of the central component does not match the sign expected from thermal bremsstrahlung emission. We will discuss possible interpretations for this in Section 4.8.

4.7 The Large-Scale Quiescent Structure

As mentioned in Section 4.2, the thermal bremsstrahlung process that dominates quiescent coronal emission at low frequencies produces a slight circular polarization signature in a magnetized plasma that depends primarily on the line-of-sight magnetic field strength. Absent of other emission mechanisms, a positive LOS field should produce a positive Stokes V signature of up to a few percent that depends on the field strength.

Figure 4.12 shows Stokes I , V , and V/I images on four different days for which the polarimetric signature is not dominated by a bright noise storm source or disk-center coronal hole. These days were also selected to have a mixture of positive and negative Stokes V regions so that we can compare the structure to that of the LOS field. The fourth column of Figure 4.12 shows the LOS magnetic field direction and strength in the corresponding PFSS model. The dotted circle indicates the height at which the model LOS field is

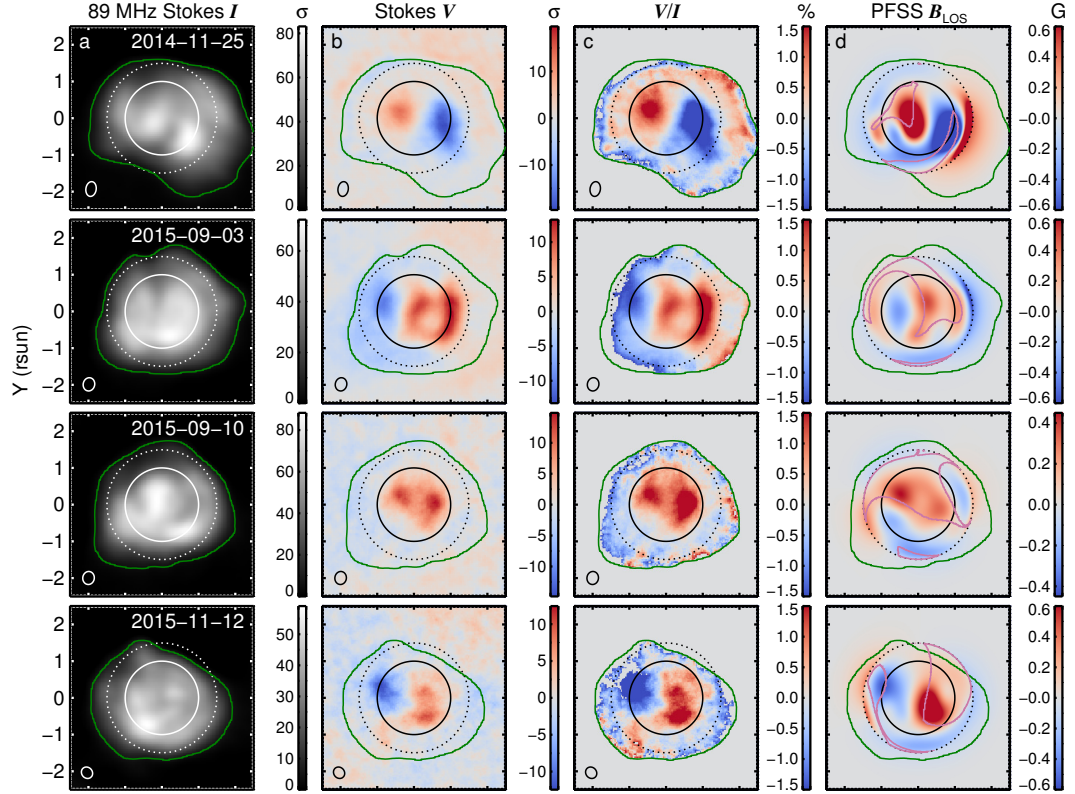


Figure 4.12: Columns **a**–**c** show Stokes I , V , and V/I images at 89 MHz on four different days for which a single compact region does not dominate the total intensity. The solid circles denote the optical limb, and the green contours show the 5σ level for Stokes I . Ellipses in the lower-left corners reflect the synthesized beams. Column **d** shows the line-of-sight magnetic field strength [B_{LOS}] in the PFSS model at a height of $1.49 R_{\odot}$, which roughly corresponds to the height of the radio limb at 89 MHz and is indicated by the dotted circles in each panel. The pink contours indicate open field regions in the model. Color bar units are in signal-to-noise [σ] for Stokes I and V , percent for V/I , and Gauss [G] for the field model. An animated version of this figure that shows all 12 frequency channels is available in the [online material](#).

Ch. 4 Spectropolarimetric Imaging of the Corona

shown, which is chosen to be roughly that of the radio limb, and the plane-of-sky field is shown beyond the dotted circle. This height is $1.49 R_{\odot}$ at 89 MHz and corresponds to the height of the plasma frequency layer in a 3-fold Newkirk (1961) density model. Pink contours indicate the open-field regions in the model at the same height, which were determined using the “topology” keyword in the **FORWARD** code. It is immediately apparent that the Stokes I and V maps show very different morphologies in general. Regions with the highest polarized intensities are often not straightforwardly correlated with those of highest total intensity. It is also interesting to note that larger polarized intensities are often associated with open field regions, which is also consistent with the coronal hole observations from the previous section. While we have not investigated this effect systematically, it may be due to there being lower densities and lower density contrasts between adjacent regions in open field regions, which then reduces the depolarizing effect of scattering by density inhomogeneities.

Figure 4.12 demonstrates that the Stokes V structure at our lowest frequencies is generally well-matched to the LOS field, at least near disk center, and that the sign of Stokes V is broadly consistent with that expected from thermal bremsstrahlung emission given the LOS field orientation. The boundaries between opposite polarization signs are roughly aligned with polarity inversion lines in the model. The agreement tends to diminish with distance from disk center, which is likely due to two effects. First, low-frequency radio emission is heavily influenced by propagation effects, namely refraction, scattering, and mode coupling, that can influence the polarization sign and fraction, and these effects become more pronounced near the limb (Shibasaki et al., 2011). Second, although the polarization fraction is expected to be highest off the limb (Sastri, 2009), the intensity is much lower there. The third column of Figure 4.12 shows that we often do find relatively high polarization fractions toward the radio limb, but these pixels are very close to the noise level in Stokes V and we do not regard them as reliable. Missing pixels in the Stokes V/I images inside the green 5σ Stokes I contour are censored because they have polarization fractions greater than 1.5% but Stokes V signals below 5σ .

Figure 4.13 shows the same parameters as Figure 4.12 but at 196 MHz. The same observation periods are used in the first three rows, but the fourth row is different because the 12 November 2015 observation becomes dominated by a noise storm source at higher frequencies. First, we note that the polarized quiet Sun emission is more localized at 196 MHz compared to 89 MHz, which is likely the combination of at least three effects. First, the spatial resolution is simply

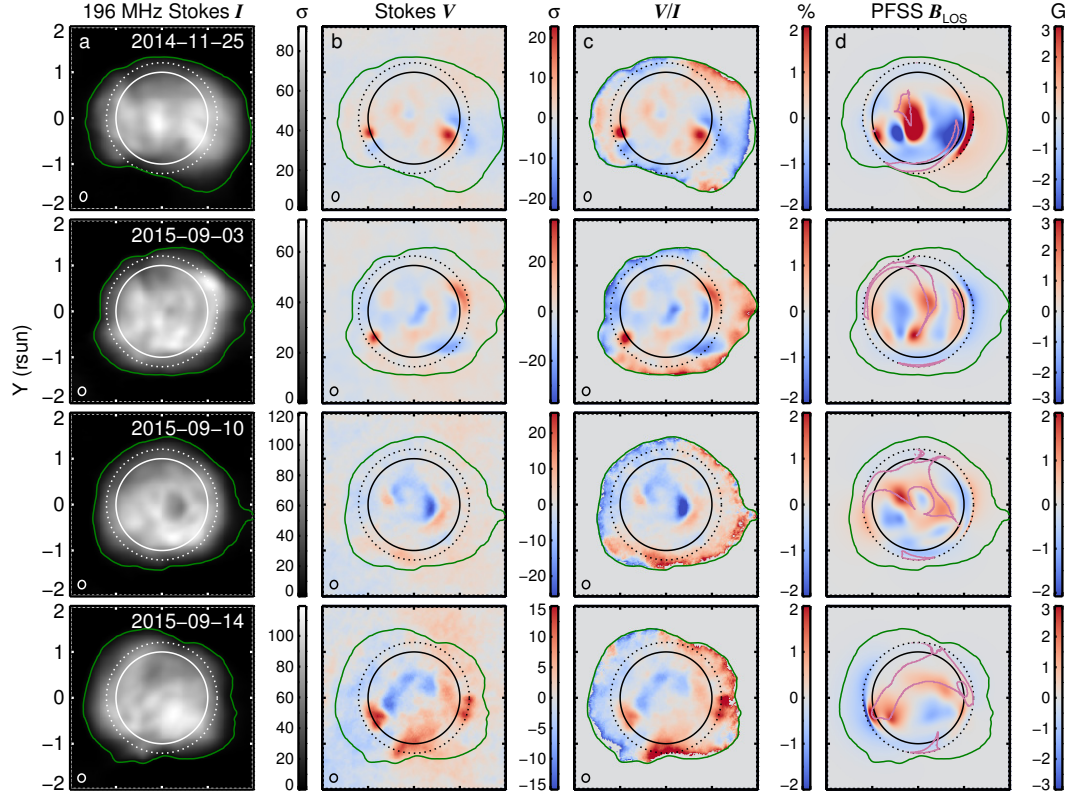


Figure 4.13: Columns **a** – **c** show Stokes I , V , and V/I images at 196 MHz on four different days for which a single compact region does not dominate the total intensity. The days are the same as Figure 4.12 except for the last row. The solid circles denote the optical limb, and the green contours show the 5σ level for Stokes I . Ellipses in the lower-left corners reflect the synthesized beams. Column **d** shows the line-of-sight magnetic field strength [B_{LOS}] in the PFSS model at a height of $1.21 R_{\odot}$, which roughly corresponds to the height of the radio limb at 196 MHz and is indicated by the dotted circles in each panel. The pink contours indicate open field regions in the model. Color bar units are in signal-to-noise [σ] for Stokes I and V , percent for V/I , and Gauss [G] for the field model.

lower at lower frequencies. Second, lower frequency emission is produced at larger heights where the corona is somewhat less finely structured, with smaller contrasts in magnetic field and density between adjacent regions. Third, lower-frequency emission is more strongly scattered, which leads to increased angular broadening with decreasing frequency.

Figure 4.13 also exhibits much less straightforward agreement between the LOS field orientation and the polarization structure. This is a gradual transition with increasing frequency that we cannot attribute to instrumental effects because we never observe such an inversion for the noise storm sources that are detected across our entire observing band from 80 to 240 MHz. Some of the differences between the Stokes V sign and that expected from the LOS field orientation can likely be attributed to the same unknown effect present in the coronal hole observations from Section 4.6. For instance in the 10 September 2015 and 14 September 2015 observations, there are coronal holes near the west limb and north pole, respectively, that exhibit this effect. However, those regions aside, there is still not the same alignment between opposite polarization signs and LOS field polarity inversion lines that we see at low frequencies.

One possible explanation for the discrepancies at higher frequencies is simply the accuracy and resolution of the potential field model. Higher frequencies correspond to lower heights, and the true coronal magnetic field becomes increasingly non-potential closer to the surface, with larger contrasts between adjacent regions. This is also true for the density and temperature, which also affect the polarization signal to some extent and will be important for future forward modeling efforts. However, our impression is that physical effects are also likely to be important, and we discuss some possibilities in the next section.

4.8 Discussion

These data offer an opportunity to probe the coronal magnetic field at heights and scales that are not easily accessed with other instruments. The intent of this article is to introduce the data and survey the range of features observed in this new regime. In a forthcoming study, we will directly compare the magnetic field strength and structure implied by our observations to model predictions of the thermal bremsstrahlung emission implied by different global models. Preliminary results suggest that we can successfully generate synthetic Stokes V/I images that reproduce the low-frequency polarization structure near disk center, but we have yet to explicitly compare the field strengths implied by the observed polarization fractions.

While these preliminary results are encouraging, there are a number of questions that will require deeper investigation. The most perplexing of these is perhaps the bullseye structure in Stokes V described in Section 4.6, which is found for many low-latitude coronal holes. At our higher frequencies (≤ 240 MHz), low-latitude coronal holes often exhibit a central circularly-polarized component surrounded by a full or partial ring of the opposite sense, and the central component is of the opposite sign than would be expected from thermal bremsstrahlung, the presumed emission mechanism. With decreasing frequency, the central component diminishes and the ring expands. By 80 MHz, there may be some trace of the central component remaining or the region may be entirely of the sign expected by bremsstrahlung emission.

We have two suggestions for what may be responsible for this effect. The first has to do with differential refraction of the x - and o -modes. The two modes have slightly different group velocities within the plasma and therefore slightly different refractive indices, as is often observed in ionospheric propagation experiments at Earth (Melrose, 1986). It may be possible to separate the two modes sufficiently via refraction so as to produce a polarization sign that is the opposite of that expected by bremsstrahlung emission. For example, the refractive index of the x -mode is further below unity than the o -mode. Emission generated by denser plasma at the edge of a coronal hole may refract at the coronal hole boundary, with the x -mode refracting more strongly in the radial direction, producing an enhancement of x -mode around the perimeter and o -mode near the center. Propagation effects do seem to be particularly important in coronal holes, as they are the preferred explanation for why some coronal holes are significantly brighter than their surroundings at low frequencies (Alissandrakis and Chiuderi-Drago, 1994; Rahman et al., 2019). However, this later question has not been resolved, and it is not obvious to us how this polarization signal would be produced. Ray tracing simulations, such as those done by Benkevitch et al. (2012) or Vocks et al. (2018), are likely needed to investigate this further.

A second possibility that we regard as less likely is that the central polarized component is produced by weak plasma emission, which generally produces the opposite sign in circular polarization compared bremsstrahlung for the same line-of-sight field. Because plasma emission may be up to 100% circularly polarized, it is possible for the total intensity to be dominated by thermal bremsstrahlung emission while the polarized component is dominated by plasma emission. This is what we expect to be happening in the low-intensity and weakly-polarized active region sources described in Section 4.5. For coro-

nal holes, the driver of this plasma emission might be the transition region network jets discovered by the Interface Region Imaging Spectrograph (Tian et al., 2014). These jets are continuously generated throughout the transition region, but they are particularly common and intense inside coronal holes (Narang et al., 2016). They strongly resemble the coronal X-ray jets associated with Type III bursts, and some attribute the network jets to small-scale reconnection events (Tian et al., 2014; Kayshap et al., 2018). However, the network jets also resemble chromospheric Type II spicules and may instead be driven by shocks (Cranmer and Woolsey, 2015) or heating fronts (De Pontieu et al., 2017). If these jets are associated with reconnection or shocks, then nonthermal electrons capable of producing plasma emission may be expected at least to some extent by analogy with solar radio bursts. We may see this emission only in coronal holes because the densities there are low enough that the plasma levels associated with our highest frequencies are in, or very close to, the transition region. This idea could be explored observationally through examining variability in the polarization signal and comparing that to the typical jet timescales.

A mixture of plasma emission and thermal emission may also help to explain why our higher-frequency Stokes V maps are not well-correlated with the LOS field structure. One of the MWA’s main contributions thus far has been to demonstrate the prevalence of very weak nonthermal emissions (Suresh et al., 2017). Sharma et al. (2018) report that up to 45% of the total intensity outside of nominal burst periods may be nonthermal during moderately active periods, and preliminary imaging analyses suggest that nonthermal components are present to varying degrees in every environment. These nonthermal emissions are attributed to plasma emission, which again is generally much more highly polarized and of the opposite sign compared to bremsstrahlung. A relatively minor total intensity contribution from plasma emission would therefore have a much greater impact on the circularly-polarized intensity and may be capable of reversing the observed sense from that expected from thermal emission. The polarization fraction could also potentially be used to disentangle the contributions of both mechanisms.

Mode coupling effects associated with quasi-transverse (QT) regions are also likely to be important at least in some regions and may contribute to differences between the observed polarization sense and that straightforwardly expected from a particular emission mechanism, along with reductions in the polarization fraction expected from plasma emission sources. QT regions refer to when the magnetic field orientation is nearly perpendicular to that of

the emission region, such that there is no magnetic field component along the ray path. Passing through such a region may cause the circular polarization sign to reverse if the emission frequency is below a certain threshold that depends on the plasma properties (Cohen, 1960; Zheleznyakov and Zlotnik, 1964; Melrose and Robinson, 1994). This concept is very important to the interpretation of polarization reversals and associated magnetic field diagnostics in high-frequency microwave observations (*e.g.* Ryabov et al., 1999; Altyntsev et al., 2017; Shain et al., 2017; Sharykin et al., 2018). At lower frequencies, QT regions are also invoked to explain the polarization properties of noise storms (Suzuki and Sheridan, 1980; White et al., 1992), Types U and N bursts (Suzuki and Sheridan, 1980; Kong et al., 2016), and zebra patterns in Type IV bursts (Kaneda et al., 2015). A natural place to start investigating the importance of QT regions in our observations would be by comparing the polarization sense of the active region noise storm sources from Section 4.5 to that expected from the magnetic field orientation assuming *o*-mode polarization from plasma emission.

Lastly, it would be useful to explore improving our calibration approach by imposing constraints specific to solar observing. We have introduced a strategy, adapted from the astrophysical literature, to mitigate an artefact referred to as “leakage,” whereby the polarimetric signal is contaminated by some fraction of the total intensity signal. This is described in Section 4.4. While we have demonstrated that our approach is reasonably effective, it is clearly not perfect given the discrepancies occasionally observed between adjacent frequency channels, as illustrated by Figure 4.11g. A better solution may be available by imposing constraints based on the expectation that we can generally assume that the linear polarizations (Stokes Q and U) are zero because Faraday rotation destroys the linear polarization signal over most observing bandwidths. Assuming Q and U are zero implies that the XX and YY instrumental polarizations are equal, and this constraint may be applied for each antenna in visibility space, allowing for a direction-dependent polarization calibration. We do not yet know the feasibility of this approach, and new software tools would need to be developed to implement it.

4.9 Conclusion

We have presented the first spectropolarimetric imaging of the Sun using the MWA. These are the first imaging observations of the low-frequency corona that are capable of measuring the weak polarization signals outside of intense burst periods. We reviewed the two dominant emission mechanisms, thermal

Ch. 4 Spectropolarimetric Imaging of the Corona

bremsstrahlung and plasma emission, and how their expected polarization signatures relate to our observations. Our data were taken from over 100 observing runs near solar maximum, and we surveyed the range of features detected in quiescent periods. These observations can be used to diagnose the coronal magnetic field at heights and scales for which the available data constraints are limited, and this will be the focus of future work. Our contributions are as follows:

- We introduced an algorithm to mitigate an instrumental artefact known as “leakage,” whereby some fraction of the total intensity [Stokes I] signal contaminates the circular polarization [Stokes V] images (Section 4.4). Leakage occurs due to differences between the actual instrumental response and the primary beam model used to convert images of the instrumental polarizations into Stokes images. These errors may be due to imperfections in the beam model itself or to other effects that change the instrument’s effective response, such as individual antenna failures or, importantly, the practice of applying calibration solutions from a calibrator source at one pointing to the target source at another pointing. We adapted an approach used for astrophysical MWA studies, which show that the leakage varies negligibly over the spatial scale of the Sun. Given that most of the pixels in our images should be very weakly polarized based on our expectations for thermal bremsstrahlung emission, we determined the leakage fractions with an algorithm that minimizes the number of pixels with polarization fractions $[|V/I|]$ greater than 0.5%.
- We developed and employed a source finding algorithm that detected around 700 compact sources in the Stokes V images (Section 4.5). Only sources detected in a least three frequency channels were analyzed further, corresponding to 112 distinct sources found at multiple frequencies. The intensities of these sites ranged from slightly below the background level to $60\times$ greater than the background. Their polarization fractions ranged from less than 0.5% to nearly 100%. At least one of these sources was present on 78% of our observing days, and we found a positive correlation between the total intensity over the background and the polarization fraction ($r = 0.64$). The high-intensity sources with large polarization fractions are noise storm continua sources produced by plasma emission and associated with active regions. As there is no obvious separation of these sources into distinct populations, we suggest that they represent a continuum of plasma emission sources down to intensities and polarization

fractions that were not previously observable in imaging observations. Although the plasma emission theory predicts 100% circular polarization for fundamental emission, very low polarizations can be explained in this context through three effects. First, the weaker sources may still be dominated by thermal bremsstrahlung emission with a minor contribution from plasma emission that then dominates the polarized component. Second, the plasma emission sites may often be considerably smaller than the beam size, leading to beam dilution that smears the polarized signal across a larger area. Third, scattering by density irregularities may also reduce the polarization fraction, even for very intense sources.

- We reported the discovery of a “bullseye” polarization structure often associated with low-latitude coronal holes in which one polarization sense is surrounded by a full or partial ring of the opposite sense (Section 4.6). The polarization of the central component is of the opposite sign from that expected from thermal bremsstrahlung, the presumed emission mechanism. Moving from our highest frequency (240 MHz) to our lowest (80 MHz), the central component diminishes and the ring expands. Some coronal holes continue to exhibit the ring structure at 80 MHz, while others are unipolar in Stokes V with a sense that matches that expected for bremsstrahlung emission. This effect was observed in 28 separate observations of 13 different coronal holes. We validated the Stokes I structure with an independent data reduction, and we noted that similar total intensity structures associated with noise storms never exhibit this effect. We speculated that the structure may be the result of propagation effects, namely refraction, that separate the x - and o -modes, but ray tracing simulations are needed to test this. Alternatively, we suggested that the polarization signature may be produced by weak plasma emission produced by the recently-discovered transition region network jets that are particularly prevalent inside coronal holes.
- We showed that at our lowest frequencies, the large-scale Stokes V structure is reasonably well-correlated with the line-of-sight magnetic field structure obtained from a global potential field source surface model (Section 4.7). The boundaries between opposite polarization signs are generally aligned with polarity inversion lines in the model, with the polarization sign matching the expectation from thermal bremsstrahlung emission given the LOS field orientation. The correspondence is best near disk center and diminishes toward the limb, where propagation ef-

Ch. 4 Spectropolarimetric Imaging of the Corona

fects become increasingly important and the signal-to-noise decreases. At our highest frequencies, there is little straightforward agreement between the LOS field orientation and the polarization sign. This may be due to the limited accuracy of the potential model, as the coronal field becomes increasingly non-potential at lower heights where higher-frequency emission generated. However, we suspect that physical effects are also important. These may include a mixture of thermal and non-thermal emission in the same region, along with propagation effects such as refraction and polarization reversals due to quasi-transverse (QT) regions.

Acknowledgements: This work was primarily supported by the Australian Government through an Endeavour Postgraduate Scholarship. P. McCauley acknowledges the Asian Office of Aerospace Research and Development (AOARD) of the United States Air Force Office of Scientific Research (AFOSR) for travel support through the Windows on Science (WOS) program. I. Cairns and J. Morgan acknowledge support from AFOSR grants FA9550-18-1-0671 and FA9550-18-1-0473, respectively. We thank Don Melrose and Sarah Gibson for helpful discussions. We also thank the anonymous referee for a careful reading and constructive comments. This scientific work makes use of the Murchison Radio-astronomy Observatory (MRO), operated by the Commonwealth Scientific and Industrial Research Organisation (CSIRO). We acknowledge the Wajarri Yamatji people as the traditional owners of the Observatory site. Support for the operation of the MWA is provided by the Australian Government’s National Collaborative Research Infrastructure Strategy (NCRIS), under a contract to Curtin University administered by Astronomy Australia Limited. We acknowledge the Pawsey Supercomputing Centre, which is supported by the Western Australian and Australian Governments. The SDO is a National Aeronautics and Space Administration (NASA) satellite, and we acknowledge the AIA and HMI science teams for providing open access to data and software. This research has also made use of NASA’s Astrophysics Data System (ADS) and the Virtual Solar Observatory (VSO, Hill et al. [2009](#)).

Chapter 5

Conclusions and Future Work

This thesis has presented novel low-frequency observations of the solar corona, and the major results of each chapter are briefly summarized in the next section. The subsequent sections elaborate on certain conclusions and outline potential next steps for future work on several open questions. As noted in Chapter 1, millions of images were reduced in the course of this work, which was the first attempt to process large amounts of MWA solar data with supercomputing facilities. The science presented here is only a fraction of what can be extracted from this dataset, which itself is a small fraction of the total MWA solar archive, and most of the following ideas for future work can be addressed with the existing images.

5.1 Results Summary

In Chapter 2 (McCauley et al., 2017), new dynamics of Type III solar radio bursts were identified, characterized, and interpreted as resulting from a divergent magnetic field configuration that was evidenced by contemporaneous EUV observations. The radio burst images were used to develop a more complete picture of the magnetic field topology, showing that these data are valuable probes of the field connectivity at heights that are not easily accessed by other data. A rough flux calibration method was also developed, and the structure of the quiescent corona was compared to model predictions. Notably, this comparison showed a coronal hole transitioning from being a relatively dark to a relatively bright structure moving from high to low frequencies in the data, which was not found in the model.

In Chapter 3 (McCauley et al., 2018), Type III bursts were used to estimate the coronal density profile. At its heart, this was a repetition of a classic experiment with updated instrumentation that confirmed earlier results for the existence of significant apparent density enhancements over standard models. The cause for these enhancements has been debated for many years, and the arguments for the two primary interpretations were reviewed in light of recent results. Some authors suggest that observable Type III bursts are produced by

Ch. 5 Conclusions and Future Work

electron beams moving along overdense structures relative to their surroundings (i.e., the density enhancements are real), while others suggest that propagation effects, namely scattering, cause the bursts to be observed at larger heights than they were produced at (i.e., the enhancements are not real). Here, a novel comparison between the observed extent of the quiescent corona and model predictions was used to conclude that the apparent density enhancements can largely but not entirely be explained by propagation effects for the events studied in Chapter 3.

Chapter 4 (McCauley et al., 2019) presented the first spectropolarimetric imaging of the quiescent corona at low frequencies. This required first developing an algorithm to mitigate calibration errors that cause a fraction of the total intensity signal to contaminate the polarization images. Over 100 observing runs near solar maximum were used to survey the principal features of the low-frequency corona in circular polarization (Stokes V). Around 700 compact polarized sources were detected with a range of polarization fractions from less than 0.5% to nearly 100%. These were interpreted as a set of plasma emission noise storm continua sources that ranged from intense and highly-polarized down to having intensities and polarization levels that could not be observed by previous instruments. Coronal holes were also found to dominate the polarization maps in the absence of intense noise storms, often exhibiting a characteristic “bullseye” structure with one polarization sense surrounded by a ring of the opposite sense. Finally, the large-scale polarized component of thermal bremsstrahlung emission was mapped for the first time, and good agreement was found between the polarization structure and that of the line-of-sight magnetic field in a global potential field model at the lowest MWA frequencies.

Some elaborations and suggestions for future work related to these conclusions are described in the following sections.

5.2 Type III Burst Source Motions

Chapter 2 (McCauley et al., 2017) presented one example of motion exhibited by Type III bursts. The burst sources were observed to repetitively and rapidly split into two components at relatively low frequencies or simply elongate in two directions at higher frequencies. A model for this motion was developed based on a divergent quasi-separatrix layer magnetic field structure that was traced out by contemporaneous EUV jet observations: Simultaneously-accelerated electrons travel along neighboring field lines that are immediately

adjacent to each other at the flare site but diverge with height, causing electrons to reach the requisite height to produce emission of a particular frequency at slightly different times. This produces an apparent motion that is nearly perpendicular to that of the actual electron beams.

While this model is well-supported by the available data for that event, it is not clear how broadly-applicable it is to other events. Based on a cursory examination of around 50 bursts, splitting motions are relatively uncommon but significant motion in at least one direction is observed for around half of the bursts. Can these motions be entirely explained by divergent magnetic field structures in essentially the same way? Such structures are known to be common, particularly in and around the active regions that generally produce Type III bursts. However, in at least one event (2015-08-25 03:15 UT), the direction of motion does not seem consistent with the magnetic field structure inferred from EUV observations and a potential field extrapolation. If a deeper investigation concludes that the McCauley et al. (2017) model is not viable for that event, what else could produce such motion, given that it is very unlikely to correspond to the actual magnetic-field-aligned motion of the electron beam(s) moving through an iso-density layer?

One possibility relates to scattering. As detailed Chapter 3 (McCauley et al., 2018), scattering in the corona may not randomly modulate the ray paths because the density inhomogeneities responsible for scattering are not necessarily randomly oriented. Instead, they are often field-aligned high-density fibers that are generally close to radial. Scattering by these structures tends to guide emission outward to larger heights before it can escape unimpeded to the observer. This is analogous to classic ducting, where radiation is actually guided within a coherent low-density structure. Scattering may behave like a “leaky duct,” where burst radiation scatters outward but escapes at slightly different heights at slightly different times. Depending on the geometries, perhaps this could also generate an apparent motion.

Another investigation using these data, currently being conducted by a collaborator, is to examine how the polarimetric structure of bursts differs between events that exhibit motion and events that do not (Rahman et al., in preparation, 2019). Preliminary results suggest that events with motion exhibit asymmetric Stokes V profiles and that the leading edge in the direction of motion tends to be somewhat more highly polarized. Scattering seems likely to play some role in this behavior given that it is strongly suspected to depolarize burst emission. However, how this relates (if at all) to the mechanism(s) responsible for source motions is unclear.

5.3 Coronal Hole Peculiarities

There are multiple open questions surrounding the appearance of coronal holes in low-frequency radio observations. As is observed in soft X-ray and EUV data, coronal holes are naively expected to be darker than their surroundings in radio observations because their lower densities imply lower emissivities. However, below around 120 MHz, many low-latitude coronal holes transition from being dark structures at higher frequencies to progressively brighter structures at lower frequencies. In fact, in the absence of intense noise storm emission, coronal holes may far exceed the brightness of nearby active regions.

This effect was first noted in a few isolated single-channel observations by Dulk and Sheridan (1974) and Lantos et al. (1987). The first observations to simultaneously observe a coronal hole on either side of this dark-to-bright transition were presented in Chapter 2 (McCauley et al., 2017). This motivated a followup MWA study that characterized coronal hole intensities in more detail, including presenting multiple examples along with counterexamples that do not exhibit significant low-frequency enhancements (Rahman et al., 2019). Following suggestions from Lantos et al. (1987) and Alissandrakis and Chiuderi-Drago (1994), Rahman et al. (2019) proposed a qualitative model in which emission generated outside a coronal hole is systematically redirected into it from an observer’s perspective via refraction at the coronal hole boundary. However, no detailed quantitative modeling of this scenario has yet been done.

In Chapter 4 (McCauley et al., 2019), low-latitude coronal holes were found to exhibit another peculiar effect. In circular polarization images, many coronal holes exhibit a “bullseye” pattern with one polarization sense surrounded by a ring of the opposite sense. The central component does not match the sign expected from thermal bremsstrahlung, the presumed emission mechanism, given the orientation of the line-of-sight magnetic field. Two speculative ideas were proposed to explain this signature. The first is that the different refractive indices of the o - and x -modes causes the two modes to separate somewhat during propagation to the observer. If the refractive effect is large enough, this may lead to an unexpectedly large polarization fraction and/or a reversal in the polarization sense.

The second idea is that the emission mechanism is not entirely thermal, instead including a small amount of plasma emission driven by the recently-discovered network jets that pervade coronal holes. This would explain the polarization sign of the central component, as plasma emission generally produces the opposite sign compared to bremsstrahlung for the same magnetic field ori-

entation. However, given that refraction is already thought to be important in the total intensities of coronal holes and that the potential for plasma emission from network jets is uncertain, the latter idea was regarded as less plausible.

To test the refraction idea, ray tracing simulations are needed. These would examine the propagation of the o - and x -modes through models of the density structure in and around a coronal hole to determine if refraction can produce the bullseye pattern in circular polarization and/or the low-frequency enhancements in total intensity.

5.4 Probing the Large-Scale Magnetic Field

In Chapter 4 (McCauley et al., 2019), the large-scale circular polarization structure at the lowest MWA frequencies was shown to be reasonably well-matched to the line-of-sight magnetic field structure inferred from a global potential field model at a height roughly corresponding to that of the radio limb. That is, the boundaries between opposite polarization signs were generally aligned with polarity inversion lines in the model, and the polarization sign was generally consistent with expectations assuming thermal bremsstrahlung emission. The same was not true at higher frequencies, which may be due to a number of effects that are outlined in Chapter 4. Perhaps the most significant import of these data for the broader solar physics community is the potential capability to probe the coronal magnetic field at heights and scales that cannot be accessed by any other data type. This can be done by comparing the observations to forward models that predict the polarized intensities given models of the global plasma parameters.

We¹ have recently upgraded the FORWARD software suite (Gibson et al., 2016) to improve the radiative transfer computation for bremsstrahlung emission. Figure 5.1 compares a synthetic image of the polarization fraction at 89 MHz to an MWA observation that was presented in Chapter 4. There is a clear correspondence in the figure between the modeled and observed emission, both qualitatively and quantitatively. The agreement is best near disk center, where propagation effects not considered by the model are likely to be least important. The synthetic image is calculated using the potential field model from Chapter 4 and an isothermal, spherically-symmetric, hydrostatic density model. The next steps are, first, to explicitly estimate the magnetic field strength implied by the observed polarization fractions at specific locations given assumed

¹The preliminary results presented in Section 5.4 were produced in collaboration with Stephen White, Sarah Gibson, and Iver Cairns.

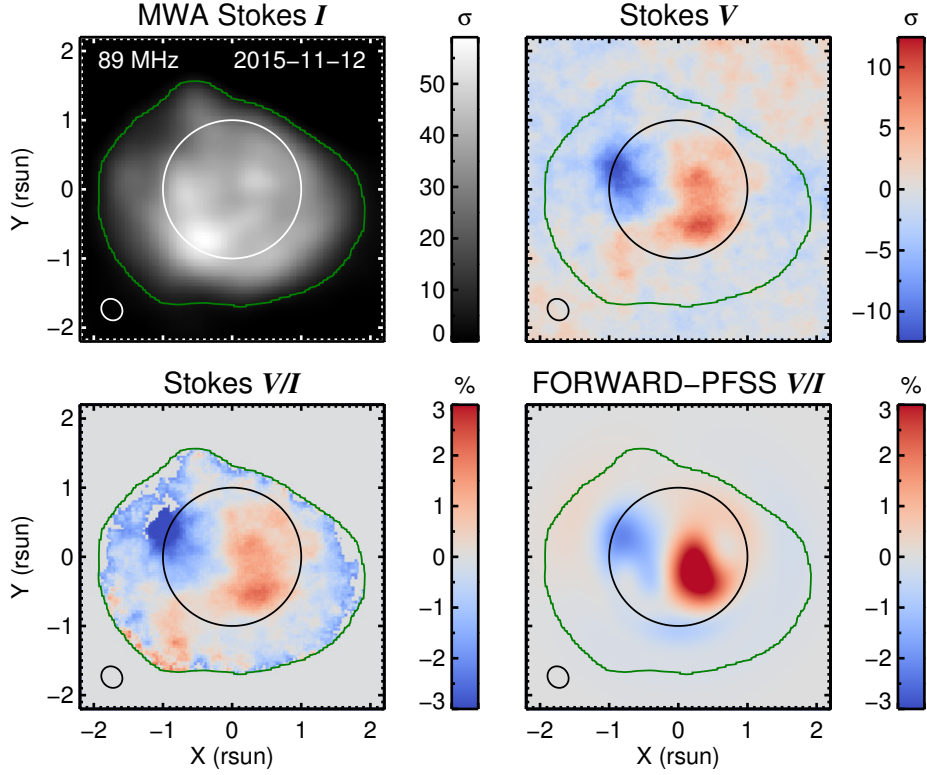


Figure 5.1: *Top*: MWA Stokes I and V images with color bars in units of signal-to-noise $[\sigma]$. *Bottom*: Observed and predicted polarization fractions $[V/I]$. Solid circles represent the optical disk, the ellipses in the lower-left corners represent the synthesized beam, and the green contours reflect the $5\text{-}\sigma$ level in Stokes I . The synthetic image predicts V/I from thermal bremsstrahlung emission assuming a potential magnetic field model and a spherically-symmetric hydrostatic atmosphere model.

plasma parameters and, second, to examine how uniformly varying the model field strength by a constant factor affects the quantitative agreement between the observed and synthetic images over some larger region. The same comparison can then be made for a more sophisticated coronal model, such as the global MHD models used in Chapters 2 and 3.

A longterm goal for these data is to make regular estimates of the global magnetic field strength that can routinely be used to improve coronal magnetic field models. However, significant advances are needed to achieve this. First, the polarization maps are intrinsically affected by the coronal density and temperature, meaning that the reliability of magnetic field strength estimates depends on the reliability of the density and temperature models used. Second, the polarization maps are influenced, likely significantly, by propagation effects (i.e. refraction, scattering, and mode coupling) that have never

been adequately modeled in this context. Third, weak nonthermal emission may have a significant influence on the polarization fraction, particularly at higher frequencies, and assessing the contribution of possible nonthermal components may be challenging. Finally, the data quality must still be improved, specifically the polarimetric calibration and dynamic range. As described in Chapter 4, the measured polarization fractions have sources of uncertainty that cannot yet be characterized or eliminated. Further, the dynamic ranges of the polarization images are often insufficient to detect the polarized component of thermal emission if a bright nonthermal source is present, which is often the case, although this may be overcome by adapting recently-developed high-dynamic-range calibration techniques for polarimetry (Mondal et al., 2019).

These are longterm challenges that will require the attention of many researchers before low-frequency polarimetry can be used to advance operational coronal magnetic field models. Chapter 4 and the future steps outlined in this section represent some of the early steps in this process.

5.5 Coronal Mass Ejections

While none of the research chapters in this thesis are directly-related to coronal mass ejections (CMEs), the image archive developed for this thesis produced at least one serendipitous CME observation. This event was recently imaged over its full duration, and additional CME data are currently being reduced.

Figure 5.2 shows the time evolution of a CME structure seen at four MWA frequencies, and Figure 5.3 overlays contours of the 80 MHz emission on EUV and white light observations. The event occurred on 26 September 2014 with a far-side prominence eruption that becomes visible in the SDO/AIA 304 Å data around 4:05 UT. The left panel of Figure 5.3 shows the development of a compact and highly-variable radio source just ahead of the erupting filament, and the right panel shows the white-light and radio structures shortly after the CME emerged beyond the occulting disk of the coronagraph.

An arc of 80 MHz emission appears to trace out the CME front structure seen in white light. In Figure 5.2, this arc can be seen first developing at higher frequencies (lower heights) and then progressively forming at lower frequencies (larger heights) as the CME propagates. Specifically, at 04:17:52 UT, the arc is dominant at 120 MHz but later becomes brightest at 98 and 80 MHz near 04:20:34 and 04:23:00, respectively. Moreover, the arc is not stationary at each individual frequency, instead expanding outward at a speed of around 480 km s⁻¹ in the 80 MHz images. Importantly, the bandwidth of emission at a given

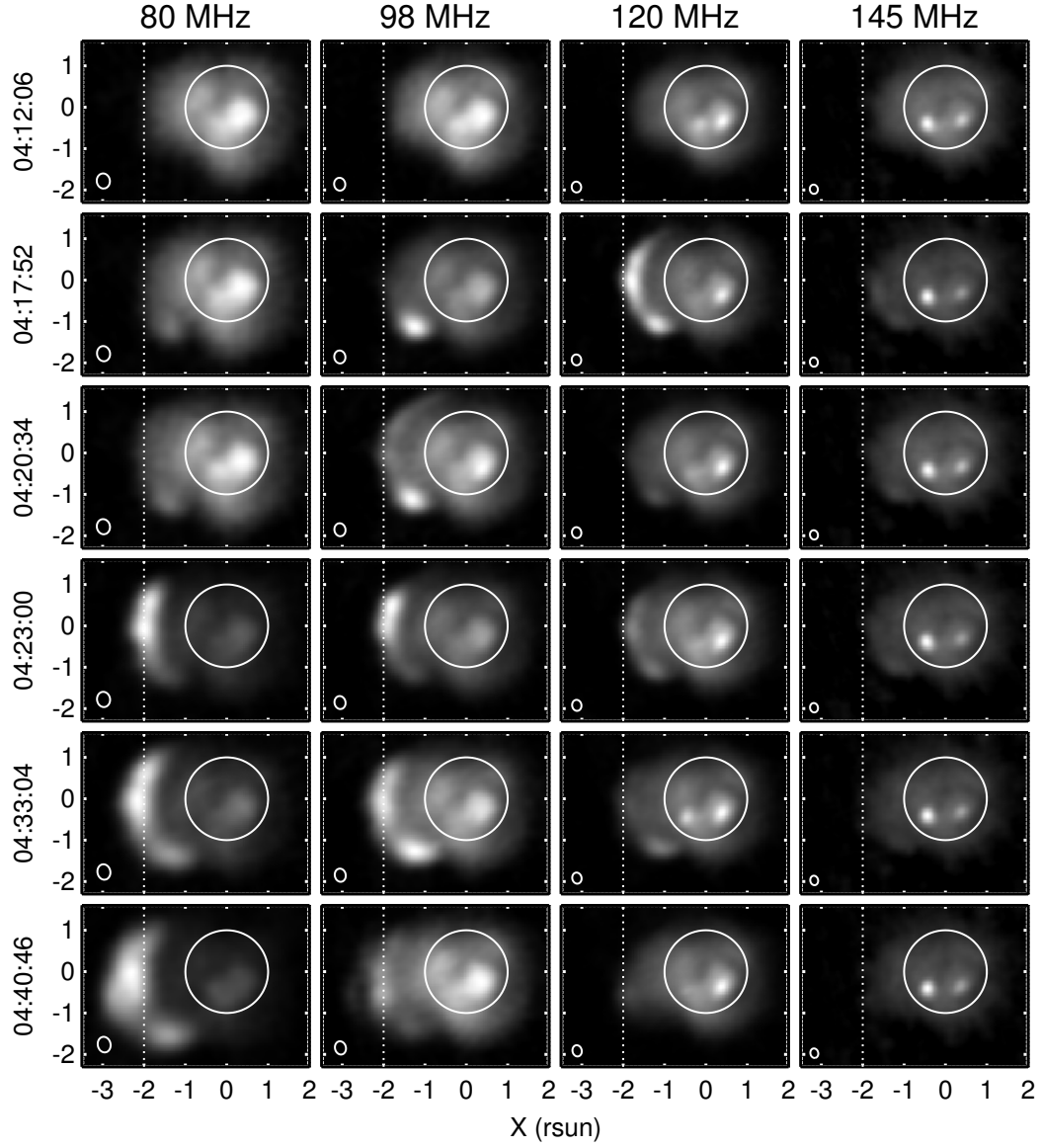


Figure 5.2: 2014-09-26 radio CME evolution at four MWA frequencies (columns) and six time steps (rows). Solid circles represent the optical disk and ellipses in the lower-left corners represent the synthesized beam sizes. A dotted line at $x = -2 R_{\odot}$ is included to help illustrate the source motion.

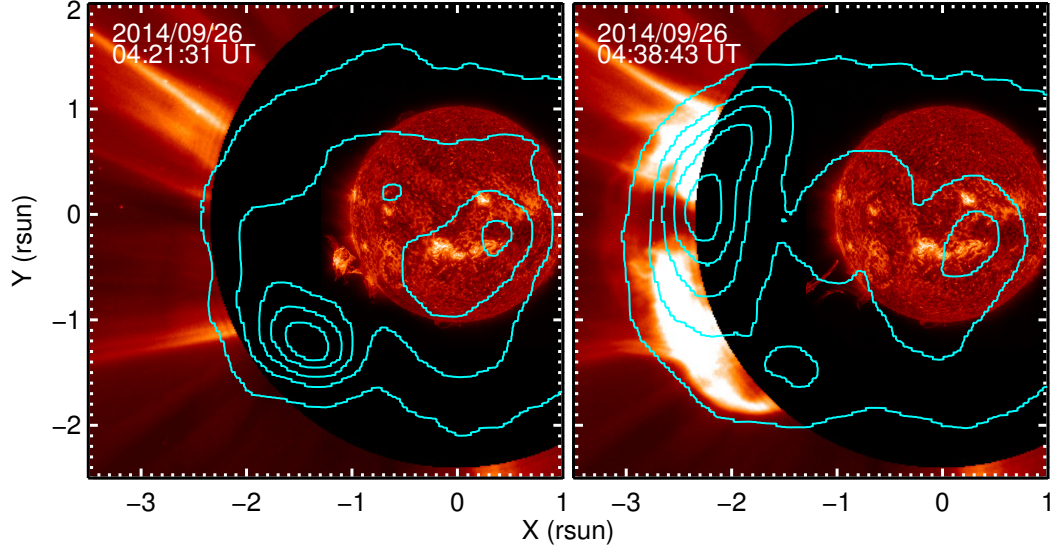


Figure 5.3: White light (LASCO C2; outer red), EUV (AIA 304 Å; inner red) and radio (MWA 80 MHz; cyan contours) CME observations. The left panel shows a compact radio source ahead of the erupting filament in the southeast, and the right panel shows an arc of radio emission across the white light CME front.

time and location appears to be relatively broad; for instance, near $(x = -2, y = 0)$ R_{\odot} , emission is enhanced between 80 and 120 MHz from roughly 04:23 to 04:40 UT. This will not be characterized here, but the relative intensity across the radio arc also fluctuates somewhat in time, with occasional compact bursts at its southern extent, and substructures within the radio and white-light sources appear to be correlated.

To the best of our knowledge, intense radio emission that is aligned and morphologically similar to the CME front seen in white light, as in Figure 5.3, has not been observed before. Preliminary results from other MWA observations suggest that while compact emission associated with the CME core can routinely be observed given sufficient dynamic range, the bright arc structure from Figures 5.2 and 5.3 is uncommon. Preliminary results from other events also suggest that the compact core emission is likely to be gyrosynchrotron emission from the central CME flux rope (Mondal et al., in preparation, 2019). We suspect that gyromagnetic emission is also the most likely mechanism for the arc structure, but no analysis has yet been done to determine this.

As described in Section 1, the primary low-frequency signatures of CMEs are Types II and IV radio bursts. There are very few reports of radio counterparts to the white light CME emission. The first example was presented by Bastian et al. (2001) using the *Nançay Radioheliograph* at frequencies above 164 MHz.

Ch. 5 Conclusions and Future Work

These observations show emission primarily associated with the lower portions of the large CME loops, with a very slight signature from loop tops at the CME front. Bastian et al. (2001) attributes the radiation to synchrotron emission from electrons injected into the expanding magnetic fields of the CME.

Our observations differ from those of Bastian et al. (2001) in that the arc-shaped loop structure is most intense near the apex at the leading edge of the CME, with comparatively less emission toward the footpoints. If the emission mechanism is the same in our case, the different morphology may be related to the lower observation frequencies or differences in the location and nature of the electron acceleration process. The frequency of gyromagnetic emission depends on the magnetic field strength, with lower field strengths producing lower-frequency emission. As the magnetic field strength is weaker toward the apexes of the expanding CME loops, lower-frequency emission might be expected to be more intense there, though the lower portions of the loops may also simply be occulted given that the event originated on the far-side. However, a detailed analysis of the MWA emission spectrum is first needed to determine the emission mechanism.

References

- Akabane, K., and M. H. Cohen (1961), Polarization Measurements of Type III Bursts and Faraday Rotation in the Corona, *Astrophys. J.*, *133*, 258, doi:10.1086/147021. [35](#)
- Akhmedov, S. B., G. B. Gelfreikh, V. M. Bogod, and A. N. Korzhavin (1982), The measurement of magnetic fields in the solar atmosphere above sunspots using gyroresonance emission, *Solar Phys.*, *79*, 41–58, doi:10.1007/BF00146972. [16](#), [110](#)
- Alissandrakis, C. E. (1986), Gyrosynchrotron Emission of Solar Flares, *Solar Phys.*, *104*(1), 207–221, doi:10.1007/BF00159964. [16](#)
- Alissandrakis, C. E., and F. Chiuderi-Drago (1994), Detection of linear polarization in the microwave emission of Solar Active Regions, *Astrophys. J. Lett.*, *428*, L73–L76, doi:10.1086/187396. [14](#), [19](#), [60](#), [99](#), [127](#), [139](#), [148](#)
- Alissandrakis, C. E., P. Lantos, and E. Nicolaidis (1985), Coronal structures observed at metric wavelengths with the Nancay radioheliograph, *Solar Phys.*, *97*, 267–282, doi:10.1007/BF00165990. [25](#), [34](#), [125](#)
- Alissandrakis, C. E., A. A. Kochanov, S. Patsourakos, A. T. Altyntsev, S. V. Lesovoi, and N. N. Lesovoya (2013), Microwave and EUV Observations of an Erupting Filament and Associated Flare and Coronal Mass Ejections, *Pub. Astron. Soc. Japan*, *65*(sp1), doi:10.1093/pasj/65.sp1.S8. [32](#)
- Alissandrakis, C. E., A. Nindos, S. Patsourakos, A. Kontogeorgos, and P. Tsitsipis (2015), A tiny event producing an interplanetary type III burst, *Astron. Astrophys.*, *582*, A52, doi:10.1051/0004-6361/201526265. [37](#), [48](#)
- Allen, C. W. (1947), Interpretation of Electron Densities from Corona Brightness, *Mon. Not. Roy. Astron. Soc.*, *107*, 426, doi:10.1093/mnras/107.5-6.426. [93](#)
- Altyntsev, A., N. Meshalkina, I. Myshyakov, V. Pal'shin, and G. Fleishman (2017), Flare SOL2012-07-06: On the Origin of the Circular Polarization Reversal Between 17 GHz and 34 GHz, *Solar Phys.*, *292*, 137, doi:10.1007/s11207-017-1152-x. [141](#)
- Alvarez, H., and F. T. Haddock (1973), Solar Wind Density Model from km-Wave Type III Bursts, *Solar Phys.*, *29*, 197–209, doi:10.1007/BF00153449. [76](#), [82](#), [95](#)
- Antiochos, S. K., C. R. DeVore, and J. A. Klimchuk (1999), A Model for Solar Coronal Mass Ejections, *Astrophys. J.*, *510*(1), 485–493, doi:10.1086/306563. [31](#)
- Appleton, E. V. (1945), Departure of Long-Wave Solar Radiation from Black-Body Intensity, *Nature*, *156*, 534–535, doi:10.1038/156534b0. [15](#)
- Archontis, V. (2008), Magnetic flux emergence in the Sun, *J. Geophys. Res. (Space Phys.)*, *113*(A3), A03S04, doi:10.1029/2007JA012422. [24](#)
- Arzner, K., and A. O. Benz (2005), Temporal Correlation of Hard X-Rays and Meter/Decimeter Radio Structures in Solar Flares, *Solar Phys.*, *231*, 117–141, doi:10.1007/s11207-005-1590-8. [51](#)
- Aschwanden, M. J. (1986), The polarization of decimetric pulsations, *Solar Phys.*, *104*, 57–65, doi:10.1007/BF00159947. [110](#), [121](#)

References

- Aschwanden, M. J. (2005), *Physics of the Solar Corona. An Introduction with Problems and Solutions (2nd edition)*, Springer-Verlag Berlin Heidelberg. [2](#), [13](#), [15](#), [22](#), [25](#), [27](#), [31](#), [108](#)
- Aschwanden, M. J., and A. O. Benz (1988), On the Electron-Cyclotron Maser Instability. II. Pulsations in the Quasi-stationary State, *Astrophys. J.*, *332*, 466, doi:10.1086/166670. [19](#)
- Aschwanden, M. J., A. O. Benz, B. R. Dennis, and R. A. Schwartz (1995), Solar Electron Beams Detected in Hard X-Rays and Radio Waves, *Astrophys. J.*, *455*, 347, doi:10.1086/176582. [76](#), [82](#), [95](#)
- Aubier, M., Y. Leblanc, and A. Boischot (1971), Observations of the Quiet Sun at Decameter Wavelengths - Effects of Scattering on the Brightness Distribution, *Astron. Astrophys.*, *12*, 435. [60](#), [99](#)
- Aulanier, G., E. Pariat, and P. Démoulin (2005), Current sheet formation in quasi-separatrix layers and hyperbolic flux tubes, *Astron. Astrophys.*, *444*, 961–976, doi:10.1051/0004-6361:20053600. [70](#)
- Aurass, H., and K.-L. Klein (1997), Spectrographic and imaging observations of solar type U radio bursts, *Astron. Astrophys. Suppl.*, *123*, doi:10.1051/aas:1997161. [78](#)
- Aurass, H., K.-L. Klein, and P. C. H. Martens (1994), First detection of correlated electron beams and plasma jets in radio and soft x-ray data, *Solar Phys.*, *155*, 203–206, doi:10.1007/BF00670741. [48](#)
- Babcock, H. D. (1959), The sun’s polar magnetic field., *Astrophys. J.*, *130*, 364. [22](#)
- Babcock, H. W. (1953), The Solar Magnetograph, *Astrophys. J.*, *118*, 387, doi:10.1086/145767. [10](#)
- Babcock, H. W. (1961), The Topology of the Sun’s Magnetic Field and the 22-YEAR Cycle, *Astrophys. J.*, *133*, 572, doi:10.1086/147060. [24](#)
- Bahcall, J. N., and R. Davis (1976), Solar neutrinos: a scientific puzzle, *Science*, *191*(4224), 264–267. [23](#)
- Bame, S. J., D. J. McComas, B. L. Barraclough, J. L. Phillips, K. J. Sofaly, J. C. Chavez, B. E. Goldstein, and R. K. Sakurai (1992), The ULYSSES solar wind plasma experiment, *Astron. Astrophys. Suppl.*, *92*(2), 237–265. [9](#)
- Bastian, T. (2010), Radiative signatures of energetic particles, in *Heliophysics: Space Storms and Radiation: Causes and Effects*, edited by C. J. Schrijver and G. L. Siscoe, p. 79, Cambridge University Press. [14](#)
- Bastian, T. S. (1994), Angular scattering of solar radio emission by coronal turbulence, *Astrophys. J.*, *426*, 774–781, doi:10.1086/174114. [19](#), [60](#), [104](#)
- Bastian, T. S. (2007), Synchrotron Radio Emission from a Fast Halo Coronal Mass Ejection, *Astrophys. J.*, *665*(1), 805–812, doi:10.1086/519246. [16](#)
- Bastian, T. S., A. O. Benz, and D. E. Gary (1998), Radio Emission from Solar Flares, *Ann. Rev. Astron. Astrophys.*, *36*, 131–188, doi:10.1146/annurev.astro.36.1.131. [91](#)
- Bastian, T. S., M. Pick, A. Kerdraon, D. Maia, and A. Vourlidas (2001), The Coronal Mass Ejection of 1998 April 20: Direct Imaging at Radio Wavelengths, *Astrophys. J. Lett.*, *558*(1), L65–L69, doi:10.1086/323421. [33](#), [153](#), [154](#)
- Basu, S. (2016), Global seismology of the sun, *Living Rev. Sol. Phys.*, *13*(1), 2, doi:10.1007/s41116-016-0003-4. [23](#)
- Bellot Rubio, L., and D. Orozco Suárez (2019), Quiet Sun magnetic fields: an observational

-
- view, *Living Rev. Sol. Phys.*, *16*(1), 1, doi:10.1007/s41116-018-0017-1. [26](#)
- Benkevitch, L. V., D. Oberoi, M. D. Benjamin, and I. V. Sokolov (2012), HART: An Efficient Modeling Framework for Simulated Solar Imaging, in *Astronomical Data Analysis Software and Systems XXI, Astronomical Society of the Pacific Conference Series*, vol. 461, edited by P. Ballester, D. Egret, and N. P. F. Lorente, p. 475. [139](#)
- Bentley, R. D., K.-L. Klein, L. van Driel-Gesztelyi, P. Démoulin, G. Trottet, P. Tassetto, and G. Marty (2000), Magnetic Activity Associated With Radio Noise Storms, *Solar Phys.*, *193*, 227–245, doi:10.1023/A:1005218007132. [35](#), [121](#)
- Benz, A. O., and D. G. Wentzel (1981), Coronal evolution and solar type I radio bursts - an ion-acoustic wave model, *Astron. Astrophys.*, *94*, 100–108. [34](#), [121](#)
- Benz, A. O., P. C. Grigis, A. Csillaghy, and P. Saint-Hilaire (2005), Survey on Solar X-ray Flares and Associated Coherent Radio Emissions, *Solar Phys.*, *226*, 121–142, doi:10.1007/s11207-005-5254-5. [37](#), [48](#), [89](#)
- Benz, A. O., R. Brajša, and J. Magdalenic (2007), Are There Radio-quiet Solar Flares?, *Solar Phys.*, *240*, 263–270, doi:10.1007/s11207-007-0365-9. [37](#), [48](#), [89](#)
- Berghmans, D., et al. (2006), SWAP onboard PROBA 2, a new EUV imager for solar monitoring, *Adv. Space Res.*, *38*(8), 1807–1811, doi:10.1016/j.asr.2005.03.070. [9](#)
- Biskamp, D. (2000), *Magnetic Reconnection in Plasmas*, vol. 3, Cambridge University Press, doi:10.1017/CBO9780511599958. [29](#)
- Bisoi, S. K., H. S. Sawant, P. Janardhan, Y. Yan, L. Chen, A. K. Awasthi, S. Srivastava, and G. Gao (2018), Decimetric Emission 500” Away from a Flaring Site: Possible Scenarios from GMRT Solar Radio Observations, *Astrophys. J.*, *862*, 65, doi:10.3847/1538-4357/aacd07. [83](#)
- Boischot, A. (1958), Étude du rayonnement radioélectrique solaire sur 169 MHz é l’aide d’un grand interféromètre à réseau, *Annales d’Astrophysique*, *21*, 273. [37](#)
- Bougeret, J. L., and J. L. Steinberg (1977), A new scattering process above solar active regions - Propagation in a fibrous medium, *Astron. Astrophys.*, *61*, 777–783. [83](#), [98](#)
- Bougeret, J.-L., J. H. King, and R. Schwenn (1984), Solar radio burst and in situ determination of interplanetary electron density, *Solar Phys.*, *90*, 401–412, doi:10.1007/BF00173965. [83](#)
- Bougeret, J.-L., et al. (1995), Waves: The Radio and Plasma Wave Investigation on the Wind Spacecraft, *Space Sci. Rev.*, *71*, 231–263, doi:10.1007/BF00751331. [51](#)
- Bouratzis, C., A. Hillaris, C. E. Alissandrakis, P. Preka-Papadema, X. Moussas, C. Caroubalos, P. Tsitsipis, and A. Kontogeorgos (2016), High resolution observations with Artemis-IV and the NRH. I. Type IV associated narrow-band bursts, *Astron. Astrophys.*, *586*, A29, doi:10.1051/0004-6361/201527229. [111](#)
- Bowman, J. D., et al. (2013), Science with the Murchison Widefield Array, *Pub. Astron. Soc. Austral.*, *30*, e031, doi:10.1017/pas.2013.009. [41](#), [49](#), [112](#)
- Bridge, H. S., J. W. Belcher, R. J. Butler, A. J. Lazarus, A. M. Mavretic, J. D. Sullivan, G. L. Siscoe, and V. M. Vasyliunas (1977), The Plasma Experiment on the 1977 Voyager Mission, *Space Sci. Rev.*, *21*(3), 259–287, doi:10.1007/BF00211542. [9](#)
- Briggs, D. S. (1995), High Fidelity Interferometric Imaging: Robust Weighting and NNLS Deconvolution, *Bull. Amer. Astron. Soc.*, *27*, 112.02. [54](#), [84](#), [113](#)

References

- Brown, J. C., and D. B. Melrose (1977), Collective plasma effects and the electron number problem in solar hard X-ray bursts, *Solar Phys.*, *52*, 117–131, doi:10.1007/BF00935795. [51](#)
- Brown, M. R., C. D. Cothran, M. Landreman, D. Schlossberg, and W. H. Matthaeus (2002), Experimental Observation of Energetic Ions Accelerated by Three-dimensional Magnetic Reconnection in a Laboratory Plasma, *Astrophys. J. Lett.*, *577*(1), L63–L66, doi:10.1086/344145. [29](#)
- Brueckner, G. E., et al. (1995), The Large Angle Spectroscopic Coronagraph (LASCO), *Solar Phys.*, *162*, 357–402, doi:10.1007/BF00733434. [5](#), [39](#), [89](#)
- Butterworth, S. (1930), On the theory of filter amplifiers, *Wireless Engineer*, *7*(6), 536–541. [121](#)
- Byhring, H. S., R. Esser, and Ø. Lie-Svendsen (2008), The Funnel Geometry of Open Flux Tubes in the Low Solar Corona Constrained by O VI and Ne VIII Outflow, *Astrophys. J. Lett.*, *673*, L91, doi:10.1086/527518. [105](#)
- Cairns, I. H. (1987a), Second harmonic plasma emission involving ion sound waves, *J. Plasma Phys.*, *38*(2), 179–198, doi:10.1017/S0022377800012502. [17](#)
- Cairns, I. H. (1987b), Fundamental plasma emission involving ion sound waves, *J. Plasma Phys.*, *38*(2), 169–178, doi:10.1017/S0022377800012496. [17](#)
- Cairns, I. H. (2000), Role of collective effects in dominance of scattering off thermal ions over Langmuir wave decay: Analysis, simulations, and space applications, *Phys. Plasmas*, *7*(12), 4901–4915, doi:10.1063/1.1319638. [45](#)
- Cairns, I. H. (2011), Coherent Radio Emissions Associated with Star System Shocks, in *The Sun, the Solar Wind, and the Heliosphere*, edited by M. P. Miralles and J. Sánchez Almeida, p. 267, Springer Netherlands, doi:10.1007/978-90-481-9787-3. [32](#), [35](#)
- Cairns, I. H., and R. D. Robinson (1987), Herringbone bursts associated with type II solar radio emission, *Solar Phys.*, *111*(2), 365–383, doi:10.1007/BF00148526. [35](#), [39](#)
- Cairns, I. H., S. A. Knock, P. A. Robinson, and Z. Kuncic (2003), Type II Solar Radio Bursts: Theory and Space Weather Implications, *Space Sci. Rev.*, *107*(1), 27–34, doi:10.1023/A:1025503201687. [35](#), [121](#)
- Cairns, I. H., V. V. Lobzin, A. Warmuth, B. Li, P. A. Robinson, and G. Mann (2009), Direct Radio Probing and Interpretation of the Sun’s Plasma Density Profile, *Astrophys. J. Lett.*, *706*, L265–L269, doi:10.1088/0004-637X/706/2/L265. [82](#), [94](#), [95](#), [97](#), [102](#), [103](#)
- Cairns, I. H., et al. (2018), Low Altitude Solar Magnetic Reconnection, Type III Solar Radio Bursts, and X-ray Emissions, *Sci. Rep.*, *8*, 1676, doi:10.1038/s41598-018-19195-3. [30](#), [37](#), [48](#), [49](#), [51](#), [89](#), [112](#)
- Cane, H. V., and R. G. Stone (1984), Type II solar radio bursts, interplanetary shocks, and energetic particle events, *Astrophys. J.*, *282*, 339–344, doi:10.1086/162207. [35](#)
- Cane, H. V., W. C. Erickson, and N. P. Prestage (2002), Solar flares, type III radio bursts, coronal mass ejections, and energetic particles, *J. Geophys. Res. (Space Phys.)*, *107*, 1315, doi:10.1029/2001JA000320. [89](#)
- Carley, E. P., N. Vilmer, and P. T. Gallagher (2016), Radio Diagnostics of Electron Acceleration Sites During the Eruption of a Flux Rope in the Solar Corona, *Astrophys. J.*, *833*, 87, doi:10.3847/1538-4357/833/1/87. [77](#), [95](#)

-
- Carmichael, H. (1964), A Process for Flares, in *The Physics of Solar Flares, Proceedings of the AAS-NASA Symposium held 28-30 October, 1963 at the Goddard Space Flight Center, Greenbelt, MD.*, vol. 50, edited by W. N. Hess, p. 451, National Aeronautics and Space Administration, Science and Technical Information Division. [30](#)
- Carrington, R. C. (1858), On the distribution of the solar spots in latitudes since the beginning of the year 1854, with a map, *Mon. Not. Roy. Astron. Soc.*, *19*, 1–3. [22](#)
- Carrington, R. C. (1859), Description of a Singular Appearance seen in the Sun on September 1, 1859, *Mon. Not. Roy. Astron. Soc.*, *20*, 13–15, doi:10.1093/mnras/20.1.13. [27](#)
- Carroll, P. A. (2016), Modeling the Extragalactic Epoch of Reionization Foreground, Ph.D. thesis, University of Washington. [42](#)
- Charbonneau, P. (2010), Dynamo Models of the Solar Cycle, *Living Rev. Sol. Phys.*, *7*(1), 3, doi:10.12942/lrsp-2010-3. [24](#)
- Chen, B., T. S. Bastian, S. M. White, D. E. Gary, R. Perley, M. Rupen, and B. Carlson (2013a), Tracing Electron Beams in the Sun’s Corona with Radio Dynamic Imaging Spectroscopy, *Astrophys. J. Lett.*, *763*, L21, doi:10.1088/2041-8205/763/1/L21. [49](#), [69](#), [89](#), [94](#), [96](#), [104](#)
- Chen, N., W.-H. Ip, and D. Innes (2013b), Flare-Associated Type III Radio Bursts and Dynamics of the EUV Jet from SDO/AIA and RHESSI Observations, *Astrophys. J.*, *769*, 96, doi:10.1088/0004-637X/769/2/96. [48](#)
- Clark, B. G. (1980), An efficient implementation of the algorithm ‘CLEAN’, *Astron. Astrophys.*, *89*(3), 377. [40](#)
- Cliver, E. W., and A. G. Ling (2009), Low-Frequency Type III Bursts and Solar Energetic Particle Events, *Astrophys. J.*, *690*, 598–609, doi:10.1088/0004-637X/690/1/598. [89](#)
- Cohen, M. H. (1960), Magnetoionic Mode Coupling at High Frequencies, *Astrophys. J.*, *131*, 664, doi:10.1086/146878. [20](#), [141](#)
- Committee On The Societal, and Economic Impacts Of Severe Space Weather Events (2008), Severe Space Weather Events—Understanding Societal and Economic Impacts: A Workshop Report, *Tech. rep.*, National Academies Press. [31](#)
- Craig, I. J. D., and D. I. Pontin (2014), Current Singularities in Line-tied Three-dimensional Magnetic Fields, *Astrophys. J.*, *788*, 177, doi:10.1088/0004-637X/788/2/177. [74](#)
- Cranmer, S. R. (2009), Coronal Holes, *Living Rev. Sol. Phys.*, *6*, 3, doi:10.12942/lrsp-2009-3. [26](#), [127](#)
- Cranmer, S. R., and L. N. Woolsey (2015), Driving Solar Spicules and Jets with Magnetohydrodynamic Turbulence: Testing a Persistent Idea, *Astrophys. J.*, *812*, 71, doi:10.1088/0004-637X/812/1/71. [140](#)
- Darwin, L., A. Schuster, and E. W. Maunder (1889), IX. on the total solar eclipse of august 29, 1886, *Philos. Trans. Royal Soc. A*, *180*, 291–350, doi:10.1098/rsta.1889.0009. [1](#)
- Davis Jr, R. (1964), Solar neutrinos. ii. experimental, *Phys. Rev. Lett.*, *12*(11), 303. [23](#)
- De la Rue, W. (1864), I. comparison of Mr. De la Rue’s and Padre Secchi’s eclipse photographs, *Proc. Royal Soc. Lond.*, *13*, 442–444. [1](#)
- De Moortel, I., and P. Browning (2015), Recent advances in coronal heating, *Philos. Trans. Royal Soc. A*, *373*(2042), 20140,269–20140,269, doi:10.1098/rsta.2014.0269. [2](#)
- De Pontieu, B., J. Martínez-Sykora, and G. Chintzoglou (2017), What Causes the High Ap-

References

- parent Speeds in Chromospheric and Transition Region Spicules on the Sun?, *Astrophys. J. Lett.*, *849*, L7, doi:10.3847/2041-8213/aa9272. [140](#)
- Del Zanna, G., G. Aulanier, K.-L. Klein, and T. Török (2011), A single picture for solar coronal outflows and radio noise storms, *Astron. Astrophys.*, *526*, A137, doi:10.1051/0004-6361/201015231. [34](#), [77](#), [121](#)
- Demoulin, P., J. C. Henoux, E. R. Priest, and C. H. Mandrini (1996), Quasi-Separatrix layers in solar flares. I. Method, *Astron. Astrophys.*, *308*, 643–655. [70](#)
- Dewdney, P. E., P. J. Hall, R. T. Schilizzi, and T. J. L. W. Lazio (2009), The Square Kilometre Array, *Proc. IEEE*, *97*(8), 1482–1496, doi:10.1109/JPROC.2009.2021005. [41](#)
- Domingo, V., B. Fleck, and A. I. Poland (1995), SOHO: The Solar and Heliospheric Observatory, *Space Sci. Rev.*, *72*, 81–84, doi:10.1007/BF00768758. [5](#), [9](#), [89](#)
- Downs, C., I. I. Roussev, B. van der Holst, N. Lugaz, and I. V. Sokolov (2012), Understanding SDO/AIA Observations of the 2010 June 13 EUV Wave Event: Direct Insight from a Global Thermodynamic MHD Simulation, *Astrophys. J.*, *750*, 134, doi:10.1088/0004-637X/750/2/134. [57](#)
- Dulk, G. A. (1985), Radio emission from the sun and stars, *Ann. Rev. Astron. Astrophys.*, *23*, 169–224, doi:10.1146/annurev.aa.23.090185.001125. [15](#), [16](#), [18](#), [19](#), [37](#), [38](#), [108](#), [109](#)
- Dulk, G. A. (2000), Type III Solar Radio Bursts at Long Wavelengths, *Geophys. Mono. Ser.*, *119*, 115, doi:10.1029/GM119p0115. [83](#)
- Dulk, G. A., and D. J. McLean (1978), Coronal magnetic fields, *Solar Phys.*, *57*, 279–295, doi:10.1007/BF00160102. [11](#), [110](#)
- Dulk, G. A., and K. V. Sheridan (1974), The Structure of the Middle Corona from Observations at 80 and 160 MHz, *Solar Phys.*, *36*, 191–202, doi:10.1007/BF00151560. [60](#), [127](#), [148](#)
- Dulk, G. A., D. E. Gary, and S. Suzuki (1980), The position and polarization of Type V solar bursts, *Astron. Astrophys.*, *88*(1-2), 218–229. [38](#), [91](#)
- Dulk, G. A., J. L. Steinberg, and S. Hoang (1984), Type III bursts in interplanetary space - Fundamental or harmonic?, *Astron. Astrophys.*, *141*, 30–38. [67](#), [110](#), [125](#)
- Dulk, G. A., J. L. Steinberg, A. Lecacheux, S. Hoang, and R. J. MacDowall (1985), The visibility of type III radio bursts originating behind the sun, *Astron. Astrophys.*, *150*(2), L28–L30. [19](#)
- Dulk, G. A., W. C. Erickson, R. Manning, and J.-L. Bougeret (2001), Calibration of low-frequency radio telescopes using the galactic background radiation, *Astron. Astrophys.*, *365*, 294–300, doi:10.1051/0004-6361:20000006. [78](#)
- Duncan, R. A. (1979), Wave ducting of solar metre-wave radio emission as an explanation of fundamental/harmonic source coincidence and other anomalies, *Solar Phys.*, *63*, 389–398, doi:10.1007/BF00174543. [20](#), [83](#), [98](#)
- Dziembowski, W. A., P. R. Goode, and K. G. Libbrecht (1989), The Radial Gradient in the Sun’s Rotation, *Astrophys. J. Lett.*, *337*, L53, doi:10.1086/185377. [23](#)
- Eddington, A. S. (1920), The Internal Constitution of the Stars, *Nature*, *106*(2653), 14–20, doi:10.1038/106014a0. [23](#)
- Edlén, B. (1945), The identification of the coronal lines (George Darwin Lecture), *Mon. Not. Roy. Astron. Soc.*, *105*, 323, doi:10.1093/mnras/105.6.323. [2](#)

-
- Edmondson, J. K. (2012), On the Role of Interchange Reconnection in the Generation of the Slow Solar Wind, *Space Sci. Rev.*, 172(1-4), 209–225, doi:10.1007/s11214-011-9767-y. [31](#)
- Elgarøy, E. Ø. (1977), *Solar noise storms*, Pergamon Press, Oxford, doi:10.1016/C2013-0-05754-4. [25](#), [34](#), [120](#), [125](#)
- Ellingson, S. W., T. E. Clarke, A. Cohen, J. Craig, N. E. Kassim, Y. Pihlstrom, L. J. Rickard, and G. B. Taylor (2009), The Long Wavelength Array, *Proc. IEEE*, 97(8), 1421–1430, doi:10.1109/JPROC.2009.2015683. [7](#)
- Ellis, G. R. A. (1969), Fine structure in the spectra of solar radio bursts, *Aust. J. Phys.*, 22, 177, doi:10.1071/PH690177. [39](#)
- Fabry, C., and A. Perot (1899), Theorie et applications d’une nouvelle methods de spectroscopie interferentielle, *Ann. Chim. Ser. 7*, 16, 115–144. [39](#)
- Fainberg, J., and R. G. Stone (1971), Type III Solar Radio Burst Storms Observed at Low Frequencies. III: Streamer Density, Inhomogeneities, and Solar Wind Speed, *Solar Phys.*, 17, 392–401, doi:10.1007/BF00150042. [82](#)
- Fan, Y., G. Fisher, and E. DeLuca (1993), The origin of morphological asymmetries in bipolar active regions, *Astrophys. J.*, 405, 390–401. [24](#)
- Forbes, T. G. (2000), A review on the genesis of coronal mass ejections, *J. Geophys. Res.*, 105(A10), 23,153–23,166, doi:10.1029/2000JA000005. [32](#)
- Foukal, P. V. (2004), *Solar Astrophysics, 2nd, Revised Edition*, John Wiley & Sons. [22](#)
- Frank, L. A., and D. A. Gurnett (1972), Direct Observations of Low-Energy Solar Electrons Associated with a Type III Solar Radio Burst, *Solar Phys.*, 27(2), 446–465, doi:10.1007/BF00153116. [10](#)
- Freeland, S. L., and B. N. Handy (1998), Data Analysis with the SolarSoft System, *Solar Phys.*, 182, 497–500, doi:10.1023/A:1005038224881. [55](#), [84](#), [113](#)
- Garrett, M. A. (2012), Radio Astronomy Transformed: Aperture Arrays - Past, Present & Future, in *From Antikythera to the Square Kilometre Array: Lessons from the Ancients*, p. 41. [43](#)
- Gary, D. E., and G. J. Hurford (2005), Radio spectral diagnostics, in *Solar and Space Weather Radiophysics: Current Status and Future Developments*, edited by D. E. Gary and C. U. Keller, pp. 71–87, Springer Netherlands, Dordrecht, doi:10.1007/1-4020-2814-8_4. [12](#)
- Gelfreikh, G. B. (2004), Coronal Magnetic Field Measurements Through Bremsstrahlung Emission, in *Astrophysics and Space Science Library*, vol. 314, edited by D. E. Gary and C. U. Keller, p. 115, doi:10.1007/1-4020-2814-8_6. [109](#)
- Gergely, T. E., and W. C. Erickson (1975), Decameter storm radiation. I, *Solar Phys.*, 42, 467–486, doi:10.1007/BF00149927. [25](#), [34](#), [125](#)
- Gibson, S., T. Kucera, S. White, J. Dove, Y. Fan, B. Forland, L. Rachmeler, C. Downs, and K. Reeves (2016), FORWARD: A toolset for multiwavelength coronal magnetometry, *Frontiers Astron. Space Sci.*, 3, 8, doi:10.3389/fspas.2016.00008. [14](#), [57](#), [85](#), [99](#), [109](#), [116](#), [119](#), [149](#)
- Gibson, S. E., A. Fludra, F. Bagenal, D. Biesecker, G. del Zanna, and B. Bromage (1999), Solar minimum streamer densities and temperatures using Whole Sun Month coordinated data sets, *J. Geophys. Res.*, 104, 9691–9700, doi:10.1029/98JA02681. [93](#)
- Ginzburg, V. (1946), On solar radiation in the radio spectrum, in *CR (Doklady) Acad. Sci.*

References

- USSR*, vol. 52, p. 487. [5](#), [15](#)
- Ginzburg, V. (1970), *The propagation of electromagnetic waves in plasmas*, International series of monographs on electromagnetic waves, Pergamon Press, Oxford. [13](#)
- Ginzburg, V. L., and V. V. Zhelezniakov (1958), On the Possible Mechanisms of Sporadic Solar Radio Emission (Radiation in an Isotropic Plasma), *Soviet Astron.*, *2*, 653. [17](#), [48](#), [82](#), [109](#)
- Golub, L., and J. Pasachoff (2010), *The Solar Corona*, 2nd ed., Cambridge University Press. [1](#), [2](#), [3](#), [4](#), [7](#), [9](#), [22](#), [25](#), [26](#), [27](#), [31](#)
- Golub, L., R. Rosner, G. S. Vaiana, and N. O. Weiss (1981), Solar magnetic fields - The generation of emerging flux, *Astrophys. J.*, *243*, 309–316, doi:10.1086/158599. [24](#)
- Gopalswamy, N. (2006), Coronal Mass Ejections and Type II Radio Bursts, *Washington DC American Geophysical Union Geophysical Monograph Series*, *165*, 207, doi:10.1029/165GM20. [32](#)
- Gopalswamy, N., M. R. Kundu, and A. Szabo (1987), Propagation of electrons emitting weak type III bursts in coronal streamers, *Solar Phys.*, *108*, 333–345, doi:10.1007/BF00214168. [27](#), [83](#)
- Gopalswamy, N., M. R. Kundu, A. Raoult, and M. Pick (1994), Non-radial magnetic field structures in the solar corona, *Solar Phys.*, *150*, 317–323, doi:10.1007/BF00712893. [111](#)
- Gopalswamy, N., S. Yashiro, M. L. Kaiser, R. A. Howard, and J. L. Bougeret (2001), Characteristics of coronal mass ejections associated with long-wavelength type II radio bursts, *J. Geophys. Res.*, *106*(A12), 29,219–29,230, doi:10.1029/2001JA000234. [35](#)
- Gopalswamy, N., M. Shimojo, W. Lu, S. Yashiro, K. Shibasaki, and R. A. Howard (2003), Prominence Eruptions and Coronal Mass Ejection: A Statistical Study Using Microwave Observations, *Astrophys. J.*, *586*(1), 562–578, doi:10.1086/367614. [32](#)
- Gopalswamy, N., S. Yashiro, G. Michalek, G. Stenborg, A. Vourlidas, S. Freeland, and R. Howard (2009), The SOHO/LASCO CME Catalog, *Earth Moon and Planets*, *104*(1–4), 295–313, doi:10.1007/s11038-008-9282-7. [32](#)
- Goryaev, F., V. Slemzin, L. Vainshtein, and D. R. Williams (2014), Study of Extreme-ultraviolet Emission and Properties of a Coronal Streamer from PROBA2/SWAP, Hinode/EIS and Mauna Loa Mk4 Observations, *Astrophys. J.*, *781*, 100, doi:10.1088/0004-637X/781/2/100. [92](#), [93](#), [97](#), [101](#), [102](#)
- Gosling, J. T., E. Hildner, R. M. MacQueen, R. H. Munro, A. I. Poland, and C. L. Ross (1974), Mass ejections from the Sun: A view from Skylab, *J. Geophys. Res.*, *79*(31), 4581, doi:10.1029/JA079i031p04581. [31](#)
- Grebinskij, A., V. Bogod, G. Gelfreikh, S. Urpo, S. Pohjolainen, and K. Shibasaki (2000), Microwave tomography of solar magnetic fields, *Astron. Astrophys. Suppl.*, *144*, 169–180, doi:10.1051/aas:2000202. [110](#)
- Guhathakurta, M., T. E. Holzer, and R. M. MacQueen (1996), The Large-Scale Density Structure of the Solar Corona and the Heliospheric Current Sheet, *Astrophys. J.*, *458*, 817, doi:10.1086/176860. [93](#)
- Guidice, D. A., E. W. Cliver, W. R. Barron, and S. Kahler (1981), The Air Force RSTN System, *Bull. Amer. Astron. Soc.*, *13*, 553. [51](#), [85](#)
- Gurnett, D. A., and R. R. Anderson (1976), Electron Plasma Oscillations Associated with

-
- Type III Radio Bursts, *Science*, *194*(4270), 1159–1162, doi:10.1126/science.194.4270.1159. [10](#)
- Habbal, S. R. (1992), Coronal energy distribution and X-ray activity in the small scale magnetic field of the quiet sun, *Annales Geophysicae*, *10*(1-2), 34–46. [27](#)
- Habbal, S. R., H. Morgan, M. Druckmüller, A. Ding, J. F. Cooper, A. Daw, and E. C. Sittler (2013), Probing the Fundamental Physics of the Solar Corona with Lunar Solar Occultation Observations, *Solar Phys.*, *285*(1-2), 9–24, doi:10.1007/s11207-012-0115-5. [4](#)
- Hagyard, M. J., R. L. Moore, and A. G. Emslie (1984), The role of magnetic field shear in solar flares, *Adv. Space Res.*, *4*(7), 71–80, doi:10.1016/0273-1177(84)90162-5. [29](#)
- Hahn, M., and D. W. Savin (2016), Inferring the Coronal Density Irregularity from EUV Spectra, *Astrophys. J.*, *829*, 42, doi:10.3847/0004-637X/829/1/42. [19](#), [105](#)
- Hale, G. E. (1908), On the probable existence of a magnetic field in sun-spots, *Astrophys. J.*, *28*, 315. [10](#), [22](#)
- Hale, G. E. (1931), The Spectroheliograph and its Work. Part III. Solar Eruptions and Their Apparent Terrestrial Effects, *Astrophys. J.*, *73*, 379, doi:10.1086/143316. [31](#)
- Hale, G. E., F. Ellerman, S. B. Nicholson, and A. H. Joy (1919), The magnetic polarity of sun-spots, *Astrophys. J.*, *49*, 153. [22](#)
- Hariharan, K., R. Ramesh, P. Kishore, C. Kathiravan, and N. Gopalswamy (2014), An Estimate of the Coronal Magnetic Field near a Solar Coronal Mass Ejection from Low-frequency Radio Observations, *Astrophys. J.*, *795*, 14, doi:10.1088/0004-637X/795/1/14. [111](#)
- Hariharan, K., R. Ramesh, and C. Kathiravan (2015), Observations of Near-Simultaneous Split-Band Solar Type-II Radio Bursts at Low Frequencies, *Solar Phys.*, *290*, 2479–2489, doi:10.1007/s11207-015-0761-5. [111](#)
- Hariharan, K., R. Ramesh, C. Kathiravan, and T. J. Wang (2016), Simultaneous Near-Sun Observations of a Moving Type IV Radio Burst and the Associated White-Light Coronal Mass Ejection, *Solar Phys.*, *291*, 1405–1416, doi:10.1007/s11207-016-0918-x. [111](#)
- Harrison, R. A. (1991), Coronal transients and their relation to solar flares, *Adv. Space Res.*, *11*(1), 25–36, doi:10.1016/0273-1177(91)90085-X. [31](#)
- Harrison, R. A. (1997), EUV Blinkers: The Significance of Variations in the Extreme Ultraviolet Quiet Sun, *Solar Phys.*, *175*(2), 467–485, doi:10.1023/A:1004964707047. [27](#)
- Harvey, K. L., and F. Recely (2002), Polar Coronal Holes During Cycles 22 and 23, *Solar Phys.*, *211*(1), 31–52, doi:10.1023/A:1022469023581. [26](#)
- Harvey, K. L., and C. Zwaan (1993), Properties and emergence of bipolar active regions, *Solar Phys.*, *148*, 85–118, doi:10.1007/BF00675537. [25](#)
- Hathaway, D. H. (2015), The solar cycle, *Living Rev. Sol. Phys.*, *12*(1), 4, doi:10.1007/lrsp-2015-4. [22](#)
- Hathaway, D. H., and D. P. Choudhary (2008), Sunspot Group Decay, *Solar Phys.*, *250*(2), 269–278, doi:10.1007/s11207-008-9226-4. [26](#)
- Hayes, A. P., A. Vourlidas, and R. A. Howard (2001), Deriving the Electron Density of the Solar Corona from the Inversion of Total Brightness Measurements, *Astrophys. J.*, *548*, 1081–1086, doi:10.1086/319029. [4](#)
- He, J.-S., C.-Y. Tu, and E. Marsch (2008), Modeling of Solar Wind in the Coronal

References

- Funnel with Mass and Energy Supplied at 5 Mm, *Solar Phys.*, 250, 147–158, doi:10.1007/s11207-008-9214-8. [105](#)
- Hey, J. S. (1946), Solar Radiations in the 4-6 Metre Radio Wave-Length Band, *Nature*, 157, 47–48, doi:10.1038/157047b0. [5](#)
- Hill, F., et al. (2009), The Virtual Solar Observatory—A Resource for International Helio-physics Research, *Earth Moon and Planets*, 104, 315–330, doi:10.1007/s11038-008-9274-7. [56](#), [106](#), [144](#)
- Hirayama, T. (1974), Theoretical Model of Flares and Prominences. I: Evaporating Flare Model, *Solar Phys.*, 34(2), 323–338, doi:10.1007/BF00153671. [30](#)
- Hoang, S., and J. L. Steinberg (1977), About the computed meter-wavelength thermal radiation from coronal streamers and coronal holes, *Astron. Astrophys.*, 58, 287–290. [60](#)
- Hodgson, R. (1859), On a curious Appearance seen in the Sun, *Mon. Not. Roy. Astron. Soc.*, 20, 15–16, doi:10.1093/mnras/20.1.15. [27](#)
- Högbom, J. A. (1974), Aperture Synthesis with a Non-Regular Distribution of Interferometer Baselines, *Astron. Astrophys. Suppl.*, 15, 417. [40](#)
- Holzer, T. E. (1989), Interaction between the solar wind and the interstellar medium, *Ann. Rev. Astron. Astrophys.*, 27, 199–234, doi:10.1146/annurev.aa.27.090189.001215. [3](#)
- Hong, J., Y. Jiang, J. Yang, H. Li, and Z. Xu (2017), Minifilament Eruption as the Source of a Blowout Jet, C-class Flare, and Type-III Radio Burst, *Astrophys. J.*, 835, 35, doi:10.3847/1538-4357/835/1/35. [48](#)
- Howard, R. A., et al. (2008), Sun Earth Connection Coronal and Heliospheric Investigation (SECCHI), *Space Sci. Rev.*, 136, 67–115, doi:10.1007/s11214-008-9341-4. [90](#)
- Hudson, H., B. Haisch, and K. T. Strong (1995), Comment on “The solar flare myth” by J. T. Gosling, *J. Geophys. Res.*, 100(A3), 3473–3478, doi:10.1029/94JA02710. [31](#)
- Hundhausen, A. (1999), Coronal Mass Ejections, in *The many faces of the sun: a summary of the results from NASA’s Solar Maximum Mission.*, edited by K. T. Strong, J. L. R. Saba, B. M. Haisch, and J. T. Schmelz, p. 143. [32](#)
- Hurlburt, N., et al. (2012), Heliophysics Event Knowledgebase for the Solar Dynamics Observatory (SDO) and Beyond, *Solar Phys.*, 275(1-2), 67–78, doi:10.1007/s11207-010-9624-2. [44](#)
- Hurley-Walker, N., et al. (2014), The Murchison Widefield Array Commissioning Survey: A Low-Frequency Catalogue of 14 110 Compact Radio Sources over 6 100 Square Degrees, *Pub. Astron. Soc. Austral.*, 31, e045, doi:10.1017/pasa.2014.40. [53](#), [84](#), [113](#)
- Hurley-Walker, N., et al. (2017), GaLactic and Extragalactic All-sky Murchison Widefield Array (GLEAM) survey - I. A low-frequency extragalactic catalogue, *Mon. Not. Roy. Astron. Soc.*, 464, 1146–1167, doi:10.1093/mnras/stw2337. [53](#), [61](#), [84](#), [113](#)
- IAU (1973), Commission 40: Radio astronomy (radio astronomie), *Transactions of the International Astronomical Union*, 15(2), 165–167, doi:10.1017/S0251107X00031606. [113](#)
- IEEE (1969), Ieee standard definitions of terms for radio wave propagation, *IEEE Transactions on Antennas and Propagation*, 17(3), 270–275, doi:10.1109/TAP.1969.1139448. [113](#)
- Ingale, M., P. Subramanian, and I. Cairns (2015), Coronal turbulence and the angular broadening of radio sources - the role of the structure function, *Mon. Not. Roy. Astron. Soc.*,

-
- 447, 3486–3497, doi:10.1093/mnras/stu2703. [19](#), [60](#), [104](#)
- Ingleby, L. D., S. R. Spangler, and C. A. Whiting (2007), Probing the Large-Scale Plasma Structure of the Solar Corona with Faraday Rotation Measurements, *Astrophys. J.*, *668*, 520–532, doi:10.1086/521140. [14](#)
- Innes, D. E., R. Bučík, L.-J. Guo, and N. Nitta (2016), Observations of solar X-ray and EUV jets and their related phenomena, *Astronomische Nachrichten*, *337*, 1024, doi:10.1002/asna.201612428. [48](#), [89](#)
- Iwai, K., H. Misawa, F. Tsuchiya, A. Morioka, S. Masuda, and Y. Miyoshi (2012), Survey of Accelerated Particles in a Solar Active Region Using Hinode/XRT and Ground-Based Type-I Radio Burst Observations, in *Hinode-3: The 3rd Hinode Science Meeting, Astrophysical Society of the Pacific Conference Series*, vol. 454, edited by T. Sekii, T. Watanabe, and T. Sakurai, p. 249. [34](#), [121](#)
- Jaeggli, S. A., and A. A. Norton (2016), The Magnetic Classification of Solar Active Regions 1992–2015, *Astrophys. J. Lett.*, *820*(1), L11, doi:10.3847/2041-8205/820/1/L11. [25](#)
- Janssen, P. (1873), The Coronal Atmosphere of the Sun: II, *Nature*, *8*(190), 149–150, doi:10.1038/008149a0. [1](#)
- Janvier, M., G. Aulanier, E. Pariat, and P. Démoulin (2013), The standard flare model in three dimensions. III. Slip-running reconnection properties, *Astron. Astrophys.*, *555*, A77, doi:10.1051/0004-6361/201321164. [70](#)
- Janvier, M., A. Savcheva, E. Pariat, S. Tassev, S. Millholland, V. Bommier, P. McCauley, S. McKillop, and F. Dougan (2016), Evolution of flare ribbons, electric currents, and quasi-separatrix layers during an X-class flare, *Astron. Astrophys.*, *591*, A141, doi:10.1051/0004-6361/201628406. [70](#)
- Kahler, S. W. (1992), Solar flares and coronal mass ejections, *Ann. Rev. Astron. Astrophys.*, *30*, 113–141, doi:10.1146/annurev.aa.30.090192.000553. [31](#)
- Kai, K. (1962), Some Characteristics of Type I Burst, *Pub. Astron. Soc. Japan*, *14*, 1. [110](#)
- Kaiser, M. L., T. A. Kucera, J. M. Davila, O. C. St. Cyr, M. Guhathakurta, and E. Christian (2008), The STEREO Mission: An Introduction, *Space Sci. Rev.*, *136*(1-4), 5–16, doi:10.1007/s11214-007-9277-0. [9](#)
- Kaneda, K., H. Misawa, K. Iwai, F. Tsuchiya, and T. Obara (2015), Frequency Dependence of Polarization of Zebra Pattern in Type-IV Solar Radio Bursts, *Astrophys. J. Lett.*, *808*, L45, doi:10.1088/2041-8205/808/2/L45. [20](#), [110](#), [141](#)
- Kaneda, K., H. Misawa, K. Iwai, F. Tsuchiya, T. Obara, Y. Katoh, and S. Masuda (2017), Polarization Characteristics of Zebra Patterns in Type IV Solar Radio Bursts, *Astrophys. J.*, *842*, 45, doi:10.3847/1538-4357/aa74c1. [20](#), [37](#), [110](#)
- Kaplan, D. L., et al. (2015), Murchison Widefield Array Observations of Anomalous Variability: A Serendipitous Night-time Detection of Interplanetary Scintillation, *Astrophys. J. Lett.*, *809*, L12, doi:10.1088/2041-8205/809/1/L12. [42](#), [112](#)
- Kayshap, P., K. Murawski, A. K. Srivastava, and B. N. Dwivedi (2018), Rotating network jets in the quiet Sun as observed by IRIS, *Astron. Astrophys.*, *616*, A99, doi:10.1051/0004-6361/201730990. [140](#)
- Kennewell, J., and G. Steward (2003), Solar Radio Spectrograph [SRS] Data Viewer, *Tech. rep.*, Sydney, IPS Radio and Space Serv. [51](#), [85](#)

References

- Kerdran, A., and J.-M. Delouis (1997), The Nançay Radioheliograph, in *Coronal Physics from Radio and Space Observations, Lecture Notes in Physics, Berlin Springer Verlag*, vol. 483, edited by G. Trottet, p. 192, doi:10.1007/BFb0106458. [7](#), [49](#), [111](#)
- Kishore, P., R. Ramesh, C. Kathiravan, and M. Rajalingam (2015), A Low-Frequency Radio Spectropolarimeter for Observations of the Solar Corona, *Solar Phys.*, *290*, 2409–2422, doi:10.1007/s11207-015-0705-0. [111](#)
- Kishore, P., C. Kathiravan, R. Ramesh, and E. Ebenezer (2017), Coronal Magnetic Field Lines and Electrons Associated with Type III-V Radio Bursts in a Solar Flare, *J. Astrophys. Astron.*, *38*, #24, doi:10.1007/s12036-017-9444-y. [76](#), [82](#), [95](#), [111](#)
- Klassen, A., M. Karlický, and G. Mann (2003), Superluminal apparent velocities of relativistic electron beams in the solar corona, *Astron. Astrophys.*, *410*, 307–314, doi:10.1051/0004-6361:20031247. [77](#), [95](#)
- Klein, K.-L. (1998), Suprathermal Electrons in Non-flaring Active Regions (Invited review), in *Three-Dimensional Structure of Solar Active Regions, Astronomical Society of the Pacific Conference Series*, vol. 155, edited by C. E. Alissandrakis and B. Schmieder, p. 182. [34](#), [120](#)
- Klimchuk, J. A. (2006), On Solving the Coronal Heating Problem, *Solar Phys.*, *234*(1), 41–77, doi:10.1007/s11207-006-0055-z. [2](#)
- Komesaroff, M. (1958), Polarization Measurements of the Three Spectral Types of Solar Radio Burst, *Aust. J. Phys.*, *11*, 201, doi:10.1071/PH580201. [35](#)
- Kong, X., et al. (2016), Observation of a Metric Type N Solar Radio Burst, *Astrophys. J.*, *830*, 37, doi:10.3847/0004-637X/830/1/37. [20](#), [111](#), [141](#)
- Kontar, E. P., S. Yu, A. A. Kuznetsov, A. G. Emslie, B. Alcock, N. L. S. Jeffrey, V. N. Melnik, N. H. Bian, and P. Subramanian (2017), Imaging spectroscopy of solar radio burst fine structures, *Nature Comm.*, *8*, 1515, doi:10.1038/s41467-017-01307-8. [83](#), [91](#)
- Kopp, R. A., and G. W. Pneuman (1976), Magnetic reconnection in the corona and the loop prominence phenomenon, *Solar Phys.*, *50*(1), 85–98, doi:10.1007/BF00206193. [30](#)
- Koskinen, H. E. J. (2011), Waves in cold plasma approximation, in *Physics of Space Storms: From the Solar Surface to the Earth*, pp. 113–139, Springer, Berlin, Heidelberg, doi:10.1007/978-3-642-00319-6_4. [13](#)
- Kosugi, T., et al. (2007), The Hinode (Solar-B) Mission: An Overview, *Solar Phys.*, *243*(1), 3–17, doi:10.1007/s11207-007-9014-6. [9](#)
- Koutchmy, S. (1988), Space-borne coronagraphy, *Space Sci. Rev.*, *47*(1-2), 95–143, doi:10.1007/BF00223238. [5](#)
- Koutchmy, S. (1994), Coronal physics from eclipse observations, *Adv. Space Res.*, *14*, doi:10.1016/0273-1177(94)90156-2. [93](#)
- Koutchmy, S., and M. Livshits (1992), Coronal Streamers, *Space Sci. Rev.*, *61*(3-4), 393–417, doi:10.1007/BF00222313. [27](#)
- Kramar, M., H. Lin, and S. Tomczyk (2016), Direct Observation of Solar Coronal Magnetic Fields by Vector Tomography of the Coronal Emission Line Polarizations, *Astrophys. J. Lett.*, *819*(2), L36, doi:10.3847/2041-8205/819/2/L36. [11](#)
- Krieger, A. S., A. F. Timothy, and E. C. Roelof (1973), A Coronal Hole and Its Identification as the Source of a High Velocity Solar Wind Stream, *Solar Phys.*, *29*(2), 505–525, doi:

-
- 10.1007/BF00150828. [26](#)
- Krucker, S., E. P. Kontar, S. Christe, and R. P. Lin (2007), Solar Flare Electron Spectra at the Sun and near the Earth, *Astrophys. J. Lett.*, *663*, L109–L112, doi:10.1086/519373. [51](#)
- Krupar, V., E. P. Kontar, J. Soucek, O. Santolik, M. Maksimovic, and O. Kruparova (2015), On the speed and acceleration of electron beams triggering interplanetary type III radio bursts, *Astron. Astrophys.*, *580*, A137, doi:10.1051/0004-6361/201425308. [82](#)
- Kumari, A., R. Ramesh, C. Kathiravan, and T. J. Wang (2017), Strength of the Solar Coronal Magnetic Field - A Comparison of Independent Estimates Using Contemporaneous Radio and White-Light Observations, *Solar Phys.*, *292*, 161, doi:10.1007/s11207-017-1180-6. [111](#)
- Kundu, M. R., and R. G. Stone (1984), Observations of solar radio bursts from meter to kilometer wavelengths, *Adv. Space Res.*, *4*, 261–270, doi:10.1016/0273-1177(84)90194-7. [27](#), [83](#), [103](#)
- Kundu, M. R., and L. Vlahos (1982), Solar microwave bursts - A review, *Space Sci. Rev.*, *32*, 405–462, doi:10.1007/BF00177449. [39](#), [99](#)
- Kundu, M. R., T. E. Gergely, and W. C. Erickson (1977), Observations of the quiet Sun at meter and decameter wavelengths, *Solar Phys.*, *53*(2), 489–496, doi:10.1007/BF00160291. [26](#)
- Kundu, M. R., W. C. Erickson, T. E. Gergely, M. J. Mahoney, and P. J. Turner (1983), First results from the Clark Lake Multifrequency Radioheliograph, *Solar Phys.*, *83*, 385–389, doi:10.1007/BF00148288. [7](#), [49](#)
- Kundu, M. R., J. P. Raulin, N. Nitta, H. S. Hudson, M. Shimojo, K. Shibata, and A. Raoult (1995), Detection of Nonthermal Radio Emission from Coronal X-Ray Jets, *Astrophys. J. Lett.*, *447*, L135, doi:10.1086/309567. [48](#)
- Lang, K. R. (2001), *The Cambridge Encyclopedia of the Sun*, 268 pp., Cambridge University Press. [3](#)
- Lang, K. R. (2006), The violent sun, in *Sun, Earth and Sky*, pp. 136–163, Springer, New York, NY, doi:10.1007/978-0-387-33365-6_7. [30](#)
- Lantos, P. (1999), Low Frequency Observations of the Quiet Sun: a Review, in *Proceedings of the Nobeyama Symposium*, vol. 479, edited by T. S. Bastian, N. Gopalswamy, and K. Shibasaki, pp. 11–24. [26](#), [60](#), [99](#), [127](#)
- Lantos, P., C. E. Alissandrakis, T. Gergely, and M. R. Kundu (1987), Quiet sun and slowly varying component at meter and decameter wavelengths, *Solar Phys.*, *112*, 325–340, doi:10.1007/BF00148787. [60](#), [127](#), [148](#)
- Lau, Y.-T., and J. M. Finn (1990), Three-dimensional kinematic reconnection in the presence of field nulls and closed field lines, *Astrophys. J.*, *350*, 672–691, doi:10.1086/168419. [70](#)
- Lazarian, A., G. Eyink, E. Vishniac, and G. Kowal (2015), Turbulent reconnection and its implications, *Philos. Trans. Royal Soc. A*, *373*(2041), 20140,144–20140,144, doi:10.1098/rsta.2014.0144. [30](#)
- Le Squeren, A. M. (1963), Étude des orages radioélectriques solaires sur 169 MHz à l’aide de l’interféromètre en croix de la station de Nançay, *Annales d’Astrophysique*, *26*, 97. [25](#), [34](#), [125](#)
- Leblanc, Y. (1973), Scattering Effects on the Relative Positions and Intensities of Fundamental and Harmonic Emission of Solar Radio Bursts, *Astrophys. Lett.*, *14*, L41. [83](#)

References

- Leblanc, Y., and J. de La Noe (1977), Solar radio type III bursts and coronal density structures, *Solar Phys.*, *52*, 133–139, doi:10.1007/BF00935796. [83](#)
- Leblanc, Y., T. B. H. Kuiper, and S. F. Hansen (1974), Coronal Density Structures in Regions of Type III Activity, *Solar Phys.*, *37*, 215–233, doi:10.1007/BF00157858. [83](#)
- Leblanc, Y., G. A. Dulk, and J.-L. Bougeret (1998), Tracing the Electron Density from the Corona to 1au, *Solar Phys.*, *183*, 165–180, doi:10.1023/A:1005049730506. [82](#)
- Lecacheux, A., J.-L. Steinberg, S. Hoang, and G. A. Dulk (1989), Characteristics of type III bursts in the solar wind from simultaneous observations on board ISEE-3 and Voyager, *Astron. Astrophys.*, *217*, 237–250. [83](#)
- Lee, J. (2007), Radio Emissions from Solar Active Regions, *Space Sci. Rev.*, *133*(1-4), 73–102, doi:10.1007/s11214-007-9206-2. [25](#)
- Leighton, R. B., R. W. Noyes, and G. W. Simon (1962), Velocity fields in the solar atmosphere. i. preliminary report., *Astrophys. J.*, *135*, 474. [23](#)
- Lemen, J. R., et al. (2012), The Atmospheric Imaging Assembly (AIA) on the Solar Dynamics Observatory (SDO), *Solar Phys.*, *275*, 17–40, doi:10.1007/s11207-011-9776-8. [9](#), [56](#), [89](#), [125](#)
- Lenc, E., et al. (2017), The Challenges of Low-Frequency Radio Polarimetry: Lessons from the Murchison Widefield Array, *Pub. Astron. Soc. Austral.*, *34*, e040, doi:10.1017/pasa.2017.36. [114](#), [115](#), [119](#), [130](#)
- Lenc, E., T. Murphy, C. R. Lynch, D. L. Kaplan, and S. N. Zhang (2018), An all-sky survey of circular polarization at 200 MHz, *Mon. Not. Roy. Astron. Soc.*, *478*, 2835–2849, doi:10.1093/mnras/sty1304. [115](#)
- Li, B., and I. H. Cairns (2013), Type III bursts produced by power law injected electrons in Maxwellian background coronal plasmas, *J. Geophys. Res. (Space Phys.)*, *118*, 4748–4759, doi:10.1002/jgra.50445. [91](#), [105](#)
- Li, B., and I. H. Cairns (2014), Fundamental Emission of Type III Bursts Produced in Non-Maxwellian Coronal Plasmas with Kappa-Distributed Background Particles, *Solar Phys.*, *289*, 951–976, doi:10.1007/s11207-013-0375-8. [91](#), [105](#)
- Li, B., P. A. Robinson, and I. H. Cairns (2006), Numerical Simulations of Type-III Solar Radio Bursts, *Phys. Rev. Lett.*, *96*(14), 145005, doi:10.1103/PhysRevLett.96.145005. [45](#)
- Li, B., I. H. Cairns, and P. A. Robinson (2008), Simulations of coronal type III solar radio bursts: 1. Simulation model, *J. Geophys. Res. (Space Phys.)*, *113*(A6), A06104, doi:10.1029/2007JA012957. [45](#)
- Li, B., I. H. Cairns, and P. A. Robinson (2011a), Effects of Spatial Variations in Coronal Electron and Ion Temperatures on Type III Bursts. II. Variations in Ion Temperature, *Astrophys. J.*, *730*, 21, doi:10.1088/0004-637X/730/1/21. [78](#), [105](#)
- Li, B., I. H. Cairns, and P. A. Robinson (2011b), Effects of Spatial Variations in Coronal Temperatures on Type III Bursts. I. Variations in Electron Temperature, *Astrophys. J.*, *730*, 20, doi:10.1088/0004-637X/730/1/20. [78](#), [105](#)
- Li, B., I. H. Cairns, and P. A. Robinson (2012), Frequency Fine Structures of Type III Bursts Due to Localized Medium-Scale Density Structures Along Paths of Type III Beams, *Solar Phys.*, *279*, 173–196, doi:10.1007/s11207-012-0001-1. [78](#), [105](#)
- Li, C. Y., Y. Chen, B. Wang, G. P. Ruan, S. W. Feng, G. H. Du, and X. L. Kong (2017),

-
- EUV and Magnetic Activities Associated with Type-I Solar Radio Bursts, *Solar Phys.*, *292*, 82, doi:10.1007/s11207-017-1108-1. [34](#), [35](#), [121](#)
- Lin, H., and T. Rimmele (1999), The Granular Magnetic Fields of the Quiet Sun, *Astrophys. J.*, *514*(1), 448–455, doi:10.1086/306925. [26](#)
- Lin, R. P., L. G. Evans, and J. Fainberg (1973), Simultaneous Observations of Fast Solar Electrons and Type III Radio Burst Emission Near 1 AU, *Astrophys. Lett.*, *14*, 191. [10](#)
- Lin, R. P., et al. (2002), The Reuven Ramaty High-Energy Solar Spectroscopic Imager (RHESSI), *Solar Phys.*, *210*, 3–32, doi:10.1023/A:1022428818870. [9](#), [51](#)
- Lionello, R., J. A. Linker, and Z. Mikić (2009), Multispectral Emission of the Sun During the First Whole Sun Month: Magnetohydrodynamic Simulations, *Astrophys. J.*, *690*, 902–912, doi:10.1088/0004-637X/690/1/902. [57](#), [85](#), [99](#), [116](#)
- Liu, H., Y. Chen, K. Cho, S. Feng, V. Vasanth, A. Koval, G. Du, Z. Wu, and C. Li (2018), A Solar Stationary Type IV Radio Burst and Its Radiation Mechanism, *Solar Phys.*, *293*(4), 58, doi:10.1007/s11207-018-1280-y. [19](#), [111](#)
- Lobzin, V. V., I. H. Cairns, P. A. Robinson, A. Warmuth, G. Mann, R. V. Gorgutsa, and V. V. Fomichev (2010), Evidence for Gently Sloping Plasma Density Profiles in the Deep Corona: Type III Observations, *Astrophys. J.*, *724*, 1099–1107, doi:10.1088/0004-637X/724/2/1099. [95](#)
- Lockyer, W. J. S. (1920), Helium: Its Discovery and Applications, *Nature*, *105*(2638), 360–363, doi:10.1038/105360a0. [1](#)
- Loi, S. T., I. H. Cairns, and B. Li (2014), Production of Fine Structures in Type III Solar Radio Bursts Due to Turbulent Density Profiles, *Astrophys. J.*, *790*, 67, doi:10.1088/0004-637X/790/1/67. [78](#), [105](#)
- Lonsdale, C., et al. (2018), Solar Imaging using Low Frequency Arrays, *ArXiv e-prints*. [92](#)
- Lonsdale, C. J., et al. (2009), The Murchison Widefield Array: Design Overview, *Proc. IEEE*, *97*, 1497–1506, doi:10.1109/JPROC.2009.2017564. [42](#), [49](#), [112](#)
- Lyot, B. (1939), The study of the solar corona and prominences without eclipses (George Darwin Lecture, 1939), *Mon. Not. Roy. Astron. Soc.*, *99*, 580, doi:10.1093/mnras/99.8.580. [5](#)
- Maclean, R. C., J. Büchner, and E. R. Priest (2009), Relationship between the topological skeleton, current concentrations, and 3D magnetic reconnection sites in the solar atmosphere, *Astron. Astrophys.*, *501*, 321–333, doi:10.1051/0004-6361:20078664. [71](#)
- Maia, D. J. F., R. Gama, C. Mercier, M. Pick, A. Kerdraon, and M. Karlický (2007), The Radio-Coronal Mass Ejection Event on 2001 April 15, *Astrophys. J.*, *660*(1), 874–881, doi:10.1086/508011. [33](#)
- Malitson, H. H., and W. C. Erickson (1966), Observations of Type III and Type IV Solar Radio Bursts at 26.3 Mc/s, *Astrophys. J.*, *144*, 337, doi:10.1086/148608. [82](#), [103](#)
- Mandrini, C. H., D. Baker, P. Démoulin, G. D. Cristiani, L. van Driel-Gesztelyi, S. Vargas Domínguez, F. A. Nuevo, A. M. Vásquez, and M. Pick (2015), Parallel Evolution of Quasi-separatrix Layers and Active Region Upflows, *Astrophys. J.*, *809*, 73, doi:10.1088/0004-637X/809/1/73. [34](#), [121](#)
- Mann, G., F. Jansen, R. J. MacDowall, M. L. Kaiser, and R. G. Stone (1999), A heliospheric density model and type III radio bursts, *Astron. Astrophys.*, *348*, 614–620. [82](#), [93](#)

References

- Mann, G., et al. (2018), Tracking of an electron beam through the solar corona with LOFAR, *Astron. Astrophys.*, *611*, A57, doi:10.1051/0004-6361/201629017. [20](#), [96](#), [97](#), [98](#), [99](#), [103](#), [104](#)
- Martyn, D. F. (1946), Temperature Radiation from the Quiet Sun in the Radio Spectrum, *Nature*, *158*, 632–633, doi:10.1038/158632a0. [15](#)
- Masson, S., G. Aulanier, E. Pariat, and K.-L. Klein (2012), Interchange Slip-Running Reconnection and Sweeping SEP Beams, *Solar Phys.*, *276*, 199–217, doi:10.1007/s11207-011-9886-3. [70](#), [71](#), [77](#)
- Masson, S., P. McCauley, L. Golub, K. K. Reeves, and E. E. DeLuca (2014), Dynamics of the Transition Corona, *Astrophys. J.*, *787*, 145, doi:10.1088/0004-637X/787/2/145. [70](#), [71](#), [77](#), [89](#)
- Maunder, E. (1903), Spoerer’s law of zones, *The Observatory*, *26*, 329–330. [22](#)
- Maunder, E. W. (1904), Note on the distribution of sun-spots in heliographic latitude, 1874–1902, *Mon. Not. Roy. Astron. Soc.*, *64*, 747–761. [22](#)
- Maxwell, A., and G. Swarup (1958), A New Spectral Characteristic in Solar Radio Emission, *Nature*, *181*, 36–38, doi:10.1038/181036a0. [78](#)
- McAteer, R. T. J., P. T. Gallagher, and J. Ireland (2005), Statistics of Active Region Complexity: A Large-Scale Fractal Dimension Survey, *Astrophys. J.*, *631*(1), 628–635, doi:10.1086/432412. [25](#)
- McCauley, P. I., I. H. Cairns, J. Morgan, S. E. Gibson, J. C. Harding, C. Lonsdale, and D. Oberoi (2017), Type III Solar Radio Burst Source Region Splitting due to a Quasi-separatrix Layer, *Astrophys. J.*, *851*, 151, doi:10.3847/1538-4357/aa9cee. [26](#), [37](#), [43](#), [45](#), [47](#), [84](#), [85](#), [86](#), [89](#), [96](#), [100](#), [112](#), [113](#), [127](#), [145](#), [146](#), [147](#), [148](#)
- McCauley, P. I., I. H. Cairns, and J. Morgan (2018), Densities Probed by Coronal Type III Radio Burst Imaging, *Solar Phys.*, *293*, 132, doi:10.1007/s11207-018-1353-y. [20](#), [27](#), [37](#), [45](#), [81](#), [112](#), [113](#), [114](#), [145](#), [147](#)
- McCauley, P. I., I. H. Cairns, S. M. White, S. Mondal, E. Lenc, J. Morgan, and D. Oberoi (2019), The Low-Frequency Solar Corona in Circular Polarization, *Solar Phys.*, *294*(8), 106, doi:10.1007/s11207-019-1502-y. [11](#), [14](#), [35](#), [41](#), [43](#), [45](#), [107](#), [146](#), [148](#), [149](#)
- McIntosh, P. S. (1990), The Classification of Sunspot Groups, *Solar Phys.*, *125*(2), 251–267, doi:10.1007/BF00158405. [25](#)
- McLean, D. J. (1959), Solar Radio Emission of Spectral Type IV and its Association with Geomagnetic Storms, *Aust. J. Phys.*, *12*, 404, doi:10.1071/PH590404. [31](#)
- McLean, D. J., and N. R. Labrum (1985), *Solar radiophysics: Studies of emission from the sun at metre wavelengths*, Cambridge University Press. [15](#), [35](#), [37](#), [38](#)
- Meléndez, J. L., H. S. Sawant, F. C. R. Fernandes, and A. O. Benz (1999), Statistical analysis of high-frequency decimetric type III bursts, *Solar Phys.*, *187*, 77–88, doi:10.1023/A:1005110111620. [76](#), [82](#), [95](#)
- Melrose, D. B. (1980), The Emission Mechanisms for Solar Radio Bursts, *Space Sci. Rev.*, *26*(1), 3–38, doi:10.1007/BF00212597. [16](#), [108](#)
- Melrose, D. B. (1986), *Instabilities in Space and Laboratory Plasmas*, 288 pp., Cambridge University Press, doi:10.1017/CBO9780511564123. [13](#), [14](#), [15](#), [139](#)
- Melrose, D. B. (1989), Depolarization of solar bursts due to scattering by low-frequency

-
- waves, *Solar Phys.*, *119*, 143–156, doi:10.1007/BF00146218. [110](#)
- Melrose, D. B. (2006), Depolarization of Radio Bursts Due to Reflection off Sharp Boundaries in the Solar Corona, *Astrophys. J.*, *637*, 1113–1121, doi:10.1086/498499. [20](#), [37](#), [110](#)
- Melrose, D. B. (2009), Coherent emission, in *Universal Heliophysical Processes, IAU Symposium*, vol. 257, edited by N. Gopalswamy and D. F. Webb, pp. 305–315, doi:10.1017/S1743921309029470. [16](#), [17](#), [18](#), [48](#), [82](#), [109](#), [110](#)
- Melrose, D. B., and G. A. Dulk (1988), Implications of Liouville’s theorem on the apparent brightness temperatures of solar radio bursts, *Solar Phys.*, *116*, 141–156, doi:10.1007/BF00171719. [19](#), [99](#)
- Melrose, D. B., and P. A. Robinson (1994), Reversal of the sense of polarisation in solar and stellar radio flares, *Pub. Astron. Soc. Austral.*, *11*, 16–20. [20](#), [141](#)
- Melrose, D. B., G. A. Dulk, and S. F. Smerd (1978), The polarization of second harmonic plasma emission, *Astron. Astrophys.*, *66*, 315–324. [110](#)
- Mercier, C. (1990), Polarisation of type III bursts between 164 and 435 MHz - Structure and variation with frequency, *Solar Phys.*, *130*, 119–129, doi:10.1007/BF00156783. [111](#)
- Mercier, C., and G. Chambe (2009), High Dynamic Range Images of the Solar Corona Between 150 and 450 MHz, *Astrophys. J. Lett.*, *700*, L137–L140, doi:10.1088/0004-637X/700/2/L137. [101](#)
- Mercier, C., and G. Chambe (2012), Morphology of the quiet Sun between 150 and 450 MHz as observed with the Nançay radioheliograph, *Astron. Astrophys.*, *540*, A18, doi:10.1051/0004-6361/201118163. [60](#)
- Mercier, C., and G. Chambe (2015), Electron density and temperature in the solar corona from multifrequency radio imaging, *Astron. Astrophys.*, *583*, A101, doi:10.1051/0004-6361/201425540. [93](#)
- Mercier, C., and H. Rosenberg (1974), Type III solar radio bursts observed at 169 MHz - Height and relative positions in pairs, *Solar Phys.*, *39*, 193–206, doi:10.1007/BF00154980. [82](#)
- Michelson, A. A., and E. W. Morley (1887), On the Relative Motion of the Earth and of the Luminiferous Ether, *Sidereal Messenger*, *6*, 306–310. [39](#)
- Mikić, Z., J. A. Linker, D. D. Schnack, R. Lionello, and A. Tarditi (1999), Magnetohydrodynamic modeling of the global solar corona, *Phys. Plasmas*, *6*, 2217–2224, doi:10.1063/1.873474. [57](#), [100](#)
- Mohan, A., and D. Oberoi (2017), 4D Data Cubes from Radio-Interferometric Spectroscopic Snapshot Imaging, *Solar Phys.*, *292*, 168, doi:10.1007/s11207-017-1193-1. [86](#), [112](#)
- Mohan, A., S. Mondal, D. Oberoi, and C. J. Lonsdale (2019a), Evidence for Super-Alfvénic Oscillations in Solar Type III Radio Burst Sources, *Astrophys. J.*, *875*(2), 98, doi:10.3847/1538-4357/ab0ae5. [112](#), [126](#)
- Mohan, A., P. I. McCauley, A. Mastrano, and D. Oberoi (2019b), A weak coronal heating event associated with periodic particle acceleration episodes, *arXiv e-prints*. [112](#)
- Mondal, S., A. Mohan, D. Oberoi, J. S. Morgan, L. Benkevitch, C. J. Lonsdale, M. Crowley, and I. H. Cairns (2019), Unsupervised Generation of High Dynamic Range Solar Images: A Novel Algorithm for Self-calibration of Interferometry Data, *Astrophys. J.*, *875*(2), 97, doi:10.3847/1538-4357/ab0a01. [112](#), [115](#), [129](#), [151](#)

References

- Morgan, J. S., J.-P. Macquart, R. Ekers, R. Chhetri, M. Tokumaru, P. K. Manoharan, S. Tremblay, M. M. Bisi, and B. V. Jackson (2018), Interplanetary Scintillation with the Murchison Widefield Array I: a sub-arcsecond survey over 900 deg^2 at 79 and 158 MHz, *Mon. Not. Roy. Astron. Soc.*, *473*, 2965–2983, doi:10.1093/mnras/stx2284. [42](#), [112](#)
- Morimoto, M. (1964), The Height and Scatter of Sources of Type III Bursts of Solar Radio Emission, *Pub. Astron. Soc. Japan*, *16*, 163. [82](#), [103](#)
- Morosan, D. E., et al. (2014), LOFAR tied-array imaging of Type III solar radio bursts, *Astron. Astrophys.*, *568*, A67, doi:10.1051/0004-6361/201423936. [49](#), [77](#), [90](#), [94](#), [96](#), [97](#), [103](#)
- Morosan, D. E., et al. (2015), LOFAR tied-array imaging and spectroscopy of solar S bursts, *Astron. Astrophys.*, *580*, A65, doi:10.1051/0004-6361/201526064. [39](#)
- Morosan, D. E., P. Zucca, D. S. Bloomfield, and P. T. Gallagher (2016), Conditions for electron-cyclotron maser emission in the solar corona, *Astron. Astrophys.*, *589*, L8, doi:10.1051/0004-6361/201628392. [19](#), [94](#)
- Morosan, D. E., E. K. J. Kilpua, E. P. Carley, and C. Monstein (2019), Variable emission mechanism of a Type IV radio burst, *Astron. Astrophys.*, *623*, A63, doi:10.1051/0004-6361/201834510. [37](#)
- Mugundhan, V., R. Ramesh, C. Kathiravan, G. V. S. Gireesh, A. Kumari, K. Hariharan, and I. V. Barve (2018), The First Low-frequency Radio Observations of the Solar Corona on $\approx 200 \text{ km}$ Long Interferometer Baseline, *Astrophys. J. Lett.*, *855*, L8, doi:10.3847/2041-8213/aaaf64. [27](#), [83](#), [110](#), [111](#), [121](#)
- Mulay, S. M., D. Tripathi, G. Del Zanna, and H. Mason (2016), Multiwavelength study of 20 jets that emanate from the periphery of active regions, *Astron. Astrophys.*, *589*, A79, doi:10.1051/0004-6361/201527473. [48](#)
- Müller, D., R. G. Marsden, O. C. St. Cyr, and H. R. Gilbert (2013), Solar Orbiter . Exploring the Sun-Heliosphere Connection, *Solar Phys.*, *285*(1-2), 25–70, doi:10.1007/s11207-012-0085-7. [32](#)
- Müller, D., et al. (2017), JHelioviewer. Time-dependent 3D visualisation of solar and heliospheric data, *Astron. Astrophys.*, *606*, A10, doi:10.1051/0004-6361/201730893. [106](#)
- Nakajima, H., et al. (1994), The Nobeyama radioheliograph, *Proc. IEEE*, *82*(5), 705–713. [7](#)
- Narang, N., R. T. Arbacher, H. Tian, D. Banerjee, S. R. Cranmer, E. E. DeLuca, and S. McKillop (2016), Statistical Study of Network Jets Observed in the Solar Transition Region: a Comparison Between Coronal Holes and Quiet-Sun Regions, *Solar Phys.*, *291*, 1129–1142, doi:10.1007/s11207-016-0886-1. [140](#)
- Neidig, D. F. (1989), The Importance of Solar White-Light Flares, *Solar Phys.*, *121*(1-2), 261–269, doi:10.1007/BF00161699. [27](#)
- Nelson, G. J., and D. B. Melrose (1985), Type II bursts, in *Solar radiophysics: Studies of emission from the sun at metre wavelengths*, edited by D. J. McLean and N. R. Labrum, pp. 333–359, Cambridge University Press. [32](#)
- Newkirk, G., Jr. (1961), The Solar Corona in Active Regions and the Thermal Origin of the Slowly Varying Component of Solar Radio Radiation, *Astrophys. J.*, *133*, 983, doi:10.1086/147104. [15](#), [54](#), [92](#), [93](#), [97](#), [102](#), [103](#), [108](#), [118](#), [132](#), [136](#)
- Nindos, A., H. Aurass, K. L. Klein, and G. Trottet (2008), Radio Emission of Flares

-
- and Coronal Mass Ejections. Invited Review, *Solar Phys.*, 253(1-2), 3–41, doi:10.1007/s11207-008-9258-9. [16](#), [33](#)
- Oberoi, D., et al. (2011), First Spectroscopic Imaging Observations of the Sun at Low Radio Frequencies with the Murchison Widefield Array Prototype, *Astrophys. J. Lett.*, 728, L27, doi:10.1088/2041-8205/728/2/L27. [49](#)
- Oberoi, D., et al. (2014), Observing the Sun with the Murchison Widefield Array, *ArXiv e-prints*. [49](#)
- Oberoi, D., R. Sharma, and A. E. E. Rogers (2017), Estimating Solar Flux Density at Low Radio Frequencies Using a Sky Brightness Model, *Solar Phys.*, 292, #75, doi:10.1007/s11207-017-1096-1. [62](#), [112](#)
- Offringa, A. R., J. J. van de Gronde, and J. B. T. M. Roerdink (2012), A morphological algorithm for improving radio-frequency interference detection, *Astron. Astrophys.*, 539, A95, doi:10.1051/0004-6361/201118497. [53](#), [84](#), [113](#)
- Offringa, A. R., et al. (2014), WSCLEAN: an implementation of a fast, generic wide-field imager for radio astronomy, *Mon. Not. Roy. Astron. Soc.*, 444, 606–619, doi:10.1093/mnras/stu1368. [41](#), [54](#), [84](#), [113](#)
- Offringa, A. R., et al. (2015), The Low-Frequency Environment of the Murchison Widefield Array: Radio-Frequency Interference Analysis and Mitigation, *Pub. Astron. Soc. Austral.*, 32, e008, doi:10.1017/pasa.2015.7. [53](#), [84](#), [113](#)
- Ogawara, Y., T. Takano, T. Kato, T. Kosugi, S. Tsuneta, T. Watanabe, I. Kondo, and Y. Uchida (1991), The SOLAR-A Mission - An Overview, *Solar Phys.*, 136(1), 1–16, doi:10.1007/BF00151692. [9](#)
- Ogilvie, K. W., and M. D. Desch (1997), The wind spacecraft and its early scientific results, *Adv. Space Res.*, 20(4-5), 559–568, doi:10.1016/S0273-1177(97)00439-0. [9](#)
- Ord, S. M., S. Johnston, and J. Sarkissian (2007), The Magnetic Field of the Solar Corona from Pulsar Observations, *Solar Phys.*, 245, 109–120, doi:10.1007/s11207-007-9030-6. [14](#)
- Ord, S. M., et al. (2015), The Murchison Widefield Array Correlator, *Pub. Astron. Soc. Austral.*, 32, e006, doi:10.1017/pasa.2015.5. [53](#), [84](#), [113](#)
- Paesold, G., A. O. Benz, K.-L. Klein, and N. Vilmer (2001), Spatial analysis of solar type III events associated with narrow band spikes at metric wavelengths, *Astron. Astrophys.*, 371, 333–342, doi:10.1051/0004-6361:20010358. [77](#)
- Parenti, S., B. J. I. Bromage, G. Poletto, G. Noci, J. C. Raymond, and G. E. Bromage (2000), Characteristics of solar coronal streamers. Element abundance, temperature and density from coordinated CDS and UVCS SOHO observations, *Astron. Astrophys.*, 363, 800–814. [93](#)
- Parker, E. N. (1975), The generation of magnetic fields in astrophysical bodies. X. Magnetic buoyancy and the solar dynamo, *Astrophys. J.*, 198, 205–209, doi:10.1086/153593. [24](#)
- Pawsey, J. L. (1946), Observation of Million Degree Thermal Radiation from the Sun at a Wavelength of 1.5 Metres, *Nature*, 158(4018), 633–634, doi:10.1038/158633a0. [5](#), [15](#), [43](#)
- Pawsey, J. L., and S. F. Smerd (1953), Solar Radio Emission, in *The Sun*, edited by G. P. Kuiper, p. 466, University of Chicago Press. [43](#)
- Pawsey, J. L., R. Payne-Scott, and L. L. McCready (1946), Radio-Frequency Energy from the Sun, *Nature*, 157(3980), 158–159, doi:10.1038/157158a0. [43](#)

References

- Payne-Scott, R., D. Yabsley, and J. Bolton (1947), Relative times of arrival of bursts of solar noise on different radio frequencies, *Nature*, *160*(4060), 256. [6](#), [18](#)
- Perley, R. A., C. J. Chandler, B. J. Butler, and J. M. Wrobel (2011), The Expanded Very Large Array: A New Telescope for New Science, *Astrophys. J. Lett.*, *739*, L1, doi:10.1088/2041-8205/739/1/L1. [7](#)
- Pesnell, W. D., B. J. Thompson, and P. C. Chamberlin (2012), The Solar Dynamics Observatory (SDO), *Solar Phys.*, *275*, 3–15, doi:10.1007/s11207-011-9841-3. [56](#), [89](#), [125](#)
- Petrie, G. J. D., and K. J. Haislmaier (2013), Low-latitude Coronal Holes, Decaying Active Regions, and Global Coronal Magnetic Structure, *Astrophys. J.*, *775*(2), 100, doi:10.1088/0004-637X/775/2/100. [26](#)
- Petrosian, V. (1999), Plasma Turbulence and Stochastic Acceleration in Solar Flares, in *Plasma Turbulence and Energetic Particles in Astrophysics*, edited by M. Ostrowski and R. Schlickeiser, pp. 135–146. [29](#)
- Phillips, K. J. H., et al. (2000), SECIS: The Solar Eclipse Coronal Eclipse Imaging System, *Solar Phys.*, *193*, 259–271, doi:10.1023/A:1005274827585. [4](#)
- Pick, M., and N. Vilmer (2008), Sixty-five years of solar radioastronomy: flares, coronal mass ejections and Sun Earth connection, *Astron. Astrophys. Rev.*, *16*, 1–153, doi:10.1007/s00159-008-0013-x. [5](#), [38](#)
- Pick, M., A. Kerdraon, F. Auchère, G. Stenborg, A. Bouteille, and E. Soubrié (2009), Coronal and Interplanetary Structures Associated with Type III Bursts, *Solar Phys.*, *256*, 101–110, doi:10.1007/s11207-009-9359-0. [89](#)
- Pick-Gutmann, M. (1961), Évolution des émissions radioélectriques solaires de type IV et leur relation avec d’autres phénomènes solaires et géophysiques, *Annales d’Astrophysique*, *24*, 183. [38](#)
- Pontin, D. I., and P. F. Wyper (2015), The Effect of Reconnection on the Structure of the Sun’s Open-Closed Flux Boundary, *Astrophys. J.*, *805*, 39, doi:10.1088/0004-637X/805/1/39. [74](#)
- Pontin, D. I., E. R. Priest, and K. Galsgaard (2013), On the Nature of Reconnection at a Solar Coronal Null Point above a Separatrix Dome, *Astrophys. J.*, *774*, 154, doi:10.1088/0004-637X/774/2/154. [70](#)
- Poquerusse, M. (1994), Relativistic type 3 solar radio bursts, *Astron. Astrophys.*, *286*, 611–625. [76](#), [95](#)
- Poquerusse, M., J. L. Steinberg, C. Caroubalos, G. A. Dulk, and R. M. MacQueen (1988), Measurement of the 3-dimensional positions of type III bursts in the solar corona, *Astron. Astrophys.*, *192*, 323–334. [19](#), [98](#), [101](#)
- Prabhakar, M., K. P. Raju, and T. Chandrasekhar (2019), Characteristics of the Solar Coronal Line Profiles from Fabry-Perot Interferometric Observations, *Solar Phys.*, *294*(3), 26, doi:10.1007/s11207-019-1409-7. [39](#)
- Prestage, N. P., R. G. Luckhurst, B. R. Paterson, C. S. Bevins, and C. G. Yuile (1994), A new radiospectrograph at Culgoora, *Solar Phys.*, *150*, 393–396, doi:10.1007/BF00712901. [51](#), [85](#)
- Priest, E. (2014), *Magnetohydrodynamics of the Sun*, Cambridge University Press, doi:10.1017/CBO9781139020732. [2](#), [22](#), [25](#), [27](#), [31](#)

-
- Priest, E. (2019), Chapter 7 - magnetohydrodynamics and solar dynamo action, in *The Sun as a Guide to Stellar Physics*, edited by O. Engvold, J.-C. Vial, and A. Skumanich, pp. 239 – 266, Elsevier, doi:<https://doi.org/10.1016/B978-0-12-814334-6.00009-1>. [24](#)
- Priest, E., and T. Forbes (Eds.) (2000), *Magnetic reconnection : MHD theory and applications*. [29](#)
- Priest, E. R., and P. Démoulin (1995), Three-dimensional magnetic reconnection without null points. 1. Basic theory of magnetic flipping, *J. Geophys. Res.*, *100*, 23,443–23,464, doi:[10.1029/95JA02740](https://doi.org/10.1029/95JA02740). [70](#)
- Pucci, S., Ø. Lie-Svendsen, and R. Esser (2010), Elemental Abundances in the Fast Solar Wind Emanating from Chromospheric Funnels, *Astrophys. J.*, *709*, 993–1002, doi:[10.1088/0004-637X/709/2/993](https://doi.org/10.1088/0004-637X/709/2/993). [105](#)
- Puschmann, K. G., et al. (2012), The GREGOR Fabry-Pérot Interferometer, *Astronomische Nachrichten*, *333*(9), 880, doi:[10.1002/asna.201211734](https://doi.org/10.1002/asna.201211734). [39](#)
- Rahman, M. M., P. I. McCauley, and I. H. Cairns (2019), On the Relative Brightness of Coronal Holes at Low Frequencies, *Solar Phys.*, *294*, 7, doi:[10.1007/s11207-019-1396-8](https://doi.org/10.1007/s11207-019-1396-8). [26](#), [45](#), [112](#), [127](#), [139](#), [148](#)
- Ramaty, R., B. Kozlovsky, and R. E. Lingenfelter (1975), Solar gamma rays, *Space Science Reviews*, *18*(3), 341–388, doi:[10.1007/BF00212911](https://doi.org/10.1007/BF00212911). [9](#)
- Ramesh, R. (2000), Low Frequency Radio Emission from the ‘Quiet Sun’, *J. Astrophys. Astron.*, *21*, 237, doi:[10.1007/BF02702398](https://doi.org/10.1007/BF02702398). [27](#)
- Ramesh, R., K. R. Subramanian, M. S. Sundararajan, and C. V. Sastry (1998), The Gau-ribidanur Radioheliograph, *Solar Phys.*, *181*, 439–453, doi:[10.1023/A:1005075003370](https://doi.org/10.1023/A:1005075003370). [7](#), [49](#), [111](#)
- Ramesh, R., A. S. Narayanan, C. Kathiravan, C. V. Sastry, and N. U. Shankar (2005), An estimation of the plasma parameters in the solar corona using quasi-periodic metric type III radio burst emission, *Astron. Astrophys.*, *431*, 353–357, doi:[10.1051/0004-6361:20041130](https://doi.org/10.1051/0004-6361:20041130). [7](#), [49](#)
- Ramesh, R., H. S. Nataraj, C. Kathiravan, and C. V. Sastry (2006), The Equatorial Background Solar Corona during Solar Minimum, *Astrophys. J.*, *648*, 707–711, doi:[10.1086/505677](https://doi.org/10.1086/505677). [99](#)
- Ramesh, R., C. Kathiravan, M. S. Sundararajan, I. V. Barve, and C. V. Sastry (2008), A Low-Frequency (30 - 110 MHz) Antenna System for Observations of Polarized Radio Emission from the Solar Corona, *Solar Phys.*, *253*, 319–327, doi:[10.1007/s11207-008-9272-y](https://doi.org/10.1007/s11207-008-9272-y). [111](#)
- Ramesh, R., C. Kathiravan, I. V. Barve, G. K. Beeharry, and G. N. Rajasekara (2010a), Radio Observations of Weak Energy Releases in the Solar Corona, *Astrophys. J. Lett.*, *719*, L41–L44, doi:[10.1088/2041-8205/719/1/L41](https://doi.org/10.1088/2041-8205/719/1/L41). [111](#)
- Ramesh, R., C. Kathiravan, and C. V. Sastry (2010b), Estimation of Magnetic Field in the Solar Coronal Streamers Through Low Frequency Radio Observations, *Astrophys. J.*, *711*, 1029–1032, doi:[10.1088/0004-637X/711/2/1029](https://doi.org/10.1088/0004-637X/711/2/1029). [111](#)
- Ramesh, R., C. Kathiravan, and A. S. Narayanan (2011), Low-frequency Observations of Polarized Emission from Long-lived Non-thermal Radio Sources in the Solar Corona, *Astrophys. J.*, *734*, 39, doi:[10.1088/0004-637X/734/1/39](https://doi.org/10.1088/0004-637X/734/1/39). [111](#)
- Ramesh, R., K. Sasikumar Raja, C. Kathiravan, and A. S. Narayanan (2013), Low-frequency

References

- Radio Observations of Picoflare Category Energy Releases in the Solar Atmosphere, *Astrophys. J.*, 762, 89, doi:10.1088/0004-637X/762/2/89. 111
- Raulin, J. P., M. R. Kundu, N. Nitta, and A. Raoult (1996), Radio Continuum and Type III Bursts Associated with Coronal X-Ray Structures, *Astrophys. J.*, 472, 874, doi:10.1086/178117. 48
- Rausche, G., H. Aurass, and G. Mann (2008), Fiber Bursts and the Coronal Magnetic Field, *Central European Astrophysical Bulletin*, 32, 43–50. 39
- Raymond, J. C., P. I. McCauley, S. R. Cranmer, and C. Downs (2014), The Solar Corona as Probed by Comet Lovejoy (C/2011 W3), *Astrophys. J.*, 788, 152, doi:10.1088/0004-637X/788/2/152. 19, 105
- Reale, F. (2014), Coronal Loops: Observations and Modeling of Confined Plasma, *Living Rev. Sol. Phys.*, 11(1), 4, doi:10.12942/lrsp-2014-4. 26
- Reames, D. V. (1999), Particle acceleration at the Sun and in the heliosphere, *Space Sci. Rev.*, 90, 413–491, doi:10.1023/A:1005105831781. 29
- Reames, D. V. (2013), The Two Sources of Solar Energetic Particles, *Space Sci. Rev.*, 175(1-4), 53–92, doi:10.1007/s11214-013-9958-9. 32
- Reber, G. (1944), Cosmic Static, *Astrophys. J.*, 100, 279, doi:10.1086/144668. 5
- Reeves, K. K., and L. Golub (2011), Atmospheric Imaging Assembly Observations of Hot Flare Plasma, *Astrophys. J. Lett.*, 727, L52, doi:10.1088/2041-8205/727/2/L52. 57
- Régnier, S. (2013), Magnetic Field Extrapolations into the Corona: Success and Future Improvements, *Solar Phys.*, 288, 481–505, doi:10.1007/s11207-013-0367-8. 77
- Reid, H. A. S., and E. P. Kontar (2017), Imaging spectroscopy of type U and J solar radio bursts with LOFAR, *Astron. Astrophys.*, 606, A141, doi:10.1051/0004-6361/201730701. 78
- Reid, H. A. S., and H. Ratcliffe (2014), A review of solar type III radio bursts, *Res. Astron. Astrophys.*, 14, 773–804, doi:10.1088/1674-4527/14/7/003. 37, 38, 39, 48, 68, 81, 110, 121
- Reid, H. A. S., and N. Vilmer (2017), Coronal type III radio bursts and their X-ray flare and interplanetary type III counterparts, *Astron. Astrophys.*, 597, A77, doi:10.1051/0004-6361/201527758. 37, 48
- Reid, H. A. S., N. Vilmer, and E. P. Kontar (2014), The low-high-low trend of type III radio burst starting frequencies and solar flare hard X-rays, *Astron. Astrophys.*, 567, A85, doi:10.1051/0004-6361/201321973. 77, 104
- Reid, M. J., and J. M. Moran (1981), Masers, *Ann. Rev. Astron. Astrophys.*, 19(1), 231–276, doi:10.1146/annurev.aa.19.090181.001311. 18
- Reid, M. J., M. H. Schneps, J. M. Moran, C. R. Gwinn, R. Genzel, D. Downes, and B. Roen-naeng (1988), The distance to the center of the Galaxy - H₂O maser proper motions in Sagittarius B2(N), *Astrophys. J.*, 330, 809–816, doi:10.1086/166514. 92
- Riddle, A. C. (1974), The Slowly Varying Component of Solar Meter Wavelength Radiation: A Non-Thermal Radio Source, *Solar Phys.*, 36, 375–381, doi:10.1007/BF00151208. 60, 83
- Riley, P., R. Lionello, J. A. Linker, Z. Mikic, J. Luhmann, and J. Wijaya (2011), Global MHD Modeling of the Solar Corona and Inner Heliosphere for the Whole Heliosphere Interval, *Solar Phys.*, 274, 361–377, doi:10.1007/s11207-010-9698-x. 57, 59
- Robbrecht, E., D. Berghmans, and R. A. M. Van der Linden (2009), Automated LASCO

-
- CME Catalog for Solar Cycle 23: Are CMEs Scale Invariant?, *Astrophys. J.*, *691*, 1222–1234, doi:10.1088/0004-637X/691/2/1222. [44](#)
- Roberts, J. A. (1959), Solar Radio Bursts of Spectral Type II, *Aust. J. Phys.*, *12*, 327, doi:10.1071/PH590327. [35](#)
- Robinson, P. A., and I. H. Cairns (1994), Fundamental and harmonic radiation in type III solar radio bursts, *Solar Phys.*, *154*, 335–360, doi:10.1007/BF00681103. [67](#)
- Robinson, P. A., and I. H. Cairns (1998), Fundamental and Harmonic Emission in Type III Solar Radio Bursts - I. Emission at a Single Location or Frequency, *Solar Phys.*, *181*, 363–394, doi:10.1023/A:1005018918391. [91](#)
- Robinson, P. A., and I. H. Cairns (2000), Theory of Type III And Type II Solar Radio Emissions, *Washington DC American Geophysical Union Geophysical Monograph Series*, *119*, 37, doi:10.1029/GM119p0037. [17](#), [18](#), [37](#), [48](#), [82](#), [109](#)
- Robinson, R. D. (1977), A study of type V solar radio bursts. I: Observations, *Solar Phys.*, *55*(2), 459–472, doi:10.1007/BF00152587. [38](#)
- Robinson, R. D. (1978), A study of type V solar radio bursts. II. A theoretical model, *Solar Phys.*, *56*(2), 405–416, doi:10.1007/BF00152480. [38](#)
- Robinson, R. D. (1983), Scattering of radio waves in the solar corona, *Pub. Astron. Soc. Austral.*, *5*, 208–211, doi:10.1017/S132335800001688X. [19](#), [83](#), [98](#), [101](#)
- Rusin, V. (2000), Shape and Structure of the White-Light Corona over Solar Cycles (Invited review), in *Last Total Solar Eclipse of the Millennium*, *Astronomical Society of the Pacific Conference Series*, vol. 205, edited by W. Livingston and A. Özgüç, p. 17. [4](#)
- Ryabov, B. (2004), Coronal Magnetic Field Measurements Through Quasi-Transverse Propagation, in *Astrophysics and Space Science Library*, *Astrophysics and Space Science Library*, vol. 314, edited by D. E. Gary and C. U. Keller, p. 135, doi:10.1007/1-4020-2814-8_7. [20](#), [109](#)
- Ryabov, B. I., N. A. Pilyeva, C. E. Alissandrakis, K. Shibasaki, V. M. Bogod, V. I. Garaimov, and G. B. Gelfreikh (1999), Coronal Magnetography of an Active Region From Microwave Polarization Inversion, *Solar Phys.*, *185*, 157–175, doi:10.1023/A:1005114303703. [20](#), [141](#)
- Sabine, E. (1852), On Periodical Laws Discoverable in the Mean Effects of the Larger Magnetic Disturbances. No. II, *Philos. Trans. Royal Soc.*, *142*, 103–124. [31](#)
- Saint-Hilaire, P., S. Krucker, S. Christe, and R. P. Lin (2009), The X-ray Detectability of Electron Beams Escaping from the Sun, *Astrophys. J.*, *696*, 941–952, doi:10.1088/0004-637X/696/1/941. [49](#)
- Saint-Hilaire, P., N. Vilmer, and A. Kerdran (2013), A Decade of Solar Type III Radio Bursts Observed by the Nançay Radioheliograph 1998-2008, *Astrophys. J.*, *762*, 60, doi:10.1088/0004-637X/762/1/60. [62](#), [78](#)
- Saito, K., and N. Owaki (1967), An Active Region Streamer of the Solar Corona, *Pub. Astron. Soc. Japan*, *19*, 535. [93](#)
- Saito, K., A. I. Poland, and R. H. Munro (1977), A study of the background corona near solar minimum, *Solar Phys.*, *55*, 121–134, doi:10.1007/BF00150879. [15](#), [92](#), [93](#), [102](#), [108](#)
- Sasikumar Raja, K., and R. Ramesh (2013), Low-frequency Observations of Transient Quasi-periodic Radio Emission from the Solar Atmosphere, *Astrophys. J.*, *775*, 38, doi:10.1088/0004-637X/775/1/38. [111](#)

References

- Sasikumar Raja, K., C. Kathiravan, R. Ramesh, M. Rajalingam, and I. V. Barve (2013), Design and Performance of a Low-frequency Cross-polarized Log-periodic Dipole Antenna, *Astrophys. J. Supp.*, *207*, 2, doi:10.1088/0067-0049/207/1/2. [111](#)
- Sasikumar Raja, K., R. Ramesh, K. Hariharan, C. Kathiravan, and T. J. Wang (2014), An Estimate of the Magnetic Field Strength Associated with a Solar Coronal Mass Ejection from Low Frequency Radio Observations, *Astrophys. J.*, *796*, 56, doi:10.1088/0004-637X/796/1/56. [111](#)
- Sastry, C. V. (1994), Observations of the continuum radio emission from the undisturbed Sun at a wavelength of 8.7 meters, *Solar Phys.*, *150*, 285–294, doi:10.1007/BF00712890. [99](#)
- Sastry, C. V. (2009), Polarization of the Thermal Radio Emission from Outer Solar Corona, *Astrophys. J.*, *697*, 1934–1939, doi:10.1088/0004-637X/697/2/1934. [109](#), [116](#), [136](#)
- Savcheva, A., E. Pariat, S. McKillop, P. McCauley, E. Hanson, Y. Su, E. Werner, and E. E. DeLuca (2015), The Relation between Solar Eruption Topologies and Observed Flare Features. I. Flare Ribbons, *Astrophys. J.*, *810*, 96, doi:10.1088/0004-637X/810/2/96. [70](#)
- Savcheva, A., E. Pariat, S. McKillop, P. McCauley, E. Hanson, Y. Su, and E. E. DeLuca (2016), The Relation between Solar Eruption Topologies and Observed Flare Features. II. Dynamical Evolution, *Astrophys. J.*, *817*, 43, doi:10.3847/0004-637X/817/1/43. [70](#)
- Scherrer, P. H., et al. (1995), The Solar Oscillations Investigation - Michelson Doppler Imager, *Solar Phys.*, *162*(1-2), 129–188, doi:10.1007/BF00733429. [10](#)
- Scherrer, P. H., et al. (2012), The Helioseismic and Magnetic Imager (HMI) Investigation for the Solar Dynamics Observatory (SDO), *Solar Phys.*, *275*, 207–227, doi:10.1007/s11207-011-9834-2. [9](#), [10](#), [56](#), [132](#)
- Schlickeiser, R. (2003), Particle acceleration processes in cosmic plasmas, in *Energy Conversion and Particle Acceleration in the Solar Corona*, pp. 230–260, Springer. [29](#)
- Schmieder, B., V. Archontis, and E. Pariat (2014), Magnetic Flux Emergence Along the Solar Cycle, *Space Sci. Rev.*, *186*(1-4), 227–250, doi:10.1007/s11214-014-0088-9. [24](#)
- Schrijver, C. J., and M. L. De Rosa (2003), Photospheric and heliospheric magnetic fields, *Solar Phys.*, *212*, 165–200, doi:10.1023/A:1022908504100. [71](#), [132](#)
- Schrijver, C. J., A. W. Sandman, M. J. Aschwanden, and M. L. De Rosa (2004), The Coronal Heating Mechanism as Identified by Full-Sun Visualizations, *Astrophys. J.*, *615*, 512–525, doi:10.1086/424028. [57](#), [100](#)
- Schwab, F. R. (1984), Relaxing the isoplanatism assumption in self-calibration; applications to low-frequency radio interferometry, *Astron. J.*, *89*, 1076–1081, doi:10.1086/113605. [40](#)
- Schwabe, H. (1844), Sonnenbeobachtungen im jahre 1843. von herrn hofrath schwabe in dessau, *Astronomische Nachrichten*, *21*, 233. [22](#)
- Schwarz, U. J. (1978), Mathematical-statistical Description of the Iterative Beam Removing Technique (Method CLEAN), *Astron. Astrophys.*, *65*, 345. [40](#)
- Schwenn, R., H. Rosenbauer, and H. Miggenrieder (1975), Das Plasmaexperiment auf Helios (E1), *Raumfahrtforschung*, *19*, 226–232. [9](#)
- Schwenn, R., et al. (2006), Coronal Observations of CMEs, in *Coronal Mass Ejections, Space Sciences Series of ISSI*, vol. 21, p. 127, Springer, doi:10.1007/978-0-387-45088-9_9. [32](#)
- Segre, S. E., and V. Zanza (2001), Evolution of Polarization for Radiation Crossing a Plasma

-
- Layer of Quasi-transverse Propagation and the Interpretation of Radioastronomical Measurements, *Astrophys. J.*, *554*, 408–415, doi:10.1086/321352. [14](#)
- Shain, A. V., V. F. Melnikov, and A. S. Morgachev (2017), The Role of Quasi-Transverse Propagation in Observed Polarization of Flare Loop Microwave Radiation, *Geomag. Aeron.*, *57*, 988–995, doi:10.1134/S0016793217080217. [141](#)
- Sharma, R., D. Oberoi, and M. Arjunwadkar (2018), Quantifying Weak Nonthermal Solar Radio Emission at Low Radio Frequencies, *Astrophys. J.*, *852*, 69, doi:10.3847/1538-4357/aa9d96. [110](#), [112](#), [140](#)
- Sharykin, I. N., A. A. Kuznetsov, and I. I. Myshyakov (2018), Probing Twisted Magnetic Field Using Microwave Observations in an M Class Solar Flare on 11 February, 2014, *Solar Phys.*, *293*, 34, doi:10.1007/s11207-017-1237-6. [20](#), [141](#)
- Sheridan, K. V., N. R. Labrum, and W. J. Payten (1972), Multiple-frequency Operation of the Culgoora Radioheliograph, *Nature Phys. Sci.*, *238*, 115–116, doi:10.1038/physci238115a0. [6](#), [49](#)
- Sheridan, K. V., N. R. Labrum, W. J. Payten, G. J. Nelson, and E. R. Hill (1983), Preliminary observations of solar radio sources with the Culgoora radioheliograph operating at four frequencies, *Solar Phys.*, *83*, 167–177, doi:10.1007/BF00148251. [6](#), [49](#)
- Shibasaki, K., C. E. Alissandrakis, and S. Pohjolainen (2011), Radio Emission of the Quiet Sun and Active Regions (Invited Review), *Solar Phys.*, *273*, 309–337, doi:10.1007/s11207-011-9788-4. [25](#), [60](#), [136](#)
- Shibata, K., and S. Tanuma (2001), Plasmoid-induced-reconnection and fractal reconnection, *Earth, Planets, and Space*, *53*, 473–482, doi:10.1186/BF03353258. [30](#)
- Shibata, K., et al. (1992), Observations of X-Ray Jets with the YOHKOH Soft X-Ray Telescope, *Pub. Astron. Soc. Japan*, *44*, L173–L179. [31](#)
- Slottje, C. (1972), Peculiar absorption and emission microstructures in the type IV solar radio outburst of March 2, 1970, *Solar Phys.*, *25*(1), 210–231, doi:10.1007/BF00155758. [39](#)
- Smerd, S. F. (1950), Radio-Frequency Radiation from the Quiet Sun, *Aust. J. Sci. Res. A*, *3*, 34, doi:10.1071/PH500034. [26](#)
- Spadaro, D., R. Susino, R. Ventura, A. Vourlidis, and E. Landi (2007), Physical parameters of a mid-latitude streamer during the declining phase of the solar cycle, *Astron. Astrophys.*, *475*, 707–715, doi:10.1051/0004-6361:20077873. [93](#)
- Spangler, S. R. (2007), A Technique for Measuring Electrical Currents in the Solar Corona, *Astrophys. J.*, *670*, 841–848, doi:10.1086/521995. [14](#)
- Spicer, D. S., A. O. Benz, and J. D. Huba (1982), Solar type I noise storms and newly emerging magnetic flux, *Astron. Astrophys.*, *105*, 221–228. [34](#), [121](#)
- Spiegel, E. A., and J. P. Zahn (1992), The solar tachocline, *Astron. Astrophys.*, *265*, 106–114. [23](#)
- Steinberg, J. L., S. Hoang, A. Lecacheux, M. G. Aubier, and G. A. Dulk (1984), Type III radio bursts in the interplanetary medium - The role of propagation, *Astron. Astrophys.*, *140*, 39–48. [83](#), [104](#)
- Steinberg, J. L., S. Hoang, and G. A. Dulk (1985), Evidence of scattering effects on the sizes of interplanetary Type III radio bursts, *Astron. Astrophys.*, *150*, 205–216. [19](#), [83](#), [104](#)

References

- Stewart, R. T. (1972), Relative Positions of Fundamental and Second Harmonic Type III Bursts, *Pub. Astron. Soc. Austral.*, *2*, 100–101, doi:10.1017/S1323358000013059. [83](#)
- Stewart, R. T. (1974), Harmonic ratios of inverted-U type III bursts, *Solar Phys.*, *39*, 451–458, doi:10.1007/BF00162437. [98](#)
- Stewart, R. T. (1976), Source heights of metre wavelength bursts of spectral types I and III, *Solar Phys.*, *50*, 437–445, doi:10.1007/BF00155305. [20](#), [82](#), [98](#), [103](#)
- Stone, E. C., A. M. Frandsen, R. A. Mewaldt, E. R. Christian, D. Margolies, J. F. Ormes, and F. Snow (1998), The Advanced Composition Explorer, *Space Sci. Rev.*, *86*, 1–22, doi:10.1023/A:1005082526237. [9](#)
- Sturrock, P. A. (1961), Spectral Characteristics of Type II Solar Radio Bursts, *Nature*, *192*(4797), 58, doi:10.1038/192058a0. [35](#)
- Sturrock, P. A. (1966), Model of the High-Energy Phase of Solar Flares, *Nature*, *211*(5050), 695–697, doi:10.1038/211695a0. [30](#)
- Subramanian, K. R. (2004), Brightness temperature and size of the quiet Sun at 34.5 MHz, *Astron. Astrophys.*, *426*, 329–331, doi:10.1051/0004-6361:20047120. [99](#)
- Suresh, A., et al. (2017), Wavelet-based Characterization of Small-scale Solar Emission Features at Low Radio Frequencies, *Astrophys. J.*, *843*, 19, doi:10.3847/1538-4357/aa774a. [49](#), [110](#), [112](#), [140](#)
- Sutinjo, A., J. O’Sullivan, E. Lenc, R. B. Wayth, S. Padhi, P. Hall, and S. J. Tingay (2015), Understanding instrumental Stokes leakage in Murchison Widefield Array polarimetry, *Radio Science*, *50*, 52–65, doi:10.1002/2014RS005517. [55](#), [84](#), [113](#), [114](#), [115](#)
- Suzuki, S., and G. A. Dulk (1985), Bursts of type III and type V, in *Solar radiophysics: Studies of emission from the sun at metre wavelengths*, edited by D. J. McLean and N. R. Labrum, pp. 289–332, Cambridge University Press. [38](#)
- Suzuki, S., and K. V. Sheridan (1980), The polarization of metre-wave solar emission, *Pub. Astron. Soc. Austral.*, *4*, 56–59, doi:10.1017/S1323358000018786. [20](#), [141](#)
- Tang, J. F., D. J. Wu, and C. M. Tan (2013), Electron Cyclotron Maser Emission in Coronal Arches and Solar Radio Type V Bursts, *Astrophys. J.*, *779*(1), 83, doi:10.1088/0004-637X/779/1/83. [19](#), [38](#)
- Taylor, G. B., C. L. Carilli, and R. A. Perley (Eds.) (1999), *Synthesis Imaging in Radio Astronomy II*, *Astronomical Society of the Pacific Conference Series*, vol. 180. [40](#)
- Thejappa, G., and M. R. Kundu (1992), Unusually low coronal radio emission at the solar minimum, *Solar Phys.*, *140*, 19–39, doi:10.1007/BF00148427. [99](#)
- Thejappa, G., and M. R. Kundu (1994), The Effects of Largescale and Smallscale Density Structures on the Radio Emission from Coronal Streamers, *Solar Phys.*, *149*(1), 31–49, doi:10.1007/BF00645176. [27](#)
- Thejappa, G., and R. J. MacDowall (2008), Effects of Scattering on Radio Emission from the Quiet Sun at Low Frequencies, *Astrophys. J.*, *676*, 1338–1345, doi:10.1086/528835. [19](#), [60](#), [99](#)
- Thompson, A. R., J. M. Moran, and G. W. Swenson, Jr. (2017), *Interferometry and Synthesis in Radio Astronomy*, *3rd Edition*, Springer, doi:10.1007/978-3-319-44431-4. [40](#)
- Thompson, B. J., and C. A. Young (2016), Persistence Mapping Using EUV Solar Imager Data, *Astrophys. J.*, *825*, 27, doi:10.3847/0004-637X/825/1/27. [69](#)

-
- Thompson, W. T. (2006), Coordinate systems for solar image data, *Astron. Astrophys.*, *449*, 791–803, doi:10.1051/0004-6361:20054262. [55](#)
- Tian, H., et al. (2014), Prevalence of small-scale jets from the networks of the solar transition region and chromosphere, *Science*, *346*(27), 1255711, doi:10.1126/science.1255711. [140](#)
- Timothy, A. F., A. S. Krieger, and G. S. Vaiana (1975), The Structure and Evolution of Coronal Holes, *Solar Phys.*, *42*(1), 135–156, doi:10.1007/BF00153291. [26](#)
- Tingay, S. J., et al. (2013a), The Murchison Widefield Array: The Square Kilometre Array Precursor at Low Radio Frequencies, *Pub. Astron. Soc. Austral.*, *30*, e007, doi:10.1017/pasa.2012.007. [7](#), [42](#), [43](#), [49](#), [53](#), [84](#), [111](#), [112](#), [114](#)
- Tingay, S. J., et al. (2013b), The Murchison Widefield Array: solar science with the low frequency SKA Precursor, *Journal of Physics Conference Series*, *440*, 012033, doi:10.1088/1742-6596/440/1/012033. [49](#)
- Titov, V. S. (2007), Generalized Squashing Factors for Covariant Description of Magnetic Connectivity in the Solar Corona, *Astrophys. J.*, *660*, 863–873, doi:10.1086/512671. [70](#)
- Titov, V. S., Z. Mikic, T. Török, J. A. Linker, and O. Panasenco (2012), 2010 August 1-2 Sympathetic Eruptions. I. Magnetic Topology of the Source-surface Background Field, *Astrophys. J.*, *759*, 70, doi:10.1088/0004-637X/759/1/70. [71](#)
- Tomczyk, S., J. Schou, and M. J. Thompson (1995), Measurement of the Rotation Rate in the Deep Solar Interior, *Astrophys. J. Lett.*, *448*, L57, doi:10.1086/309598. [23](#)
- Tomczyk, S., et al. (2008), An Instrument to Measure Coronal Emission Line Polarization, *Solar Phys.*, *247*(2), 411–428, doi:10.1007/s11207-007-9103-6. [11](#)
- Tonks, L., and I. Langmuir (1929), Oscillations in Ionized Gases, *Physical Review*, *33*(2), 195–210, doi:10.1103/PhysRev.33.195. [16](#)
- Török, T., G. Aulanier, B. Schmieder, K. K. Reeves, and L. Golub (2009), Fan-Spine Topology Formation Through Two-Step Reconnection Driven by Twisted Flux Emergence, *Astrophys. J.*, *704*, 485–495, doi:10.1088/0004-637X/704/1/485. [71](#)
- Tousey, R. (1973), The solar corona, in *Space Research Conference*, vol. 2, pp. 713–730. [31](#)
- Tousey, R., J. D. F. Bartoe, J. D. Bohlin, G. E. Brueckner, J. D. Purcell, V. E. Scherrer, J. Sheeley, N. R., R. J. Schumacher, and M. E. Vanhoosier (1973), A Preliminary Study of the Extreme Ultraviolet Spectroheliograms from Skylab, *Solar Phys.*, *33*(2), 265–280, doi:10.1007/BF00152418. [9](#)
- Treumann, R. A. (2006), The electron-cyclotron maser for astrophysical application, *Astron. Astrophys. Rev.*, *13*(4), 229–315, doi:10.1007/s00159-006-0001-y. [18](#)
- Trottet, G. (2003), Coronal signatures of accelerated electrons, *Adv. Space Res.*, *32*, 2403–2413, doi:10.1016/j.asr.2003.02.004. [48](#)
- Trottet, G., M. Pick, L. House, R. Illing, C. Sawyer, and W. Wagner (1982), An association between coronal structures and type III burst sources, *Astron. Astrophys.*, *111*, 306–311. [27](#), [83](#)
- Trujillo Bueno, J., N. Shchukina, and A. Asensio Ramos (2004), A substantial amount of hidden magnetic energy in the quiet Sun, *Nature*, *430*(6997), 326–329, doi:10.1038/nature02669. [26](#)
- Tsuchiya, A. (1963), Polarization of Storm Bursts of Solar Radio Emission at 200 Mc/s, *Pub. Astron. Soc. Japan*, *15*, 368. [110](#)

References

- Tun, S. D., and A. Vourlidas (2013), Derivation of the Magnetic Field in a Coronal Mass Ejection Core via Multi-frequency Radio Imaging, *Astrophys. J.*, 766, 130, doi:10.1088/0004-637X/766/2/130. [111](#)
- Turck-Chieze, S., W. Däppen, E. Fossat, J. Provost, E. Schatzman, and D. Vignaud (1993), The solar interior, *Phys. Rep.*, 230(2-4), 57–235. [23](#)
- Vaiana, G. S., A. S. Krieger, and A. F. Timothy (1973a), Identification and Analysis of Structures in the Corona from X-Ray Photography, *Solar Phys.*, 32(1), 81–116, doi:10.1007/BF00152731. [8](#)
- Vaiana, G. S., J. M. Davis, R. Giacconi, A. S. Krieger, J. K. Silk, A. F. Timothy, and M. Zombeck (1973b), X-Ray Observations of Characteristic Structures and Time Variations from the Solar Corona: Preliminary Results from SKYLAB, *Astrophys. J. Lett.*, 185, L47, doi:10.1086/181318. [9](#)
- van Ballegooijen, A. A. (1999), Photospheric Motions as a Source of Twist in Coronal Magnetic Fields, *Washington DC American Geophysical Union Geophysical Monograph Series*, 111, 213–220, doi:10.1029/GM111p0213. [29](#)
- van de Hulst, H. C. (1950), The electron density of the solar corona, *Bull. Astron. Inst. Netherlands*, 11, 135. [4](#)
- van Driel-Gesztelyi, L. (1998), Evolution and Decay of Active Regions (Invited review), in *Three-Dimensional Structure of Solar Active Regions*, *Astronomical Society of the Pacific Conference Series*, vol. 155, edited by C. E. Alissandrakis and B. Schmieder, p. 202. [26](#)
- van Driel-Gesztelyi, L., et al. (2012), Magnetic Topology of Active Regions and Coronal Holes: Implications for Coronal Outflows and the Solar Wind, *Solar Phys.*, 281, 237–262, doi:10.1007/s11207-012-0076-8. [71](#)
- van Haarlem, M. P., et al. (2013), LOFAR: The LOw-Frequency ARray, *Astron. Astrophys.*, 556, A2, doi:10.1051/0004-6361/201220873. [7](#), [49](#)
- Vernazza, J. E., E. H. Avrett, and R. Loeser (1973), Structure of the Solar Chromosphere. Basic Computations and Summary of the Results, *Astrophys. J.*, 184, 605–632, doi:10.1086/152353. [3](#)
- Vernazza, J. E., E. H. Avrett, and R. Loeser (1976), Structure of the solar chromosphere. II. The underlying photosphere and temperature-minimum region, *Astrophys. J. Supp.*, 30, 1–60, doi:10.1086/190356. [3](#)
- Vernazza, J. E., E. H. Avrett, and R. Loeser (1981), Structure of the solar chromosphere. III. Models of the EUV brightness components of the quiet sun, *Astrophys. J. Supp.*, 45, 635–725, doi:10.1086/190731. [3](#)
- Vocks, C., et al. (2018), LOFAR observations of the quiet solar corona, *Astron. Astrophys.*, 614, A54, doi:10.1051/0004-6361/201630067. [139](#)
- Waldmeier, M. (1981), Cyclic Variations of the Polar Coronal Hole, *Solar Phys.*, 70(2), 251–258, doi:10.1007/BF00151332. [26](#)
- Wang, C. B. (2015), A Scenario for the Fine Structures of Solar Type IIIb Radio Bursts Based on Electron Cyclotron Maser Emission, *Astrophys. J.*, 806(1), 34, doi:10.1088/0004-637X/806/1/34. [19](#)
- Wang, H. (1993), Flows; Evolution of Magnetic Fields; and Flares (Invited), in *IAU Colloq. 141: The Magnetic and Velocity Fields of Solar Active Regions*, *Astronomical Society of*

-
- the Pacific Conference Series*, vol. 46, edited by H. Zirin, G. Ai, and H. Wang, p. 323. [29](#)
- Wang, T., N. L. Reginald, J. M. Davila, O. C. St. Cyr, and W. T. Thompson (2017), Variation in Coronal Activity from Solar Cycle 24 Minimum to Maximum Using Three-Dimensional Reconstructions of the Coronal Electron Density from STEREO/COR1, *Solar Phys.*, *292*, 97, doi:10.1007/s11207-017-1130-3. [93](#)
- Wang, Y. M., N. R. Sheeley, D. G. Socker, R. A. Howard, and N. B. Rich (2000), The dynamical nature of coronal streamers, *J. Geophys. Res.*, *105*(A11), 25,133–25,142, doi:10.1029/2000JA000149. [27](#)
- Wang, Y. M., E. Robbrecht, A. P. Rouillard, J. Sheeley, N. R., and A. F. R. Thernisien (2010), Formation and Evolution of Coronal Holes Following the Emergence of Active Regions, *Astrophys. J.*, *715*(1), 39–50, doi:10.1088/0004-637X/715/1/39. [26](#)
- Wayth, R. B., et al. (2018), The Phase II Murchison Widefield Array: Design overview, *Pub. Astron. Soc. Austral.*, *35*, doi:10.1017/pasa.2018.37. [42](#), [112](#)
- Weber, R. R. (1978), Low frequency spectra of type III solar radio bursts, *Solar Phys.*, *59*, 377–385, doi:10.1007/BF00951843. [78](#)
- Wedemeyer, S., et al. (2016), Solar Science with the Atacama Large Millimeter/Submillimeter Array—A New View of Our Sun, *Space Sci. Rev.*, *200*(1-4), 1–73, doi:10.1007/s11214-015-0229-9. [7](#)
- Weiss, L. A. A., and R. T. Stewart (1965), Solar radio bursts of spectral type V, *Aust. J. Phys.*, *18*, 143, doi:10.1071/PH650143. [38](#)
- Wen, Y.-Y., J.-X. Wang, and Y.-Z. Zhang (2007), Magnetic Properties of Metric Noise Storms Associated with Coronal Mass Ejections, *CJAA*, *7*, 265–280, doi:10.1088/1009-9271/7/2/11. [77](#)
- Wentzel, D. G. (1984), Polarization of fundamental type III radio bursts, *Solar Phys.*, *90*, 139–159, doi:10.1007/BF00153791. [37](#), [110](#)
- Wentzel, D. G., P. Zlobec, and M. Messerotti (1986), A test for large-angle radio scattering in the solar corona, *Astron. Astrophys.*, *159*, 40–48. [20](#), [37](#), [110](#)
- Wheaton, B. R. (2009), Bremsstrahlung, in *Compendium of Quantum Physics*, edited by D. Greenberger, K. Hentschel, and F. Weinert, pp. 78–81, Springer Berlin Heidelberg, Berlin, Heidelberg, doi:10.1007/978-3-540-70626-7_23. [15](#)
- White, S. M. (1999), Radio Versus EUV/X-Ray Observations of the Solar Atmosphere, *Solar Phys.*, *190*, 309–330, doi:10.1023/A:1005253501584. [108](#)
- White, S. M. (2005), Coronal magnetic field measurements through gyroresonance emission, in *Solar and Space Weather Radiophysics: Current Status and Future Developments*, edited by D. E. Gary and C. U. Keller, pp. 89–113, Springer Netherlands, Dordrecht, doi:10.1007/1-4020-2814-8_5. [16](#)
- White, S. M., and M. R. Kundu (1997), Radio Observations of Gyroresonance Emission from Coronal Magnetic Fields, *Solar Phys.*, *174*, 31–52, doi:10.1023/A:1004975528106. [11](#), [16](#), [25](#), [110](#)
- White, S. M., G. Thejappa, and M. R. Kundu (1992), Observations of mode coupling in the solar corona and bipolar noise storms, *Solar Phys.*, *138*, 163–187, doi:10.1007/BF00146202. [20](#), [123](#), [125](#), [141](#)
- White, S. M., et al. (2011), The Relationship Between Solar Radio and Hard X-ray Emission,

References

- Space Sci. Rev.*, 159, 225–261, doi:10.1007/s11214-010-9708-1. [51](#)
- Wild, J. P. (1970), Some Investigations of the Solar Corona: The First Two Years of Observation With the Culgoora Radioheliograph, *Pub. Astron. Soc. Austral.*, 1(8), 365–370, doi:10.1017/S1323358000012364. [6](#)
- Wild, J. P., and L. L. McCready (1950), Observations of the Spectrum of High-Intensity Solar Radiation at Metre Wavelengths. I. The Apparatus and Spectral Types of Solar Burst Observed, *Aust. J. Sci. Res. A*, 3, 387, doi:10.1071/PH500387. [6](#), [32](#), [34](#), [48](#), [82](#)
- Wild, J. P., K. V. Sheridan, and A. A. Neylan (1959), An Investigation of the Speed of the Solar Disturbances responsible for Type III Radio Bursts, *Aust. J. Phys.*, 12, 369, doi:10.1071/PH590369. [82](#), [103](#)
- Willes, A. J., and D. B. Melrose (1997), The Polarisation of Second Harmonic Coronal Type III Bursts, *Solar Phys.*, 171, 393–418, doi:10.1023/A:1004993601351. [110](#)
- Willson, R. F. (2005), Very Large Array and SOHO Observations of Type I Noise Storms, Large-Scale Loops and Magnetic Restructuring in the Corona, *Solar Phys.*, 227, 311–326, doi:10.1007/s11207-005-1104-8. [34](#), [121](#)
- Winglee, R. M., and G. A. Dulk (1986), The electron-cyclotron maser instability as the source of solar type V continuum, *Astrophys. J.*, 310, 432–443, doi:10.1086/164696. [19](#), [38](#)
- Winske, D., T. Peter, and D. A. Boyd (1983), Synchrotron emission from runaway electron distributions, *Phys. Fluids*, 26(12), 3497–3507, doi:10.1063/1.864110. [16](#)
- Woo, R. (2007), Filamentary Structures of Coronal White-Light Images, *Solar Phys.*, 241, 251–261, doi:10.1007/s11207-007-0250-6. [19](#), [105](#)
- Wu, C. S., and L. C. Lee (1979), A theory of the terrestrial kilometric radiation, *Astrophys. J.*, 230, 621–626, doi:10.1086/157120. [18](#)
- Xu, Z. (1990), Solar observations in ancient china and solar variability, *Philos. Trans. Royal Soc. A*, 330(1615), 513–515. [22](#)
- Yamada, M., R. Kulsrud, and H. Ji (2010), Magnetic reconnection, *Rev. Mod. Phys.*, 82(1), 603–664, doi:10.1103/RevModPhys.82.603. [29](#)
- Yashiro, S., and N. Gopalswamy (2009), Statistical relationship between solar flares and coronal mass ejections, in *Universal Heliophysical Processes, IAU Symposium*, vol. 257, edited by N. Gopalswamy and D. F. Webb, pp. 233–243, doi:10.1017/S1743921309029342. [31](#)
- Yashiro, S., N. Gopalswamy, G. Michalek, O. C. St. Cyr, S. P. Plunkett, N. B. Rich, and R. A. Howard (2004), A catalog of white light coronal mass ejections observed by the SOHO spacecraft, *J. Geophys. Res. (Space Phys.)*, 109(A7), A07105, doi:10.1029/2003JA010282. [32](#)
- Young, C. A. (1895), *The Sun*, revised edition, international science library ed., The Werner Co., Akron, Ohio. [1](#)
- Yurchyshyn, V., S. Yashiro, V. Abramenko, H. Wang, and N. Gopalswamy (2005), Statistical Distributions of Speeds of Coronal Mass Ejections, *Astrophys. J.*, 619(1), 599–603, doi:10.1086/426129. [32](#)
- Zheleznyakov, V. V. (1970), *Radio emission of the sun and planets*, Pergamon Press, Oxford, doi:10.1016/C2013-0-02176-7. [20](#), [109](#)

-
- Zheleznyakov, V. V. (1977), *Electromagnetic waves in cosmic plasma. Generation and propagation*, Nauka, Moscow. [108](#)
- Zheleznyakov, V. V., and V. V. Zaitsev (1968), The Origin of Type-V Solar Radio Bursts, *Soviet Astron.*, 12, 14. [38](#)
- Zheleznyakov, V. V., and E. Y. Zlotnik (1964), Polarization of Radio Waves Passing through a Transverse Magnetic Field Region in the Solar Corona, *Soviet Astron.*, 7, 485. [20](#), [141](#)
- Zirker, J. B. (1977), Coronal holes and high-speed wind streams, *Rev. Geophys. Space Phys.*, 15, 257–269, doi:10.1029/RG015i003p00257. [26](#)